İSTANBUL TEKNİK ÜNİVERSİTESİ ★ FEN BİLİMLERİ ENSTİTÜSÜ

KARMAŞIK TOPOĞRAFYA ÜZERİNDE SCHWARZ-CHRISTOFFEL DÖNÜŞÜMÜ KULLANILARAK İKİ BOYUTLU ATMOSFERİK AKIŞ MODELLEMESİ

DOKTORA TEZİ

Y. Müh. Hakan ERDUN

Tezin Enstitüye Verildiği Tarih	:	3 Ekim 1996
Tezin Savunulduğu Tarih	:	9 Haziran 1997
Tez Danışmanı	:	Prof. Dr. Selahattin İNCECİK
Diğer Jüri Üyeleri	:	Prof. Dr. Metin DEMİRALP
	:	Prof. Dr. Gürdal TUNCEL
	:	Doç. Dr. Mikdat KADIOĞLU
	:	Doç. Dr. Haluk ÖRS

HAZİRAN 1997

İSTANBUL TECHNICAL UNIVERSITY ★ INSTITUTE OF SCIENCE AND TECHNOLOGY

TWO-DIMENSIONAL ATMOSPHERIC FLOW MODELING BY USING SCHWARZ-CHRISTOFFEL TRANSFORMATION OVER COMPLEX TOPOGRAPHY

Ph.D. THESIS

Hakan ERDUN, M.Sc.

Date of Submission	:	October 3, 1996
Date of Approval	:	June 9, 1997
Supervisor	:	Prof. Dr. Selahattin İNCECİK
Members	:	Prof. Dr. Metin DEMİRALP
	:	Prof. Dr. Gürdal TUNCEL
	:	Assoc. Prof. Mikdat KADIOĞLU
	:	Assoc. Prof. Haluk ÖRS

JUNE 1997

ACKNOWLEDGMENTS

I would like to thank my supervisor Prof. Dr. Selahattin İncecik for his encouragement and valuable support at each step of this thesis.

I would like also to thank to my dear friends Assoc. Prof. Dr. Metin O. Kaya and Assoc. Prof. Dr. İbrahim Özkol for their valuable helpings about the transformations of the model equations, and numerical modeling.

I would really like to say my deepest thankfullness to Assoc. Prof. Dr. Mikdat Kadıoğlu, Prof.Dr. Fevzi Ünal, Dr. Zafer Boybeyi, Prof. Dr. Ruhi Kaykayoğlu and Prof. Dr. Rauf Gardosov for their valuable supports at some steps of my thesis study.

And the last but not the least my thanks goes to my parents and all persons in our department.

October, 1996 Hakan ERDUN

CONTENTS

SYMBOL LIST

ρ : density of air
u : Instantaneous wind component in x-direction
v : Instantaneous wind component in y-direction
w : Instantaneous wind component in z-direction
$\overline{u}$: Mean wind component in x-direction
$\overline{v}$: Mean wind component in y-direction
$\overline{w}$: Mean wind component in z-direction
u' : Fluctuation of wind component in x-direction
v' : Fluctuation of wind component in y-direction
w' : Fluctuation of wind component in z-direction
u_g : Geostrophic wind component in x-direction
v_g : Geostrophic wind component in y-direction
p : Instantaneous atmospheric pressure
$\overline{p}$: Mean atmospheric pressure
p' : Atmospheric pressure perturbation
T : Temperature ($°C$)
θ : Instantaneous potential temperature
$\overline{\theta}$: Mean potential temperature
θ' : Potential temperature perturbation
g : Gravitational acceleration
Ω : Angular velocity of the Earth
S_θ : Source-sink term
α : Specific volume
f : Coriolis parameter
t : Time
L_x : Length of the domain
L_z : Height of the domain
ϕ : Latitude
σ : Sigma coordinate variable
σ_p : Terrain-following sigma coordinate variable
$\tilde{p}$: Logarithmic-pressure coordinate variable
η : Step-mountain coordinate variable
σ_θ : Terrain-following isentropic coordinate variable
$\tilde{s}$: Entropy coordinate system variable
$\underline{z}$: Simple height coordinate variable
S : Terrain-following S-coordinate variable
σ_z : Terrain-following height coordinate variable
ζ : Zeta coordinate system variable

z_L	:	Logarithmic height coordinate variable
z_η	:	Logarithmic height coordinate variable
$\tilde{z}$	:	Logarithmic height coordinate variable
s	:	Logarithmic height coordinate variable
z_p	:	Pseudo-height coordinate system variable
λ	:	Transformed plane
x, y	:	Physical coordinate variables
$\overline{x}, \overline{y}$	:	Auxiliary coordinate variables
ξ, η	:	Computational coordinate variables
τ	:	Reynolds stress
K_m	:	Subgrid scale mixing coefficient
$\mathcal{D}$	:	Deformation tensor
Def	:	Total deformation
$\tilde{\lambda}$	:	Characteristic turbulence length scale
Δ	:	Representative grid interval
Pr	:	Prandtl number
Ri	:	Richardson number
$\mathbf{a}_i$	:	Covariant base vector
$\mathbf{a}^i$	:	Contravariant base vector
g_{ij}	:	Covariant base vector
g^{ij}	:	Contravariant base vector
J	:	Jacobian of the transformation
Δx	:	Horizontal grid interval
Δz	:	Vertical grid interval
Δt	:	Time step

FIGURE LIST

Page Number

TABLE LIST

Page Number

SUMMARY

Local weather over complex topography is greatly influenced by the modification of flow by blocking and channeling. An understanding of these mesoscale mechanisms, through both modeling and field studies, should lead to greater forecasting skill in these regions. In addition, the dispersion of pollution from industry sited in valleys is often hampered by meteorological conditions resulting directly from orographically induced wind systems.

In this study, the results of the atmospheric flow modeling over complex topography by using Schwarz-Christoffel transformation have been given.

In most of the meteorological models, non-orthogonal grid system is used for the modeling of an atmospheric phenomenon over the complex topography. In using this kind of non-orthogonal grid system, the errors especially in the calculation of pressure gradient in the lower atmosphere increase where the slopes of topography were not much less than 45 degrees. Furthermore, in a non-orthogonal system, transformation equations that are used in the model include extra terms according to an orthogonal system. Consequently, the computational time increases.

We used here Schwarz-Christoffel transformation to eliminate the above problems. This kind of transformations is used to generate the orthogonal grid points over the topography that has any slopes and scales. The reason of using widely non-orthogonal systems (for example, terrain-following height coordinate system) by modelers is due to simplicity on writing the computer code.

In this thesis, the two-dimensional atmospheric flow model over complex topography is developed. The model formulation is based on the shallow convection system and meso-β scale. The model includes the non-hydrostatic and the buoyancy terms in addition to geostrophic and Coriolis terms. For the turbulence model, Smagorinsky and Lilly's subgrid-scale mixing formulation is used. The model does not include radiative processes and PBL (Planetary Boundary Layer) parameterizations.

In order to test the model, a Gaussian-shaped mountain within a domain having a width of 40 km and a height of 4 km. Domain has 50x21 grid-points. The horizontal grid interval is 810 m, and time step is taken to be 2.5 sec.

According to model results, the flow field over the given topography has been modeled realistically in global meaning.

ÖZET

Küçük, bölgesel ve büyük ölçekli meteorolojik modeller, atmosferik olayların anlaşılmasında, atmosferik parametrelerin gelecekteki durumlarının belirlenmesinde ve hava kirliliği modelleri için gerekli olan giriş bilgilerini sağlamada yardımcı olduklarından meteorologlar için vazgeçilmez bir araçtır. Günümüzde oldukça fazla sayıda meteorolojik modellerin olması da modellerin ve modellemenin önemini açıkça göstermektedir

Bir meteorolojik modelin geliştirilmesinde, ilk planda karşılaşılan en büyük zorluk, topografyanın etkisinin modele katılmasında ortaya çıkmaktadır. Büyük ölçekli modellerde topografya üzerindeki ayrıntılar çok önemli değildir ve topografya modele kaba bir tarifle dahil edilebilir. Bölgesel ve küçük ölçekli modellerde ise, topografya ve üzerindeki şekilller atmosferik akışa doğrudan etki eden en önemli parametredirler ve model, topografyanın detaylı bir tarifini içermek zorundadır. Bununla beraber, topografyanın tarifi aynı zamanda modelde kullanılan grid-aralığına bağlı olarak belirlenir.

Meteorolojik modellerde yaygın olarak kullanılan "düşey koordinat dönüşümleri" küçük ve bölgesel ölçekli modeller için belirli şartlar altında kullanılmaktadır. Bu koordinat dönüşümlerinin kullanımında, topografyadaki eğimlerin 45 dereceden çok çok küçük olması gerekmektedir. Bunun sağlanmaması durumunda yere yakın yerlerde gradyan hesaplarında hatalar önemli derecede artış göstermektedir. Bu yüzden, dik yamaçlı dağlık veya dik inişli vadi olan bölgelerde bu koordinat dönüşümlerini içeren modellerin kullanımı mümkün olmamaktadır.

Bu tez çalışmasında topografyanın ölçeğinden, topografyanın eğimlerinden ve üzerindeki şekillerden (binalar, kuleler v.b.) bağımsız olarak çalışabilecek iki boyutlu bir model geliştirilmiştir.

Modelde topografyanın detaylı olarak tanımlanması için Schwarz-Christoffel olarak adlandırılan dönüşüm kullanılmıştır. Schwarz-Christoffel dönüşümü, poligon şeklinde tanımlanmış olan topografyanın düz bir şekle (eğimlerin sıfır olduğu topografyaya) çevrilmesinde ve aynı zamanda model denklemlerin çözümünün yapılacağı ortogonal grid noktalarının üretilmesinde kullanılmıştır.

Schwarz-Christoffel dönüşümünde Davis (1979) tarafından geliştirilen "*değiştirilmiş orta-nokta trapezoid kuralı*"nın kullanımı ile birlikte, grid üretme işlemleri sırasında topografyanın keskin köşelerinde ortaya çıkan tekillikler giderilmekte ve üretilen grid-ağının ortogonal olması bakımından atmosferik modellerde kullanımı için büyük avantajlar sağlamaktadır.

Schwarz-Christoffel dönüşümününde topografyanın düz biçime çevrilmesi ve grid noktalarının üretimi, iteratif olarak yapılmaktadır. Geleneksel meteorolik modellerde, kullanılan grid noktaların en uygun biçimde üretilmemesi ve yapılan kordinat dönüşümünün ortogonal olmamasına rağmen, sadece kullanımındaki kolaylıktan dolayı ortogonal olmayan dönüşümler (örneğin, araziyi-izleyen kordinat sistemi) yaygın olarak kullanılmaktadır.

Modelde bir ortogonal grid-ağının kullanımı, dönüşüm denklemlerinde ortogonal olmayan sistemdekine göre fazladan terimlerin atılmasını ve böylece hesap zamanından tasarruf edilmesini sağlar. Ayrıca ortogonal sistemde yere yakın bölgelerdeki gradyan hesapları daha doğru olarak yapılır. Böylece model, topografik özelliklerden mümkün olduğunca bağımsız hale getirilmiş olur.

Bu çalışmada, atmosferik akış modeli, 2-boyutlu (yatay-ve-düşey eksenler) olarak dizayn edilmiştir. Model, sığ konveksiyon sistemi yaklaşımı, ve meso-β ve alt ölçekleri için formüle edilmiştir. Buna göre modelin geçerli olduğu uzaysal alan, düşeyde 4km ölçeği ile sınırlıdır.

Model, hidrostatik olmayan terim (non-hydrostatic), Buoyancy terimi, jeostofik ve Coriolis terimlerini içermektedir. Model denklemlerinin tanımlanmasında anelastik ve sıkıştırılamazlık kabulleri kullanılmıştır. Böylece model sinoptik ölçekteki etkileri de kısmen içermektedir.

Türbülans modeli için Smagorinsky ve Lilly tarafindan verilen alt-grid ölçeği karışma formülasyonu kullanılmıştır. Bu formülasyonun bir avantajı 2- veya 3-boyutlu modellerde türbülans terimlerinin doğrudan sonlu-farklar şemasında yazılabilmesidir.

Model, radyatif modülünü ve sınır tabaka parametreleştirme işlevlerini içermemektedir.

Model denklemlerinin çözümü için sonlu-farklar metodu kullanılmıştır. Uzaysal türevler için merkezi şema, zamansal türevler için başlangıçta ileri şema ve sonrası için leapfrog şeması kullanılmıştır. Advektif terimleri hesabında ise "upwind" şeması kullanılmıştır. Model denklemleri, matris formuna getirilerek çözülmüştür.

Geliştirilen model, örnek bir topografya üzerinde çalıştırılmıştır. Bu test için 50x21 lik bir grid-ağı kullanılmıştır. Grid aralığı yatayda 810 m ve zaman adımı ise kararlılık kriterine göre 2.5 saniye olarak alınmıştır.

Karmaşık topografya üzerinde türbülanslı akışın yeterli bir tanımlaması için ilk planda atmosferdeki pertürbasyon basınçı büyüklüğünün göz önüne alınması gereklidir. Modelde hesaplanan pertürbasyon basınç değerlerine göre örnek topografyanın rüzgar altı tarafinda yüksek pertürbasyonlar ve rüzgar üstü tarafinda ise düşük pertürbasyonlar görülmektedir. Bu durum, dağın rüzgar alan kısmında rüzgarın dağ yamacını tırmanırken akımın zorlanması ile ifade edilebilir.

Türbülanslı akış alanını kuşatan topografyanın etkilerini gösteren diğer önemli bir gösterge, gerçek atmosferik basınçtır. Gerçek atmosferik basıncı, hesaplanan pertürbasyon basınç değerlerinin başlangıç basınç değerlerine eklenmesi ile bulunur. Elde edilen gerçek atmosferik basınç değerlerine göre örnek topografyanın rüzgar altı tarafinda yüksek pertürbasyondan dolayı yüksek basınç bölgesi ve rüzgar altı tarafinda ise düşük pertürbasyon basıncından dolayı düşük basınç bölgesi görülmektedir. Ayrıca eş basınç çizgileri (isobarik yüzeyler) dağ tepesinde rüzgar altı tarafina doğru büküldüğü ve bu bükülme modelin ileri adımlarında daha belirgin olduğu görülmektedir. Bu da, akım üzerinde dağ etkilerini gösteren en belirgin göstergelerden biridir.

Ayrıca elde edilen bu gerçek basınç değerlerinden elde edilen boyutsuz sürükleme (drag) katsayıları, Durran (1986) tarafından yapılmış 3 boyutlu model çalışmasındaki sürükleme katsayıları ile karşılaştırılmıştır. Bu karşılaştırma sonucunda sürükleme katsayılarının uygun olduğu görülmektedir. Ortaya çıkan farklar, modelde kullanılan dağ profilinin Durran'ın modelindeki dağ profiline göre daha sivri olması ve modelin 2 boyutlu olması sebebiyledir.

Türbülanslı akımın modellenmesinde önemli olan diğer bir parametre de alt-grid karışım katsayılarıdır (K_m). Model için kararlı bir atmosfer şartları kabulü yapıldığından modelde elde edilen alt-grid karışım katsayıları 0.001 ile 2m^2/s arasında olduğu görülmüştür. Hesaplanan alt-ölçek karışım katsayıları değerlerine göre örnek topografyanın üzerinde bir yüksek karışım katsayısı bölgesi oluşmaktadır. Bu bölge, modelin ilerleyen adımlarında dağın rüzgar altı tarafına doğru akımın etkisi ile kaymakta ve sonra akım ayrılmasından dolayı tepenin hemen ardında parçalara bölünmektedir. Akım ayrılması ayrıca hesaplanan rüzgar alanı değerlerine bakıldığında açıkça görülebilir. Rüzgar alanı değerlerine göre, rüzgar başlangıçta topografyanın şekline göre kendini ayarlamakta ve sonra topografyanın etkisinin rüzgar üzerindeki değişimi açıkça ortaya çıkmaktadır.

Model radyasyon modülü içermediğinden dolayı, sıcaklık alanı sadece advektif terimler vasıtasıyla etkilenmektedir. Türbülansın modelde sadece rüzgarın etkileri ile oluşmasını sağlamak için başlangıç sıcaklık alanı, düşük seviyelerde soğuk hava ve yukarda sıcak hava olacak şekilde (termik olarak kararlı bir atmosfer) seçilmiştir. Bununla beraber, modelde radyasyon modulünün etkisini, ve hem buoyancy hem de advektif terimlerinin etkilerini göstermek için başlangıç sıcaklık alanına süni bir pertürbasyon verilmiştir. Pertürbasyon değerleri yerde 1°C ve modelin üstünde 0 °C olacak şekilde yükseklikle doğrusal bir değişim alınmıştır. Model sonuçlarına göre pertürbasyon sıcaklık değerlerinin büyüklüğünde önemli değişiklik görülmemektedir. Pertürbasyon sıcaklık alanının başlangıçta sıcaklık alanına eklenerek elde edilen gerçek sıcaklık değerleri incelendiğinde de, sıcaklık alanında da önemli değişiklikler olmadığı, fakat sadece adveksiyondan dolayı sıcaklık alanının akım yönünde hareket ettiği görülmektedir.

Elde edilen bu sonuçlara göre model global anlamda gerçekçi sonuçlar vermektedir. Model sonuçlarının hassasiyeti, modele rasyon modülünün ve sınır tabaka parametreleştirmelerinin katılmasıyla arttırılabilir. Ayrıca modelde kullanılan kabuller değiştirilerek ve yeni formülasyonlar ekleyerek aşağıda verilen çalışmalara genişletilebilir:

- Model sığ konveksiyon sisteminden derin konveksiyon sistemine göre tekrar düzenlenerek, yukarı atmosferdeki gravite-dalgalarının modellenmesi için kullanılabilir.
- Taşınım ve konsantrasyon denklemleri katılarak, kirleticilerin atmosferde dağılımı ve taşınımı modellenebilir.
- Radyasyon modülü, ısı ve su buharının korunumu denklemleri eklenerek topografik etkilerden dolayı bulut ve sis oluşumu modellenebilir.
- Radyasyon modülü, ısı ve su buharının korunumu denklemleri eklenerek dağlık bölgelerde göllerin etkileri ve kara-deniz etkileşimi ve meltemler modellenebilir.
- Model, ayrıca Schwarz-Christoffel ile elde edilecek iki boyutlu grid ağlarının y-ekseni yönünde sıralanması ve sonra bunların ortogonal olmayan araziyi-izleyen kordinat dönüşümü ile birleştirilmesi sonucunda 3-boyuta genişletilebilir.

CHAPTER 1

INTRODUCTION

The capabilities of regional and mesoscale meteorological models make them attractive to understand meteorological phenomena and to provide the meteorological inputs, for example, required by air pollution models.

The complex topography plays an important role in influencing and forcing atmospheric motion ranging from microscale to planetary system. The complex topography should be taken into consideration in the numerical modeling (for example, in the control of emissions into atmosphere, the dispersion and transport of pollutants, the determination of wind-turbine locations, etc.,).

In numerical simulations of the atmospheric flow, most of the problems come from irregular lower boundary conditions. Various coordinate systems can be used to define the topography and to represent the vertical structure of the atmosphere. Vertical coordinate systems are generally classified in means of the using any variable which monotonously changes in the atmosphere.

In principle, two approaches are available in numerically simulation of the flow above the topography. The first one is to retain the Cartesian framework and apply special techniques for the lower boundary which is accepted as the surface topography. The other is to use a coordinate transformation which transforms the complicated lower boundary of domain into a simple one where the surface is flat but the original and transformed systems are identical. The equations of the simulated model can be solved numerically in the transformed coordinates, and the results retransform into the Cartesian system for graphical displays.

In the Cartesian coordinates, the topography can be represented by a series of blocks. Consequently physical boundaries coincide with cell boundaries, avoiding the major difficulty associated with the flow over complex topography. Approximating topography by a series of blocks is a zero-order approximation to real topography (first term in Taylor expansion). Therefore, the shape of the resultant topography is important in determining the flow properties (Orville 1965,1967,1968; Orville and Sloan, 1970; Hirt and Cook 1972; Vicelli 1971). Due to the slopes of topographical, it sometimes requires a very small vertical grid-interval. If this interval is much smaller than the requirement to resolve the meteorological features, the simulation may be inefficient and expensive, perhaps prohibitively so.

The use of the coordinate transformations for the meteorological applications has been limited to the simplest types of transformations. In these types of transformations, only vertical coordinate variable is transformed to coincide with the lower boundary. A generalized transformation formulation of the Navier-Stokes equations for a non-orthogonal coordinate system has been given by Gal-Chen and Somerville, (1975b). The cost of this kind of numerical models in non-orthogonal coordinates has an increased complexity of the governing equations. Sharman *et al.*, (1988) used a *quasi*-orthogonal grid mesh in the numerical simulation of incompressible and anelastic flows over the complex topography. They also showed the formulations of the orthogonal coordinate transformation of the governing equations. Since the orthogonal system produces fewer additional terms in the transformed governing equations, it has reduced the required computer time. The differences between non-orthogonal and orthogonal systems are discussed in Chapter 5.

In order to generate a well fitted two-dimensional grid-mesh which is most suitable to represent the atmospheric domain with an irregular lower boundary due to topography, the framework is transformed into one of the simplest geometry (i.e., rectangular) on which the solution is known, since the conformal mapping techniques have such a property with which it is possible to preserve angles (so, preserves orthogonality) and invariance of stretching (Thompson *et al.*, 1976). Consequently, in this thesis we preferred the use of the *Schwarz-Christoffel transformation* which is one of the well-known conformal mapping techniques in order to generate orthogonal grid-points. The use of Schwarz-Christoffel transformation in the atmospheric flow modeling is introduced by Erdun *et al.*, (1996). It is also formulated in Chapter 3.

It is essential that the boundary conditions must be represented accurately by the finite-difference schemes for the numerical solution of the governing equations in the immediate vicinity of the surfaces. The pressure and the other forces on the surface are directly dependent on the large gradients that prevail in the near surface, and accurate pressure and force coefficients require that these large gradients must be represented accurately (Pielke, 1984). A main reason occurring of large errors in the simulations appear in the calculation of gradients near the surface when of using the non-orthogonal grid mesh. Therefore, for mesoscale modeling, the orthogonality in the coordinate transformations should be provided. Besides, the fine mesh, where the large gradients appear, must be used. The Schwarz-Christoffel transformation can generate *orthogonal fine mesh* on the near surface and *orthogonal coarse mesh* in the upper levels. Since Schwarz-Christoffel transformation can remove the singularities in the vicinity of very sharp edges of the topography in the process of mesh generation, it can be used for any topography even if it has very sharp edges, for example, with 90° slopes. With these properties, the Schwarz-Christoffel transformation can be used to get accurate results in the numerical simulation of atmospheric flows *over any complex topography* and *on any spatial scales.* Therefore, in this thesis, Schwarz-Christoffel transformation is preferred to be used as a grid generator. The model equations are designed for two-dimensional (only x- and z-directions) flow simulations. The model has non-hydrostatic and buoyancy affects under the assumptions of anelastic and incompressible. Therefore, the model may be valid up to meso-β scale.

In this thesis, the atmospheric flow model is designed as two-dimensional. The model formulation is based on the shallow convection system and meso-β scale. The model includes the non-hydrostatic and the buoyancy terms in addition to geostrophic and Coriolis terms, under the anelastic and incompressibility assumptions. For the turbulence model, Smagorinsky and Lilly's subgrid scale mixing formulations are used, since these are convenient to write directly by using the finite difference schemes in 2-D and 3-D models. In the model, radiative processes and PBL (Planetary Boundary Layer) parameterizations are not used. In order to test the model, a modified form of "Witch of Agnesi" mountain profile is used. This mountain is steeper than the original mountain profile and is centered in a computational domain having a width of 40 km and a height of 4 km. The domain has 50×21 grid-points.

CHAPTER 2

MESOSCALE MODELING

Local weather over complex topography is greatly influenced by the modification of synoptic flow by blocking and channeling. An understanding of these mesoscale mechanisms, through both modeling and field studies, should lead to greater forecasting skill in these regions. In addition, the dispersion of pollution from industry sited in valleys is often hampered by meteorological conditions resulting directly from orographically induced wind systems (for example, deep and multiple temperature inversions and reversals of wind direction with height).

Complex topography plays an important role in influencing and forcing atmospheric motion ranging over several spatial scales. A number of meteorologists for whom there is a wide variety of problems of interest, have devoted many efforts to the study of topographic effects on the general circulation and synoptic processes. Mostly the problems, faced up for the solution of the model equations of which fluid flow and thermodynamics properties are contained, need to be solved on limited-area models. These models have generally irregular lower boundary surfaces on small spatial scale. Mountain drag studies, air flow over advection of pollutants and boundary layer parameterization studies where the non-hydrostatic dynamics require explicit treatment, are frequent types of these models.

There are two fundamental methods of simulating mesoscale atmospheric flows: *physical models* and *mathematical models.* According to the first technique, scale model replicas of observed ground surface characteristics (e.g., topographic relief, buildings) are constructed and inserted into a chamber such as a wind tunnel or a water tank. The flow of air or other gases or liquids in this chamber is adjusted so as to best represent the larger scale, observed atmospheric conditions. Mathematical modeling, by contrast, utilizes such basic analysis techniques as algebraic and calculus based for solving directly all or a subset of meteorological equations. These equations can be solved exactly, including the complete system of the equations, requiring the approximate solution technique called numerical modeling.

Primitive equations are nonlinear, and they cannot be solved analytically in their complete form. Therefore, numerical techniques must be used to obtain their solutions. Although the atmosphere and the equations used to represent the atmosphere are continuous, to solve these partial differential equations numerically requires approximating the equations by rewriting them in discrete or finite-difference form.

When the topography is simple or has regular blocks, rectangular grid mesh is generated easily, and primitive equations are solved directly in their finite differenced forms. Because the lower part of atmospheric domain is complexdue to the topography, the structure of grid mesh becomes complex. In this case the lower boundary conditions of atmospheric domain for primitive equations cannot be given simply. To simplify lower boundary conditions, the complex structure of grid mesh is converted to a rectangular grid mesh form and then primitive equations are transformed to adapt a new grid mesh before the discretization process.

The various coordinate systems are used to represent the vertical structure of the atmosphere or to generate grid-mesh over the topography for the atmospheric numerical flow modeling using primitive equations. The vertical coordinate variable can be any monotonously changing variable. The choice determines the exact form of the primitive equations.

Geometrical altitude was considered as a vertical coordinate after Richardson's study (1922). Despite of the conceptual simplicity of geometrical height, it had never been used extensively in the modeling of atmosphere until Kasahara and Washington (1967) who reformulated Richardson's approach for high-speed computers. The use of pressure as a vertical coordinate became very popular during the 1950s. Most of the numerical models which use pressure coordinates were successfully tested. Charney and Phillips (1953) used a quasi-geostrophic model, Hinkelmann (1959) and Leith (1965) used primitive equation models. In the 1970s, interest had been reviewed in the use of potential temperature as a vertical coordinate for objective synoptic analysis (Shapiro and Hastings, 1973) and for weather prediction with a quasi-geostrophic model (Bleck, 1973) and with primitive equation models (Eliassen and Raustein, 1968, 1970; Shapiro, 1973). The use of potential temperature as a vertical coordinate seems to be particularly suitable for resolving details of frontal structure. Kasahara (1974) and Sundquist (1979) have discussed various types of vertical coordinates. Kasahara (1974) derived the primitive equations using a generalized vertical coördinate. He also showed the transformation of the equations. Gal-Chen and Somerville, (1975a) showed the transformation equations of the height coordinate system for the non-orthogonal system. After this study, the height coordinate transformations were used widely in the mesoscale modeling (Clark, 1977; Mengelkamp, 1991; Boybeyi and Raman, 1992). The use of the orthogonal coordinates in the atmospheric modeling was introduced by Sharman *et al.*, (1988) who is used a quasi-conformal transformation and Erdun *et al.*, (1996) who is used a full-conformal transformation.

2.1 Governing Equations

Pielke (1984) gives a wealth of information on the present status of skill and summarizes most of the inherent problems.

The governing equations employed in this study based on conservation principles and their derivation can be found in, for example, Pielke (1984). The equations are shown in Einstein's summation notation because all components of the equations can be represented in just one term.

The instantaneous continuity, momentum and heat equations are, respectively,

$$\frac{\partial \rho}{\partial t} = -\frac{\partial}{\partial x_j}(\rho u_j) \tag{2.1}$$

$$\frac{\partial u_j}{\partial t} = -u_j \frac{\partial u_i}{\partial x_j} - \frac{1}{\rho}\frac{\partial p}{\partial x_j} - g\delta_{i3} - 2\varepsilon_{ijk}\Omega_j u_k \tag{2.2}$$

$$\frac{\partial \theta}{\partial t} = -u_j \frac{\partial \theta}{\partial x_j} + S_\theta \tag{2.3}$$

where the subscripts i, j, and k = 1,2 and 3 correspond to coordinate directions of the independent spatial variables, $x_j = (x_1, x_2, x_3) = (x, y, z)$ (summation is implied whenever an index repeats in the same term), $u_j = (u_1, u_2, u_3) = (u, v, w)$ velocity components, Ω_j is a component of the earth's angular velocity; g gravitational acceleration, p atmospheric pressure, ρ density, θ potential temperature, S_θ all sources and sinks.

Kronecker Delta,

$$\delta_{ij} = \begin{bmatrix} 1 & 0 & 0 \\ 0 & 1 & 0 \\ 0 & 0 & 1 \end{bmatrix} = \begin{cases} 0 & \text{for } i \neq j \\ 1 & \text{for } i = j \end{cases}$$

where i refers to row, and j refers to column.

Alternating unit tensor,

$$\varepsilon_{ijk} = \underbrace{\overbrace{\begin{bmatrix} 0 & 0 & 0 \\ 0 & 0 & 1 \\ 1 & -1 & 0 \end{bmatrix}}^{j} \begin{bmatrix} 0 & 0 & -1 \\ 0 & 0 & 0 \\ 1 & 0 & 0 \end{bmatrix} \begin{bmatrix} 0 & 1 & 0 \\ -1 & 0 & 0 \\ 0 & 0 & 0 \end{bmatrix}}_{k} \left.\vphantom{\begin{bmatrix} 0 \\ 0 \\ 0 \end{bmatrix}}\right\} i$$

where the following device has been used: for 0, $i = j$, $i = k$, and $j = k$; for 1, even permutations of i, j, and k; for -1, odd permutations of i, j, and k.

Since the mesoscale circulations have horizontal scales on the order of 10 to 100 km and a vertical size of up to approximately 10 km, it is necessary to integrate the conservation equations over the specified spatial and temporal scales. For a specific mesoscale system, the smaller these scales, the better the *resolution* of the circulation.

In performing the integration of the equations (Eq. 2.1-2.3), it is convenient to carry the Reynold decomposition. According to the Reynolds decomposition, mean and turbulent components:

$$\phi = \overline{\phi} + \phi'',$$

where ϕ represent any one of the dependent variables, and $\overline{\phi}$ can be defined as

$$\overline{\phi} = \frac{1}{\Delta t \Delta x \Delta y \Delta z} \int_t^{t+\Delta t} \int_x^{x+\Delta x} \int_y^{y+\Delta y} \int_z^{z+\Delta z} \phi \, dz \, dy \, dx \, dt. \tag{2.4}$$

Here $\overline{\phi}$ represents any the average of any dependent variable ϕ over the finite time increment Δt and space intervals Δx, Δy, and Δz. The variable ϕ'' is the deviation of ϕ from this average and is often called the *subgrid scale perturbation*. In a numerical model, Δt is the *time step*, and Δx, Δy, and Δz represent the model *grid intervals*.

Note that the validity of the Reynolds assumption requires the existence of a spectral gap scale separation between resolvable motions and parameterized subgrid processes (Pielke, 1984). In some observations such a separation generally does not exist (Young, 1987; Courtney and Troen, 1990). This assumption is questionable and therefore it should be applied carefully (Thunis and Bornstein, 1996).

As performed on ϕ in Eq. (2.4), one convenient decomposition is to define the averaging volume such that the subgrid scale perturbation includes the non-hydrostatic part of the solution and the resolvable scale is accurately represented by the hydrostatic assumption. Thus the influence of the non-hydrostatic component of a model would be parameterized and the hydrostatic portion would be explicitly resolved.

$$\overline{(\ )} = \frac{1}{\Delta t \Delta x \Delta y \Delta z} \int_{t}^{t+\Delta t} \int_{x}^{x+\Delta x} \int_{y}^{y+\Delta y} \int_{z}^{z+\Delta z} (\ )\, dz\, dy\, dx\, dt. \tag{2.5}$$

This operation is often called as *grid-volume averaging* since it is performed over the spatial increments Δx, Δy and Δz.

In Eq. (2.4), $\overline{\phi}$ can be written by assuming

$$\overline{\phi} = \phi_o + \phi',$$

where

$$\phi_o = \frac{1}{L_x L_y} \int_{x}^{x+\Delta x} \int_{y}^{y+\Delta y} \overline{\phi}\, dy\, dx\,. \tag{2.6}$$

is called the *layer-domain-averaged variable.* The symbols L_x and L_y represent the distances which are comparable large to the mesoscale system (ϕ_o is assumed to represent the synoptic scale atmospheric conditions). The variable ϕ', then, represents the mesoscale deviations from this larger scale.

2.2 Scale Analysis

The method of scale analysis has been used to determine the relative importance of the individual terms in the conservation equations. This technique involves the estimation of their order of magnitude through the use of representative values of the dependent variables and constants that make up these terms. Scale analysis can be applied either to individual terms in the fundamental conservation equations or to analytical solutions of a coupled set of the conservation equations.

The most rigorous analysis procedure is to evaluate specific solutions of the conservation equations with and without particular terms to establish their importance. An example of such an analysis, for the hydrostatic assumption, is sea breeze simulations.

a) Scale analysis of conservation of mass equation

To determine an appropriate and consistent approximate form of mass conservation equation, parts of the scale analysis of this equation by Dutton and Fichtl (1969) are utilized in the following.

Using the relationship between density and specific volume is given by

$$\rho = 1/\alpha,$$

Eq. (2.1) can be rewritten as

$$\frac{\partial \alpha}{\partial t} = -u_j \frac{\partial \alpha}{\partial x_j} + \alpha \frac{\partial u_j}{\partial x_j} \tag{2.7}$$

where $\alpha_\circ$ is defined as a synoptic scale reference specific volume and α' is the mesoscale perturbation, and assuming that $\alpha = \alpha_\circ + \alpha'$, then Eq. (2.7) can be rewritten as

$$\frac{\partial}{\partial t}(\alpha_\circ + \alpha') = -u_j \frac{\partial}{\partial x_j}(\alpha_\circ + \alpha') + (\alpha_\circ + \alpha')\frac{\partial u_j}{\partial x_j}. \tag{2.8}$$

To simplify the scale analysis of this equation, it is assumed that

$$\left|\frac{\partial \alpha_\circ}{\partial t}\right| \ll \left|\frac{\partial \alpha'}{\partial t}\right|; \qquad \left|\frac{\partial \alpha_\circ}{\partial x}\right| \ll \left|\frac{\partial \alpha'}{\partial x}\right|; \qquad \left|\frac{\partial \alpha_\circ}{\partial y}\right| \ll \left|\frac{\partial \alpha'}{\partial y}\right|, \tag{2.9}$$

so that Eq. (2.8) becomes

$$\frac{\partial \alpha'}{\partial t} = -u\frac{\partial \alpha'}{\partial x} - v\frac{\partial \alpha'}{\partial y} - w\frac{\partial \alpha'}{\partial z} - w\frac{\partial \alpha_\circ}{\partial z} + \alpha_\circ\left(1 + \frac{\alpha'}{\alpha_\circ}\right)\left(\frac{\partial u}{\partial x} + \frac{\partial v}{\partial y} + \frac{\partial w}{\partial z}\right) \tag{2.10}$$

For mesoscale atmospheric circulations, the adaptation of the assumptions given in Eq. (2.9) requires that the synoptic state change much more slowly than the mesoscale system and the horizontal synoptic gradients be much less than the mesoscale gradients.

It is also assumed that

$$\left|\frac{\alpha'}{\alpha_o}\right| \ll 1,$$

so that Eq. (2.10) reduces to

$$\frac{\partial \alpha'}{\partial t} = -u\frac{\partial \alpha'}{\partial x} - v\frac{\partial \alpha'}{\partial y} - w\frac{\partial \alpha'}{\partial z} - w\frac{\partial \alpha_o}{\partial z} + \alpha_o\left(\frac{\partial u}{\partial x} + \frac{\partial v}{\partial y} + \frac{\partial w}{\partial z}\right). \tag{2.11}$$

This requirement on the ratio of the mesoscale perturbation specific volume to the synoptic scale reference value is reasonable when realistic values of temperature and pressure are inserted into the ideal gas law ($p\alpha = RT$).

The method of scale analysis is used to estimate the magnitude of the remaining terms in Eq. (2.11), so that

$$\left|\frac{\partial \alpha'}{\partial t}\right| \sim \frac{\alpha'}{t_\alpha},$$

$$\left|u\frac{\partial \alpha'}{\partial x}\right| \sim U\frac{\alpha'}{L_x}, \qquad \left|v\frac{\partial \alpha'}{\partial y}\right| \sim V\frac{\alpha'}{L_y}, \qquad \left|w\frac{\partial \alpha'}{\partial z}\right| \sim W\frac{\alpha'}{L_z},$$

$$\left|w\frac{\partial \alpha_o}{\partial z}\right| \sim W\frac{\alpha_o}{H_\alpha}, \tag{2.12}$$

$$\left|\alpha_o\frac{\partial u}{\partial x}\right| \sim \alpha_o\frac{U}{L_x}, \qquad \left|\alpha_o\frac{\partial v}{\partial y}\right| \sim \alpha_o\frac{V}{L_y}, \qquad \left|\alpha_o\frac{\partial w}{\partial z}\right| \sim \alpha_o\frac{W}{L_z},$$

where t_α^{-1} represents the characteristic frequency of variations in specific volume on the mesoscale; U, V, and W are representative values of the components of velocity; L_x, L_y, and L_z are the spatial scales of the mesoscale disturbance; and H_α, the *density-scaled height* of the atmosphere, is defined as

$$H_\alpha^{-1} = \frac{1}{\alpha_o}\frac{\partial \alpha_o}{\partial z}.$$

In the troposphere H_α is approximately 8 km, as illustrated schematically in Fig (2.1) (Pielke, 1984).

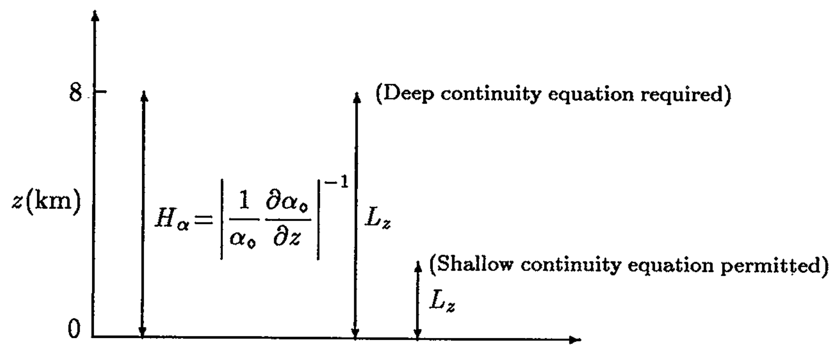

Fig 2.1 Schematic illustration contrasting deep and shallow atmospheric circulations. The depth L_z corresponds to the vertical of the circulation. In the earth's atmosphere $H_\alpha \simeq 8$ km.

i) Deep continuity equation

To examine the necessity for retaining individual terms in Eq. (2.11), it is customary to examine their ratio relative to one of the terms that is expected to remain. In the first case to be examined, the terms are divided by the order of magnitude estimate for $w\partial\alpha_o/\partial z$, resulting in

$$\left|\frac{\partial\alpha'}{\partial t}\right| \Big/ \left|w\frac{\partial\alpha_o}{\partial z}\right| \sim \frac{\alpha'}{\alpha_o}\frac{H_\alpha}{t_\alpha W}, \qquad \left|u\frac{\partial\alpha'}{\partial x}\right| \Big/ \left|w\frac{\partial\alpha_o}{\partial z}\right| \sim \frac{\alpha'}{\alpha_o}\frac{U}{W}\frac{H_\alpha}{L_x},$$

$$\left|v\frac{\partial\alpha'}{\partial y}\right| \Big/ \left|w\frac{\partial\alpha_o}{\partial z}\right| \sim \frac{\alpha'}{\alpha_o}\frac{V}{W}\frac{H_\alpha}{L_y}, \quad \left|w\frac{\partial\alpha'}{\partial z}\right| \Big/ \left|w\frac{\partial\alpha_o}{\partial z}\right| \sim \frac{\alpha'}{\alpha_o}\frac{H_\alpha}{L_z},$$

$$\left|\alpha_o\frac{\partial u}{\partial x}\right| \Big/ \left|w\frac{\partial\alpha_o}{\partial z}\right| \sim \frac{U}{W}\frac{H_\alpha}{L_x}, \qquad \left|\alpha_o\frac{\partial v}{\partial y}\right| \Big/ \left|w\frac{\partial\alpha_o}{\partial z}\right| \sim \frac{V}{W}\frac{H_\alpha}{L_y},$$

$$\left|\alpha_o\frac{\partial w}{\partial z}\right| \Big/ \left|w\frac{\partial\alpha_o}{\partial z}\right| \sim \frac{H_\alpha}{L_z}.$$

Since $|\alpha'/\alpha_o| \ll 1$, the terms $u\partial\alpha'/\partial x$, $v\partial\alpha'/\partial y$, and $w\partial\alpha'/\partial z$ are much less than $\alpha_\circ \partial u/\partial x$, $\alpha_\circ \partial v/\partial y$, and $\alpha_\circ \partial w/\partial z$ and can be neglected in Eq. (2.11), provided

$$(i)\ L_z \sim H_\alpha, \quad (ii)\ \frac{U}{W}\frac{H_\alpha}{L_x} \sim 1, \quad (iii)\ \frac{V}{W}\frac{H_\alpha}{L_y} \sim 1, \quad (iv)\ \frac{H_\alpha}{t_\alpha W} \sim 1. \tag{2.13}$$

Then Eq. (2.11) can be written as

$$w\frac{\partial \alpha_\circ}{\partial z} - \alpha_\circ\left(\frac{\partial u}{\partial x} + \frac{\partial v}{\partial y} + \frac{\partial w}{\partial z}\right) = 0. \tag{2.14}$$

Since L_z is approximately equal to H_α, conditions (ii) and (iii) in Eq. (2.13) require that $U/L_x \sim W/L_z$ and $V/L_y \sim W/L_z$.

In accordance with the fact that L_x is larger than L_z as one or two orders of magnitude, it is expected that the vertical velocity W should be one or two orders of magnitude less than U and V (e.g., for $L_x \sim 80$ km and $L_z \sim 8$ km, then $W \sim 0.1U$). This relation between velocities and the horizontal and vertical scales of atmospheric circulations comes from the condition of $|\alpha'/\alpha_\circ| \ll 1$. Because of this constraint, velocities in a longer, horizontal leg of an atmospheric circulation must be proportionately stronger to preserve mass continuity without creating large fluctuations in specific volume.

The last requirement that needs to be justified in Eq. (2.13) is condition (iv). The scaled variable t_α represents a time period in which significant variations in specific volume occur on the mesoscale and can be approximated by

$$t_\alpha \sim L/C, \tag{2.15}$$

where L is the wavelength over which variations occur and C the rate of movement of these variations. If the changes are caused by advection, then U, V, or W is used to represent C, whereas a characteristic group velocity C_g is utilized if wave propagation is dominant. The wavelength L is estimated as L_x and L_y for horizontal motion and L_z for vertical movement. When changes in specific volume are assumed primarily to be caused by advection or when the wave group velocity has approximately the same speed as the wind velocity, then

$$t_\alpha W \sim LW/C \sim \begin{cases} L_x W/U \sim L_y W/V \sim H_\alpha, \\ L_z W/W \sim L_z \sim H_\alpha, \end{cases}$$

where conditions $(i) - (iii)$ in Eq. (2.13) have been used. Therefore,

$$\left|\frac{\partial \alpha'}{\partial t}\right| \Big/ \left|w\frac{\partial \alpha_\circ}{\partial z}\right| \sim \left|\frac{\alpha'}{\alpha_\circ}\right|,$$

so that local variations in density can be neglected in the conservation of mass relation if $|\alpha'/\alpha_\circ| \ll 1$.

Finally, if $L_y \gg L_x$, mesoscale variations in the x direction are expected to be dominant and the derivatives on y in Eq. (2.14) can be ignored. In this case, the equation reduces to the two-dimensional form given by

$$w\frac{\partial \alpha_\circ}{\partial z} - \alpha_\circ\left(\frac{\partial u}{\partial x} + \frac{\partial w}{\partial z}\right) = 0.$$

Equation (2.14) is customarily written to include the terms $u\partial\alpha_\circ/\partial x$ and $v\partial\alpha_\circ/\partial y$ and is given by

$$\frac{\partial}{\partial x_j}(\alpha_\circ^{-1}u_j) = 0,$$

or, returning to the use of density instead of specific volume,

$$\frac{\partial}{\partial x_j}(\rho_\circ u_j) = 0, \tag{2.16}$$

where $\rho_\circ = 1/\alpha_\circ$.

Dutton and Fichtl (1969) refer to this relation as the *deep convection continuity equation* because the vertical depth of the circulation is on the same order as the density scale depth. As originally shown by Ogura and Phillips (1962), and discussed by Lipps and Hemler (1982), the use of this form of the conservation-of-mass relation eliminates sound waves as a possible solution, which led Ogura and Phillips (1962) to refer to Eq. (2.16) as the *anelastic*, or *soundproof assumption*. Because such waves are of no direct interest in most applications of mesoscale meteorology, this equation is often employed to represent mass conservation in mesoscale models in lieu of the more complete prognostic conservation-of-mass equation given by Eq. (2.7). Moreover, the elimination of sound waves permits more economical use of certain numerical solution techniques because their computational stability is dependent on having a time step less than or equal to the time it takes a wave to travel between grid points. Sound waves are the fastest non-electromagnetic waveform in the atmosphere.

ii) Shallow continuity equation

A more restrictive mass-conservation relation is derived by dividing the scaled terms in Eq. (2.12) by the scaled form of $\alpha_\circ \partial w/\partial z$ resulting in

$$\left|\frac{\partial \alpha'}{\partial t}\right| \Big/ \left|\alpha_\circ \frac{\partial w}{\partial z}\right| \sim \frac{\alpha'}{\alpha_\circ}\frac{L_z}{t_\alpha W}, \qquad \left|u\frac{\partial \alpha'}{\partial x}\right| \Big/ \left|\alpha_\circ \frac{\partial w}{\partial z}\right| \sim \frac{\alpha'}{\alpha_\circ}\frac{U}{W}\frac{L_z}{L_x},$$

$$\left|v\frac{\partial \alpha'}{\partial y}\right| \Big/ \left|\alpha_\circ \frac{\partial w}{\partial z}\right| \sim \frac{\alpha'}{\alpha_\circ}\frac{V}{W}\frac{L_z}{L_y}, \qquad \left|w\frac{\partial \alpha'}{\partial z}\right| \Big/ \left|\alpha_\circ \frac{\partial w}{\partial z}\right| \sim \frac{\alpha'}{\alpha_\circ},$$

$$\left|w\frac{\partial \alpha_\circ}{\partial z}\right| \Big/ \left|\alpha_\circ \frac{\partial w}{\partial z}\right| \sim \frac{L_z}{H_\alpha}, \qquad \left|\alpha_\circ\frac{\partial u}{\partial x}\right| \Big/ \left|\alpha_\circ \frac{\partial w}{\partial z}\right| \sim \frac{U}{W}\frac{L_z}{L_x},$$

$$\left|\alpha_\circ\frac{\partial v}{\partial y}\right| \Big/ \left|\alpha_\circ \frac{\partial w}{\partial z}\right| \sim \frac{V}{W}\frac{L_z}{L_y}.$$

As in the previous analysis, since $|\alpha'/\alpha_\circ| \ll 1$, $u\partial\alpha'/\partial x$, $v\partial\alpha'/\partial y$, and $w\partial\alpha'/\partial z$ can be neglected in Eq. (2.11), provided

$$L_z/Wt_\alpha \sim 1, \qquad L_z/H_\alpha \ll 1. \tag{2.17}$$

Then Eq. (2.11) can be written as

$$\alpha_\circ\left(\frac{\partial u}{\partial x} + \frac{\partial v}{\partial y} + \frac{\partial w}{\partial z}\right) = 0. \tag{2.18}$$

It is easier to satisfy the first condition of Eq. (2.27) than the equivalent requirement in Eq. (2.13) because of $L_z \ll H_\alpha$. This requirement implies that the neglect of specific volume variations in Eq. (2.18) is even less important than in Eq. (2.16). The second condition in Eq. (2.17) requires that the depth of the circulation should be much less than the scale height of the atmosphere. In accordance with Dutton and Fichtl (1969) referred to Eq. (2.18) as *shallow convection equation.* Eq. (2.18) in tensor notation is given by

$$\frac{\partial u_j}{\partial x_j} = 0, \tag{2.19}$$

and this relation is often referred to as *incompressibility assumption.* This expression not only removes soundwaves, but also ignores the spatial variations in density. For the case of *homogeneous (constant density)* fluid, this would be the exact form of the conservation-of-mass equation.

Most of the mesoscale models utilize this expression to represent the conservation of mass. There is a certain irony in its use, because although air closely follows the ideal gas law, it is also accurately approximated by the incompressible form of the mass-conservation equation when the atmospheric circulations have a limited vertical extent. This apparent discrepancy is explained by realizing that air is, generally, not physically constrained in its movement. For example, air moves into one side of a parcel, the density can either increase by compression or an equivalent mass of air can move out of the other side of the parcel. As long as the atmospheric parcel is not restricted to a fixed volume, the creation of a pressure gradient between the two sides of the parcel as a result of the different velocities will force the air out of one side so that mass conservation is closely approximated by the incompressible relation (Eq. 2.19)

In mesoscale models either the *prognostic equation* (time-dependent equation) for density (Eq. 2.1), or the *diagnostic equation* (no time-tendency term) Eqs. (2.16) or (2.19) can be used to represent mass conservation.

b) Scale analysis of conservation of heat equation

In mesoscale meteorology, an equivalent rather exhaustive, scale analysis of the conservation of heat relation Eq. (2.3) is not generally made. This is because of the complex mathematical form of the source-sink term S_θ. The conservation-of-mass relation, in contrast, has no such source-sink term so that analysis is relatively simple.

Eq. (2.3) is modified by making the simplifying assumptions regarding the form of S_θ. The development of simplified mathematical representations for any of the source-sink terms is one type of parameterization. The most stringent assumption for the conservation of potential temperature is the requirement of *adiabatic* for all motions in the atmosphere. Therefore, $S_\theta = 0$ and Eq. (2.3) reduces to

$$\frac{\partial \theta}{\partial t} = -u_j \frac{\partial \theta}{\partial x_j} \qquad \text{or equivalently,} \qquad \frac{d\theta}{dt} = 0. \tag{2.20}$$

It is valid to use this assumption in representing the mesoscale atmospheric systems provided as;

$$|S_\theta| \ll \left|\frac{\partial \theta}{\partial t}\right|; \quad \left|u\frac{\partial \theta}{\partial x}\right|; \quad \left|v\frac{\partial \theta}{\partial y}\right|; \quad \left|w\frac{\partial \theta}{\partial z}\right|.$$

This condition is most closely fulfilled when the following are met:

(1) the atmosphere is dry,

(2) comparatively short time periods are involved, so that radiational heating or cooling of the air is relatively small,

(3) the heating or cooling of the lowest levels of the atmosphere by the bottom surface is comparatively small.

c) Scale analysis of conservation of motion equation

A wide range of assumptions have been utilized either to simplify or to alter the form of the conservation of motion equation (Eq. 2.2). In performing scale analysis on this equation it is convenient to decompose the equation into its vertical and horizontal components since the gravitational acceleration is only included in the vertical acceleration equation.

i) Vertical equation of motion

The vertical component of Eq. (2.2) can be written as

$$\frac{\partial w}{\partial t} + u\frac{\partial w}{\partial x} + v\frac{\partial w}{\partial y} + w\frac{\partial w}{\partial z} = -\frac{1}{\rho}\frac{\partial p}{\partial z} - g + 2\Omega u \cos\phi. \tag{2.21}$$

or, equivalently,

$$\frac{dw}{dt} = -\frac{1}{\rho}\frac{\partial p}{\partial z} - g + 2\Omega u \cos\phi. \tag{2.22}$$

These terms can be estimated by the methods-of-scale analysis. The terms on the left side of Eq. (2.21) can be estimated as

$$\left|\frac{\partial w}{\partial t}\right| \sim \frac{W}{t_w}; \qquad \left|u\frac{\partial w}{\partial x}\right|; \quad \left|v\frac{\partial w}{\partial y}\right|; \quad \left|w\frac{\partial w}{\partial z}\right| \sim \frac{U}{L_x}W,$$

where t_w is a time scale related to the period of required for the significant changes in vertical velocity. W and U are characteristic vertical and horizontal velocities, which, if $|\alpha'/\alpha_o| \ll 1$, and $U/L_x \sim W/L_z$ and $V/L_y \sim W/L_z$ to be used to relate the magnitudes of the two velocities. Using the same justification for the vertical velocity time scale t_w as used for t_α, then

$$t_w \sim L_x/U,$$

so that the four terms on the left of Eq. (2.21), and, therefore, the total vertical acceleration given on the left of Eq. (2.22), has a scale of:

$$\left|\frac{\partial w}{\partial t}\right|; \quad \left|u\frac{\partial w}{\partial x}\right|; \quad \left|v\frac{\partial w}{\partial y}\right|; \quad \left|w\frac{\partial w}{\partial z}\right|; \quad \left|\frac{dw}{dt}\right| \sim \frac{UW}{L_x} = \frac{U^2 L_z}{{L_x}^2}.$$

To estimate the vertical pressure gradient term in Eq. (2.22), it is convenient to utilize the ideal gas law ($p\alpha = R_d T_v$),

$$\alpha\frac{\partial p}{\partial z} = R_d\frac{\partial T}{\partial z} - \frac{RT}{\alpha}\frac{\partial \alpha}{\partial z},$$

where the subscripts d and v have been removed from R and T for convenience. To simplify the scale analysis it is assumed that the atmosphere is *isothermal* ($\partial T/\partial z = 0$) and that

$$\frac{1}{\alpha}\frac{\partial \alpha}{\partial z} \simeq \frac{1}{\alpha_o}\frac{\partial \alpha_o}{\partial z} = H_\alpha^{-1} \qquad \text{so that} \qquad \alpha\frac{\partial p}{\partial z} \sim R_d T/H_\alpha.$$

The two remaining terms are given as $|g|$ and $|2\Omega u \cos\phi| \sim 2\Omega U$.

The ratio of the orders of magnitude of the vertical acceleration to the vertical pressure gradient is given by

$$\left|\frac{dw}{dt}\right| \Big/ \left|\alpha\frac{\partial p}{\partial z}\right| \sim \frac{H_\alpha L_x}{L_x^2}\frac{U^2}{RT} = R_w. \tag{2.23}$$

when Eq. (2.14) was used as the continuity equation, $L_z \sim H_\alpha$ so that,

$$\left|\frac{dw}{dt}\right| \Big/ \left|\alpha\frac{\partial p}{\partial z}\right| \sim \frac{{H_\alpha}^2}{L_x^2}\frac{U^2}{RT} = R_w. \tag{2.24}$$

Eq. (2.24) implies that the vertical accelerations become more important as the horizontal velocity increases, whereas higher temperatures and longer horizontal wavelength decrease its importance.

According to scale analysis, to neglect the vertical acceleration term in Eq. (2.22), R_w must be less than unity. Unfortunately, however, this analysis is not complete because we have shown only that the magnitude of the gravitational and pressure gradient accelerations are separately much larger than the vertical acceleration. The magnitude of the difference between these two terms has more significance. To better examine this relationship, it is convenient to define a large-scale averaged atmosphere that has an exact balance between the gravitational and pressure gradient terms. This can be defined as

$$\frac{\partial p_\circ}{\partial z} = -\rho_\circ g,$$

where the zero subscript is used to indicate a *large-scale average* (such as layer-domain average). If any dependent variable is defined to be equal to such an average value plus a deviation from that average (i.e., $\phi = \phi_\circ + \hat{\phi}$, where ϕ is any one of the dependent variables), then Eq. (2.22) can also be written as

$$\frac{dw}{dt} = -\alpha_\circ\frac{\partial \hat{p}}{\partial z} + g\frac{\hat{\alpha}}{\alpha_\circ} + 2\Omega u \cos\phi, \tag{2.25}$$

where $|\hat{\alpha}|/\alpha_\circ \ll 1$. In Eq. (2.25) the first two terms on the right-hand side are much less in magnitude than the first two terms on the right-hand side of Eq. (2.22).

The magnitude of the vertical pressure gradient perturbation can be estimated from

$$\left|\frac{1}{\rho_\circ}\frac{\partial\hat{p}}{\partial z}\right| \simeq \frac{1}{\rho_\circ}\left|T_\circ R\frac{\partial\hat{\rho}}{\partial z}+R\hat{T}\frac{\partial\rho_\circ}{\partial z}+R\rho_\circ\frac{\partial\hat{T}}{\partial z}\right| \sim \left|R\frac{\delta T}{L_z}+R\frac{\delta T}{H_\alpha}+R\frac{\delta T}{L_z}\right| \sim R\frac{|\delta T|}{L_z},$$

where for the purpose of this scale analysis the large-scale atmosphere is assumed isothermal and the linearized ideal gas law of the form $\delta\rho/\rho \simeq -(\delta T/T)+(\delta p/p) \simeq -\delta T/T$ has been used. For this analysis, if $L_z \ll H_\alpha$, the term with the vertical gradient of the large-scale density $\rho_\circ$ can be neglected.

The ratio of the vertical acceleration to the pressure gradient perturbation term is thus given as

$$\hat{R}_w = \frac{L_z^2}{L_x^2}\frac{UC_x}{R\delta T} = \frac{H_\alpha^2}{L_x^2}\frac{UC_x}{R\delta T} \qquad (\text{when } L_x \sim H_\alpha). \tag{2.26}$$

This relationship is more restrictive than R_w since δT is in the denominator rather than T (note that $\hat{R}_w$ does not increase without bound because UC_x results from horizontal gradients in temperature, as δT goes to zero in Eq. (2.26)). If $\hat{R}_w \ll 1$, $g\hat{\alpha}/\alpha_\circ$ must be of the same order of magnitude as the perturbation of the vertical pressure gradient (since $2\Omega u\cos\phi$ is small relative to the first two terms in Eq. (2.25) under all expected atmospheric conditions as discussed shortly).

To illustrate the magnitude of $\hat{R}_w$ for representative values on the mesoscale, δT and U are set equal to 10.0°C and 10 m s^{-1}, respectively (based on observations), C_x is set equal to U, and R is equal to 287 J K^{-1} kg^{-1}. This yields $\hat{R}_w = 0.03H_\alpha^2/L_x{}^2$, where $H_\alpha \simeq 8$ km (Wallace and Hobbs,1977). If the depth of the circulation is less than the scale height ($L_z < H_\alpha$), $\hat{R}_w$ is proportionately smaller (e.g., if $L_z = 0.1H_\alpha$, and $\hat{R}_w = 0.0003$). Accordingly a conservative estimation for neglecting vertical accelerations relative to the vertical pressure gradient term in Eq. (2.22) is

$$H_\alpha/L_x \tilde{<} 1. \tag{2.27}$$

The remaining two terms are evaluated by $g/|\alpha\partial p/\partial z| \sim gH_\alpha/RT$ and $|2\Omega u\cos\phi|/|\alpha\partial p/\partial z| \sim 2\Omega UH_\alpha/RT$, and if $g \sim 10$ m s^{-2}, T=270 K, $\Omega \sim$

$7 \times 10^{-5} s^{-1} = 2\pi \text{day}^{-1}$, $U \sim 20$ m s^{-1}, $H_\alpha \sim 8$ km, and R=287 JK^{-1}kg^{-1}, for example, then $g/|\alpha \partial p/\partial z| \sim 1$ and $|2\Omega u \cos\phi|/|\alpha \partial p/\partial z| \sim 3 \times 10^{-4}$.

Thus the influence of the rotation of the earth on the vertical acceleration is inconsequential for any reasonable velocity and can be neglected in Eq. (2.22). The gravitational acceleration cannot be neglected, however, relative to the vertical pressure gradient.

If Eq. (2.27) is valid, Eq. (2.22) reduces to

$$\frac{\partial p}{\partial z} = -g/\alpha = -\rho g \tag{2.28}$$

and is called *hydrostatic equation.* In utilizing this relationship it must be emphasized that the results of the scale analysis imply only that the magnitude of the vertical acceleration is much less than the magnitude of the pressure gradient force not that the magnitude of the vertical acceleration is identically zero (e.g., $|dw/dt| \ll |\alpha \partial p/\partial z|$ not that $|dw/dt| = 0$).

ii) Horizontal equation of motion

The horizontal components of Eq. (2.2) can be written as

$$\frac{\partial u}{\partial t} = -u\frac{\partial u}{\partial x} - v\frac{\partial u}{\partial y} - w\frac{\partial u}{\partial z} - \frac{1}{\rho}\frac{\partial p}{\partial x} + 2v\Omega\sin\phi - 2w\Omega\cos\phi \tag{2.29}$$

and

$$\frac{\partial v}{\partial t} = -u\frac{\partial v}{\partial x} - v\frac{\partial v}{\partial y} - w\frac{\partial v}{\partial z} - \frac{1}{\rho}\frac{\partial p}{\partial y} - 2u\Omega\sin\phi. \tag{2.30}$$

To estimate the approximate magnitude of the pressure gradient term in Eqs. (2.29) and (2.30), two methods will be used here. First, it is useful to use the vertically integrated form of Eq. (2.28), assuming the density ρ is a constant ρ^* so that

$$p_{z=0} = \int_{z=0}^{z=z_p} \rho^* g \, dz = \rho^* g \int_{z=0}^{z=z_p} dz = \rho^* g \, z_p,$$

where the pressure at heigth z_p is assumed equal to zero. Thus if the magnitude of the pressure gradient at $z = 0$ is representative of the pressure gradient at any level in the troposphere, then

$$\left|\frac{1}{\rho}\frac{\partial p}{\partial x}\right| \sim g\frac{\delta z_p}{L_x}, \qquad \left|\frac{1}{\rho}\frac{\partial p}{\partial y}\right| \sim g\frac{\delta z_p}{L_y},$$

where L_x and L_y are the representative horizontal scales of the mesoscale system and δz_p is the representative change of z_p over L_x and L_y. The parameter δz_p represents the relation between horizontal pressure gradient and horizontal gradients in the depth of a homogeneous atmosphere (i.e., $\delta p/L_x \sim \rho^* g \delta z_p/L_x$).

The second technique involves replacing pressure in Eq. (2.29) with the ideal gas law yielding for the x derivative (for convenience subscripts d and v have been dropped)

$$\frac{\partial p}{\partial x} = \rho R\frac{\partial T}{\partial x} + TR\frac{\partial \rho}{\partial x} \simeq \rho_\circ R\frac{\partial T}{\partial x}, \tag{2.31}$$

where, to estimate the magnitude of the pressure gradient, the term $T\partial\rho/\partial x$ is neglected and $\rho_\circ$ is used to approximate ρ.

Thus utilizing these two analysis,

$$\left|\frac{1}{\rho}\frac{\partial p}{\partial x}\right| \sim \frac{R\delta T}{L_x} \sim g\frac{\delta z_p}{L_x}, \qquad \left|\frac{1}{\rho}\frac{\partial p}{\partial y}\right| \sim \frac{R\delta T}{L_y} \sim g\frac{\delta z_p}{L_y},$$

where δT is the representative magnitude of the horizontal temperature variations across the mesoscale system form. Additionally $\delta z_p \sim (R/g)\delta T$.

The advection terms are given by

$$\begin{aligned} &|u\partial u/\partial x| \sim U^2/L_x, \quad |v\partial u/\partial y| \sim UV/L_y, \quad |w\partial u/\partial z| \sim WU/L_z, \\ &|u\partial v/\partial x| \sim UV/L_x, \quad |v\partial v/\partial y| \sim V^2/L_y, \quad |w\partial v/\partial z| \sim WV/L_z. \end{aligned} \tag{2.32}$$

If $U \sim V$ and $L_x \sim L_y$ (as would be expected in general) and since $W/L_z \sim U/L_x$, then these terms are of the same order. If $L_y \gg L_x$, derivative terms on y in Eq. (2.32) can be neglected, and Eqs. (2.29) and (2.30) reduced to their two-dimensional forms. U^2/L_x can be used to represent the advective terms and V and L_y can be replaced by U and L_x whenever they appear.

The local tendency terms in Eq. (2.29) and Eq. (2.30) are estimated by

$$|\partial u/\partial t| \sim U/t_u \sim UC/L_x, \qquad |\partial v/\partial t| \sim V/t_v \sim UC/L_y, \sim UC/L_x,$$

where, as for the vertical component of the conservation-of-motion equation, $C \simeq U$ for both advective and internal gravity wave changes in mesoscale systems can often be assumed.

The remaining three terms in Eq. (2.29) and Eq. (2.30) can be represented as

$$|2u\Omega\sin\phi| \sim |fu| \sim |f|U,$$

$$|2v\Omega\sin\phi| \sim |fv| \sim |f|V \sim |f|U,$$

$$|2w\Omega\sin\phi| \sim |\hat{f}w| \sim |\hat{f}|W \sim |\hat{f}|(L_z/L_x)U,$$

where $f = 2\Omega\sin\phi$ and is called the *Coriolis parameter* and $\hat{f} = 2\Omega\cos\phi$. Consequently;

(1) The local time tendency terms $\partial u/\partial t$ and $\partial v/\partial t$ can be neglected if the movement of the mesoscale system is much less than the advecting wind speed (e.g., $C \sim C_g \ll U$). Such a system is said to be *steady state* if $C_g = 0$ or *quasi-steady* if $C_g \neq 0$ but $C_g \ll U$.

(2) The terms associated with the rotation of the Earth (fu, fv, and $\hat{f}w$) can be neglected if $Ro \gg 1$ ($Ro = U/|f|L_x$ is the Rosbby number). Since Ro is inversely proportional to L_x, the larger the horizontal scale of the mesoscale system, the more inappropriate it becomes to neglect those terms. The magnitude of the $\hat{f}w$ term is dependent on the ratio of L_z/L_x (e.g., if $L_z = 0.1L_x$, it is expected to be about 10% of fu and fv).

(3) The ratio of the pressure gradient force and advective terms is inversely proportional to the square of the wind speed and proportional to the horizontal temperature gradient. Since the horizontal pressure gradient is ap-

proximately a linear term (e.g.,

$$\frac{1}{\rho}\frac{\partial p}{\partial x} \simeq \frac{1}{\rho_\circ}\frac{\partial p}{\partial x} \qquad \text{since} \quad \left|\frac{\rho'}{\rho_\circ}\right| \sim \left|\frac{\alpha'}{\alpha_\circ}\right| \ll 1),$$

whereas the advective terms are nonlinear, solutions to the conservation relations are greatly simplified if the ratio is large and the nonlinear contribution of advection to the equations can be ignored. Eqs. (2.29) and (2.30) are then linearized if $\rho_\circ = \rho$ is used in the pressure gradient term.

Representative values of Ro, z_p, and δz_p can be estimated for mesoscale systems in the troposphere. For $|f| \sim 10^{-4}s^{-1}$, $U \sim 20$ m s^{-1}, $p_{z=0} \sim 1000$ mb, g=10 m s^{-2}, $\rho_\circ$ =1.25 kg m^{-3}, $\delta T \sim 5°C$, L_x=100 km, and $L_z = z_p$, we may find $z_p = 8\ km \sim H_\alpha, \quad Ro = 2.0, \quad \delta z_p = 143\ m, \quad L_z/L_x = 0.08.$

Thus for this case it would be appropriate to neglect the term $\hat{f}w$ but not fu and fv. Furthermore, because of the ratio of the magnitudes of the pressure gradient force term to the advective terms is on the order of four, none of these terms can be neglected in Eqs. (2.29) and (2.30). The local tendency terms $\partial u/\partial t$ and $\partial v/\partial t$ can also not be ignored if $C \sim U$, since for this case their ratio to the pressure gradient force term is approximately 0.3.

These scaled terms need to be reevaluated for each study of different mesoscale systems to determine the appropriate form of Eqs. (2.29) and (2.30) to use. In the limiting case of $Ro \ll 1$, $L_z \ll L_x$, $U \sim C$, and $R\delta T \gg U^2$ with $\delta z_p \sim |f|UL_x/g$ (which is the same as $\delta T \sim |f|UL_x/R$) Eqs. (2.29) and (2.30) reduce to

$$v_g = \frac{1}{f\rho}\frac{\partial p}{\partial x}, \qquad u_g = -\frac{1}{f\rho}\frac{\partial p}{\partial y}, \tag{2.33}$$

where v_g and u_g are called the *geostrophic wind components.* This is called the *geostrophic assumption.* On the other hand, if $Ro \gg 1$, Coriolis terms can be neglected relative to the advective terms. This assumption is used for the cumulus and other smaller scale models.

Final analysis of the vertical and horizontal equations of motion is to examine the magnitude of the molecular viscous forces to the terms in Eq. (2.2). Molecular forces are insignificant on the mesoscale and are ignored in this equation. To justify this assumption, the method of scale analysis is used in which the D molecular dissipation of motion is approximated by

$$D_i = \nu\frac{\partial^2 u_i}{\partial x_j \partial x_j}, \qquad |D| \sim \nu S/L^2, \tag{2.34}$$

where L represents L_x, L_y or L_z (for j=1, 2, or 3) and S represents U, V, or W (for i=1, 2, or 3), and kinematic viscosity ν is about $1.5 \times 10^{-5} m^2 s^{-1}$ for air. To examine the significance of the viscous force, it is customary to compare it with the advective terms, which have a magnitude of U^2/L_x in the horizontal equation and W^2/L_z in the vertical equation of motion. Assuming $L_x \sim L_z \sim L$, and $W \sim U \sim S$; the ratio of the magnitude of the advective terms to the viscous force is given by

$$\frac{S^2/L}{\nu S/L^2} = \frac{SL}{\nu} = Re,$$

where Re is *Reynolds number.* When $Re \gg 1$ changes in motion by advection are much more important than the dissipation of velocity by molecular interactions. Under this condition the flow is turbulent and transfers of all properties of the air (e.g., heat, moisture) are performed through the movement of air from one point to another. By contrast, when $Re \ll 1$, the molecular dissipation of velocity dominates and the flow is said to be laminar. According to this condition properties of the air are transferred to the molecular scale. When $Re \sim 1$ both effects are important and initial and boundary conditions imposed on the flow determine whether laminar or turbulent mixing predominates.

On the mesoscale the Reynolds number is very large and the flow is highly turbulent. With $S = W = 1.5$ cm s^{-1} and $L = L_z$ =1 km, we may find $Re = 10^6$. Molecular transfers become important only near the surface. For this situation, microscale circulations with the value of $L_z \sim 0.1$ mm and $W \sim 1.5$ cm s^{-1}, give the Reynolds number of 0.1. That means the movement of air is laminar.

Using the scale analysis, a more formal definition of mesoscale can be given. The criteria are that:

(1) the horizontal scale should be sufficiently large so that the hydrostatic equation can be applied.

(2) The horizontal scale should be sufficiently small so that the Coriolis term is small (although it can still be significant) relative to the advective and pressure gradient forces.

2.3 Approximations

Approximations in atmospheric models depend on the scaling assumptions. The different flow depths of the various mesoscale flow types imply governing dynamics and thermodynamic equations that can be simplified via scaling assumptions.

It is clearly desirable to have a more explicit statement about the acceptability or otherwise approximations that may be made to the suite of equations that form the basis of modeling. The approximations are considered as:

1) the omission of **beta-effects,**
2) the omission of **Coriolis effects,**
3) the use of the **geostrophic approximation,**
4) the use of the **hydrostatic approximation,**
5) the use of the **Boussinesq approximation,**
6) the use of the so-called **anelastic approximation.**

The last two approximations are closely related, and apply to the continuity equation, which is the expression for the conservation of mass.

The crux of the *Boussinesq approximation* (Boussinesq, 1903) for a stratified, incompressible fluid is the variations in density which are ignored except where they are multiplied by the acceleration of gravity in the vertical component of the equation of motion. The idea was extended in 1960 (Spiegel and Veronis 1960) to apply to certain flows of compressible fluids, but this necessitated a restriction to the vertical scale of the motion. This approximation, which substantially simplifies the continuity equation, has been widely used in analyzing atmospheric flows of only at most a few kilometers in depth. Such a statement allows for both deep and shallow flows (Dutton and Fichtl 1969; Pielke 1984). According to Businger (1982), further impose a condition that perturbation pressure influences in the buoyancy term can be neglected, which restricts the approximation to shallow flows. Mahrt (1986) and Stull (1988) point out that this extra condition is limited to only nonneutral shallow flows.

The *anelastic approximation* was derived by Ogura and Phillips (1962). This kind of approximation eliminates the "elastic" effects and hence the production of sound waves in numerical models. It is finer tuning than the Boussinesq approximation, restraining to zero only the local time derivative of the density in the continuity equation. Its great value in numerical models is that it not only eliminates sound waves but also allows much longer time steps than would otherwise be possible.

An analysis by Pielke (1984) indicates the form of Eq. (2.28) of the vertical motion equation. It is known as the *hydrostatic assumption* in numerical modeling, and can be used when the horizontal length scale of the phenomenon modeled is greater than the density-scaled height of the atmosphere. The smallest resolvable feature, in terms of accuracy, in a numerical model is $4\Delta x$, it seems that use of the hydrostatic assumption in numerical modeling is valid when the horizontal grid length Δx employed is about 2 km or greater. This is merely a qualitative indication and does not mean that Eq. (2.28) cannot be used for grid-lengths less than 2 km. It should be noted that in mountain wave modeling, the square of the ratio of vertical to horizontal wavelength determines the validity of the hydrostatic approximation.

A major disadvantage of the hydrostatic method is that it yields less realistic results if Δx is small. The advantages of the hydrostatic method are the fact that it is easy coding, and that it requires much less computation time per time step. However, it is important to note that the other advantage is partly (or even entirely) counterbalanced by the necessity of taking a smaller time step for the hydrostatic computation. The reason is the hydrostatic computation. The time step is restricted by the necessity of avoiding numerical instability due to gravity waves with a horizontal wave vector. If the non-hydrostatic method is used, this kind of numerical instability does not occur, as is shown by a straightforward numerical stability analysis.

The majority of the mesoscale models that have been adapted to study flow over complex topography make use of the hydrostatic method to calculate the pressure. These methods are easy to use since the pressure is calculated directly from the density profile. If the horizontal grid distance Δx of the interested domain is as small as 2 km or so, the hydrostatic pressure calculation may lead to less realistic results. As discussed in Pielke (1984) and Physick (1988), there are two kinds of methods for non-hydrostatic pressure calculation: one is that use the fully compressible continuity equation, and other is that employ the anelastic continuity equation. The advantages and disadvantages of the fully compressible method are discussed in Physick (1988). If the anelastic method is preferred, an elliptic partial differential equation for the pressure p has to be solved for each time step. This is discussed in Meesters (1992). Several efficient methods to solve this equation are known. They include block cyclic reduction of the coefficient matrix (Rosmond and Faulkner 1976), spectral analysis (Williams 1969), and a combination of both (Wilhelmson and Ericksen 1977). However, the feasibility of these methods is restricted to models with an equidistant grid; spectral analysis moreover requires periodicity of the boundary conditions. These situations cannot usually be seen. In the case of complex topography in mesoscale models. Hence, in this field it is usual (Physick, 1988) to find an approximate solution to the anelastic pressure equation by some relaxation technique. An overview of such techniques is given by Leslie and McAvaney (1973).

The accuracy of the Pielke and Orlanski schemes as a function of horizontal length scale, large-scale stability, subgrid-scale heat diffusion, strength of surface heating and friction have been evaluated by Song *et al.*, (1985) using an exact solution for the residual in the context of a linear analytic model. Martin and Pielke (1983) also examined the adequacy of the hydrostatic assumption for sea breezes using a nonlinear numerical model with simple turbulence parameterizations. A general result from these studies seems to be that hydrostatic assumption becomes less valid as the intensity of the surface heating increase, and as the synoptic temperature lapse rate becomes less stable. The hydrostatic approximation is especially compromised if an explicit approach to condensation processes is adopted (Physick, 1988).

The quasi-nonhydrostatic technique of Song *et al.*, (1985) has been adapted to a nonlinear finite-element model by Fast and Takle (1988 a,b) and applied successfully to neutral flow over gentle topography. It should be noted that the typical grid spacing in this experiment, where the domain size is only 300 m, is much smaller than used in the meso-β scale models of this review.

In engineering terminology, the convection is used to describe vertical or horizontal movements of mass or energy by either the mean or turbulent component of thermally forced flow. In meteorology, convection needs to be differentiated from both advection and diffusion. The smallest scale of the vertical movement of energy, mass and/or momentum is random (disorganized) microscale turbulent diffusion (with a zero-mean vertical velocity). The next largest scale of such movement is organized (non-hydrostatic) mesoscale or microscale (thermal or mechanical) convection, with vertical velocities large enough (same order of magnitude as horizontal velocities) to significantly alter or produce the horizontal flow component (mainly) by mass continuity. Finally, the largest scale of vertical movement is the organized mesoscale (and larger) advective circulation cells, in which advective vertical velocities are at least an order smaller than the horizontal component and arise from horizontal convergence again via mass continuity. One impact of such nomenclature is that motions such as sea-land breezes, mountain-valley winds, and urban circulations would no longer be referred to as convective but as advective. Another result of this classification is that hydrostatic mountain waves are considered to be advective, while nonlinear lee waves are convective. Note, this does not imply that all non-hydrostatic flows are convective, that is, neutral-stability advective flows over surface discontinuities in which vertical motions are limited by advection are also non-hydrostatic (Fig. 2.2). Besides hydrostatic flows are thus advective, but not all advective flows are hydrostatic.

Non-hydrostatic models are being used in cloud modeling studies (Klemp and Wilhelmson, 1978; Tripoli and Cotton, 1982) which use horizontal grid-lengths of the order of a few hundred meters. In such models, pressure term cannot be computed diagnostically in a simple manner from an equation such as hydrostatic assumption (Eq. 2.28). Therefore, the equation of state ($P = \rho RT$) is used in conjunction with the fully compressible continuity equation, Eq. (2.1). However, use of the latter allows fast moving sound waves as solutions and thus imposes a relatively small time step to ensure numerical stability. This inconvenience has been minimized in the above studies by using small time step only for those terms generating sound waves, and a larger time interval for those terms producing the slower-moving gravity waves. Gadd (1978) has used a similar approach (the split explicit method) in a hydrostatic model by using a longer time-step for the advective terms than for those producing gravity-inertia oscillations. The non-hydrostatic compressible British Meteorological Office mesoscale model (Tapp and White, 1976; Carpenter, 1979) treats the acoustic terms implicitly, thus allowing a larger time-step than for explicit finite-difference schemes.

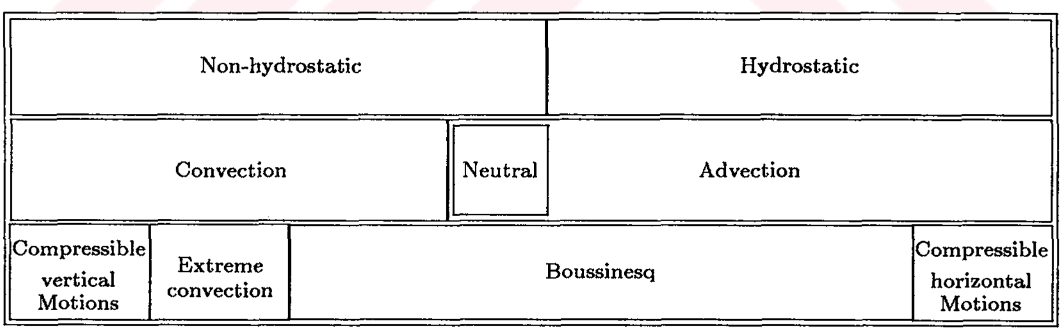

Fig 2.2. Schematic of basic flow subclass and assumptions (after Thunis and Bornstein, 1996).

Some of the non-hydrostatic models (Neumann and Mahrer, 1971; Clark, 1979) use the anelastic form of the continuity equation (2.16) which involves solving a Poisson-type equation for pressure by a relaxation technique. This is a time-consuming task, although Fulton *et al.*, (1986) reports that multi-grid methods are able to decrease considerably the time taken for the numerical solution of Poisson equations. Gross (1985) also used the anelastic equation in a non-hydrostatic model, employing an iterative process involving pressure and velocities until the continuity equation is satisfied to a specified error value. This technique can be shown to be equivalent to solving a Poisson equation for pressure (Cebeci, 1981).

It is concluded that a non-hydrostatic treatment allows a larger time step than a hydrostatic treatment. As a consequence, the disadvantage of the non-hydrostatic method that requires a larger computation time per time step is at least partly canceled. In certain cases, the non-hydrostatic method even allows a faster computation than the hydrostatic method.

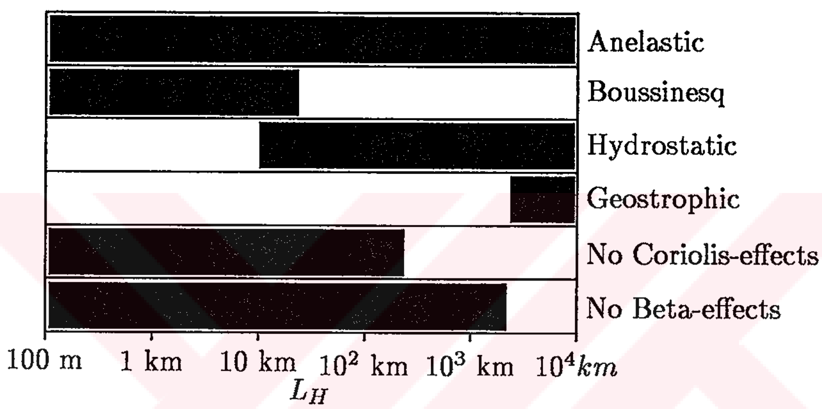

Fig 2.3. Limits of applicability of model approximations. The black areas indicate over what horizontal scales the approximations are valid (after Wipperman, 1981).

The results of the comparison of the six approximations in mesoscale modeling are shown in Fig (2.3). It is clearly justifiable to ignore Coriolis and beta effects in modeling systems with a typical horizontal length of less than 1000 km. The assumption of geostrophy is valid at scales above approximately 2500 km. The hydrostatic approximation is valid for systems with the horizontal size of more than 10 km. The Boussinesq approximation is valid only for a length scale less than 25 km. It is only the anelastic approximation which is valid across the whole range of scales. Noting previously defined range for the meso-scale as 1 to 100 km these results are important reminders that the Boussinesq and hydrostatic approximations, widely used in so-called mesoscale modeling over the past decades, must be employed with great care.

Additionally, there are many problems involved in incorporating other physical processes as to better simulate the real atmosphere. Some of these processes and effects have been satisfactorily included in large-scale models but meso-scale dynamics require different emphasis within the equations of motion and, in turn, this requires careful incorporation of terms that can justifiably be ignored on larger scales. For example, the early numerical models of the large-scale atmosphere omitted the turbulent transfer terms in the equations of motion, a procedure justified by the fact that the models were formulated for one level only, at a height of about 5 km. In most meso-scale models, the turbulent transfer terms cannot be ignored. Indeed their incorporation remains a major problem of parameterization, which is the inclusion of the effects of events smaller in scale than are taken into account directly by the modeling process. Much of the turbulence theories are as yet of little value to modelers of the real, rather complicated flows found in the atmosphere. Hence, to those with a primary interest in the nature of turbulence, its representation in atmospheric models will appear to be rather primitive. The K-formulation is the most elementary and most widely used of the ways of incorporating turbulent transfer and some 20-30 forms of K (the eddy diffusivity) exist in the literature of the last 60 years. Besides, the Monin-Obukhov theory applicable in the lowest 10-50 meters of the atmosphere have proved exceedingly valuable over the past fifteen years, but it is true to say that the representation of turbulent fluxes in models still leaves much to be desired. The fluxes are particularly important in the lowest kilometers or so of the atmosphere, the so-called Planetary Boundary Layer (PBL), and it is here that much research effort is being concentrated. The planetary boundary layer has a host of theoretical and observational problems of its own, and the satisfactory inclusion of this layer into meso-scale models is proving to be very difficult. It will remain a high priority problem throughout the decade.

2.4 Atmospheric Space Scales

Different opinions currently exist concerning definitions of the time and space boundaries of the micro-, meso-, and macro-meteorological scales. The standardization of the mid-1970s atmospheric scale classification schemes by Orlanski (1975) contained eight horizontal space and time subdivisions (Table 2.1) because of the wide range of phenomena encompassed by the three basic scales (micro, meso, and macro). Orlanski (1975) defined a mesoscale to cover motions with a scale of 2-2000 km, with subdivisions of meso-α (200-2000 km), meso-β (20-200 km) and meso-γ (2-20 km). By using previous definition of the mesoscale he quoted was intermediate states between macroscale ("*space scales* *more that 1000 km and time scales of the order of a week*") and microscale ("*space scales of several meters and time scales on the order of minute*"). His proposed new upper bound (2000 km) was of the same order of magnitude as the old one, but his new lower bound (2 km) significantly enlarged the range of microscale phenomena. However, he pointed out that as it was not generally possible to identify "*a relationship between geophysical parameters and the intrinsic spatial scale, ... all horizontal scale divisions are somewhat arbitrary and ill-defined.*"

However, some mesoscale texts have proposed alternative definitions for mesoscale phenomena. In terms of dynamics, Emanuel (1982) assigned the terms mesoscale to atmospheric systems in which both ageostrophic advection and Coriolis accelerations are important. Arya (1988) defines the micrometeorological phenomena as limited to those that "*originate in and are dominated by*" the PBL, excluding phenomena whose "*dynamics are largely governed by mesoscale and macroscale weather systems.*" However, Pielke (1984) defined mesoscale phenomena as having a horizontal length scale large enough to be hydrostatic but small enough so that the Coriolis force is small relative to the advective and pressure gradient forces. While Pielke mentions that this upper boundary is thus latitude dependent, it is also true that his lower boundary would be PBL stability dependent. His definition confines mesoscale to the Orlanski meso-β scale.

The mesoscale bounds of Pielke were consistent with phenomena that contemporaneous mesomodels could simulate, that is, meso-β. Such models generally used meso-α (and larger) values as external forcing and parameterized *subgrid/subscale* non-hydrostatic (meso-γ and smaller) effects. However, current non-hydrostatic mesoscale models are capable of simulating motions on the smaller meso-γ and micro-α scales, while model nesting allows them to simulate meso-α (and larger) flows. Stull (1988) places the lower limit of the mesoscale at 3 km. He also reproduces part of the Orlanski's table (meso-α to micro-γ) but with an additional micro-δ scale extending from 2 m down to 2 mm. In addition, he shows an overlap between the micro- and mesoscales that extends downward from the middle of meso-γ to the lower end of micro-α. Pielke (1984) also defines the vertical bounds of mesoscale phenomena as extending "from tens of meters (i.e. above the surface boundary layer) to the depth of troposphere." While shallow mesoscale motions (like sea breezes) are all or mostly contained within the PBL, deep mesoscale motions (like thunderstorms) can extend well above it.

The current variety of definitions for both mesoscale bounds given by Thunis and Bornstein (1996) seeks to update Orlanski's subdivisions. The new proposed scale boundaries include the following changes: addition of a micro-δ scale, renaming meso-α to macro-γ, and renaming micro-α to meso-δ. These last two changes shift mesoscale down one class toward smaller-scale flows. These changes thus incorporate contributions from Stull (1988), except that his scheme showed an overlap of the micro- and mesoscales covering the current meso-δ and half of the current meso-γ.

Both new mesoscale boundaries are thus dynamically based. Its upper boundary corresponds to that proposed by Pielke (1984), in which atmospheric motions have a horizontal extent small enough so that the Coriolis force is not latitude dependent. By analogy, the new lower boundary includes all phenomena in which Coriolis effects are strong enough to determine rotational direction. Note that both new mesoscale bounds are stability dependent, because as stability increases, motions become more horizontal and thus more influenced by Coriolis forcing.

However only plume and urban effects differ from that in Orlanski (1975) and Stull (1988); that is, plumes and urban effects are each moved up one scale. Current mesomodels can simulate flows on all proposed meso subscales, including non-hydrostatic meso-γ and meso-δ phenomena.

2.5 Flow Classification

Separate graphical representations of the Boussinesq mesoscale flow subclasses during stable and unstable conditions were constructed from the order of magnitude estimates of the various length scales and flow-class separation criteria (ignoring effects from condensation). Note that while these values are (for convenience) representative of the Earth atmosphere in its midlatitudes, they could be derived for other latitudes.

Boundaries between unstable condition flow subclasses described above are defined in Fig 2.4 by the following limits: zones of unrealized atmospheric flows, upper and lower limits on thermal convection, upper limit on the micro-β scale, hydrostatic-nonhydrostatic transition, and shallow-deep flow limit. All flow-class boundaries in this and the next figure represent best estimates consistent with scale arguments. As each flow-class limit line really represents a transition zone, more precise limits and slopes could be developed via numerical model simulation of impacts resulting from the approximations discussed above. For example, on its vertical axis, a daytime PBL depth of 1 km was assumed for the boundary between shallow and deep Boussinesq, while the 10 km height assumed for the corresponding density scale-height H_α was also taken as the deep Boussinesq limit. The horizontal axis ranges over all currently defined mesoscale subclasses and the micro-β scale, whose vertical limit has been set equal to its 200 m horizontal limit (assuming mainly isotrophic microscale motions). Note, the smallest large scale (macro-δ) is represented by horizontal and vertical extensions of the deep end of the meso-β scale. The figure excludes flows with physically unreasonable combinations of L_H (L_x or L_y) and L_z, for example, flows with L_H of 200 m and L_z of 200 m, or with L_H of 200 m and L_z of 10 km. The transition from hydrostatic to non-hydrostatic has an approximate slope of unity, as the scale analysis of Pielke (1984) indicated non-hydrostatic effects when L_z became greater than L_H. It has further been assumed that the smallest horizontal hydrostatic length scale is about 5 km at a height of 200 m, the horizontal size at which non-hydrostatic effects began in the vertical velocity field for island breeze simulations by Thunis (1995). The hydrostatic-nonhydrostatic line, in combination with the deep-shallow flow line, produces four flow regions. Note first the transition from thermal advection to thermodynamic advection with increasing circulation depth for hydrostatic flows. Also note that part of the deep convection is divided off by criteria $L_z \ll rH_\alpha$ to produce a deep thermal convection, while part of the shallow convection is likewise divided off by criteria $r = 1$ to produce shallow thermal convection. Note, the $r = 1$ criteria denotes a transition between vertical pressure gradient force and buoyancy-dominated non-hydrostatic flows, and not a physical extension of the hydrostatic flow region. Note also, the dashed horizontal line that denotes the internal division between the two thermal convection sub-classes. Fig 2.5 shows that corresponding stable atmosphere representation with a lower-density scale height, a lower boundary layer depth, and an assumed factor of 2 reduction in the meso-β-scale upper limit. These changes result from the reduction of vertical motion magnitude in stable atmospheres, while the latter is a reasonable estimate of the known reduced horizontal extent of the thermal circulations with such stability, for example, land versus sea-breeze circulations. Numerical simulations could help better define these limits. Note also that both exclusion zone limits have been moved, consistent with the larger horizontal to vertical length-scale ratios in stable flows.

While the microscale limit is unchanged, the hydrostatic-nonhydrostatic transition line is shifted toward smaller scales to reflect that circulations are more likely hydrostatic in stable conditions (Martin and Pielke 1983). Thermodynamic advection, thermal advection, and shallow convection still exist, but thermal convection flows (with $r > 1$) cannot exist in stable conditions. Vertical motions in stable condition deep convection flows are thus forced by the vertical pressure gradient force and/or advection but not by buoyancy. Thus, nighttime convective motions have buoyancy acting as a restoring force and include gravity waves associated with mountain-induced flows, frontal lifting, and jet streaks.

The equations of each subclass in Fig 2.4 and 2.5 are less likely to accurately reproduce associated atmospheric phenomena as one moves upward and/or leftward within a subclass area.

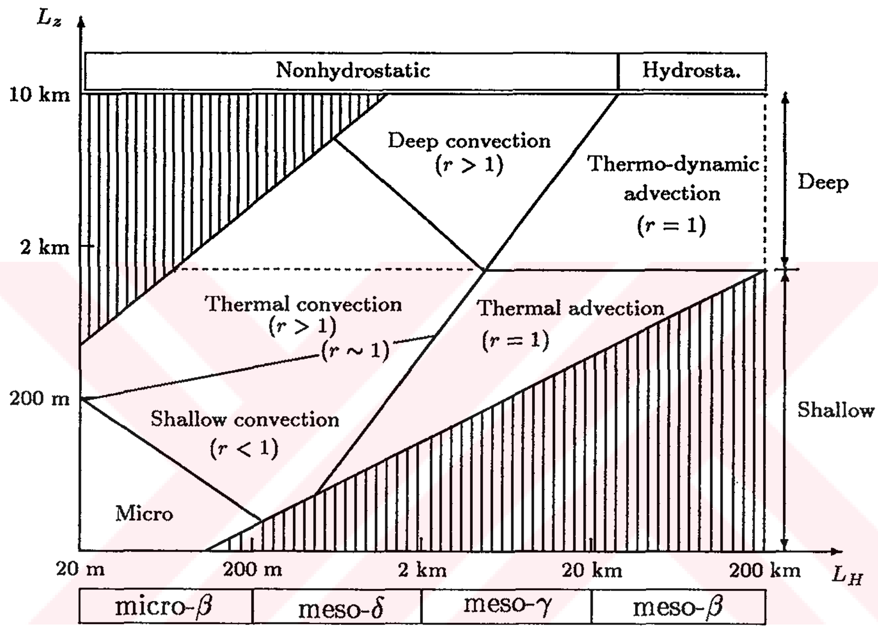

Fig 2.4 Schematic of flow subclass under stability conditions, where hatched zones indicate nonphysical phenomena, dotted line indicates merging of thermodynamic advection with macroscale, r represents scaled ratio of buoyancy and vertical pressure gradient force perturbations, and the dashed line represents division of thermal convection into its deep and shallow regimes (after Thunis and Bornstein, 1996).

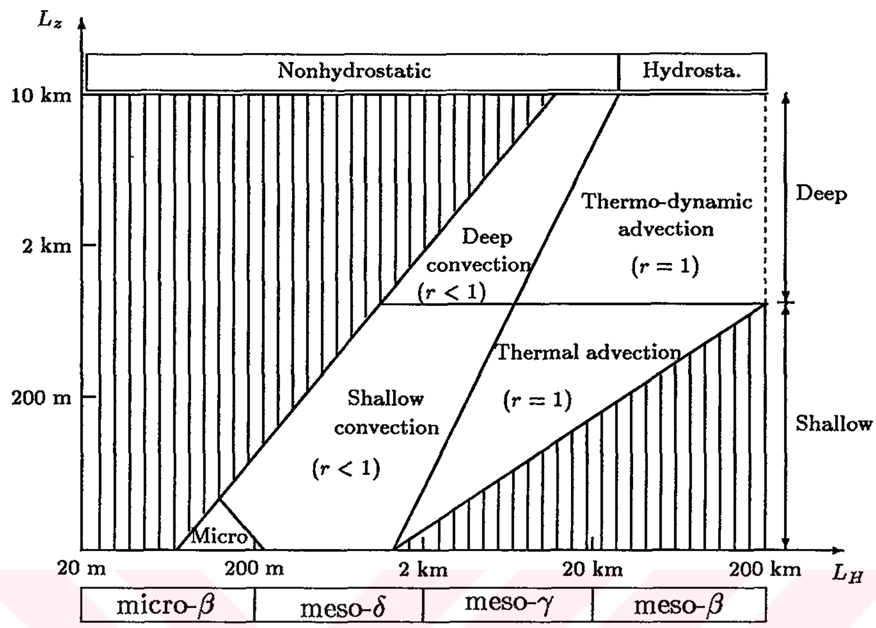

Fig 2.5. As in Fig 2.4 except for stable stability conditions (after Thunis and Bornstein, 1996).

Table 2.1 Atmospheric scale definitions, where L_H is horizontal scale height (after Thunis and Bornstein, 1996)

L_H	Lifetime	Stull (1988)	Pielke (1984)	Orlanski (1975)	Thunis & Bornstein (1996)	Atmospheric Phenomena
10000 km	1 month	Macro	Synoptic / regional	Macro-α	Macro-α	General circulation, long waves
2000 km	1 week			Macro-β	Macro-β	Synoptic cyclones
200 km	1 day			Meso-α	Macro-α	Fronts, hurricanes
20 km		Meso	Meso	Meso-β	Meso-β	Low-level jets, thunderstrom groups, mountain winds and waves, sea breeze, urban circulations
2000 m	1 h			Meso-γ	Meso-γ	Thunderstorm, clear-air turbulence
200 m	30 min	Micro		Micro-α	Meso-α	Cumulus, tornodoes, katabatic jumps
20 m	1 min		Micro	Micro-β	Micro-β	Plumes, wakes, waterspouts, dust devils
2 m	1 s	Micro-δ		Micro-γ	Micro-γ / Micro-δ	Turbulence, sound waves

CHAPTER 3

GRID GENERATION TECHNIQUES USED IN MESOSCALE MODELLING – VERTICAL COORDINATES

3.1 Grid Generation Techniques

Fluid mechanics is understood in a descriptive way through experimental observation, mathematical analysis, and numerical simulation. When the understanding is required for flows with complex internal structure and with complicated regional boundaries, insight is gained primarily from experiments and simulations. Numerical simulations are motivated by the prospect of economically obtaining a detailed flow-field description. In each instance, a governing system of flow equations is analytically formulated over the region and is solved in an approximate form on a computer.

Various numerical methods have been devised for such approximations, and most depend upon some representation of the flow-field region by means of finitely many points and the interconnections between them. When each regional boundary is given by a sequence of connected points, the efficiency and accuracy of the various methods are enhanced, since boundary conditions can be applied without interpolation. Further enhancement comes when the connectivity pattern is regular. The most regular and thus preferable patterns are those that result from *coordinate transformations.*

Generally most of the useful coordinate transformations are *nonorthogonal.* While many two-dimensional regions or surfaces can efficiently be given *conformal coordinates* to match a variety of geometric configurations. Upon specification, conformality with its simple metric structure is no longer available. The next best structure comes from *orthogonal coordinates*: availability is also limited, but not as severely as with conformal coordinates.

With a transformation, Cartesian coordinates on a rectangular region are typically mapped into coordinates that cover the physical region and match boundaries. When the transformation is applied to a discrete representation, the connectivity pattern is preserved. In a rectangular region, regularity arises naturally from uniform spacing in each Cartesian direction. The simplest pattern occurs when the points are connected only along coordinate directions. It is called as *Cartesian grid.* Under the mapping, the Cartesian grid goes into a corresponding physical-space grid where boundaries are defined by discrete coordinate curves. With the transformation, the flow-field computations can be performed entirely on the fixed Cartesian grid, regardless of the geometry or motion of the boundaries. The Cartesian grid then represents the rectangular computational space.

The same computational space can be used to treat multiply connected physical regions that rise when there are a number of solid bodies in the field. The basic methods come from the identification of Cartesian-coordinate sections with artificial or actual boundaries. Artificial boundaries are used to connect the bodies with the physical boundary to essentially reduce the number of bodies. These connections are transmissive boundaries for the fluid and are called branch cuts, patches, or simply cuts. Actual boundaries are determined by the geometry of the physical bodies. These are prescribed in correspondence with either internal or boundary Cartesian sections. The internal sections are used alone as a slit or in a combination to remove a local region. In physical space, the mapped result is wrapped around the given body. With the local region, the boundary grid inherits the Cartesian corners or edges even if they do not physically exist. In the contrary sense, any Cartesian section may also map a physical boundary with corners or edges. Barring irregularities in physical boundaries, Cartesian identifications tend to produce further irregularities that appear as coordinate singularities on the boundaries. While special numerical treatment can usually be applied to singularities, the accuracy of a simulation can suffer, particularly if significant properties of the fluid occur near the boundaries. The fundamental reason for the singularities comes from the direct considerition on a multiply connected physical region. The use of a single coordinate transformation and the associated computational space is the primary cause for the placement of the singularities directly on the boundaries.

To move the singularities off the boundaries and away from potentially large flow variations, more than one coordinate system is required. The immediate consequence is an assembly of computational spaces and identifications. This may appear as a general rectilinear region covered by a Cartesian grid. With junctures between systems corresponding to the identifications, coordinate transformations are then applied to produce grids for each system, which upon assembly cover the physical region in a patchwise fashion.

On a local level, the physical-space grid retains the simple, regular connectivity pattern of each coordinate grid. The only places where the pattern is altered are those that correspond to the moved singularities and that consequently represent only a minor part of the entire region. On a global level, the grid connectivity is changed in a way that usually represents a higher degree of conformity with the actual topology of the region. This occurs because solid bodies in the field often get individual local coordinate grids wrapped around them. The local grids essentially provide a good structure for the modeling of nearby fluid-mechanical phenomena.

From a global perspective, the outer boundaries of the local systems are considered to be a new collection of bodies that can be fewer in number if some of them are joined together. The physical-space grid is typically constructed from such collections with the introduction of further artificial transmissive boundaries, which altogether determine its global topology.

With the selection of grid topology, certain families of coordinate curves of s are selected for enhancement in a number on a purely local basis. The local body-oriented grids provide an immediate example: the number of coordinate curves or surfaces that wrap around each body can be adjusted separately. As a consequence, the simulation process can be optimized in the vicinity of each body. A similar optimization is not generally available for one global transformation, since local requirements cause global changes that would be wasteful and possibly conflicting. As in the case of a single transformation, the simulation process can be done entirely with respect to a fixed computational space, even when the physical grid is in motion. The movement is restricted only by the fixed choice of grid topology, which is a possible problem when distinct bodies collapse upon each other.

Once a grid has been generated to match the physical boundaries and to have some conformity with the regional topology, simulation accuracy can be enhanced through grid movement. While maintaining the simple, regular connectivity pattern, points are pushed into positions that more accurately represent the desired solution to the governing system of fluid equations. Although the entire solution would theoretically be needed to drive the pointwise motion, the intrinsic character is often quite accurately detected by a small number of salient quantities. Altogether, the collection of salient quantities efficiently summarizes the solution data. On application, a feedback cycle is formed in which the solution is advanced by some computational algorithm and the grid is moved in response. Such cycles that couple movement with solution procedures are called *adaptive grid techniques* (Fig 3.1). When the motion is supplemented or replaced by arbitrary local changes in the number of points, the adaptive procedures lose the logically regular ordering of grids and inherit a data-management problem.

Two primary categories for arbitrary coordinates generation have been developed, which include both fixed and moving grids. These are

- *algebraic* methods,
- *partial differential* methods.

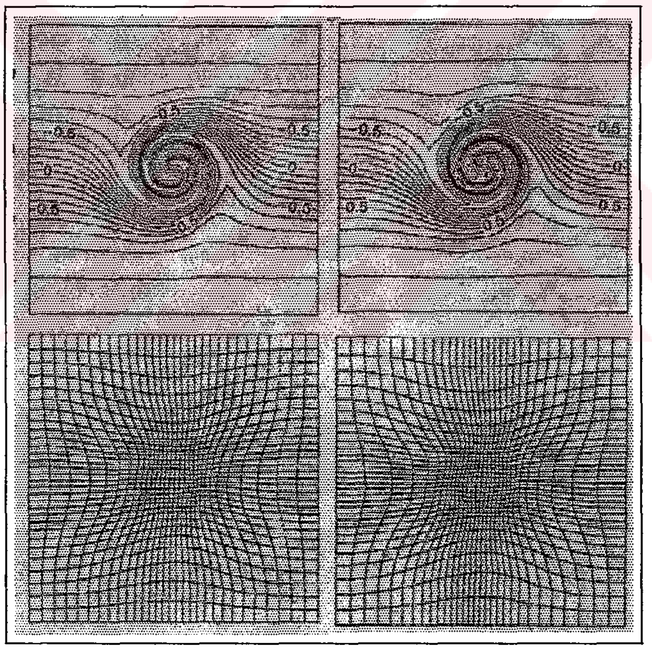

Fig 3.1 Results for the kinematic frontogenesis problem and the using grid structures (Dietchmayer, 1992).

3.1.1 Algebraic grid generation

The physical region with coordinate transformations defined by algebraic formulas can be given in a continuous description which it is often done in an explicit manner. With the application of such transformations, arbitrarily large grids can be efficiently generated. This process is known as *algebraic grid generation*.

Classically, transformations have been globally defined by analytic functions of a complex variable and by direct shearing. The analytic functions produce conformal coordinates that are inherently non-singular and over which the fluid-dynamic equations assume their simplest general form. In addition, potential-flow solutions are readily available and are often quite useful. The fundamental limitations, however, are a loss of control over boundary distributions and a practical restriction to two-dimensions (Moretti, 1980; Ives, 1982).

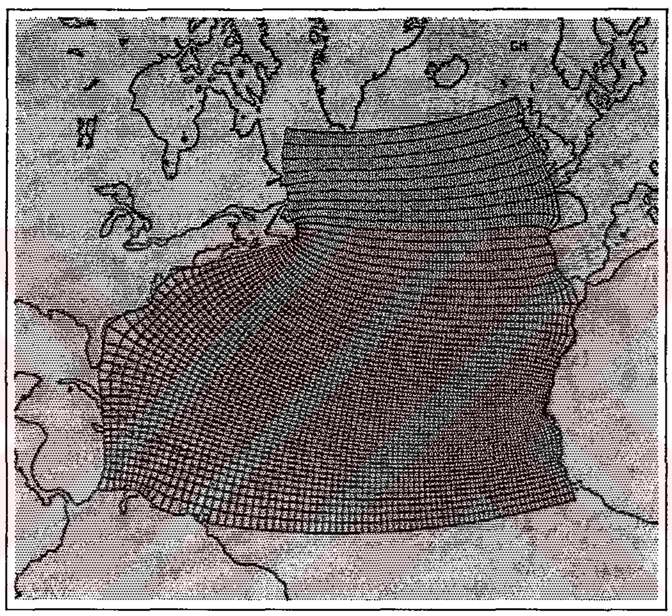

Fig 3.2 Orthogonal curvilinear horizontal grid approximating the geometry of the North Atlantic Ocean ($10° - 60°$ N) (Adams *et al.*, 1992).

The limitations of conformal coordinates are removed with the classical shearing transformations. The price is nonorthogonality, which typically adds complication to the fluid-dynamic equations. In a practical sense, the complications have a minor impact and may not even appear in the discrete form. As a consequence, the primary development starts with shearing transformations. These and the closely related Hermit transformations are just global interpolations in one direction. The first and most fundamental objective is to insert the maximum possible amount of control over the grid in a given direction. This is provided by the *multisurface transformation* (Fig 3.2) that includes both shearing and Hermit transformations as special cases. The same control is available in all directions by using Boolean sums of multisurface transformations. In the earlier shearing and Hermit cases, the transformations were often called transfinite in view of the fact that a generally infinite number of boundary points were interpolated when directions were combined. This is in comparison with the finite use of only vertex data.

The automation required to systematically generate algebraic grids for a wide variety of applications was established in two-dimensions with the software system developed by Eiseman (1982).

3.1.2 Partial differential equations methods

The techniques for the generation of arbitrary curvilinear coordinates come from either explicit or implicit definitions. Correspondingly, the coordinates are usually given either algebraically or as the solution to differential equations. In the latter category, a numerical solution procedure is required to find the grid-point locations from the defining system and the associated boundary conditions that must represent the physical geometry.

Hyperbolic Methods. When only one physical boundary is specified, hyperbolic partial differential equations may be used to obtain a grid by spatially marching from the given boundary. The remaining boundaries are determined by the solution and are geometrically unimportant in cases such as the external flow about a single object. With the requirement to prescribe only the object and the spacing along it, the hyperbolic methods proceed in marching steps that give the spacing in the outward direction. The inherent efficiency of the methods is due to the use of a single sweep through physical space. In two dimensions, orthogonal grids are obtained and are smooth, provided that the boundary is free from slope discontinuities. A fundamental development was given by Stadius (1977), and one which was well suited to body concavity was presented by Steger and Sorenson (1980). The hyperbolic methods, however, are restricted in the amount of control that can be applied.

Elliptic Methods. The element of control over the grid has been more fully developed with the methods based upon elliptic partial differential equations. We shall refer to these as *elliptic methods.* As in previous algebraic development, conformal mapping can be done in two dimensions with specifications of only boundary geometry. Typically, a pair of Laplace equations is solved subject to *Cauchy-Riemann boundary conditions.* The basic departure from conformal mapping comes with the specification of pointwise distributions along the boundaries. From this departure, some resolution requirement for the flow can be inserted. In comparison, the boundary distributions conflict with conformal conditions and produce nonorthogonal coordinates.

The earliest successful development was formally reported by Winslow (1967), who started with a Laplace system. This system determines a conformal mapping from the physical region into the space of curvilinear variables. Since the grid had to be generated in the physical space, the system had to be reformulated by an interchange of dependent and independent variables. Physical boundaries with the formulation are then represented by pointwise (Dirichlet) boundary conditions on the rectangular region of curvilinear variables. When the basic Laplace system determines a nonsingular mapping, the inverse mapping is biased toward conformal conditions. This tends to impose a global smoothness. The conflicting Dirichlet data produce nonorthogonality, which is most intense at the boundaries and gradually decays toward conformality as the interior is approached. From the discrete viewpoint of grid mappings, conformality is observed when small Cartesian squares are approximately mapped into squares of varying size.

The next important step in the development of elliptic methods was given by Thompson *et al.*, 1974). They added periodic boundary conditions to produce branch cuts for various topological configurations and also suggested that control over the grid could be accomplished by altering the original Laplace system. The alteration is to consider a pair of Poisson equations by including specifications for the right-hand sides. These are called forcing terms and are general functions of the curvilinear variables. The particular form to be used was established later by Thompson *et al.*, (1977). In higher dimensions or with forcing functions, nonsingularity is not generally assured. However, in two dimensions, the implication is that the basic system will reliably produce nonoverlapping grids, and that departures therefrom can be balanced against a solidly established reliability factor.

3.2 Vertical Coordinates Used in Mesoscale Modeling

Vertical coordinate systems in the modeling of atmosphere are generally classified using any monotonously chancing variable:

- *pressure,*
- *potential temperature,*
- *geometrical height.*

In these coordinate systems, a special procedure is needed in order to take into account the effect of the surface topography. The topography and grid-points (mesh) which are generated over it, are represented by using a vertical coordinate variable. Vertical coordinate systems are briefly reviewed in the following subsections.

3.2.1 Pressure coordinate systems

Isobaric coordinate system $- p$

When the hydrostatic approximation is valid, there are advantages to introduce pressure as the vertical coordinate, because it provides the availability of the continuity equation, the pressure gradient force, the calculation of vertical motion and some other dynamically terms in simple forms (Haltiner, 1971). On the other hand, since the surface grid line of pressure does not represent the topography exactly, which can intersect the topography, the pressure coordinate system has certain computational disadvantages in the vicinity of the mountains. It is therefore used over smooth topographies. The p-coordinate system is shown in Fig 3.3.

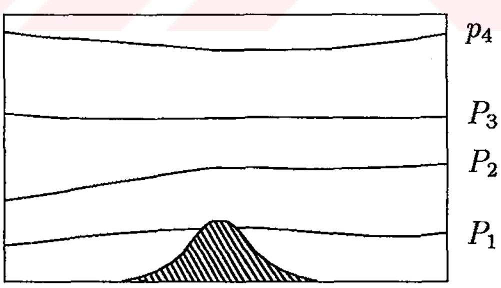

Fig 3.3 Schematic representation of isobaric coordinate system.

In earlier baroclinic forecast models, the theoretical analysis of large-scale motions and quasi-geostrophic models were built upon using the pressure p as the vertical coordinate. For example, Meschoso *et.al.*, (1982) and many others designed their models using the pressure coordinate.

Sigma coordinate system $-\ \sigma$

In Philip's study (1957), a modified pressure coordinate was used to define the independent vertical coordinate in order to eliminate the intersection problem of coordinate lines with the surface. The sigma coordinate system is defined as the pressure at the level of interest divided by the pressure at the model's lower boundary which is the earth's surface. Haltiner (1971) also showed this system which is to be formulated as follows:

$$\sigma = \frac{P}{P_s} \tag{3.1}$$

where P_s is the surface pressure, and P the pressure at any level with condition of $P_s \geq P > 0$.

In Eq. (3.1) surface pressure is used to represent the topography. So it is defined with only x and y coordinate variables, $P_s = P_s(x, y)$. Since the surface pressure is taken to be constant in time during the simulation (the surface pressure is a function of time and space), the vertical σ-coordinate values are simply seen as a ratio of pressures, or a normalization of pressure in vertical.

In the sigma coordinate system the horizontal grid lines for $\sigma = 1$ correspond to the ground surface ($P = P_s$). The top of the atmosphere is represented by $\sigma = 0$ where pressure-p is zero In order to define horizontal grid lines over the surface, the pressure values are automatically transformed from 1 to 0 limits since the pressure decreases upward (Fig 3.4).

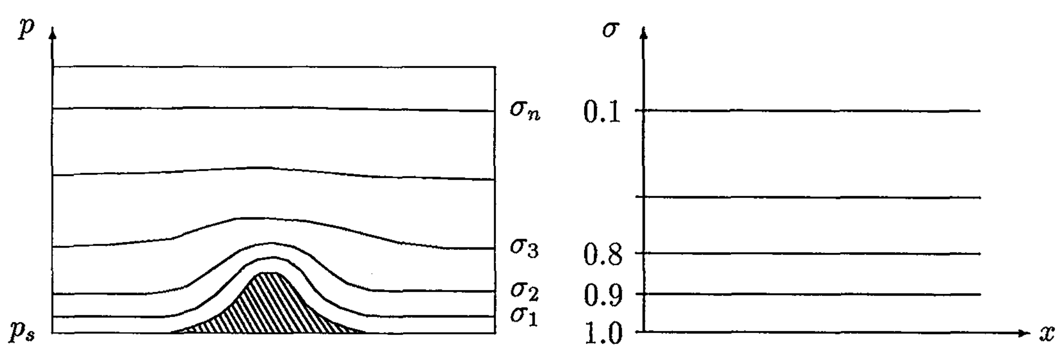

Fig 3.4 Schematic representation of the sigma coordinate system.

The main problem in the sigma coordinates is that the surface pressure does not change in time. Since the surface pressure is only a function of x, y and time, it is needed to calculate during the simulation. When the surface pressure is taken to be changeable in time, the represented topography is changed in each time step during the simulation. This produces some errors. Some of these problems become particularly apparent in models which are designed for stratospheric simulations (Ji-Fan, 1986).

Terrain-following sigma coordinate system – σ_p

The terrain-following sigma coordinate system is the modified form of the sigma coordinate system. In the terrain-following sigma coordinate σ_p-values are calculated with the normalization of the pressure between top and ground levels, and formulated as follows,

$$\sigma_p = \frac{P - P_t}{P_s - P_t} \tag{3.2}$$

where P_t is the pressure on the top of interested atmospheric domain, P_s the surface pressure, and P the pressure at any level given by $P_s \geq P \geq P_t$. In general, P_s and P_t are used as the constants in time and space during the simulation, although in some studies their temporal spatial variations are used on the top coordinates (Mahrer and Pielke 1975). Terrain-following sigma σ_p-values change from 1 at $P = P_s$ to 0 at $P = P_t$ level (Fig 3.5).

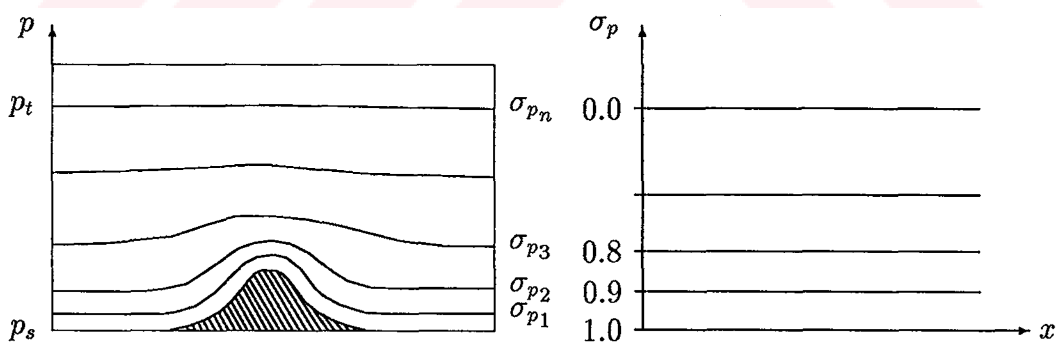

Fig 3.5 Schematic representation of the terrain-following sigma coordinate system.

The main advantage of the terrain-following sigma system is that it allows simplified treatment of the lower boundary conditions in models which include topography. σ_p-coordinates do not intersect the topography while σ-coordinates do. In addition, the solving governing equations have simple formulation, which bring about some advantages. However, in order to use this coordinate system, the slope of the topography in each horizontal grid interval must be much less than 45^o (Pielke, 1984). Over steeply sloped topography, the calculation of the sigma-coordinate pressure gradient force involves computing the difference between two large terms of opposite signs which results in a large truncation error in the governing equations (Smagorinsky *et al.*, 1967; Kurihara, 1968; Corby *et al.*, 1972; Gary, 1973; Phillips, 1974; Sundqvist, 1975).

In some 2-D model studies, the lowest sigma-layer (i.e., $\sigma = 1$) is not taken as surface layer (Suarez and Arakawa, 1979; Deardorff *et al.*, 1984). The lowest layer of these models comprises an assumed well-mixed layer of variable depth. The mixed layer extends from the surface, where the pressure P is $P_s(x,t)$, to the mixed-layer top height where $P = P_B(x,t)$.

$$\sigma_p = \begin{cases} \dfrac{P - P_B}{P_s - P_B} + 1 & \text{for} \quad P_s \geq P \geq P_B \\ \dfrac{P - P_t}{P_B - P_t} & \text{for} \quad P_B \geq P \geq P_t \end{cases} \tag{3.3}$$

For the first part of the sigma coordinate levels (i.e., mixed-layer), sigma coordinate values change between $2 \geq \sigma_p \geq 1$, and for the second part between $1 > \sigma_p \geq 0$.

Logarithmic-pressure coordinate system – $\tilde{P}$

A logarithmic-pressure vertical coordinate system is used such that

$$\tilde{P} = P_s e^{-z/H} \qquad \text{or} \quad \tilde{z} = -H \ln\left(\tilde{P}/P_s\right) = -H \ln \sigma, \tag{3.4}$$

where H is the scale height, which is taken to be constant. In logarithmic-pressure coordinates, $\tilde{P} = P_s$ at the surface level ($z = 0$), and $\tilde{P} = P_s \cdot e^{-1}$ at the top of atmosphere ($z = H$). This coordinate system is especially useful in where the coarse mesh (a few pressure coordinate lines) near the surface and the fine mesh (many pressure coordinate lines) on upper part of domain are needed.

Zhang and Geller (1994) used this coordinate transformation to analyze for Klevin and Rossby-gravity waves in a three-dimensional adiabatic model.

Step-mountain eta coordinate system – η

In the sigma system using the hydrostatically consistent schemes, increasing the steepness of the mountains or hills in the model topography and increasing the vertical resolution may lead to a violation of the hydrostatic consistency of the scheme (Tibaldi, 1985). Additionally, it has some numerical problems which result from the lateral diffusion, analysis and required interpolations, whereas they are not important (Sadourny *et al.*, 1981; Simmons and Burridge, 1981; Simmons and Strüfing, 1981). In fact, all problems result from the slope of sigma coordinate surfaces. However it is not possible to reduce the effects of and the slopes of sigma surfaces by increasing the horizontal resolution. Therefore, "*hybrid*" coordinate system which includes sigma coordinates, is needed.

For representation of the topography with steeper mountains, a hybrid vertical coordinate system defined as a modified sigma-pressure or terrain-following sigma pressure system in which height coordinates are used, can be utilized. The hybrid sigma system and a blocking procedure to deal with steep wall-type mountains have been proposed for lee cyclogenesis studies by Egger (1972a; 1972b; and 1974). In these studies, the vertical walls were used to block the flow in a given layer or layers and to simulate the barrier effect of steep mountains.

Mesinger (1984) also suggested a new pressure coordinate system called "*eta-η*" which is derived from Egger's approach (1972a and b). In this system, η-coordinate surfaces remain at fixed elevations at the places where they define the ground surface. It is formulated as follows,

$$\eta = \sigma \frac{P_{\rm ref}(z_s)}{P_{\rm ref}(0)}, \qquad \sigma = \frac{P}{P_s}$$

or

$$\eta = \sigma_p \frac{P_{\rm ref}(z_s) - P_t}{P_{\rm ref}(0) - P_t}, \qquad \sigma_p = \frac{P - P_t}{P_s - P_t} \tag{3.5}$$

where the subscripts t and s stand for the top and the ground surface values of the model atmosphere, respectively; z is geometrical height, and $P_{\rm ref}$ is a suitably defined reference pressure as a function of z. It can be given as follows,

$$P_{\rm ref}(z) = P_{\rm ref}(0)\ e^{-\pi z/RT}. \tag{3.6}$$

where $P_{\rm ref}(0)$ is the pressure on sea level.

The ground surface heights z_s are taken only as a discrete set of values so that mountains are formed of the three-dimensional grid boxes of the model. Therefore it is also called *step-mountain* coordinate and symbolized with "η".

A schematic representation of the mountains with this "*step-mountain*" coordinate is shown in Fig 3.6. In this figure, u, T and P_s represent the x-component of velocity, temperature and surface pressure, respectively, and N is the maximum number of the η-layers.

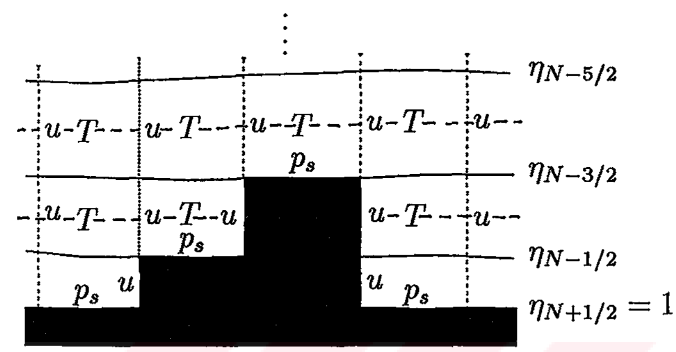

Fig 3.6 The vertical grid structure and indexing used in the eta coordinate using step-like (or block) representation of mountains. The step-mountains are indicated by shading. (After Mesinger, 1984).

The coordinate surfaces of the eta coordinate are quasi-horizontal as opposite to the sigma coordinate. Furthermore, although the η-coordinate surfaces intersect the ground surface, it has still simple boundary conditions as well as a simple continuity equation, the same as those of the hybrid coordinate system of Simmons and Burridge (1981). In addition, a model computer code using the eta coordinate can be also run in the sigma mode. Thus a direct comparison between the two vertical coordinates can be made with an identical model (Mesinger 1985, Mesinger and Janjić 1987; Mesinger *et al.*, 1988). In several parallel runs, the model run in the eta mode outperformed its sigma mode counterpart. In an atmospheric model using the eta coordinate, three major problems can be anticipated: internal boundaries at the vertical sides of the mountain walls, vectorization, and physical package. These problems are discussed in detail by Mesinger (1984), Mesinger and Janjić (1987); Mesinger *et al.*, (1988), Janjić (1990).

3.2.2 Potential temperature coordinate systems

Isentropic coordinate system $-\ \theta$

In description of adiabatic motions, in which the potential temperature θ of an air parcel is conserved, the potential temperature can be used for a vertical coordinate variable. Potential temperature is defined as

$$\theta = T\left(\frac{P}{P_{\text{ref}}}\right)^{-R/C_p} \tag{3.7}$$

After the first successful integration of the hydrostatic equations using an isentropic coordinate system (Eliassen and Raustein, 1968), potential temperature is used increasingly as a vertical coordinate in analyzing and forecasting atmospheric processes.

In many meteorological phenomena, particularly in the free atmosphere, air motions may be assumed to be isentropic. In the case of the air parcel which has the same potential temperature, it always remains on the same isentropic (potential temperature) surface. Therefore it is useful for tracing the actual paths of the travel of individual air parcels. Under these circumstances the pattern of isentropic surfaces represents the vertical structure of the adiabatic atmosphere. The isentropic coordinate system provides such an allowance with which it is possible to produce much finer vertical resolution where the potential temperature gradient is large. Through vertical clustering of grid points in regions of high potential temperature gradients, the isentropic coordinate system is not only used for adiabatic motions but also for the objective analysis (Shapiro and Hasting, 1973), solving of frontal structure details (Bleck and Shapiro, 1976) and weather prediction models (Kasahara, 1974; Bleck, 1973, 1974, and 1978; Eliassen and Raustein, 1968, and 1970; Shapiro, 1973; Trevisan, 1976).

In addition, the model formulation in isentropic coordinates is rather simple because there is no need to calculate the vertical motion in an adiabatic atmosphere.

Despite these advantages, isentropic coordinates have two disadvantages. One of them, monotonic variation of potential temperature is not always guaranteed whereas it is initially required for its use as a vertical coordinate. The other one is coordinate surfaces that can intersect the surfaces in regions of contrast horizontal temperature (Fig 3.7). Although the intersection of isentropic lines with the surface does not seem to be a serious obstacle (Eliassen and

Raústein, 1968, and 1970; Bleck, 1974; Shapiro, 1975; Trevisan, 1976), the existence of superadiabatic and adiabatic layers, which occur most frequently in the boundary layer, cannot be tolerated. It can cause folding of the isentropic surfaces which can lead to instability when the strong diabatic heating near the earth's surface exists, whether the methods of incorporating orographic effects appear to be sufficient.

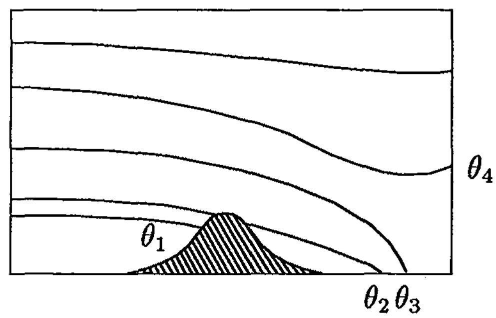

Fig 3.7 Schematic representation of isentropic coordinate system.

Terrain-following isentropic coordinate system $-\ \sigma_\theta$

The isentropic coordinate system has computational disadvantages which are similar to those of the pressure coordinate system in the vicinity of the mountains. The lower boundary conditions of the isentropic coordinate system are not given easily since the surface potential temperature varies in space and time. Therefore, to eliminate some of these difficulties, a new vertical coordinate system should be used. Terrain-following isentropic system (σ_θ) representation, which is introduced by Branković (1981), is the modified form of the isentropic system. In this system σ_θ-coordinate values are calculated, with the normalization of the potential temperature formulated as follows,

$$\sigma_\theta = \frac{\theta - \theta_t}{\theta_s - \theta_t}. \tag{3.8}$$

where θ_t is a constant potential temperature at the top of the model, θ_s a variable potential temperature at the earth's surface with $\theta_s < \theta_t$ condition, and θ potential temperature as the vertical coordinate variable which increases with height. With this formulation the potential temperature θ values are automatically transformed from 1 to 0 for upward vertical levels. We have $\sigma_\theta = 1$ at the surface which has $\theta = \theta_s$, and $\sigma_\theta = 0$ at the top of the upper level which has $\theta = \theta_t$. In using the terrain-following isentropic system, the lower boundary conditions become simpler than those of the θ-isentropic coordinate system. However, as long as surface potential gradients are holding relatively smooth, the angle between θ surface and σ_θ surfaces is small and a loss of the features mentioned above is not significant (Branković, 1981).

A schematic representation of the cross section of the frontal zone in the terrain-following isentropic coordinate system is illustrated in Fig 3.8.

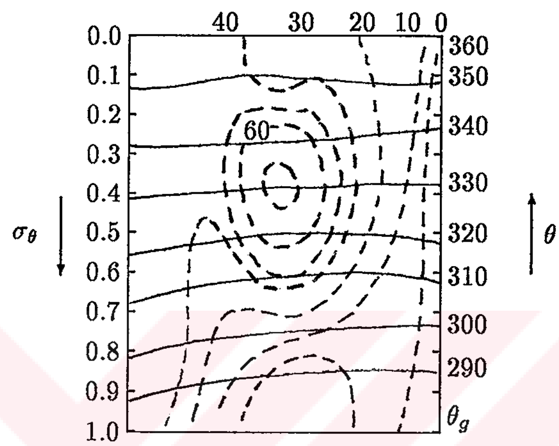

Fig 3.8. The representation of frontal zone and θ surfaces in normalized potential temperature (σ_θ) coordinate. (after Bleck and Shapiro, 1976)

Hybrid theta–sigma pressure coordinate system – $(\theta - \sigma_p)$

Another use of the θ-system is within the σ_p-coordinate domain, which is called *hybrid theta-sigma model*, described in detail by Bleck,1978 and Uccellini *et al.*, (1979). The intersection of isentropes with the surface, the existence of superadiabatic and adiabatic conditions, and the general lack of vertical resolution near the earth's surface in less stable regions inhibit incorporating boundary layer dynamic and thermodynamic processes into isentropic models. Without an adequate representation of the boundary layer, isentropic models are limited in their application to subsynoptic- and synoptic-scale diagnostic and forecasts. These deficiencies of isentropic coordinates are avoided by utilizing sigma coordinates within the boundary layer which maintains a uniform grid spacing throughout, avoiding the intersection between coordinate surfaces and the ground, and thus providing a suitable framework for incorporating boundary-layer processes into the model.

The hybrid $\theta - \sigma_p$ model combines an isentropic representation of the free atmosphere with a sigma-coordinate representation of the bottom 200 mb of the troposphere. Four possible representations which have different ways of joining σ_p and θ coordinate domains are shown in Fig 3.9.

In Fig 3.9 (a) The interface is held at a constant pressure $P_\circ$ (Friend *et al.*, 1977); (b) The interface is held at a fixed pressure interval above ground, i.e., $P_s - P_\circ$ =constant (Uccellini *et al.*, 1979); (c) The interface is initially defined to coincide with a pressure surface, but is treated subsequently as a material surface subject to vertical displacement (Deaven, 1976); (d) The interface is chosen to coincide with an isentropic surface high enough in the atmosphere to clear the ground in the geographical area covered by the horizontal mesh (310°K surface is generally suitable for this purpose).

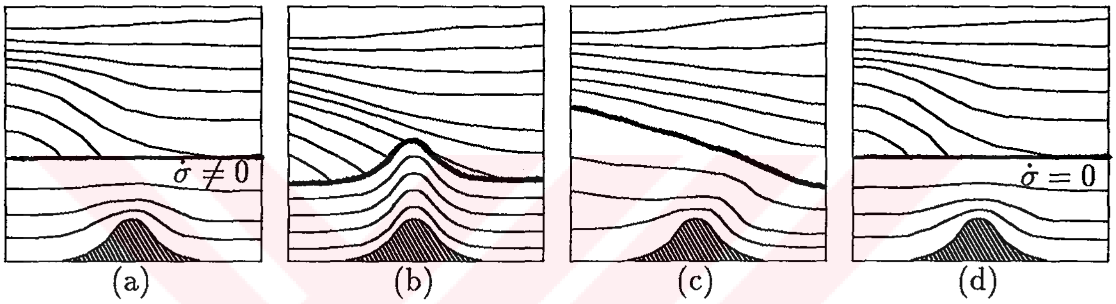

Fig 3.9 Four possible ways of joining σ_p and θ coordinate domains (Bleck, 1978).

However, the hybrid theta-sigma domain has some problems. The primary problem with hybrid models is matching the boundary conditions across the interface which provides for full interaction between the model domains in the presence of diabatic heating and viscous forces, without introducing spurious sources of mass, momentum or energy. The solution matches boundary conditions at the interface using the flux form of the primitive equations (Uccellini *et al.*, 1979; Johnson and Uccellini, 1983). In addition to this solution, it is found that non-hybrid model versions produce higher noise levels than the hybrid formulations (Bleck, 1978).

Entropy coordinate system $- \tilde{s}$

The entropy coordinate model is based on the primitive equations expressed in terms of a vertical coordinate

$$\tilde{s} = C_p \left(\frac{\theta}{\theta_\circ}\right). \tag{3.9}$$

Model levels are equally spaced in $\tilde{s}$, giving slightly higher resolution in the stratosphere than the mesosphere. The reference potential temperature θ_o may be set arbitrarily, and a value of 1 °K can be used (Manney *et al.*, 1994). Entropy coordinate lines can intersect the ground as isentropic coordinate lines.

3.2.3 Geometrical height coordinate system

Rectangular coordinate system – z

Since the rectangular coordinate system has a regular grid-mesh structure, the primitive equations are solved directly from their finite-differenced forms. In the rectangular coordinate system, the topography (Fig 3.10a) is in the shape of step-mountain with constant grid spacing horizontally and vertically (Fig 3.10b). The best representation of topography is made by decreasing horizontal and vertical spacing in the grid structure (Fig 3.10c. However, this requires more computer time. Some way of solving this difficulty is to use another topography convenient grid mesh structure. Namely, a coordinate transformation which will transform the complicated atmospheric domain into a rectangular one is used to provide less computer time with a suitable number of the grid points as physically as possible in solution of discretized primitive equations.

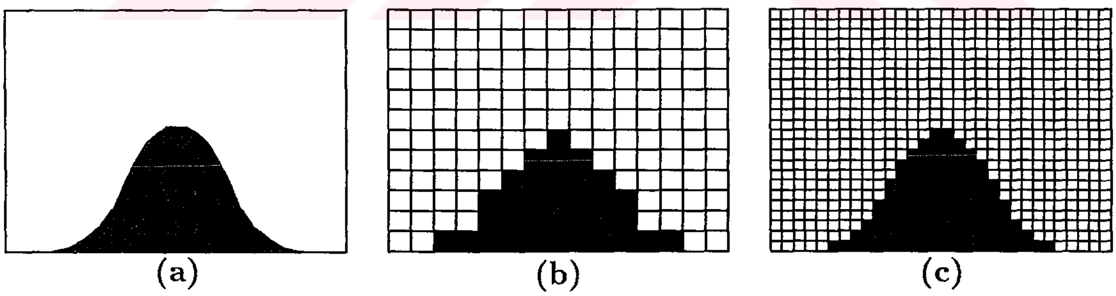

Fig 3.10 Schematic representation of the rectangular coordinate system.

Two-dimensional graded-cartesian grids using the box-method

The graded systems have a smooth transition into the large-scale system with no additional computations being needed to merge the systems, whereas the non-Cartesian-type grids often incur added computations (and perhaps approximations) where the grids joint together. The box method has the desirable property that the momentum and mass of the system are preserved under the finite-difference formulation to within time-differencing errors because the equations are expected in flux form. The graded grids are shown in Fig 3.11.

Variable increment-space meshes have been used with some success in studies of models possessing one horizontal space dimension (Koss,1971). For two horizontal space-dimensioned models, the interest has been in the embedding of a fine-resolution mesh in a relatively coarse grid to resolve interesting small-scale features that are present in a large-scale environment.

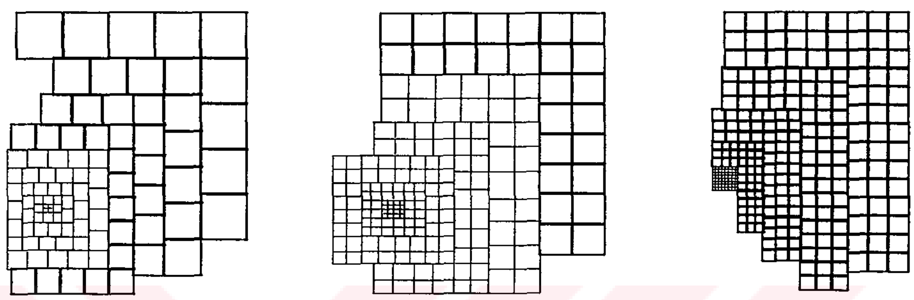

a) Single annulus b) Double annulus c) Triple annulus

Fig 3.11 Graded mesh constructions for (a) single annulus, (b) double annulus, and (c) triple annulus (after Walter, 1971).

The variable resolution grids are of two basic types: (1) a constant fine mesh embedded in a constant coarse mesh and (2) a grid system that becomes progressively coarser with distance from the central region. Both types are members of a generalized family of grids, the construction and characteristics.

The basic construction element of the variable-resolution grids is a square having the side length. Each graded grid has the following properties:

1) The area elements (boxes) of the grid structure are squares with side lengths that are integral multiples of the basic side length.

2) The boxes increase in the area outward from the center in a systematic manner.

3) The geometry of contiguous boxes having equal area is that of a "square annulus" (except for the central region).

Simple height coordinate system $-$ $\underline{z}$

In the simple height coordinate system, horizontal and vertical grid spacing are the same but the grid-mesh structure is not in rectangular form. This coordinate system is formulated simply as follows

$$\underline{z} = h(x) + \mathrm{i} \cdot \Delta z \tag{3.10}$$

where $h(x)$ is the geometrical height of the topography, Δz a vertical constant grid spacing, and i the index of levels (i=0,...,n; where $i = 0$ at the ground, and $i = n$ at the top of domain). The grid structure of the coordinate system is shown in Fig 3.12.

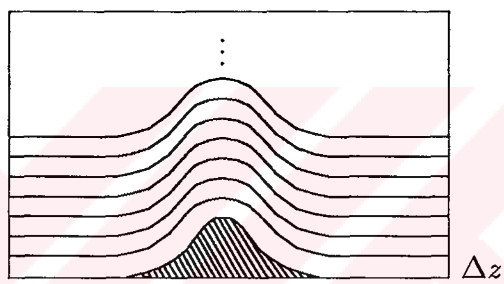

Fig 3.12 Schematic representation of the simple height coordinate system.

Here, there is an important problem about boundary conditions. Boundary conditions for the top of atmospheric domain are not given directly. In general, this coordinate system may be used if the top level of the model is too high or height which the effects of topography is insignificant or where the boundary condition is simple. In the United Kingdom Meteorological Office's mesoscale forecasting model which uses the simple-height coordinate system, the highest level and also the top of the model is at 12 km which is normally in the stratosphere (Golding, 1990).

Terrain-following S**-coordinate system** $-$ σ_z

The S-coordinate system is commonly used in the atmospheric modeling, and it is formulated as follows,

$$S = \left[\frac{z - h(x)}{H - h(x)}\right] \tag{3.11}$$

where z is the geometrical height above sea level, H is the height at which the S-surfaces reduce to z surfaces (often H is set equal to the model's top level), and $h(x)$ is the topography elevation. This system follows the topography at levels below $z = H$. If the model extends above $z = H$, the vertical coordinate variable typically reverts to z. S coordinate values for levels are transformed from 0 to 1 for $h(x)$ to H (Fig 3.13)

The terrain-following S-coordinate system is the modified form of the S-coordinate system. It is formulated as follows

$$\sigma_z = H\left[\frac{z - h(x)}{H - h(x)}\right] \tag{3.12}$$

where σ_z-coordinate values is from 0 to H between $h(x)$ and H. σ_z-coordinate value at surface level is equal to 0 since $z = 0$, and at top of atmosphere is equal to H value since $z = H$. So σ_z-coordinates are transformed from 0 to H (Fig 3.13).

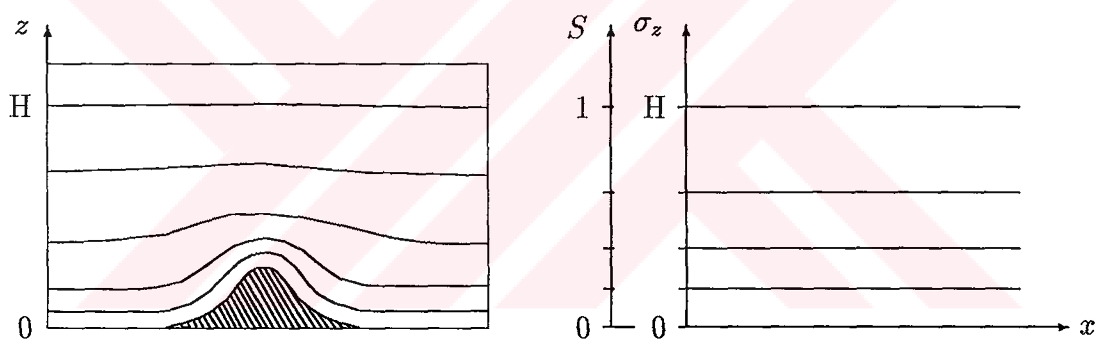

Fig 3.13 Schematic representation of the S-coordinate system and the terrain-following coordinate system.

The geometric height coordinate is the only coordinate where is the location over the topography with respect to the coordinate surface does not change in time during the calculation of primitive equations. So the blocking process in the height coordinate is simpler than that of the pressure or isentropic system. The primary advantage of the terrain-following S-coordinate systems is that they allow simplified treatment of the lower boundary conditions in models which contain topography. Therefore, the model levels do not intersect the earth's surface. Gal-Chen and Somerville, (1975a) gave the transformation derivatives and transformed equations in terrain-following S-coordinate system, and Pielke and Martin (1981) discussed the transformation.

Zeta coordinate system – ζ

The zeta coordinate system is introduced by Orlanski and Gross (1994). This system is formulated as,

$$\zeta = e^{-\varepsilon S}, \tag{3.13}$$

where S is the coordinate system variable given by Eq. (3.12), and larger values of ε place more model levels and higher resolution near the ground. An additional advantage of employing such a physically based vertical coordinate is its ease of use in more applied meteorological research applications, such as four-dimensional data assimilation. In this case, a physical vertical coordinate is more compatible with the newest atmospheric observing systems currently being deployed, such as Doppler radar and VHF wind profilers that, in contrast to, rawinsondes, are not based on a pressure coordinate.

Logarithmic height coordinate systems – z_L, z_η, s, $\tilde{z}$

The first logarithmic-height coordinate system which will be discussed here, z_L, is commonly used in boundary-layer models. In the study of Paegle and David (1983), this transformation has been used in the lowest 134 m. The coordinate formulation is as follows,

$$z_L = z_\circ e^{\xi/L}, \qquad \text{or} \qquad \xi = L\ln(z_L/z_\circ). \tag{3.14}$$

where $z_\circ$ is the roughness height, L the scaling parameter.

The second coordinate system, z_η is introduced by Beljaars *et al.*, 1987 and discussed by Dapeng and Taylor (1992). Beljaars *et al.*, (1987) developed a linear spectral finite difference model for the study of neutrally stratified atmospheric surface flow over complex topography. For the vertical direction in spectral (z_η) space, a logarithmic coordinate transform,

$$z_\eta = \frac{\ln[(z + z_\circ)/z_\circ]}{\ln[(l_i + z_\circ)/z_\circ]} + \frac{z_\circ}{l_\circ}, \tag{3.15}$$

is postulated by Beljaars *et al.*, (1987). In this formula, l_i is the inner-layer thickness, and $l_\circ$ is the outer-layer thickness of boundary layer (Hunt and Simpson, 1982).

Orlanski *et al.*, (1974) tested two logarithmic-height coordinate systems similar to the above,

$$s = \frac{\ln[(z + 30.5)/30.5]}{\ln[(S_h + 30.5)/30.5]}, \quad \text{and} \quad s = \left(\frac{z}{1600}\right) + \frac{1}{17.9}\ln\left(\frac{z+15}{15}\right) \tag{3.16}$$

to represent the vertical grids. In the first formulation S_h is the top of the model (they used S_h=20 km). With the left-hand expression for s, using 70 levels, the grid resolution was 3 m near the ground and 1700 m near the top, whereas using 80 levels, the right-hand form varied more slowly from 3.7m near the surface to approximately a constant of 175 m from 4000 m to the top (which was set at 10.16 km in that representation). Orlanski *et al.*, (1974) rejected the left-hand form for s because the extremely coarse resolution in the upper levels produced a significant distortion of gravity waves, which propagated upward from the active lower layers. This problem was much less apparent using the second coordinate stretching, despite the lower top.

The last logarithmic-height coordinate system $\tilde{z}$ is also defined as the inverse of the logarithmic-pressure coordinate transformation given by Eq. (3.4). The formulation is defined as,

$$\tilde{z} = -H\ln(\sigma), \tag{3.17}$$

where σ is sigma coordinate variable. In this coordinate system the coordinate limits are $\tilde{z} = 0$ at $P = P_s$ or $\sigma = 1$ (at the ground), and $\tilde{z} = 2.3H$ at, for example $\sigma = 0.1$ (i.e. P=100 mb, and P_s=1000 mb).

Pseudo-height coordinate systems $- z_p$

Hoskins and Bretherton (1972) designed a model of upper-level frontegenesis. In this study the model is formulated in terms of the pressure-dependent pseudo-height coordinate system,

$$z_p = z_a\left[1 - \left(\frac{P}{P_\circ}\right)^{R/C_p}\right], \qquad \text{where} \qquad z_a = C_p\frac{\theta_\circ}{g}, \tag{3.18}$$

is the pseudo-height at the top of atmosphere ($P = 0$) and $\theta_\circ$ and $p_\circ$ reference values of potential temperature and pressure which are taken to be constant.

Although Hoskins and Bretherton (1972) formulated the model in terms of z-coordinates (pseudoheight coordinate system), it is solved in sigma-pressure (σ) coordinates. The model is formulated in the z-system to take advantage of the analytical properties of this and to maintain notational continuity with earlier theoretical studies beginning with Hoskins and Bretherton. In the study of Hoskins and Bretherton (1972), the reason for solving the model equations in the sigma-pressure system is because of the using of an available well-tested and documented cross-sectional version of Penn State/NCAR mesoscale model.

Curve fitting approaches (Harmonic Analysis)

In some mesoscale studies, in order to represent the surface topography, it can be used some functions which have inverse forms, for example, harmonic functions.

The harmonic analysis method can be used to represent the topography in wave-form. The representation of surface topography as a function of wavelength can be used to determine the characteristic scales of the topography (Pielke and Kennedy, 1980). A one-dimensional Fourier transformation, as shown by Panofsky and Brier (1968), given by

$$z_G(x_j) = \overline{z}_G + \sum_{n=1}^{I_x/2} \left[a_n \sin(2\pi nj\Delta x/D_x) + b_n \cos(2\pi nj\Delta x/D_x) \right] \tag{3.19}$$

where

$$a_n = \frac{2}{I_x} \sum_{n=1}^{(I_x/2)-1} z'_G(x_j) \sin(2\pi nj\Delta x/D_x); \qquad a_{I_x/2} = 0, \tag{3.20}$$

$$b_n = \frac{2}{I_x} \sum_{n=1}^{(I_x/2)-1} z'_G(x_j) \cos(2\pi nj\Delta x/D_x); \qquad b_{I_x/2} = -z'_G(x_j)/I_x. \tag{3.21}$$

In this expression I_x is an even integer number of grid points of separation Δx used to represent the height of topography within the interval D_x. The variable n is referred to as the number the topography of the harmonic. The quantity $(a_n^2 + b_n^2)^{1/2}$ represents the contribution of each wavelength of size $2\Delta x, 3\Delta x, 4\Delta x, \ldots,$ up to $I_x\Delta x/2$ to the function $z'_G(x_j)$. The domain-averaged topography height is given by $\overline{z}_G$, with z'_G the variations from this value.

Ideally one would prefer to use a two-dimensional Fourier transformation, but such programs are not routinely available for large amounts of data. Thus since only one-dimensional transforms are routinely available on most computer systems, it is necessary, at present, to perform a series of cross sections through the regions of the most rapidly varying topography. An application of Fourier transformation in the representation of topography is shown in Fig 3.14.

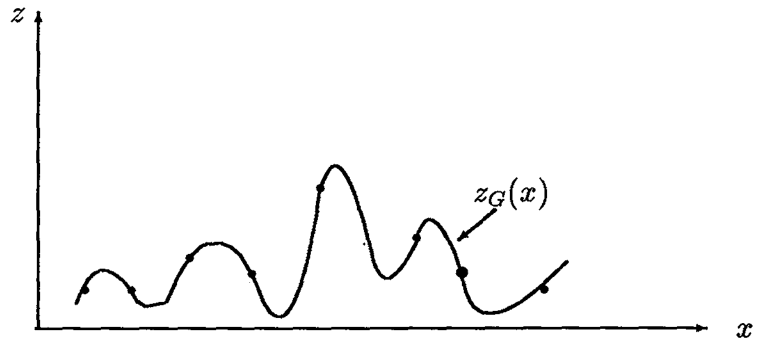

Fig 3.14 Schematic representation of the applying harmonic analysis to the topography.

Pielke and Kennedy (1980), and Young and Pielke (1983) have discussed the analysis of topography irregularities in more detail. Salmon *et al.*, (1981) have discussed the implications of high wavenumber topography features in a model and concluded that such features cause noisy solutions that tend to overemphasize the real impact of these small-scale topography variations. Unfortunately, since the horizontal gradient of a pressure perturbation is proportional to the horizontal wavenumber as well as spatial scale of topography variations; the relative contribution of short wavelength topography features to velocity accelerations would be expected to be larger than implied from a decomposition of topography variations alone (Walmsley *et al.*, 1982).

3.2.4 Another grid mesh structures and coordinate systems

In literature, some special grid mesh structures or coordinate transformations for conventional finite-difference models are rarely used by modelers. Some of these are given below.

Geostrophic coordinate system

Eliassen (1962) first introduced a transformation of the geostrophic momentum equations in a study of frontal dynamics. He called the absolute momentum coordinate as the "transformed horizontal coordinate". Hoskins and Bretherton (1972) later defined a variant of the absolute momentum geostrophic coordinate, which differs from it only by a constant factor f. They referred to the whole set of horizontal and vertical coordinates as geostrophic coordinates. Two-dimensional geostrophic coordinate transformation is given by Desroziers and Lafore (1993). An extension to the three-dimensional space has been proposed by Hoskins (1975).

An easy way to understand the impact of the geostrophic transformation is to imagine that if geostrophic wind speed U_g is a simple sinusoidal wave in geostrophic space, then the return to physical space gives every particle a displacement

$$x - x_g = -U_g/f,$$

directly proportional to U_g. As a result, cyclonic regions are contracted, whereas anticyclonic ones are stretched. All these elements tend to generate sharp fronts.

The geostrophic coordinate system are formulated as follows,

$$x_g = x + \frac{U_g(x_g, z_g = z)}{f} \tag{3.22}$$

where $\overrightarrow{U_g}$ is the alongfront geostrophic wind, f the Coriolis parameter, (x, z) cross-front physical space coordinates and (x_g, z_g) transformed coordinates. This is a nonlinear equation that can be solved by an iterative method (such Newton method).

Streamfunction as a vertical coordinate variable

To study the effect of curvature, a primitive equation model developed by Houghton *et al.*, (1981) and Van Tuyl and Young (1982) was adapted to account for jet-streak curvature. The only change was to add the effect of curvature to the initial ψ (stream-function) field. The modification was made by Van Tuyl and Young (1982) specification of ψ. In the model, once the streamfunction has been specified for the two model levels (800 mb and 400 mb). The geopotential heights are then linearly extrapolated to 1000 and 200 mb and interpolated to 600 mb. Also this coordinate system is discussed by Moore and VanKnowe (1992).

Icosahedral and hexagonal grid meshes

Williamson (1968) and Sadourny *et al.*, (1968) simultaneously introduced a new approach to more isotropically and homogeneously discretize the sphere. Their grids are constructed from spherical triangles that are nearly equal in area and that are equilateral. The grid was inspired by Buckminster Fuller's geodesic dome and is called a spherical geodesic grid. While Williamson (1968) and Sadourny *et al.*, (1968) worked finite-difference models, Cullen (1974) developed finite-element models based on spherical geodesic grids.

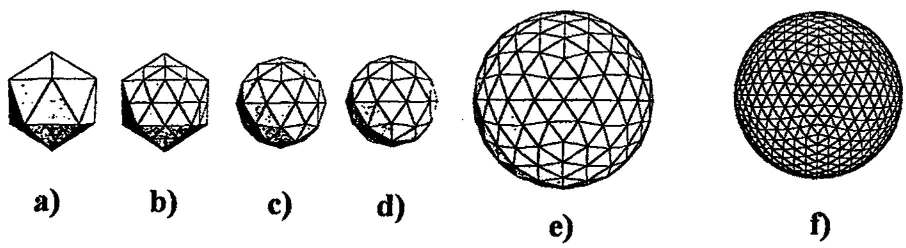

Fig 3.15 (a) An icosahedron inscribed in a unit sphere, (b) Bisect of each edge forming four new faces, (c) Projection of the new vertices onto the unit sphere, (d) Rotation of the faces in Southern Hemisphere to form a twisted icosahedron, (e,f) continuining the recursive subdivision of fig (d) (after Heikes and Randall, 1995).

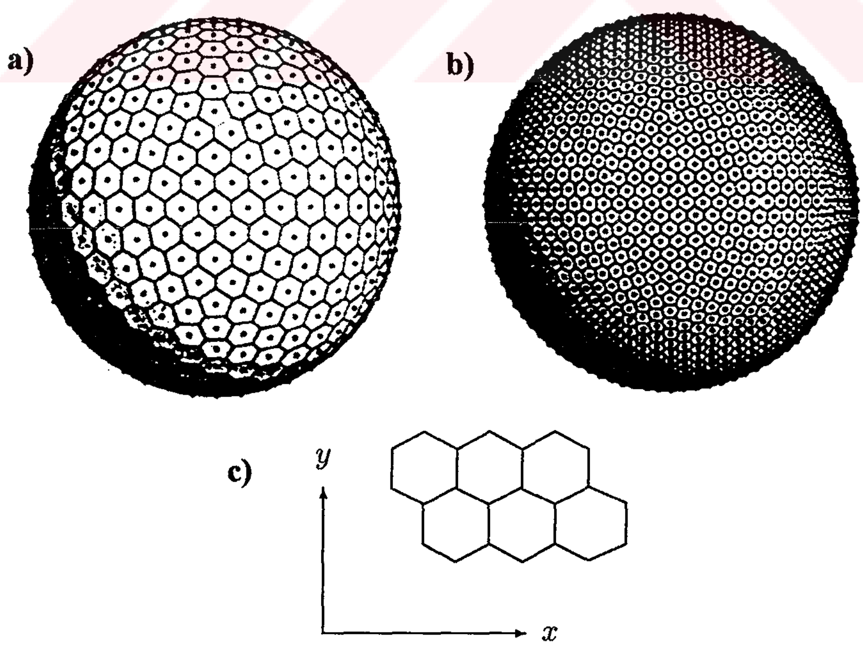

Fig 3.16 (a,b) Voronoi grids constructed with a twisted icosahedron, and (c) schematic showing the layout of the hexagonal grid (after Heikes and Randall, 1995).

An example of a simple spherical geodesic grid is shown in Fig 3.15 (Heikes and Randall, 1995; and Thuburn, 1993). Since the grid points are not regularly spaced and do not lie in orthogonal rows and columns, specially designed finite-difference schemes are needed (Masuda, 1969). Williamson (1968) and Sadourny (1968) chose the nondivergent shallow-water equations on a plane using a triangular mesh. Masuda and Ohnishi (1987) created an elegant geodesic grid model for the shallow-water equations on the sphere. The design of his model is discussed by Heikes and Randall (1995). Icosahedron grid structure are shown in Fig 3.15 and 3.16.

3.3 Schwarz-Christoffel Transformation as a Grid Generator

In order to numerically solve the flow problems efficiently and accurately, it is necessary that one find a suitable coordinate system in which to do the computations. The problem of generating a proper coordinate system is difficult since the coordinate system should be determined such that it minimizes errors in the flow solver and at the same time does not reintroduce the errors through the coordinate generator. Ultimately, the coordinate generator should be interactive with the flow solver in order to properly handle the flow problem under consideration with a minimum number of mesh points.

The difficulty of determining a good coordinate system mainly arises due to the the complicated structure of separated flows and the severe scaling laws which arise at and downstream of separation. Stewartson (1974) and others have determined the asymptotic structure near separation for several problems and it is a challenging numerical problem to develop coordinate generators which honor the scalings indicated by the asymptotic theory. It is therefore important that a coordinate generation technique be flexible enough to align coordinate lines in arbitrary directions so that the scale laws can be accommodated in the most convenient manner by stretching normal to the proper coordinate lines.

Many authors have been developed grid generators in physics and engineering, especially in magnetic field, fluid flow field, and flow of electric current studies. These methods are based on the numerical solution of partial differential equations and therefore have some difficulty with outer boundary conditions, determination of proper forcing functions for the right hand sides of the differential equations, and numerical inaccuracy at corners and other discontinuities.

Some of the most flexible and accurate methods of potential flow solution are based on the numerical solution of the integral equations resulting from source, vortex and doublet distributions on the body surface (Hess and Smith, 1966; and Bristow, 1977). These methods are attractive since they involve only the solution of boundary integrals requiring no outer boundary conditions, and allow for the removal of singularities from corners or lower order discontinuities. If the solution in the interior of the flow field is desired, integration is required. In a sense, mapping with Schwarz-Christoffel transformations (SCT) can be viewed as a coordinate generation method which is done in the same spirit, i.e. it is a boundary integral method therefore requiring no outer boundary conditions, and singularities can easily be removed. After this initial mapping of the boundary has been performed, coordinates interior to the flow field can be determined by integration in arbitrary directions and therefore virtually any coordinate system desired can be accurately determined.

A coordinate generation method for use in the atmospheric flow modeling is given here which is much simpler, more accurate, and more flexible than currently existing methods. This approach is based on numerical integration of Schwarz-Christoffel transformation for general curved lines or surfaces. It is shown to be second-order accurate in mesh size with extensions to higher-order accuracy levels identified. In addition, this method directly provides the two dimensional incompressible potential flow solution for flow past complex shapes including flows with free streamlines. Mapping with Schwarz-Christoffel transformation can be viewed as a coordinate (grid-points) generation. In the atmospheric flow modeling, the usage of Shwarz-Christoffel transformation is introduced by Erdun *et al.*, (1996). In this work SCT is formulated and discussed in detail for atmospheric flow and dispersion modeling.

Schwarz-Christoffel transformation for polygons is well known and can be found in any standard text on complex variables (Carrier *et al.*, 1966) Schwarz-Christoffel transformation is named in honor of the two German mathematicians H.A.Schwarz (1843-1921) and E.B.Christoffel (1829-1900) who discovered it independently. The extension to curved surfaces is less known and is absent from most texts. A very extensive treatment of the extension to curved surface is contained in Woods (1961).

In Walker's textbook (1964) which is the first book about Schwarz-Christoffel transformation, its applications in engineering problems have been given. Several authors have dealt with numerical integration of the Schwarz-

Christoffel transformation for polygon, i.e. the case where the sides are made up of straight lines. Trefethen (1979) has presented a method for handling this case along with a review of other work in the area. The most closely related work to the present is that of Anderson (1979) who has used straight elements to do curved channel mappings. Almost no work has been done on numerical integration of the transformation for curved surfaces.

The Schwarz-Christoffel Theorem is normally written in a form which is applicable only to polygons or surfaces which consist of straight line segments (Carrier *et al.*, 1966). However, the theorem can be extended to general surfaces which may be curved or made up of curved portions. One is referred to Woods (1961) for the generalizations of the theorem.

The most familiar form of the Schwarz-Christoffel Theorem is the one which is applicable to polygons and is given by

$$\frac{dy}{d\lambda} = M \prod_{i=1}^{n} (\lambda - a_i)^{\alpha_i/\pi} = f(\lambda) \tag{3.23}$$

where the geometry is shown in Fig 3.17. Integration of the above equation yields

$$y = M \int_0^{\lambda} \prod_{i=1}^{n} (\lambda - a_i)^{\alpha_i/\pi} d\lambda + A. \tag{3.24}$$

This formula represents a conformal mapping of the upper half of the λ−plane onto a region into the interior of the polygon shown in the y−plane (Fig 3.17). The quantity n relates to the number of corners, M and A are complex constants to be determined, and the points a_i's are real constants (on the real axis in the λ−plane) also to be determined ($i = 1, \ldots, n$). The α_i's are the outside angles of the corners, defined positive for clockwise rotation when the curve is followed in the direction of the enumeration of the corners, where the enumeration of the a_i in the λ−plane is taken from left to right. It is possible to map to more shapes if the sum of the α_i is between $-\pi$ and π.

In most cases it is quite impossible analytically to integrate Eq. (3.23). Therefore, numerical integration is hardly necessary to handle the situation. The discussion about Schwarz-Christoffel transformation solution of integration of Eq. (3.23) are given following subsection.

In the application of a coordinate transformation the following properties should be provided. A coordinate transformation should have the following properties (Gal-Chen and Somerville, 1975a):

- The transformation should be reversible, that is a one-to-one relationship should exist between the "old" coordinates and transformed coordinate.
- In cases where the topography is flat, the transformation should become the identity transformation, that is, the original Cartesian coordinates.
- The transformation should become the identity transformation at the upper boundary
- The transformation should be continuous up to second derivâtives.

Schwarz-Christoffel transformation provide all these properties.

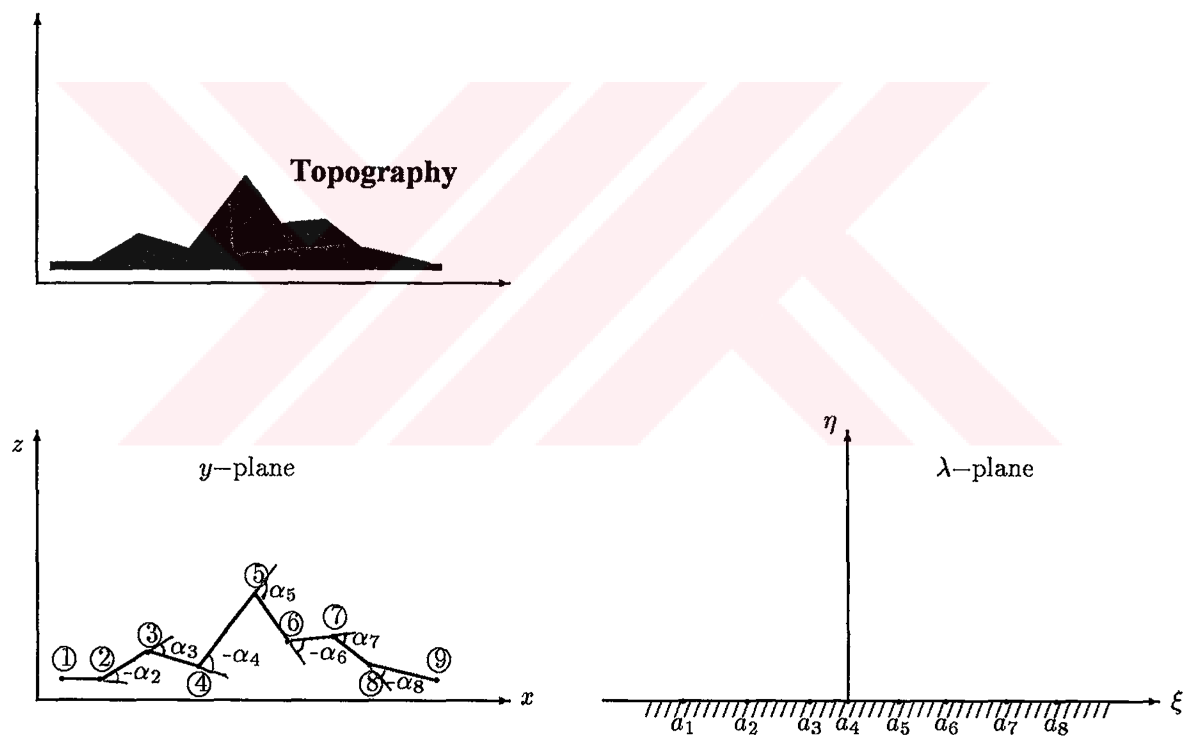

Fig 3.17 Schwarz-Christoffel transformation applied to a polygon (topography).

3.3.1 Application of the Schwarz-Christoffel transformation for numerical grid generation over complex topography

In order to represent the topography can be used a function with horizontal space coordinate variables (x, and y), or a polygon or a surface which has a finite number of line segments. If the topography is represented by a function, an exact inverse of it should exist. Taking inverse of a function is often too hard or impossible. In polygon representation, a suitable transformation should be used if it has inverse transformation.

Sharman *et al.*, (1988) used a grid mesh generation for atmospheric flow simulation over complex topography in which is in polygon form. In their study, the transformation was *semi-conformal*. Schwarz-Christoffel transformation is most convenient for the representation of the topography in polygon form because it generate *full-conformal and orthogonal* grids (Erdun *et al.*, 1996).

A difficulty arises in applying the transformation $y = f(\lambda)$ because the integral of Eq. 3.23 cannot, in general, be evaluated directly. While numerically integrating such an Eq. (3.23), large errors occur about the corners of the polygon as a result of nonanalytical behavior of the $f(\lambda)$. Besides, the constants a_i (the location of the images of the corners on the ξ-axis) and M (a complex constant which rotates and scales the mapping) are not known a priori. As it turns out, only two of the a_i may be set arbitrarily. Note that one of these may be chosen to be $a_i = \infty$, in which case the influence of this corner in the transformation vanishes. The rest of the a_i and M have to be computed iteratively so that the transformation maps the x-axis in the $\lambda-$plane to the desired location with the desired rotation and scaling in the y-plane. An algorithm to find the remaining constants has been outlined by Davis (1979). Davis developed a second order accurate integration formula by using a *modified midpoint trapezoid rule* for any two adjacent corners of the polygon. He found that the integration formula (3.34) works quite well for most applications. In the vicinity of very sharp corners for which α_i is less than $-\pi/2$, one must use some caution that the step size $(\Delta\lambda)$ used is sufficiently small for the algorithm to be accurate.

In order to integrate Eq. (3.23), it should be rewritten in expanded form,

$$\frac{dy}{d\lambda} = M\left[(\lambda - a_1)^{\alpha_1/\pi}(\lambda - a_2)^{\alpha_2/\pi}(\lambda - a_3)^{\alpha_3/\pi}\cdots(\lambda - a_n)^{\alpha_n/\pi}\right], \tag{3.25}$$

where

$$\begin{aligned} f_1(\lambda) &= (\lambda - a_1)^{\alpha_1/\pi}, \\ f_2(\lambda) &= (\lambda - a_2)^{\alpha_2/\pi}, \\ &\vdots \\ f_{n-1}(\lambda) &= (\lambda - a_{n-1})^{\alpha_{n-1}/\pi}. \end{aligned} \tag{3.26}$$

and $f_n(\lambda)$ is a well behaved function near either k or $k+1$ resulting from all of the other corners in the problem. Therefore, for near corners, writing left hand side into discretized form,

near k,

$$y_{m+1} - y_m = M\overline{f}_2\overline{f}_3 \left[\left. \frac{(\lambda - a_k)^{(\alpha_k/\pi)+1}}{(\alpha_k/\pi)+1} \right|_{\lambda_m}^{\lambda_{m+1}} \right], \tag{3.27}$$

near $k+1$,

$$y_{m+1} - y_m = M\overline{f}_1 \left[\left. \frac{(\lambda - a_{k+1})^{(\alpha_{k+1}/\pi)+1}}{(\alpha_{k+1}/\pi)+1} \right|_{\lambda_m}^{\lambda_{m+1}} \right] \overline{f}_3, \tag{3.28}$$

where m is an index which is used for midpoint integration (fig. 3.18), and $\overline{f}_1\overline{f}_2$, and $\overline{f}_3$ are values of f_1, f_2, and f_3 evaluated at $(\lambda_m + \lambda_{m+1})/2$ which is proper for well behaved functions according to the midpoint rule. It can easily be shown (as must be true) that away from each corner the functions which have been integrated exactly reduce to the midpoint rule, i.e.

near $k+1$,

$$\left. \frac{(\lambda - a_k)^{(\alpha_k/\pi)+1}}{(\alpha_k/\pi)+1} \right|_{\lambda_m}^{\lambda_{m+1}} = \overline{f}_1(\lambda_{m+1} - \lambda_m) + \cdots \tag{3.29}$$

near k,

$$\left. \frac{(\lambda - a_{k+1})^{(\alpha_{k+1}/\pi)+1}}{(\alpha_{k+1}/\pi)+1} \right|_{\lambda_m}^{\lambda_{m+1}} = \overline{f}_2(\lambda_{m+1} - \lambda_m) + \cdots \tag{3.30}$$

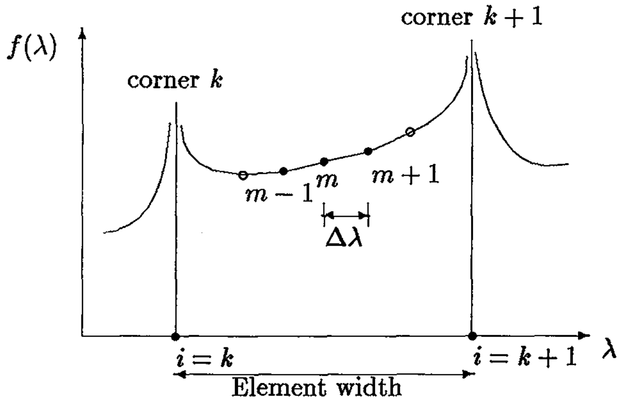

Fig 3.18 Composite integration scheme.

Denoting

$$\Delta\lambda = \lambda_{m+1} - \lambda_m \tag{3.31}$$

We see that when we are away from the corners k and $k+1$ both integral expressions become

$$y_{m+1} - y_m = \overline{f}_1 \overline{f}_2 \overline{f}_3 \, \Delta\lambda_m \tag{3.32}$$

as they should.

It can be given now a composite integration formula which is valid everywhere and contains the proper expressions to account for singularities at each corner. The most convenient expression to use for our case is a multiplicative composite of the type given by Van Dyke (1975). The composite is equivalent to multipliying the right hand side of Eq. (3.27) by Eq. (3.28) and dividing by Eq. (3.32). This results in

$$y_{m+1} - y_m = \frac{\overline{f}_3}{\Delta\lambda_m} \left. \frac{(\lambda - a_k)^{(\alpha_k/\pi)+1}}{(\alpha_k/\pi)+1} \right|_{\lambda_m}^{\lambda_{m+1}} \left. \frac{(\lambda - a_{k+1})^{(\alpha_{k+1}/\pi)+1}}{(\alpha_{k+1}/\pi)+1} \right|_{\lambda_m}^{\lambda_{m+1}} \tag{3.33}$$

Now it can be seen that since $\overline{f}_3$ may include nonanalytic terms at corners other than k and $k+1$ we must include exact integration formulas for these effects. From the above expression (Eq. 3.33) the results is

$$y_{m+1} - y_m = \frac{M}{(\Delta\lambda_m)^{n-1}} \prod_{i=1}^{n} \left. \frac{(\lambda - a_i)^{(\alpha_i/\pi)+1}}{(\alpha_i/\pi)+1} \right|_{\lambda_m}^{\lambda_{m+1}} \tag{3.34}$$

In Eq. (3.34), a_i and M are not known a priori. Therefore, these constants are determined iteratively as follows:

(i) Recall Eq. (3.34) by changing indices (i to j)

$$\frac{dy}{d\lambda} = M \prod_{j=1}^{n} (\lambda - a_j)^{\alpha_j/\pi} \tag{3.35}$$

Choose $a_1 = -1$ and $a_n = +1$ (Fig 3.19). a_J is selected as origin ($a_J = 0$).

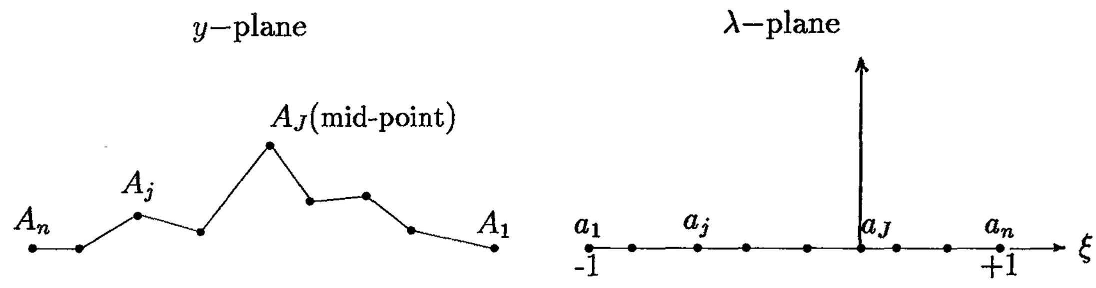

Fig 3.19 Polygon mapping via numerical Schwarz-Christoffel transformation.

(ii) Give (guess) initial values for M (may be a complex value) and other a_j.

$$M^{(1)} = 1.0 + i0.0$$

$$a_j{}^{(1)} = [(j-1)a_J + (J-j)a_1]/(J-1) \qquad j \leq J \tag{3.36}$$

$$a_j{}^{(1)} = [(n-j)a_J + (j-J)a_n]/(n-J) \qquad j \geq J \tag{3.37}$$

$a_j{}^{(1)}$'s are evenly spaced.

(iii) Eq. (3.35) is integrated as

$$y = M^{(1)} \int_{-1}^{\lambda} \left\{ \prod_{j=1}^{n} (\lambda - a_j{}^{(1)})^{\alpha_j/\pi} \, d\lambda \right\} + A_1 \tag{3.38}$$

where A_1 is the integration constant. Thus

$$A_k{}^{(1)} = M^{(1)} \int_{-1}^{a_k} \left\{ \prod_{j=1}^{n} (\lambda - a_j{}^{(1)})^{\alpha_j/\pi} \, d\lambda \right\} + A_1 \tag{3.39}$$

This gives us a set of values $A_k{}^{(1)}$, ($k = 1, \ldots, n$), which are incorrect except A_1. The exact and guessed vertices are shown in Fig (3.20a).

(iv) Notice that all turning angles are correct but the length of the straight elements and the initial slope are wrong.

Now $M^{(1)}$ is corrected to bring ${A_n}^{(1)}$ onto A_n as

$$M^{(2)} = M^{(1)} \frac{(A_n - A_1)}{({A_n}^{(1)} - A_1)} \tag{3.40}$$

Then ${A_j}^{(1)}$ moves to (see, Fig 3.20b)

$$\tilde{A}_j^{(1)} = \left(\frac{M^{(2)}}{M^{(1)}}\right)({A_j}^{(1)} - A_1) + A_1$$

Then a_2 to a_{n-1} in λ–plane is changed to bring ${\tilde{A}_2}^{(1)}$ to $\tilde{A}_{n-1}^{(1)}$ closer to correct values, i.e., change $a_j - a_1$ in proportion to $|A_j - A_1|$.

Thus

$${a_j}^{(2)} - {a_{j-1}}^{(2)} = \mathcal{K}\,({a_j}^{(1)} - {a_{j-1}}^{(1)}) \left|\frac{A_j - A_{j-1}}{{A_j}^{(1)} - {A_{j-1}}^{(1)}}\right| \tag{3.41}$$

where $\mathcal{K}$ is a scaling parameter and the terms without superscript denote the correct terms.

This retains a_1 and a_n unchanged but redistributes all the other along the ξ–axis.

(v) Now return to the step *(iii)* using the new values of M and a_j, i.e., change superscript (2) with (1), and iterate through this loop until convergency is obtained.

Numerical integration in the λ–plane is carried out by dividing the interval -1 to 1 into m elements of length $\Delta\lambda_m$. Then consider the element $(\lambda_m, \lambda_{m+1})$ and let the closest a_j point be a_l (Fig 3.20c).

$$y_{m+1} = y_m + M \int_{\lambda_m}^{\lambda_{m+1}} \left[\prod_{\substack{j=1 \\ j\neq l}}^{n} (\lambda - a_j)^{\alpha_j/\pi}\right] (\lambda - a_l)^{\alpha_l/\pi} \quad d\lambda \tag{3.42}$$

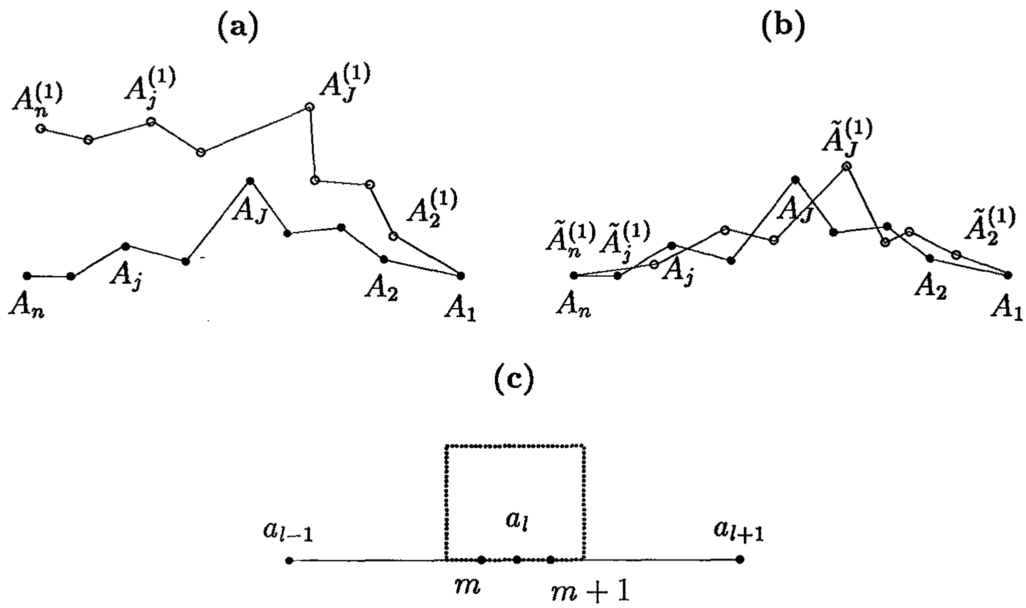

Fig 3.20 (a) and (b) Vertex correction in Schwarz-Christoffel transformation. (c) Handling of singularity occurs in numerical integration by choosing appropriate integral.

In attempting to numerically integrate Eq. (3.42) using a trapezoid rule, large errors occur near corners due to the fact that the Kernel of the integral is not analytic there. Therefore, Davis (1979) developed a modified midpoint rule for complex integration which exactly integrates any nonanalytic term which occurs at a corner.

Thus

$$y_{m+1} = y_m + M \prod_{\substack{j=1 \\ j \neq l}}^{n} \left(\frac{\lambda_{m+1} + \lambda_m}{2} - a_j \right)^{\alpha_j/\pi} \frac{(\lambda - a_l)^{\alpha_l/\pi+1}}{\alpha_l/\pi + 1} \Bigg|_{\lambda_m}^{\lambda_{m+1}} \tag{3.43}$$

Eq. (3.43) is valid only near the corner (a_l). If this equation is extended to a composite integration which is valid everywhere and contains the proper expressions to account for singularities at each corner :

$$y_{m+1} = y_m + \frac{M}{(\Delta\lambda_m)^{n-1}} \prod_{j=1}^{n} \frac{(\lambda - a_j)^{\alpha_j/\pi+1}}{\alpha_j/\pi + 1} \Bigg|_{\lambda_m}^{\lambda_{m+1}}. \tag{3.44}$$

a)

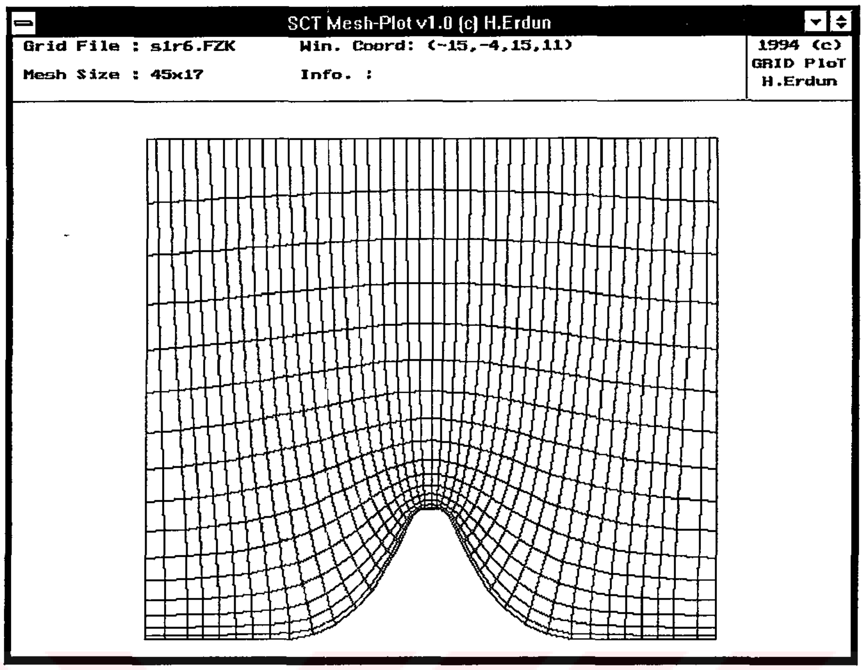

b)

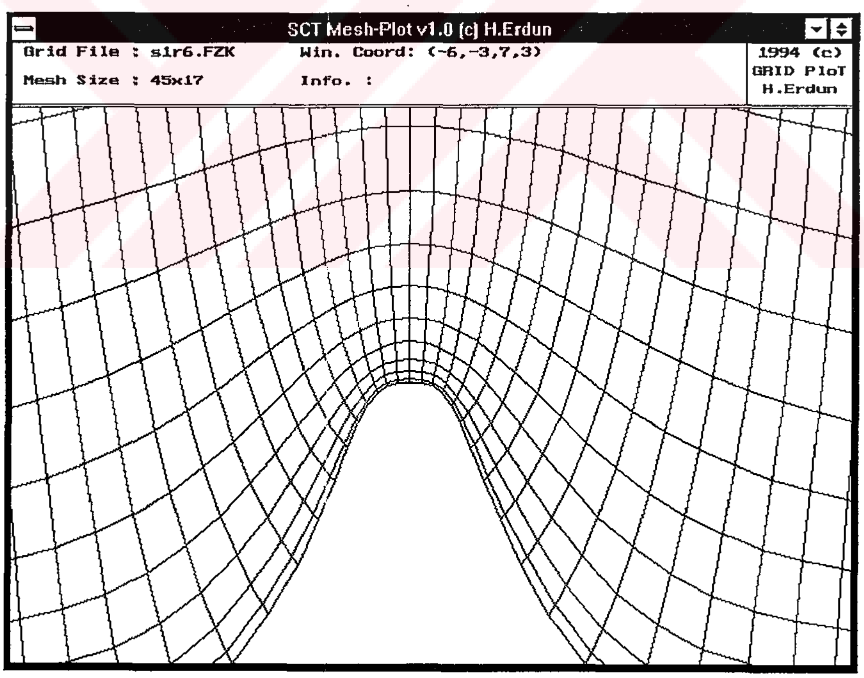

Fig 3.21 A mesh example generated by Schwarz-Christoffel transformation.

a)

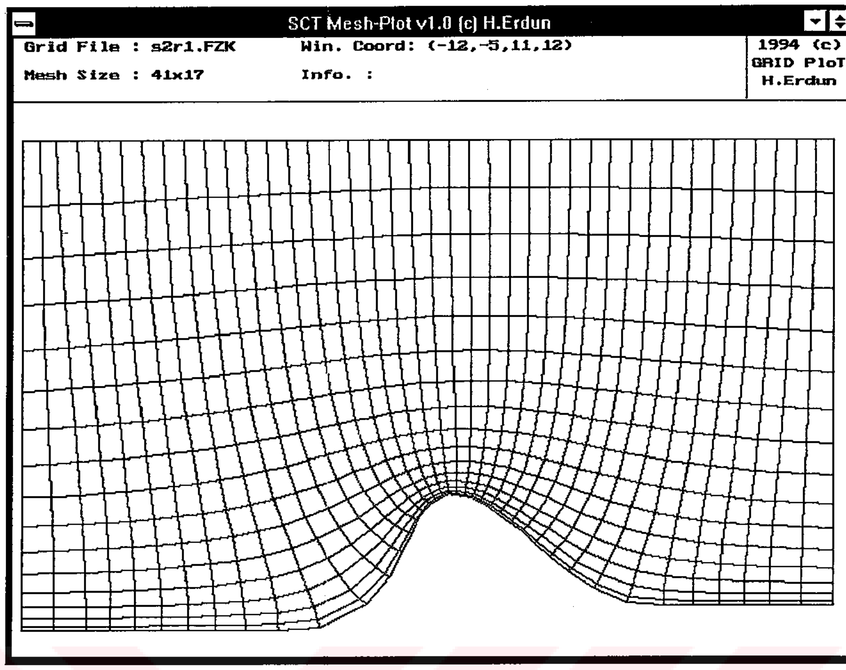

b)

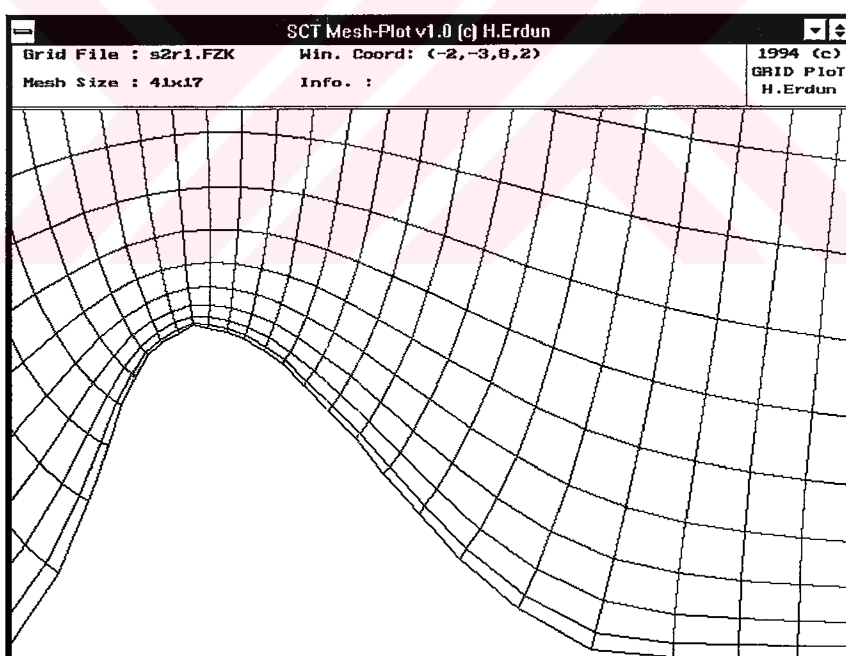

Fig 3.22 A mesh example generated by Schwarz-Christoffel transformation.

a)

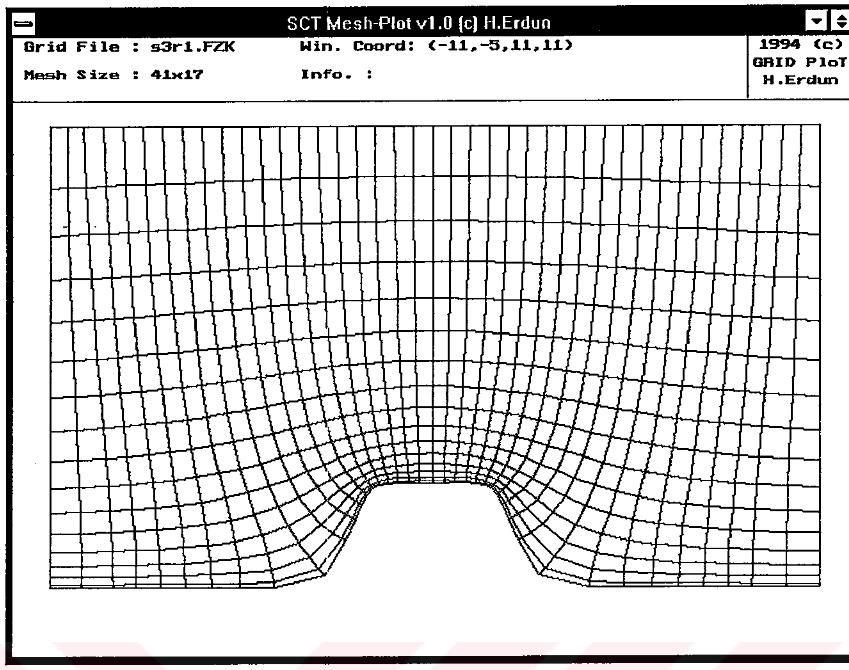

b)

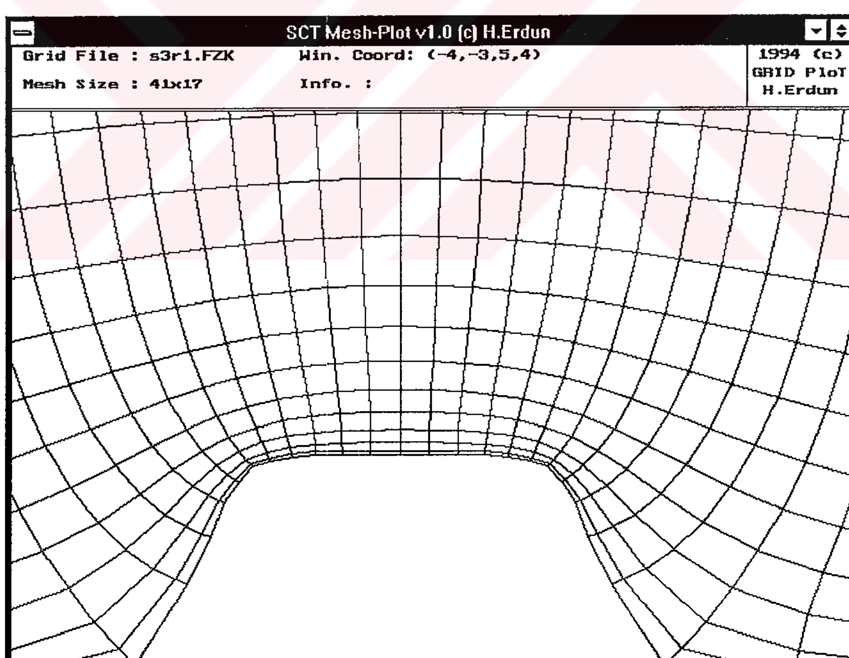

Fig 3.23 A mesh example generated by Schwarz-Christoffel transformation.

a)

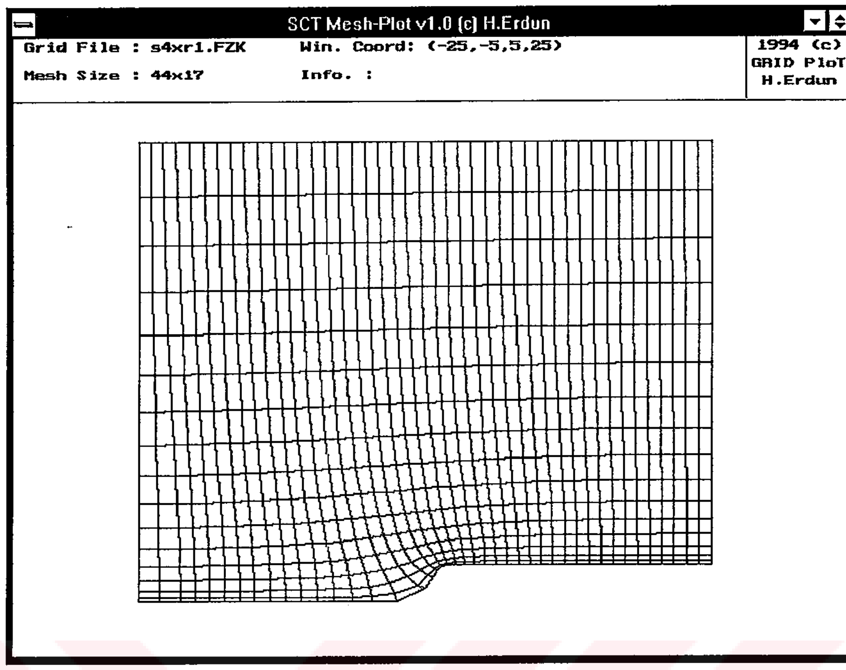

b)

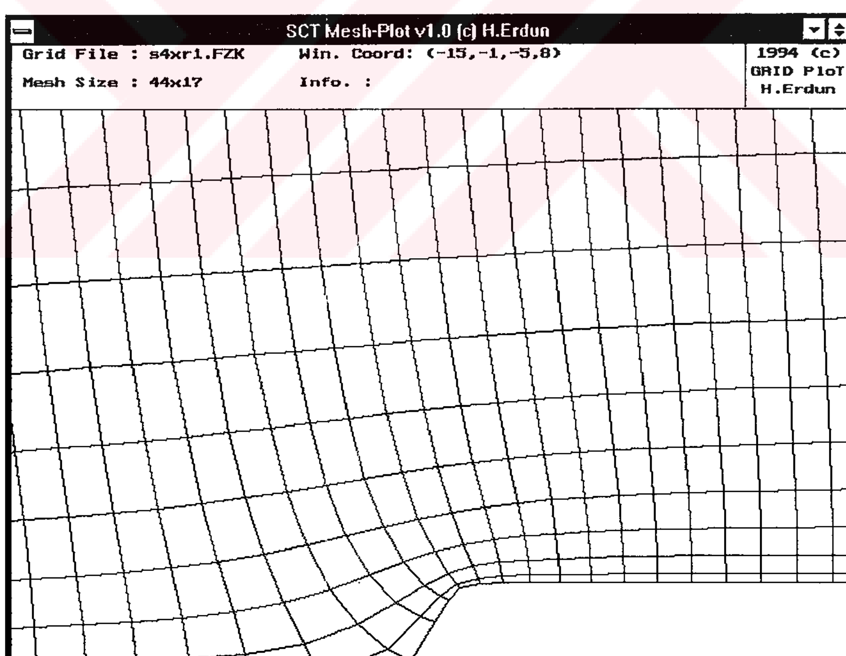

Fig 3.24 A mesh example generated by Schwarz-Christoffel transformation.

a)

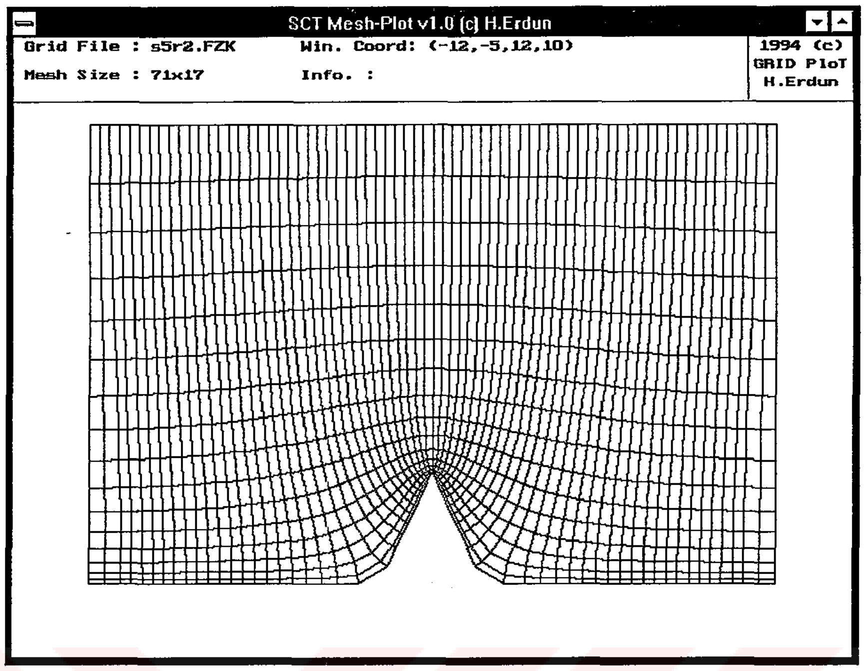

b)

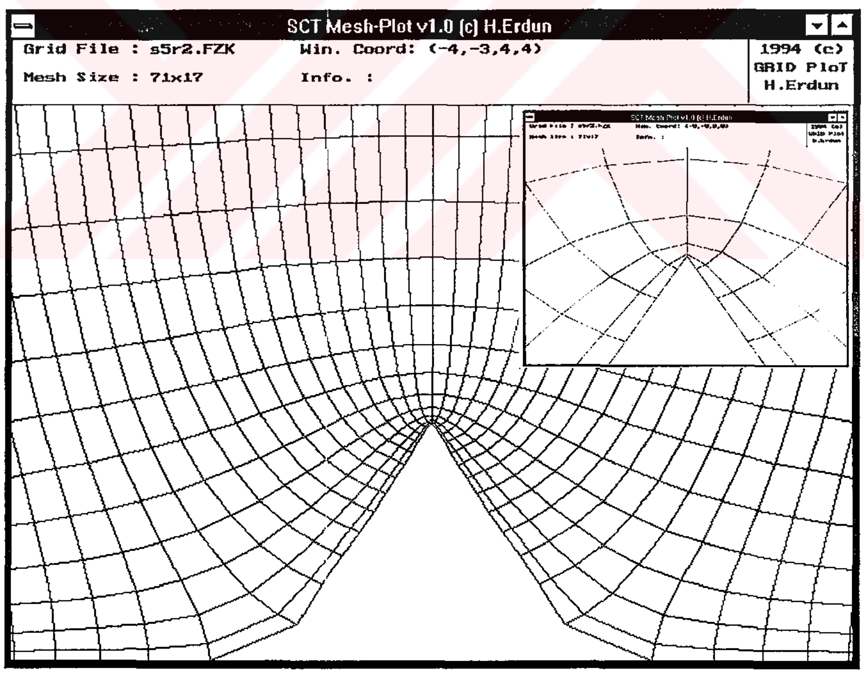

Fig 3.25 A mesh example generated by Schwarz-Christoffel transformation.

a)

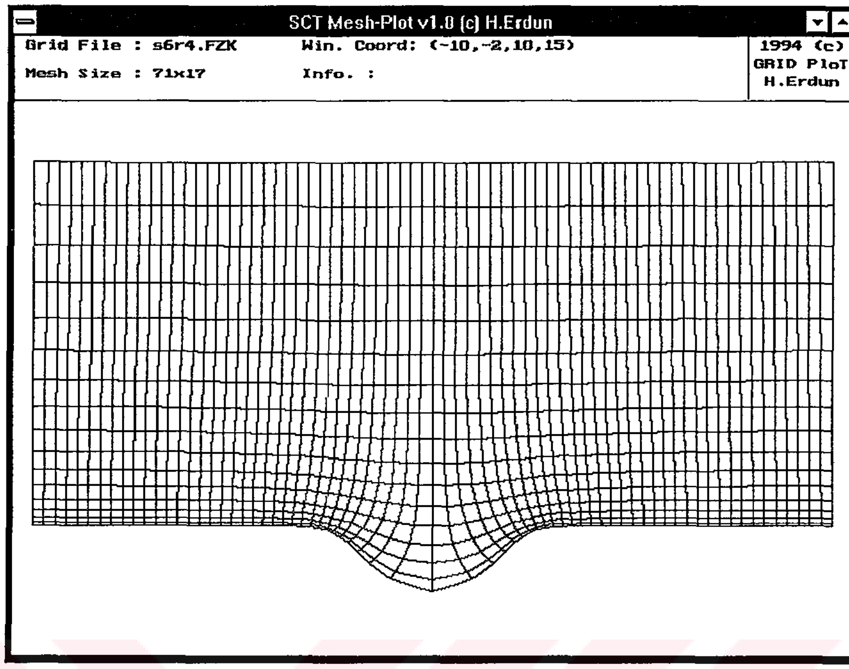

b)

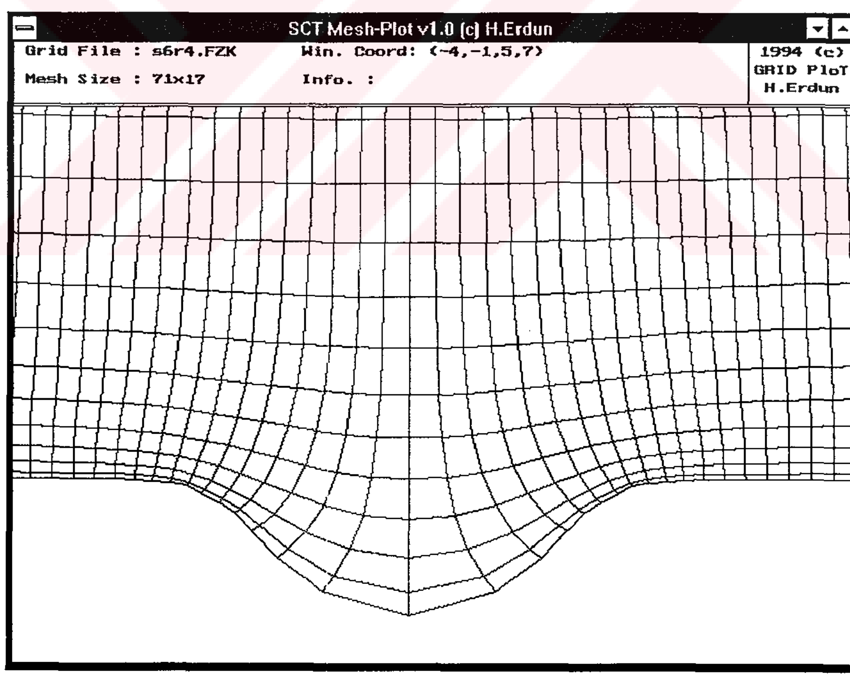

Fig 3.26 A mesh example generated by Schwarz-Christoffel transformation.

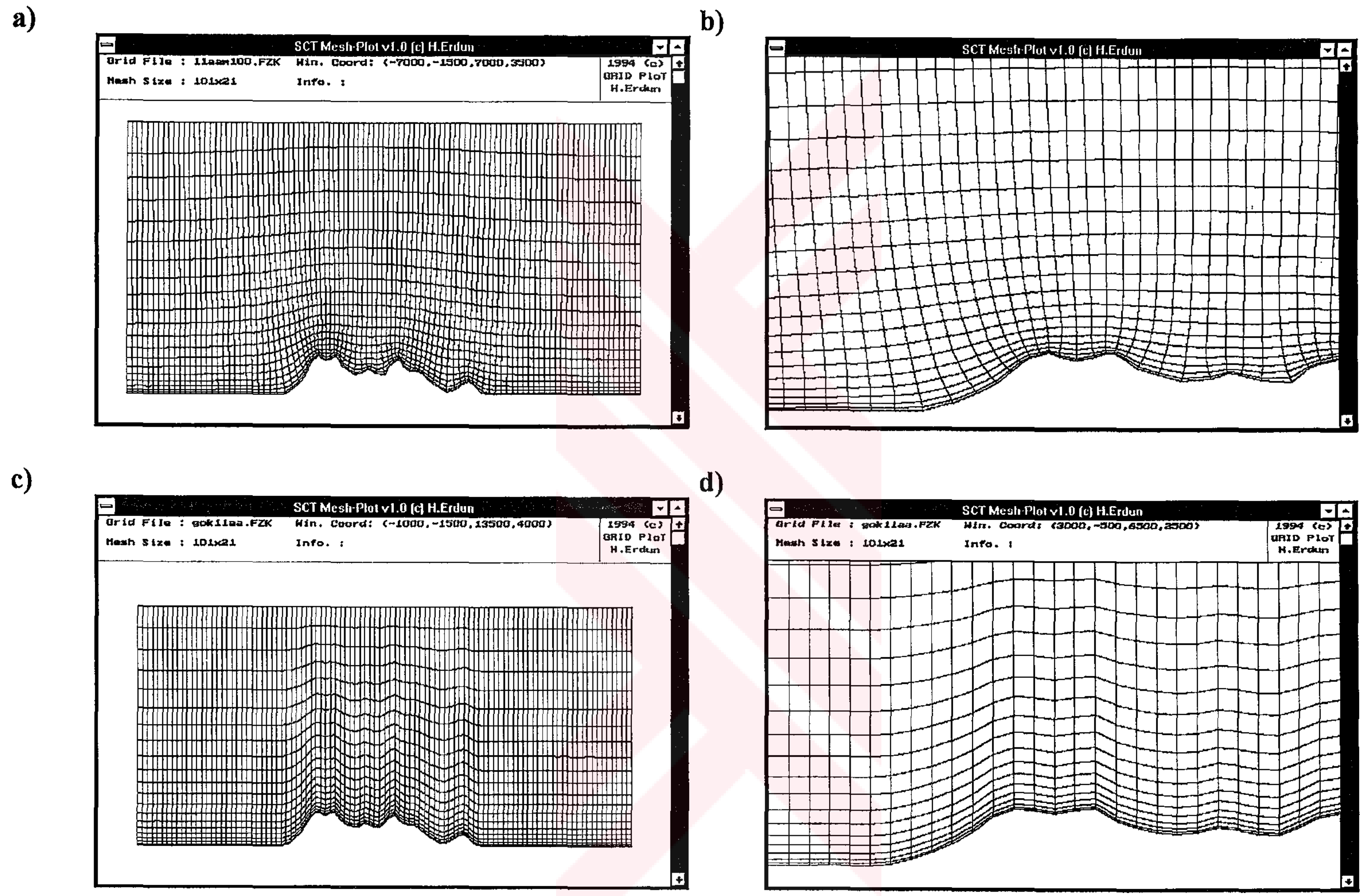

Fig 3.27 Mesh structures for real-topography generated by (a,b) Schwarz-Christoffel transformation and (c,d) Terrain-following height coordinate system.

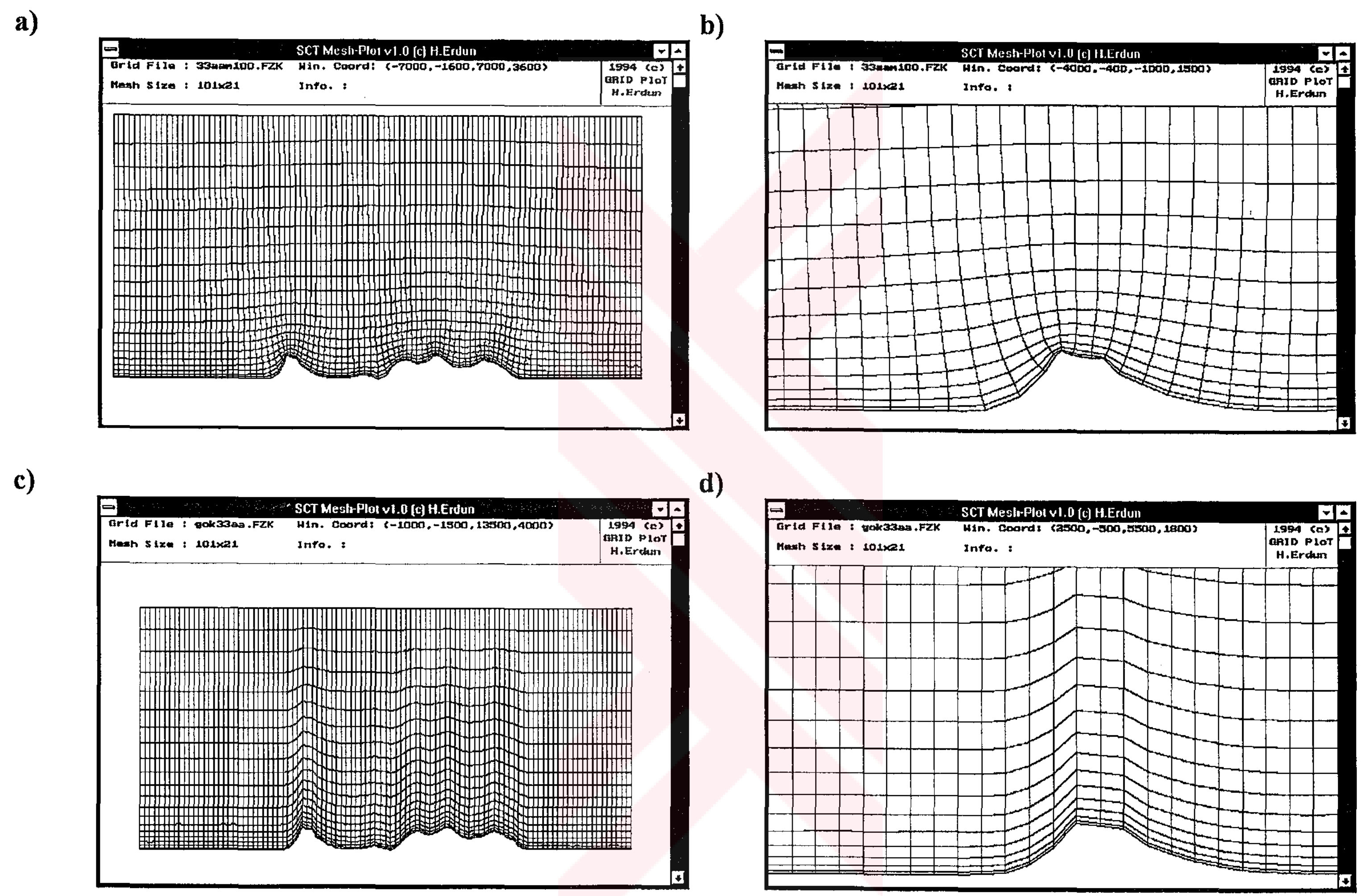

Fig 3.28 Mesh structures for real-topography generated by (a,b) Schwarz-Christoffel transformation and (c,d) Terrain-following height coordinate system.

CHAPTER 4

MODEL EQUATIONS AND PARAMETERIZATIONS

4.1 Anelastic Non-Hydrostatic Mesoscale Model

In this thesis, we used the following mean momentum, mean continuity and heat equations of *shallow convection system*, respectively,

$$\frac{\partial \overline{u}_i}{\partial t} = -\overline{u}_j \frac{\partial \overline{u}_i}{\partial x_j} + \frac{1}{\rho_\circ} \frac{\partial}{\partial x_j} \tau_{ij} - \frac{1}{\rho_\circ} \frac{\partial p'}{\partial z} \delta_{i3} + \frac{\theta'}{\theta_\circ} g \delta_{i3} - fUg_j \varepsilon_{ij3} - 2\varepsilon_{ij3} \Omega_j \overline{u}_k, \tag{4.1}$$

$$\frac{\partial \overline{u}_i}{\partial x_i} = 0, \tag{4.2}$$

$$\frac{\partial \theta'}{\partial t} = -\overline{u}_j \left(\frac{\partial \theta'}{\partial x_j} + \frac{\partial \theta_s}{\partial z} \delta_{i3} \right) + \frac{\partial}{\partial x_j} \left(K_h \frac{\partial \theta'}{\partial x_j} \right) \tag{4.3}$$

where i, j=1, and 3 for 2-D models. The main respect in which this set differs from those used in synoptic scale modeling is in the inclusion of *non-hydrostatic* and *Boussinesq* terms in the vertical equation of motion. These equations are obtained by using the assumptions described in the following paragraphs.

In the model, *sound waves are filtered* from the system by neglecting the local time derivative of density in the continuity equation, because they are of no direct interest in most applications of mesoscale meteorology. Also spatial variations of density are ignored since the model is designed for *shallow convection.*

$$\frac{\partial \rho}{\partial t} = 0, \tag{4.4}$$

$$\frac{\partial \rho}{\partial x_j} = 0. \tag{4.5}$$

These are referred to as the *anelastic* (*soundproof*), and *incompressibility assumptions.*

Since the model is designed for two-dimensional, the local derivatives in $y-$direction are removed from the model equations as follows

$$\frac{\partial}{\partial y} = 0, \qquad \frac{\partial^2}{\partial y^2} = 0, \qquad \frac{\partial^2}{\partial y \partial x} = 0, \qquad \text{and} \qquad \frac{\partial^2}{\partial y \partial z} = 0.$$

Therefore, only two components of Eq. 2.1-2.3 (x and z components) are used. Wind speed in $y-$direction are also taken to be a constant in the model ($v =$ constant). In this thesis, although 2-D simulations are showed but the expressing of the model for 3-D is straightforward.

The basic dynamical model equations (Eq. 2.1-2.3) can be solved on a finite grid. However, there will be fluctuations on a *(unresolved) subgrid-scale* in the real atmosphere being modeled which will contribute very strongly to the velocity derivatives Eq. (2.1) and (2.2). Only then the differential equations can be applied to finite differences. This filtering process will lead to additional terms in the equations. These additional terms must be parameterized in terms of mean variables in a consistent manner that it must maintain a realistic smoothness of the filtered variables from one grid point to the next. That is, the parameterization or closure assumption must be such as to simulate the transfer (or removal) of variance cascaded from resolvable small scales of motion to the unresolvable subgrid scale.

Anelastic framework requires that the dependent variables be cast into a perturbation form, given as $\phi = \overline{\phi} + \phi''$ where $\overline{\phi}$ represents mean part while ϕ'' represents fluctuation part. In a 2-D modeling, $\overline{\phi}$ given by Eq. (2.4) are rewritten as follows,

$$\overline{\phi} = \frac{1}{\Delta t \Delta x \Delta z} \int_t^{t+\Delta t} \int_x^{x+\Delta x} \int_z^{z+\Delta z} \phi \, dz \, dx \, dt \qquad \text{(in 2-D)}. \tag{4.6}$$

Thus $\overline{\phi}$ represents the average of an instantaneous variable ϕ over the finite time increment Δt and space intervals Δx and Δz. The fluctuation ϕ'' is the deviation of ϕ from this average and can also be called as the *subgrid scale perturbation.* To simplify this equation, it is convenient to assume that the variations of averaged dependent variables is much more slowly in time and space than the deviations from the average. This scale separation between the average and the perturbation implies that $\overline{\phi}$ is resolvable part of the instantaneous value and approximately constant, while ϕ'' is unresolvable part of ϕ which must be parameterized in terms of known quantities.

In 2-D modeling, another convenient decomposition is to define averaging area such that the subgrid scale perturbation includes the *non-hydrostatic part* of the solution and resolvable scale is accurately represented by the hydrostatic assumption, $\overline{\phi} = \phi_o + \phi'$ where Eq. (2.6) for representation of ϕ_o can be rewritten for 2-D as follows,

$$\phi_o = \frac{1}{L_x} \int_x^{x+\Delta x} \overline{\phi}\, dx \qquad \text{(in 2-D)}. \tag{4.7}$$

Thus the influence of the non-hydrostatic component of a model would be parameterized and the hydrostatic portion would be explicitly resolved.

Using these two decompositions (Eq. 4.6 and 4.7) and some simplifications by scale analysis (defined in section 2.2) the basic equations (Eq. 2.1-2.3) (Batchelor, 1953) can be written in tensor notation for anelastic system as below:

Mean continuity equation :

$$\frac{\partial \overline{u}_i}{\partial x_i} = 0, \qquad \text{and} \qquad \frac{\partial u_i'}{\partial x_i} = 0, \tag{4.8}$$

Mean momentum equation:

$$\frac{\partial \overline{u}_j}{\partial t} = -\overline{u}_j \frac{\partial \overline{u}_i}{\partial x_j} - \frac{1}{\overline{\rho}} \frac{\partial}{\partial x_j} (\overline{\rho}\; \overline{u_j'' u_i''}) - \frac{1}{\overline{\rho}} \frac{\partial \overline{p}}{\partial u_i} + g\delta_{i3} - 2\varepsilon_{ijk}\Omega_j \overline{u}_k \tag{4.9}$$

Mean thermodynamic equation:

$$\frac{\partial \overline{\theta}}{\partial t} = -\overline{u}_j \frac{\partial \overline{\theta}}{\partial x_j} - \frac{1}{\overline{\rho}} \frac{\partial}{\partial x_j} (\overline{\rho}\; \overline{u_j'' \theta''}) \tag{4.10}$$

where i and j is 1 and 3 in 2-D.

Some terms in these equations may be solved directly in finite difference forms, some must be parameterized.

4.1.1 Definitions and parameterization of mean momentum equation terms

Advection term

First term on right-hand side of Eq. (4.9) describes advection of mean momentum by the mean wind. This term can be represented and solved directly in a finite difference form.

Coriolis term

The Coriolis term, last term on the right-hand side of Eq. (4.9), is an acceleration of a air parcel moving in a (moving) relative coordinate system. The total acceleration of the parcel, as measured in an inertial coordinate system, may be expressed as the sum of the acceleration within the relative system, the acceleration of the relative system itself, and the Coriolis acceleration. In the case of earth, moving with angular velocity Ω, a parcel moving relative to the earth with velocity $\overline{u}_k$ has the Coriolis acceleration.

In meteorology the Coriolis force per unit mass arises solely from the earth's rotation. Thus the Coriolis force acts as a "deflecting force", normal to the velocity, to the right of motion in the northern hemisphere and to the left in southern hemisphere. It cannot alter the speed of the particle. It is only a function of latitude ϕ.

In the Coriolis term, Ω_j is the component of the Earth's angular velocity on given j^{th} direction. These are towards east, north, and zenith (Fig 4.1), respectively,

$$\begin{aligned} \Omega_1 &= 0, \\ \Omega_2 &= |\Omega|\cos\phi, \\ \Omega_3 &= |\Omega|\sin\phi, \end{aligned} \tag{4.11}$$

where ϕ is the latitude, and $|\Omega| = 2\pi/24$ hour $\cong 7.2722 \times 10^{-5}$rad/sec.

The components of the Coriolis force, $C_i = -2\varepsilon_{ijk}\Omega_j\overline{u}_k$, are showed as below, respectively,

$$\begin{aligned} C_1 &= 2v|\Omega|\sin\phi - 2w|\Omega|\cos\phi &&= fv - \hat{f}w, \\ C_2 &= -2u|\Omega|\sin\phi &&= -fu, \\ C_3 &= 2u|\Omega|\cos\phi &&= \hat{f}u, \end{aligned} \tag{4.12}$$

where $f = 2|\Omega|\sin\phi$ is called the *Coriolis parameter*, and $\hat{f} = 2|\Omega|\cos\phi = f/\tan\phi$. Physically the quantity, f, may be interpreted as twice the angular velocity of the tangent plane about the local vertical due to the rotation of the earth. It should be noted that in the analysis of certain small-scale meteorological phenomena, it is necessary to retain the terms involving w.

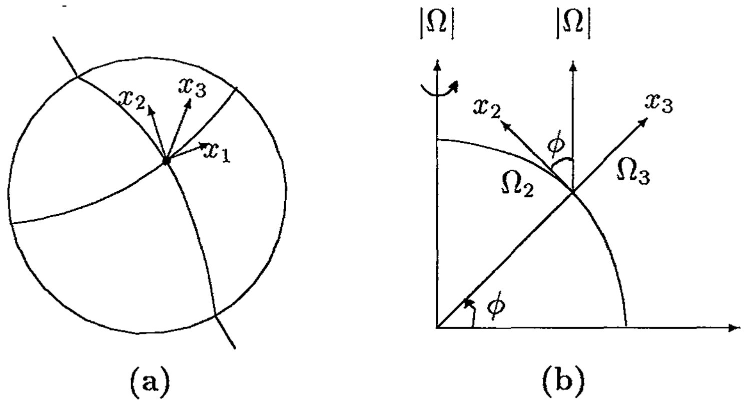

Fig 4.1 (a) Coordinate system on the earth (x_1 east, x_2 north, and x_3 zenith), (b) the components of the angular velocity of the Earth as a function of $|\Omega|$ latitude ϕ.

Pressure gradient and gravitational acceleration terms

Rewriting the thirth and fourth terms on the right-hand side of Eq. (4.9) by using of second decomposition for pressure ($\overline{p} = p_\circ + p'$) and specific volume ($\overline{\alpha} = \alpha_\circ + \alpha'$, and $\alpha = 1/\rho$), we find following equation:

$$
\begin{aligned}
-\overline{\alpha}\frac{\partial \overline{p}}{\partial x_i} + g\delta_{i3} &= -(\alpha_\circ + \alpha')\frac{\partial}{\partial x_i}(p_\circ + p') + g\delta_{i3} \\
&= \alpha_\circ\left(1 + \frac{\alpha'}{\alpha_\circ}\right)\frac{\partial p'}{\partial z} - g + g - \frac{\alpha'}{\alpha_\circ}g \\
&\simeq -\alpha_\circ\left[\frac{\partial p_\circ}{\partial x_1}\delta_{i1} + \frac{\partial p_\circ}{\partial x_2}\delta_{i2}\right] - \alpha_\circ\frac{\partial p'}{\partial x_3}\delta_{i3} + g\left(\frac{\alpha'}{\alpha_\circ}\right)\delta_{i3} \quad \text{(in 3-D)} \\
&\simeq -\alpha_\circ\frac{\partial p_\circ}{\partial x}\delta_{i1} - \alpha_\circ\frac{\partial p'}{\partial z}\delta_{i3} + g\left(\frac{\alpha'}{\alpha_\circ}\right)\delta_{i3} \quad \text{(in 2-D).}
\end{aligned}
\tag{4.13}
$$

where it has been assumed that the synoptic scale pressure field is hydrostatic,

$$\frac{\partial p_\circ}{\partial z} = -g/\alpha_\circ.$$

Eq. (4.13) includes hydrostatic and non-hydrostatic parts of pressure, and Boussinesq term.

The Boussinesq term $g(\alpha'/\alpha)$ is the only expressed retained in Eq. (4.13) and (4.20) that contains temporal variations in specific volume when $|\alpha'|/\alpha_\circ \ll 1$. Neglecting temporal variations of density (as given by α') except for $g(\alpha'/\alpha_\circ)$, is called the *Boussinesq approximation.* In order to parameterize the Boussinesq term for shallow system, it can also be rewritten by logarithmically differentiating the ideal gas law so that

$$\frac{d\alpha}{\alpha} = \frac{dT}{T} - \frac{dp}{p}. \tag{4.14}$$

When the changes of α, T, and p are assumed to be much less than their absolute magnitudes (e.g., $|d\alpha| \ll \alpha$, $|dT| \ll T$, and $|dp| \ll p$), and if $\alpha \simeq \alpha_\circ$, $T \simeq T_\circ$, and $p \simeq p_\circ$, then Eq. (4.14) can be approximated by

$$\frac{\alpha'}{\alpha_\circ} \simeq \frac{T'}{T_\circ} - \frac{p'}{p_\circ}. \tag{4.15}$$

Since $|\alpha'|/\alpha_\circ$ has already been assumed much less than unity, the requirement that $|T'|/T_\circ \ll 1$, and $|p'|/p_\circ \ll 1$ is implied from Eq. (4.15).

Finally, since $\theta = T(1000/p)^{R_d/C_p}$, then $\alpha'/\alpha_\circ$ can also be approximated by

$$\frac{\alpha'}{\alpha_\circ} \simeq \frac{\theta'}{\theta_\circ} - \frac{C_v}{C_p}\frac{p'}{p_\circ}; \tag{4.16}$$

which represent another form of the ideal gas law when $|\alpha'| \ll 1$. Here the relation $C_p = C_v + R_d$ has been used to obtain the given form. This approximate form for $\alpha'/\alpha_\circ$ can be simplified when the vertical scale of the circulation L_z is much smaller than the scale depth of the atmosphere H_α.

Using the scale analysis procedure given in section 2.2,

$$\left|\alpha_\circ \frac{\partial p'}{\partial z}\right| \sim \alpha_\circ |p'|/L_z,$$

and assuming that the vertical mesoscale pressure perturbation and the density perturbation terms are of the same order of magnitude, then

$$\left|\alpha_\circ \frac{\partial p'}{\partial z}\right| = \left|g \frac{\alpha}{\alpha_\circ}\right|;$$

so that

$$\frac{RT_\circ |p'|}{L_z p_\circ} \sim g\frac{|\alpha|}{\alpha_\circ}; \quad \text{or} \quad \frac{|p'|}{p_\circ} \sim \frac{L_z g}{RT_\circ}\frac{|\alpha'|}{\alpha_\circ} = \frac{L_z g}{p_\circ \alpha_\circ}\frac{|\alpha'|}{\alpha_\circ} = \frac{L_z}{D}\frac{|\alpha'|}{\alpha_\circ} \sim \frac{L_z}{H_\alpha}\frac{|\alpha'|}{\alpha_\circ};$$

where the results from scale analysis that $p_\circ \sim \rho_\circ g D$ and $D \sim H_\circ$ have been used. Thus if $L_z \ll H_\alpha$;

$$\frac{|p'|}{p_\circ} \ll \frac{|\alpha'|}{\alpha_\circ} \quad \text{and} \quad \frac{|\alpha'|}{\alpha_\circ} \ll \frac{|\theta'|}{\theta_\circ}.$$

for *shallow atmospheric circulation.*

By taking consideration of these approximations and assumptions, the Boussinesq term may be written for *shallow system* as follows,

$$\frac{\alpha'}{\alpha_\circ} \simeq \frac{\theta'}{\theta_\circ}. \tag{4.17}$$

where θ' is calculated from prognostic equation (Eq. 4.45 in the following section)

In Eq. (4.13) the horizontal pressure gradient terms can be explained by using geostrophic approximation as follows,

$$G_i = -\alpha_\circ \left[\frac{\partial p_\circ}{\partial x_1}\delta_{i1} + \frac{\partial p_\circ}{\partial x_2}\delta_{i2}\right] = -fUg_j\varepsilon_{ij3}, \tag{4.18}$$

where $Ug_j = (u_g, v_g, 0)$ is the geostrophic wind components which are taken to be constant in the model. The components of the G_i are defined as

$$\begin{aligned} G_1 &= -fv_g, \\ G_2 &= \;\; fu_g, \\ G_3 &= \;\; 0. \end{aligned} \tag{4.19}$$

With respect to these assumptions the equation of motion (Eq. 4.9) can be rewritten as

$$\frac{\partial \overline{u}_i}{\partial t} = -\overline{u}_j \frac{\partial \overline{u}_i}{\partial x_j} + \frac{1}{\rho_o} \frac{\partial}{\partial x_j} \tau_{ij} - \frac{1}{\rho_o} \frac{\partial p'}{\partial z} \delta_{i3} + \frac{\theta'}{\theta_o} g \delta_{i3} - f U g_j \varepsilon_{ij3} - 2\varepsilon_{ij3} \Omega_j \overline{u}_k. \tag{4.20}$$

In Eq. (4.13) and (4.24), the term $\partial p'/\partial z$ is mesoscale pressure perturbation (nonhydrostatic part of pressure) gradient which can be solved from Poisson partial differential equation (Eichhoin *et al.*, 1988).

The Poisson partial differential equation is

$$\frac{\partial^2 p'}{\partial x_j^2} = \sigma_j; \qquad (j{=}1,\ 3 \ \text{ in 2-D}) \tag{4.21}$$

where σ is a source term.

In the model, this source term σ_j is calculated by time-splitting procedures as follows :

- The solution scheme is based on a splitting method (Patrinos and Kistler, 1977) by introducing an auxiliary velocity field $\mathbf{v}^*$ resulting from the omission of the perturbation part of the pressure gradient in Eq. (4.20).

$$\frac{\partial \mathbf{v}^*}{\partial t} = \frac{\partial \mathbf{v}}{\partial t} - \left\{ -\frac{1}{\rho_o} \nabla p' \right\}; \tag{4.22}$$

  or in tensor notation,

$$\frac{\partial \mathrm{u}_i^*}{\partial t} = \frac{\partial \mathrm{u}_i}{\partial t} - \left\{ \frac{1}{\rho_o} \frac{\partial p'}{\partial x_j} \right\};$$

  and discretized in time

$$\left[\mathbf{v}^{*\,(t+\Delta t)} - \mathbf{v}^{*\,(t)}\right] = \left[\mathbf{v}^{(t+\Delta t)} - \mathbf{v}^{(t)}\right] - \Delta t \left\{ -\frac{1}{\rho_o} \nabla p' \right\}. \tag{4.23}$$

- The initial field is characterized by the equality $\mathbf{v}^*(t) = \mathbf{v}(t)$. Now, taking the divergence of Eq. (4.23) and observing Eq. (2.1) one obtains a Poisson's equation for the pressure, perturbations

$$\nabla^2 p' = \frac{\rho_o}{\Delta t} \left\{ \nabla \cdot \mathbf{v}^{*\,(t+\Delta t)} \right\} = \sigma_j. \tag{4.24}$$

- The *final velocity field* results from substituting the solution of Eq. (4.24) into Eq. (4.22).

Parameterization of the turbulence flux term

In the second term on the right hand side of Eq. (4.9), the *subgrid scale correlation term*, $(\bar{\rho}\,\overline{u_j''\,u_i''})$ represents the contributions of the smaller scales on the resolvable grid scale. This results from fluctuating velocity components, and has important role in all aspects of dynamical meteorology. This term is called the *turbulent velocity flux*, must be parameterized in terms of averaged quantities. The proper specification of this, and similar subgrid scale correlation term, as a function of resolvable, averaged quantities, is referred to as the *closure problem*.

Closure assumptions are needed for evaluation of the generalized Reynolds stresses and Reynolds fluxes; thus, the problem of turbulence has entered into even the detailed numerical calculations. It is also to be expected, however, that the sensitivity of the calculated results to the closure assumptions will be much less than in 1-D models in which the assumption directly affects the total fluxes of momentum and heat. In the 3-D model, the assumption directly affects only the subgrid scale portion of flux, and this portion typically turns out to be only 15-20% of the total flux except with stable stratification. It is for this reason that the expense of a 3-D model can be tolerated (Pielke, 1984).

The subgrid scale correlation term which is also called the Reynolds stress, can be represented by

$$\tau_{ij} = -\bar{\rho}\,\overline{u_j''\,u_i''}. \tag{4.25}$$

We can also interpret τ_{ij} as the force per unit area in the x_i–direction acting on the face of the air in a finite volume that is normal to the x_j–direction.

The turbulent flux term on the right hand side of Eq. (4.9) can be rewritten by using Eq. (4.25) as follows,

$$-\frac{1}{\rho}\frac{\partial}{\partial x_j}(\bar{\rho}\,\overline{u_j''\,u_i''}) \;=\; \frac{1}{\rho}\frac{\partial}{\partial x_j}\tau_{ij}. \tag{4.26}$$

Using the concept of eddy viscosity as introduced by Boussinesq (1903), it is often assumed Reynolds stress may be approximated by

$$-\overline{u_j''\, u_i''} = K_m \mathcal{D}_{ij},$$

where K_m is the eddy viscosity or eddy exchange coefficient for momentum and $\mathcal{D}_{ij}$ the mean rate of deformation tensor.

With these concepts the Reynolds stress tensor τ_{ij} is defined as

$$\tau_{ij} = \overline{\rho}\, K_m \mathcal{D}_{ij}. \tag{4.27}$$

The deformation tensor is

$$\mathcal{D}_{ij} = \frac{\partial \overline{u}_i}{\partial x_j} + \frac{\partial \overline{u}_j}{\partial x_i} - \frac{2}{3}\delta_{ij}\frac{\partial \overline{u}_k}{\partial x_k}, \tag{4.28}$$

or in matrix form,

$$\mathcal{D}_{ij} = \begin{bmatrix} \frac{2}{3}\left[2\frac{\partial \overline{u}}{\partial x} - \frac{\partial \overline{v}}{\partial y} - \frac{\partial \overline{w}}{\partial z}\right] & \left[\frac{\partial \overline{u}}{\partial y} + \frac{\partial \overline{v}}{\partial x}\right] & \left[\frac{\partial \overline{u}}{\partial z} + \frac{\partial \overline{w}}{\partial x}\right] \\ \left[\frac{\partial \overline{u}}{\partial y} + \frac{\partial \overline{v}}{\partial x}\right] & \frac{2}{3}\left[-\frac{\partial \overline{u}}{\partial x} + 2\frac{\partial \overline{v}}{\partial y} - \frac{\partial \overline{w}}{\partial z}\right] & \left[\frac{\partial \overline{v}}{\partial z} + \frac{\partial \overline{w}}{\partial y}\right] \\ \left[\frac{\partial \overline{u}}{\partial z} + \frac{\partial \overline{w}}{\partial x}\right] & \left[\frac{\partial \overline{v}}{\partial z} + \frac{\partial \overline{w}}{\partial y}\right] & \frac{2}{3}\left[-\frac{\partial \overline{u}}{\partial x} - \frac{\partial \overline{v}}{\partial y} + 2\frac{\partial \overline{w}}{\partial z}\right] \end{bmatrix}$$

and summation is implied over $i, j, k = 1$, and 3 in 2-D.

Recognizing that the use of K-theory provides a means of simulating the unresolved subgrid scales of Eulerian models, some have suggested that subgrid motion should somehow be linked to the resolved flow. Smagorinsky (1963) postulated that velocity deformation is that critical link. Lilly (1965) later showed that Smagorinsky's formulation is consistent with the existence of an inertial subrange in 3-D turbulence-assuming that the inertial subrange lies within the subgrid motions.

The local Reynolds stresses which arise from the averaging process have so far been simulated by about the crudest of methods: That involving an eddy coefficient with magnitude limited in someway by the size of the averaging domain. When this domain is considered to be the grid volume of a detailed numerical integration, the eddy coefficient K becomes a "*subgrid scale eddy coefficient*".

Smagorinsky (1963) suggested a formulation of subgrid-scale mixing for use in a general circulation model that depends on the magnitude of deformation tensor and grid spacing. In tensor notation, Smagorinsky's formulation for eddy diffusivity can be represented as

$$K_m = \tilde{\lambda}^2 \sqrt{\left[\frac{1}{2}\left(\frac{\partial \overline{u}_i}{\partial x_j} + \frac{\partial \overline{u}_j}{\partial x_i}\right)\left(\frac{\partial \overline{u}_i}{\partial x_j} + \frac{\partial \overline{u}_j}{\partial x_i}\right)\right]}. \tag{4.29}$$

where $\tilde{\lambda}$ is the characteristic turbulence length scale, and defined as

$$\tilde{\lambda} = (c\Delta), \tag{4.30}$$

and c is the dimensionless constant of order unity, and Δ the representative grid interval defined using as follows,

$$\begin{aligned} \Delta &= (\Delta x \, \Delta y \, \Delta z)^{1/3} \quad \text{in 3-D}, \\ \Delta &= (\Delta x \, \Delta z)^{1/2} \qquad \text{in 2-D}. \end{aligned} \tag{4.31}$$

This formulation is extended by Lilly (1962) to include the contribution of convective available potential energy through the dependency on Richardson number, Ri, and it has been widely used. This formulation allows K_m to be variable in space and time, which is used in the model.

$$K_m(x, y, z, t) \;=\; \tilde{\lambda}^2 \, |Def| \, \left(1 - \frac{Ri}{Pr}\right)^{1/2} \tag{4.32}$$

where Pr is the eddy Prandtl number whose value is to be determined for particular experiments. In the model, Pr is taken to be unity,

$$Pr = \frac{K_m}{K_h} = 1, \tag{4.33}$$

where K_m and K_h are the subgrid-scale eddy mixing coefficients for momentum and heat, respectively, taken to be equal ($K_m = K_h$), and Ri the local Richardson number,

$$Ri = \frac{g\dfrac{\mathrm{d}}{\mathrm{d}z}\ln\theta}{Def^2}. \tag{4.34}$$

The sign of Ri is determined by the sign of the lapse rate of potential temperature, and it represents the stability of the atmosphere. Therefore, K_m is calculated with following conditions as below,

$$K_m = \begin{cases} K_m = \tilde{\lambda}^2 \, |Def| \, (1 - Ri/Pr)^{1/2} & \text{for } Ri < 1, \\ K_\circ & \text{for } Ri \geq 1. \end{cases} \tag{4.35}$$

where $K_\circ$ is the background value which is taken to be 0.01 m^2 sn^{-1}. In some studies it is taken as the molecular viscosity of air ($\mu = 2.0 \times 10^{-5}$m^2 sec^{-1}) (Drake *et al.*, 1974). It also represents a value of free-convection regime where z_i is boundary layer height (Fig 4.2).

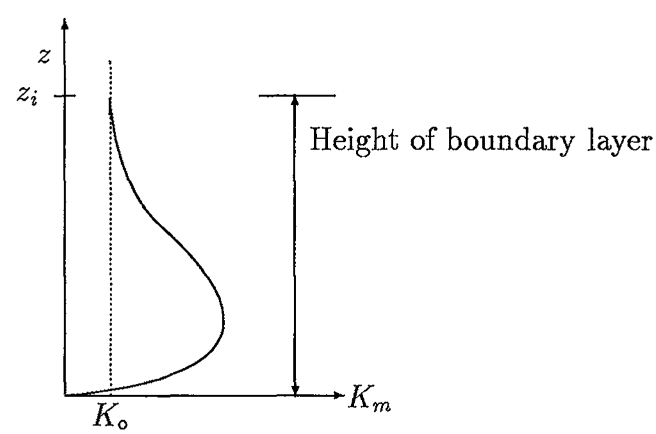

Fig 4.2 Schematic of K_m profiles in the boundary layer (after O'Brien, 1970).

The expressions given by Eq. (4.35) require that the subgrid scale fluxes be down-gradient as long as the exchange coefficients are positive (O'Brien, 1970).

In Eq. (4.32) and Eq. (4.35), Def is computed directly from finite differences between grid points and therefore is proportional to the two-point velocity correlation. It is also proportional to the kinetic energy contained in scales of motion smaller than the grid (Batchelor, 1954). In Eq. (4.22) Def the total deformation is defined as follows,

$$\begin{aligned} Def^2 &= \frac{1}{2}\sum_i^3\sum_j^3 \mathcal{D}_{ij} \\ &= \frac{1}{2}\left[\mathcal{D}_{11}^2 + \mathcal{D}_{22}^2 + \mathcal{D}_{33}^2 + 2\mathcal{D}_{12}^2 + 2\mathcal{D}_{13}^2 + 2\mathcal{D}_{23}^2\right] \end{aligned} \tag{4.36}$$

where the term $\mathcal{D}_{22}$ is removed from Eq. (4.28) and (4.36) due to previous assumptions for 2-D. Also the local derivatives of v wind component in $x-$ and z-directions are ignored from all terms of Eq. (4.36).

$$v = \text{constant}, \qquad \frac{\partial v}{\partial x} = 0, \quad \text{and} \quad \frac{\partial v}{\partial z} = 0.$$

The dimensionless constant c should be estimated for the model. This estimation can be done by theoretically or numerically (Deardorff, 1971). In the model c is taken to be 0.20.

4.1.2 Definitions and parameterization of mean thermodynamic equation terms

Parameterization of the source-sink term

In Eq. (2.3) the source-sink term, S_θ, can be divided two parts that are mean and perturbed.

$$S_\theta = \overline{S}_\theta + S'_\theta. \tag{4.37}$$

The mean term above can be represented as follows,

$$\overline{S}_\theta = \left.\frac{\partial\overline{\theta}}{\partial t}\right|_{\text{rad}} = -\frac{1}{\rho C_p}\frac{\partial \overline{R}}{\partial x_j}, \tag{4.38}$$

where $\partial\overline{R}/\partial x_j$ is the grid-volume averaged gradient of observed irradiance (i.e., radiative energy per area per time) due to all wavelengths of electromagnetic energy. Although it is important that $\overline{R}$ contains subgrid scale as well as resolvable effects, the divergence of $\overline{R}$ is ignored because there is no radiation processes in the model. Therefore, the turbulence occurs primarily due to topographical effects rather than radiation in the model.

$$\frac{\partial\overline{R}}{\partial x_j} = 0. \tag{4.39}$$

Thus, in the model, the source-sink term is assumed as

$$S_\theta = S'_\theta, \tag{4.40}$$

and the perturbation source-sink term is defined as follows,

$$S'_\theta = -\frac{1}{\rho_o}\frac{\partial}{\partial x_j}(\rho\,\overline{u''_j\,\theta''}) = \frac{\partial}{\partial x_j}\left(K_h\frac{\partial\theta}{\partial x_j}\right).$$

With these assumptions Eq. 2.3 can be rewritten as

$$\frac{\partial\theta}{\partial t} = -\frac{\partial\theta}{\partial x_j} + \frac{\partial}{\partial x_j}\left(K_h\frac{\partial\theta}{\partial x_j}\right) \tag{4.41}$$

Calculation of potential temperature perturbation.

The potential temperature can be represented in the form of mean and perturbation parts by using second decomposition.

$$\theta = \theta_s + \theta', \tag{4.42}$$

where θ_s is the initial temperature field, and assumed those

$$\theta_s = \theta_s(z),\ \frac{\partial\theta_s}{\partial t} = 0,\ \frac{\partial\theta_s}{\partial x} = 0,\ \frac{\partial\theta_s}{\partial y} = 0,\ \frac{\partial^2\theta_s}{\partial z^2} = 0.$$

In the buoyancy term of Eq. (4.17) and (4.20), $\theta_\circ$ is the mean value of a level, defined as,

$$\theta_{\circ(j)} = \frac{1}{N_x}\sum_{i=1}^{N_x}\theta_{(i,j)} \qquad \text{for } j^{th} \text{ level,} \tag{4.43}$$

where

$$\theta_{(i,j)} = \theta_{s(i,j)} + \theta'_{(i,j)}, \tag{4.44}$$

and N_x is the number of grid points in horizontal of the solution domain, the subscript parenthesis ( ) the represent the index number of grid-point.

With above assumptions and definitions, the final form of Eq. (2.3) can be written as,

$$\frac{\partial\theta'}{\partial t} = -\overline{u}_j\left(\frac{\partial\theta'}{\partial x_j} + \frac{\partial\theta_s}{\partial z}\delta_{i3}\right) + \frac{\partial}{\partial x_j}\left(K_h\frac{\partial\theta'}{\partial x_j}\right) \tag{4.45}$$

where there is summation on j (j=1 and 3 in 2-D).

CHAPTER 5

TRANSFORMATION OF THE MODEL EQUATIONS

First step in the numerical modeling of atmosphere is the selection of coordinate system which depends on the interested phenomenon since it is important in finding of model results accurately. In the mesoscale modeling the various coordinate system are used (discussed in chapter 3). The use of coordinate transformations for meteorological applications has been limited to the simplest types of transformations in which only the vertical coordinate is transformed to coincide with the lower boundary (i.e., the topography). All these systems have some disadvantages as well as advantages for 2-D or 3-D models (Erdun *et al.*, 1996).

In this model a general coordinate transformation called the Schwarz-Christoffel transformation is used to eliminate the disadvantages, due to resulting from non-orthogonal grid mesh, of coordinate systems used in the numerical atmospheric modeling. Schwarz-Christoffel transformation can be used to generate grid points on which can be performed for any topography in any size, shapes, and slopes (even if equal to 90°). After the performing of Schwarz-Christoffel transformation, the topography will be flat which is suitable for writing in finite difference forms of the model equations.

In order to have the best representation of the topography and the most suitable grid points for two-dimensional atmospheric flow modeling, following properties should be provided:

- Generated grid mesh should be *conformal* (Fig 5.5),
- Generated grid mesh should be *orthogonal* (Fig 5.5),
- *Fine* grid mesh near the ground, and *coarse* mesh near the top should be provided (Fig 5.1a).

Schwarz-Christoffel transformation provides all of these conditions.

In our model, one more coordinate transformation are used for convenience as well as Schwarz-Christoffel transformation. First transformation is from *physical coordinate system* which includes the coordinates of the defined topography, to *auxiliary coordinate system* by using Schwarz-Christoffel transformation. The grid mesh in the auxiliary coordinates is rectangular but not convenient to use directly for finite differences because grid points are not equally spaced (small grid intervals near the ground, "fine mesh"; large grid intervals near the top, "coarse mesh"). The second transformation is from the auxiliary plane to the computational plane which is required to provide equally spaced grid points. In computational system the grid point intervals are the same, and it is ready to write in finite difference schemes.

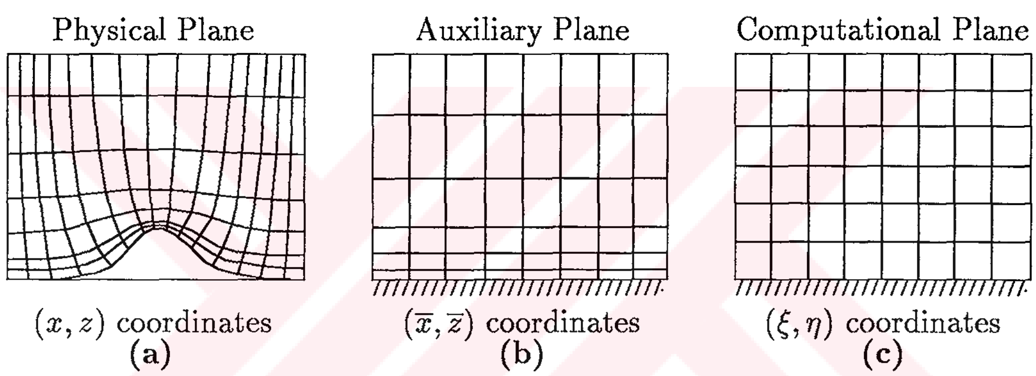

Fig 5.1 Coordinate transformations used in the model.

5.1 Coordinate Transformation and Invariant Differential Forms

The model equations given in chapter 4 are valid in physical coordinate system. In order to use the equation in computational system, all model equations should be transformed depending on ξ, and η instead of x, and z coordinate variables. Derivatives in the equations (Eq. 2.1, 4.20, 4.45) are rewritten by using chain-rule and Schwarz-Christoffel transformation.

Consider a transformation from Cartesian coordinates (x, z) to curvilinear coordinates $(\overline{x}, \overline{z})$ (Fig 5.1a-b), both taken to be right-handed systems:

$$x = x(\overline{x}, \overline{z}), \qquad \text{and} \qquad z = z(\overline{x}, \overline{z}). \tag{5.1}$$

Transformation formulas in the general case can be provided in literature (Stratton (1940); Pielke (1984); Dutton (1976)). These formulas will be reproduced in this section to make intelligible, and show the advantages of, the methodology used in the grid generations. Since $(\overline{x}, \overline{z})$ are not Cartesian, it is necessary to distinguish between contravariant and covariant quantities. ($\overline{x}$ and $\overline{z}$ will be themselves taken as contravariant.)

The curvilinear coordinate lines of a three-dimensional system are space curves formed by the intersection of surfaces on which one coordinate is constant. One coordinate varies along a coordinate line while the other two are constant there on. The tangents to the coordinate line and the normals to the coordinate surface are the base vectors of the coordinate system.

Base vectors

Consider first a coordinate line along which only the coordinate $\overline{x}$ varies (Fig 5.2). Clearly a tangent vector to the coordinate line is given by

$$\lim_{d\overline{x} \to 0} \frac{\vec{r}(\overline{x} + d\overline{x}) - \vec{r}(\overline{x})}{d\overline{x}} = \frac{\partial r}{\partial \overline{x}} \tag{5.2}$$

These tangent vectors to the three coordinate lines are the three *covariant base vectors* of the curvilinear coordinate system, designed

$$\mathbf{a}_i = \frac{\partial r}{\partial \overline{x}_i} \tag{5.3}$$

where the three curvilinear coordinates are represented by $\overline{x}_i (i = 1, 2, 3)$, and the subscript i indicates the base vector corresponding to the $\overline{x}_i$ coordinate, i.e., the tangent to the coordinate line along which only $\overline{x}_i$ varies.

A normal vector to a coordinate surface on which the coordinate $\overline{x}$ is constant is given by $\nabla \overline{x}$ (Fig 5.3).

These normal vectors to the three coordinate surfaces are the three *contravariant base vectors* of the curvilinear coordinate system, designed

$$\mathbf{a}^i = \nabla \overline{x}_i. \tag{5.4}$$

Here the coordinate index i appears as a superscript on the base vector to differentiate these contravariant base vectors from the covariant vectors. The two types of base vectors are illustrated in Fig 5.4, showing an element of volume with six sides, each of which lies on some coordinate surface.

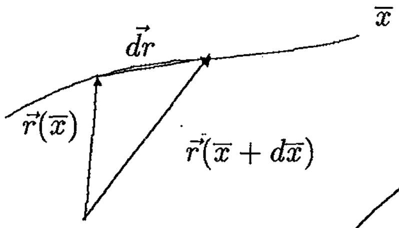

Fig 5.2 A tangent vector to a coordinate line.

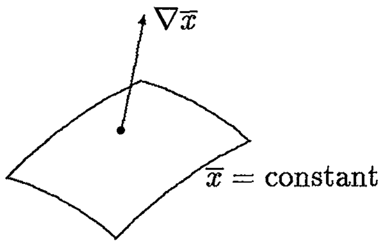

Fig 5.3 A normal vector to a coordinate surface.

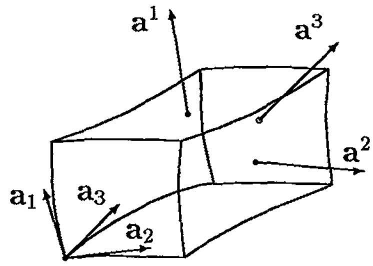

Fig 5.4 Covariant and contravariant base vectors.

Metric tensors

The *covariant metric tensor* components:

$$g_{ij} = g_{ji} = \mathbf{a}_i \cdot \mathbf{a}_j \tag{5.5}$$

$$\sqrt{g} = \sqrt{\det|g_{ij}|} = J(x,z) \tag{5.6}$$

where coordinate subscripts denote differentiation and $\sqrt{g}$ is the Jacobian of the transformation with respect to $(\overline{x},\overline{z})$.

An increment of arc length on a coordinate line along which $\overline{x}_i$ varies is given by

$$ds_i = |\mathbf{a}_i| d\overline{x}_i = \sqrt{g_{ii}}\, d\overline{x}_i, \tag{5.7}$$

and also an increment of a area on a coordinate surface of constant $\overline{x}_i$, and volume element, respectively,

$$dS_i = |\mathbf{a}_j \times \mathbf{a}_k|\, d\overline{x}_j d\overline{x}_k = \sqrt{g_{jj}g_{kk} - g_{jk}^2}\, d\overline{x}_j d\overline{x}_k. \tag{5.8}$$

$$dV = \mathbf{a}_1 \cdot (\mathbf{a}_2 \times \mathbf{a}_3)\, d\overline{x}_1 d\overline{x}_2 d\overline{x}_3 = \sqrt{g}\, d\overline{x}_1 d\overline{x}_2 d\overline{x}_3. \tag{5.9}$$

The *contravariant metric tensor* are as follows

$$g^{ij} = g^{ji} = \mathbf{a}^i \cdot \mathbf{a}^j \tag{5.10}$$

and

$$\det|g^{ij}| = \frac{1}{\det|g_{ij}|} = \frac{1}{g} = \frac{1}{J^2} \tag{5.11}$$

so that, in terms of the contravariant base vectors, the Jacobian is

$$\sqrt{g} = \left(\det|g^{ij}|\right)^{-1/2} \tag{5.12}$$

5.2 Two-Dimensional Forms

The covariant and contravariant base vectors are rewritten in 2-D as follows, respectively,

$$\begin{aligned} \mathbf{a}_1 &= \frac{\partial x}{\partial \overline{x}}\mathbf{i} + \frac{\partial z}{\partial \overline{x}}\mathbf{k}, \\ \mathbf{a}_2 &= \frac{\partial x}{\partial \overline{z}}\mathbf{i} + \frac{\partial z}{\partial \overline{z}}\mathbf{k}, \end{aligned} \tag{5.13}$$

and

$$\begin{aligned} \mathbf{a}^1 &= g^{11}\mathbf{a}_1 + g^{12}\mathbf{a}_2 = \frac{1}{\sqrt{g}}\left(\frac{\partial z}{\partial \overline{z}}\mathbf{i} - \frac{\partial x}{\partial \overline{z}}\mathbf{k}\right) \\ \mathbf{a}^2 &= g^{21}\mathbf{a}_1 + g^{22}\mathbf{a}_2 = \frac{1}{\sqrt{g}}\left(-\frac{\partial z}{\partial \overline{x}}\mathbf{i} + \frac{\partial x}{\partial \overline{x}}\mathbf{k}\right) \end{aligned} \tag{5.14}$$

The covariant and contravariant metrics of transformation are given for 2-D as follow, respectively,

$$g_{11} = \left(\frac{\partial x}{\partial \overline{x}}\right)^2 + \left(\frac{\partial z}{\partial \overline{x}}\right)^2, \qquad g_{22} = \left(\frac{\partial x}{\partial \overline{z}}\right)^2 + \left(\frac{\partial z}{\partial \overline{z}}\right)^2,$$

$$g_{12} = g_{21} = \frac{\partial x}{\partial \overline{x}}\frac{\partial x}{\partial \overline{z}} + \frac{\partial z}{\partial \overline{x}}\frac{\partial z}{\partial \overline{z}}, \tag{5.15}$$

$$\sqrt{g} = \sqrt{\det|g_{ij}|} = \left[g_{11}g_{22} - g_{12}^2\right]^{1/2} = \left(\frac{\partial x}{\partial \overline{x}}\frac{\partial z}{\partial \overline{z}} - \frac{\partial x}{\partial \overline{z}}\frac{\partial z}{\partial \overline{x}}\right) = J(x,z), \tag{5.16}$$

and

$$g^{11} = g_{22}/g, \qquad g^{22} = g_{11}/g, \qquad g^{12} = g^{21} = -g_{12}/g. \tag{5.17}$$

From Eqs. (5.13-16), it follows that

$$\begin{aligned}
\frac{\partial \overline{x}}{\partial x} &= \frac{1}{\sqrt{g}}\frac{\partial z}{\partial \overline{z}} = \frac{g_{22}}{g}\frac{\partial x}{\partial \overline{x}} - \frac{g_{21}}{g}\frac{\partial x}{\partial \overline{z}}, \\
\frac{\partial \overline{x}}{\partial z} &= -\frac{1}{\sqrt{g}}\frac{\partial x}{\partial \overline{z}} = \frac{g_{22}}{g}\frac{\partial z}{\partial \overline{x}} - \frac{g_{21}}{g}\frac{\partial z}{\partial \overline{z}}, \\
\frac{\partial \overline{z}}{\partial x} &= -\frac{1}{\sqrt{g}}\frac{\partial z}{\partial \overline{x}} = -\frac{g_{12}}{g}\frac{\partial x}{\partial \overline{x}} + \frac{g_{11}}{g}\frac{\partial x}{\partial \overline{z}}, \\
\frac{\partial \overline{z}}{\partial z} &= \frac{1}{\sqrt{g}}\frac{\partial x}{\partial \overline{x}} = -\frac{g_{12}}{g}\frac{\partial z}{\partial \overline{x}} + \frac{g_{11}}{g}\frac{\partial z}{\partial \overline{z}}.
\end{aligned} \tag{5.18}$$

In terms of the base vectors, the (contravariant) gradient operator, for example applied to a scalar ϕ, is

$$\nabla\phi = \mathbf{a}^1\frac{\partial \phi}{\partial \overline{x}} + \mathbf{a}^2\frac{\partial \phi}{\partial \overline{z}} + \tag{5.19}$$

and the divergence of a vector F is therefore

$$\nabla \cdot F = \frac{1}{\sqrt{g}}\frac{\partial}{\partial \overline{x}}(\sqrt{g}F \cdot \mathbf{a}^1) + \frac{1}{\sqrt{g}}\frac{\partial}{\partial \overline{z}}(\sqrt{g}F \cdot \mathbf{a}^2) \tag{5.20}$$

Incompressible flow models, whether anelastic or not, require the solution of an elliptic equation in each time step. In a system using the primitive equation, the elliptic equation governs the pressure. The form of such an equation may be seen by substituting $\nabla\phi$ for F in Eq. (5.20):

$$\nabla^2\phi = \frac{1}{\sqrt{g}}\frac{\partial}{\partial\overline{x}}\left[\sqrt{g}\,g^{11}\frac{\partial\phi}{\partial\overline{x}} + \sqrt{g}\,g^{12}\frac{\partial\phi}{\partial\overline{z}}\right] + \frac{1}{\sqrt{g}}\frac{\partial}{\partial\overline{z}}\left[\sqrt{g}\,g^{21}\frac{\partial\phi}{\partial\overline{x}} + \sqrt{g}\,g^{22}\frac{\partial\phi}{\partial\overline{z}}\right]. \tag{5.21}$$

5.3 Conformal Mapping and Orthogonal System

Suppose that under transformation Eq. (5.1) point $(x_\circ, z_\circ)$ of the xz-plane (Physical plane) is mapped into point $(\overline{x}_\circ, \overline{z}_\circ)$ of the $\overline{x}\,\overline{z}$-plane (here, transformed plane is the Auxiliary plane; Fig 5.1) while curves C_1 and C_2 (intersecting at $(x_\circ, z_\circ)$) are mapped respectively into curves C_1' and C_2' (intersecting $(\overline{x}_\circ, \overline{z}_\circ)$) both in magnitude and sense (Fig 5.5), the transformation or mapping is said to be *conformal* at $(x_\circ, z_\circ)$. A mapping which preserves the magnitudes of angles but not necessarily the sense is called *isogonal*.

$$\theta_{(x_\circ,z_\circ)} = \theta'_{(\overline{x}_\circ,\overline{z}_\circ)}. \tag{5.22}$$

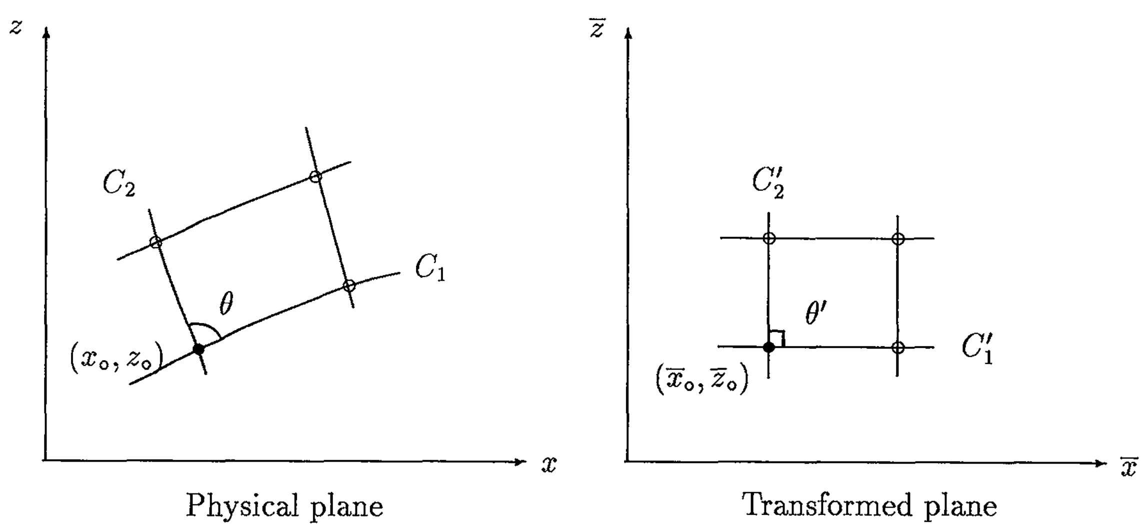

Fig 5.5 Angles in the transformation between physical plane and transformed plane.

In numerical solutions, concept of numerical orthogonality, i.e., that the off-diagonal metric coefficients vanish when evaluated numerically, is usually more important than strict analytical orthogonality, especially when the equations to be solved on the system are in the conservative law form. Orthogonal coordinate system produce fewer additional terms in transformed partial differential equations, and thus reduce the amount of computation required.

Using conformal mapping with the orthogonality condition, Eq. (5.22) is rewritten as follows

$$\theta_{(x_o,z_o)} = \theta'_{(\overline{x}_o,\overline{z}_o)} = 90^\circ. \tag{5.23}$$

In the orthogonal system, the magnitude of angles for both system would be the same, and equal to 90°. Since the computational plane has rectangular grid mesh, and both systems should be identical, this is very important.

Basically there are two types of orthogonal generation systems, based on the construction of an orthogonal system from a non-orthogonal system, and involving field solutions of partial differential equations. The first approach involves the construction of orthogonal trajectories on a given non-orthogonal system.

In only an orthogonal coordinate system, there are the two types of base vectors parallel, since for a non-orthogonal system, the normal to a coordinate surface does not necessarily coincide with the tangent to a coordinate line crossing that surface. Also for an orthogonal system the three base vectors of each type are obviously mutually perpendicular.

Base vectors and metric tensors

An orthogonal system has the defining properties that the base vectors, covariant and contravariant, are orthogonal:

$$\mathbf{a}_1 \cdot \mathbf{a}_2 = 0, \qquad \mathbf{a}^1 \cdot \mathbf{a}^2 = 0, \tag{5.24}$$

whence

$$g_{12} = g_{21} = 0, \qquad g^{12} = g^{21} = 0. \tag{5.25}$$

The convention is usually adopted to define scale factors h_i as follows,

$$
\begin{aligned}
&\mathrm{h}_1^2 = g_{11} = \left(\frac{\partial x}{\partial \overline{x}}\right)^2 + \left(\frac{\partial z}{\partial \overline{x}}\right)^2, \qquad h_2^2 = g_{22} = \left(\frac{\partial x}{\partial \overline{z}}\right)^2 + \left(\frac{\partial z}{\partial \overline{z}}\right)^2, \\
&\mathrm{h}_1 h_2 = \sqrt{g} = [g_{11} g_{22}]^{1/2}
\end{aligned}
\tag{5.26}
$$

From Eq. (5.18), it is readily inferred that

$$
\begin{aligned}
\frac{\partial \overline{x}}{\partial x} &= \frac{1}{h_1^2}\frac{\partial x}{\partial \overline{x}} = \frac{1}{h_1 h_2}\frac{\partial z}{\partial \overline{z}} \qquad & \frac{\partial \overline{x}}{\partial z} &= \frac{1}{h_1^2}\frac{\partial z}{\partial \overline{x}} = -\frac{1}{h_1 h_2}\frac{\partial x}{\partial \overline{z}} \\
\frac{\partial \overline{z}}{\partial x} &= \frac{1}{h_1^2}\frac{\partial x}{\partial \overline{z}} = -\frac{1}{h_1 h_2}\frac{\partial z}{\partial \overline{x}} \qquad & \frac{\partial \overline{z}}{\partial z} &= \frac{1}{h_1^2}\frac{\partial z}{\partial \overline{z}} = \frac{1}{h_1 h_2}\frac{\partial x}{\partial \overline{x}}
\end{aligned}
\tag{5.27}
$$

5.4 Truncation Error Between Orthogonal and Non-orthogonal Systems

In meteorological applications, the slope of topography must have an angle much less than 45° (Pielke, 1984) due to using non-orthogonal grid mesh .

We will give here truncation error due to non-orthogonality by following Thompson *et al.*, (1985). In the model, the two-dimensional transformation of the first derivative is given by

$$
\frac{\partial f}{\partial x} = \frac{1}{\sqrt{g}}\left(\frac{\partial z}{\partial \overline{z}}\frac{\partial f}{\partial \overline{x}} - \frac{\partial z}{\partial \overline{x}}\frac{\partial f}{\partial \overline{z}}\right). \tag{5.28}
$$

With two-point central difference representations for all derivatives the leading term of the truncation error is

$$
\begin{aligned}
\mathrm{T}_x = \; & \frac{1}{2\sqrt{g}}\left(\frac{\partial z}{\partial \overline{x}}\frac{\partial x}{\partial \overline{z}}\frac{\partial^2 x}{\partial \overline{z}^2} - \frac{\partial x}{\partial \overline{x}}\frac{\partial z}{\partial \overline{z}}\frac{\partial^2 x}{\partial \overline{x}^2}\right)\frac{\partial^2 f}{\partial x^2} + \frac{1}{2\sqrt{g}}\left(\frac{\partial z}{\partial \overline{x}}\frac{\partial z}{\partial \overline{z}}\right)\left(\frac{\partial^2 z}{\partial \overline{z}^2} - \frac{\partial^2 z}{\partial \overline{x}^2}\right)\frac{\partial^2 f}{\partial z^2} + \\
& \frac{1}{2\sqrt{g}}\left[\frac{\partial z}{\partial \overline{x}}\frac{\partial z}{\partial \overline{z}}\left(\frac{\partial^2 x}{\partial \overline{z}^2} - \frac{\partial^2 x}{\partial \overline{x}^2}\right) + \frac{\partial x}{\partial \overline{z}}\frac{\partial z}{\partial \overline{x}}\frac{\partial^2 z}{\partial \overline{z}^2} - \frac{\partial x}{\partial \overline{x}}\frac{\partial z}{\partial \overline{z}}\frac{\partial^2 z}{\partial \overline{x}^2}\right]\frac{\partial^2 f}{\partial x \partial z} \\
& + [\text{second order terms in the spacing}]
\end{aligned}
$$

where the coordinate derivatives are to be understood here to represent central difference expressions, e.g.,

$$\frac{\partial x}{\partial \overline{x}} = (x_{i+1,j} - x_{i-1,j})/2,$$

$$\frac{\partial x}{\partial \overline{z}} = (x_{i,j+1} - x_{i,j-1})/2,$$

$$\frac{\partial^2 x}{\partial \overline{x}^2} = x_{i+1,j} - 2x_{i,j} + x_{i-1,j},$$

$$\frac{\partial^2 x}{\partial \overline{z}^2} = x_{i,j+1} - 2x_{i,j} + x_{i,j-1}.$$

These contributions to the truncation error arise from the nonuniform spacing. The familiar terms proportional to a power of the spacing occur in addition to these terms as has been noted.

Sufficient conditions can now be stated for maintaining the order of the difference representations, with a fixed number of points in each distribution. First, as in the one-dimensional case, the ratios

$$\frac{\partial^2 x/\partial \overline{x}^2}{|\mathbf{a}_1|^2}, \qquad \frac{\partial^2 z/\partial \overline{x}^2}{|\mathbf{a}_1|^2}, \qquad \frac{\partial^2 x/\partial \overline{z}^2}{|\mathbf{a}_2|^2}, \qquad \frac{\partial^2 z/\partial \overline{z}^2}{|\mathbf{a}_2|^2},$$

must be bounded as $\partial x/\partial \overline{x}$, $\partial x/\partial \overline{z}$, $\partial z/\partial \overline{x}$, $\partial z/\partial \overline{z}$ approach zero. A second condition must be imposed which limits the rate at which the Jacobian approaches zero. This condition can be met by simply requiring that $\cot\theta$ remain bounded, where θ is the angle between the $\overline{x}$ and $\overline{z}$ coordinate lines. The fact that this bound on the nonorthogonality imposes the correct lower bound on the Jacobian follows the fact that $|\cot\theta| \leq m$ implies

$$g \geq \frac{1}{m^2+1}\,|\mathbf{a}_1|^2 \cdot |\mathbf{a}_2|^2 \tag{5.30}$$

With these conditions on the ratios of second to first derivatives, and the limit on the nonorthogonality satisfied, the order of the first derivative approximations is maintained in the sense that the contributions to the truncation error arising for the nonuniform spacing will be second-order terms in the grid spacing.

The truncation error terms for second derivatives that are introduced when using a curvilinear coordinate system are very lengthy and involve both second and third derivatives of the function f. However, it can be shown that the same sufficient conditions, together with the condition that

$$\frac{\partial^2 x/\partial\overline{x}\partial\overline{z}}{|\mathbf{a}_1|\cdot|\mathbf{a}_2|}, \qquad \frac{\partial^2 z/\partial\overline{x}\partial\overline{z}}{|\mathbf{a}_1|\cdot|\mathbf{a}_2|},$$

remain bounded, will insure that the order of the difference representations is maintained.

It was noted above that a limit on the nonorthogonality, imposed by Eq. (5.30), is required for maintaining the order of difference representations. The degree to which nonorthogonality affects truncation error can be stated more precisely, as follows. The truncation error for a first derivative $\partial f/\partial x$ can be written

$$T_x = \frac{1}{\sqrt{g}}\left(\frac{\partial z}{\partial \overline{z}}\frac{\partial T}{\partial \overline{x}} - \frac{\partial z}{\partial \overline{x}}\frac{\partial T}{\partial \overline{z}}\right) \tag{5.31}$$

where $\partial T/\partial\overline{x}$ and $\partial T/\partial\overline{z}$ are the truncation errors for the difference expressions of $\partial f/\partial\overline{x}$ and $\partial f/\partial\overline{z}$. Now all coordinate derivatives can be expressed using direction cosines of the angles lines. After some simplification, the truncation error has the form

$$T_x = \frac{1}{\sin(\phi_{\overline{z}} - \phi_{\overline{x}})}\left(\sin\phi_{\overline{z}}\,\cos\phi_{\overline{x}}\,\frac{\partial T/\partial\overline{z}}{\partial x/\partial\overline{x}} - \sin\phi_{\overline{x}}\,\cos\phi_{\overline{z}}\,\frac{\partial T/\partial\overline{z}}{\partial x/\partial\overline{z}}\right) \tag{5.32}$$

Therefore the truncation error, in general, varies inversely with the sine of the angle between the coordinate lines. Note that there is also a dependence on the direction of the coordinate lines. To further clarify the effect of nonorthogonality spacing are considered.

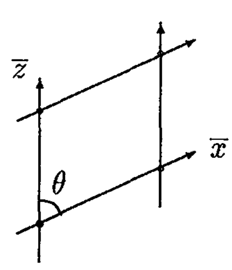

Fig 5.6 The angle between coordinate lines.

The contribution from nonorthogonality can be isolated by considering the case of skewed parallel lines with $\partial x/\partial \overline{x}= \partial^2 x/\partial \overline{x}^2= \partial^2 x/\partial \overline{x}\partial \overline{z}= \partial^2 z/\partial \overline{x}\partial \overline{x}= \partial^2 z/\partial \overline{x}\partial \overline{z}=0$ as diagrammed in Fig 5.6.

Here Eq. (5.29) reduces to

$$T_x = -\frac{1}{2}\frac{\partial^2 x}{\partial \overline{x}^2}\frac{\partial^2 f}{\partial x^2} + \frac{1}{2}\left(\frac{\partial z/\partial \overline{x}}{\partial x/\partial \overline{x}}\right)\frac{\partial^2 z}{\partial \overline{z}^2}\frac{\partial^2 f}{\partial z^2} - \frac{1}{2}\left(\frac{\partial z/\partial \overline{x}}{\partial x/\partial \overline{x}}\right)\frac{\partial^2 x}{\partial \overline{x}^2}\frac{\partial^2 f}{\partial x \partial z}. \tag{5.33}$$

Since

$$\cot\theta = \frac{\partial z/\partial \overline{x}}{\partial x/\partial \overline{x}}, \tag{5.34}$$

this may be written

$$T_x = -\frac{1}{2}\frac{\partial^2 x}{\partial \overline{x}^2}\frac{\partial^2 f}{\partial x^2} + \frac{1}{2}\left(\frac{\partial^2 z}{\partial \overline{z}^2}\frac{\partial^2 f}{\partial z^2} - \frac{\partial^2 x}{\partial \overline{x}^2}\frac{\partial^2 f}{\partial x \partial z}\right)\cot\theta. \tag{5.35}$$

This first term in Eq. (5.35) occurs even on an orthogonal system. The last two terms arise from orthogonality. For $\theta \leq 45°$, these terms are no greater than those from the nonuniform spacing. Reasonable departure from orthogonality is therefore of little concern when the rate-of-change of grid spacing is reasonable. Large departure from othogonality may be more of a problem at boundaries where one-sided difference expressions are needed. Therefore grids should probably be made as nearly orthogonal at the boundaries as is practical. Note that the contribution from nonorthogonality vanishes on a skewed uniform grid.

5.5 First Order Transformation Derivatives

The coordinate variables for these systems (Fig 5.1) are showed respectively,

1) *Physical Coordinate System* : x, z coordinates ($y-$plane),
2) *Auxiliary Coordinate System* : $\overline{x}$, $\overline{z}$ coordinates ($\overline{y}-$plane),
3) *Computational Coordinate System* : ξ, η coordinates ($\lambda-$plane).

Since the model equations are written initially for the physical coordinate system, all model equations should be transformed to computational plane. The transformations are performed on coordinate variables.

Transformations of derivatives between coordinate systems (Fig 5.1) are in the following order:

$$y(x,y)\text{-plane} \quad \overset{①}{\Longrightarrow} \quad \overline{y}(\overline{x},\overline{z})\text{-plane} \quad \overset{②}{\Longrightarrow} \quad \lambda(\xi,\eta)\text{-plane.}$$

Transformation from physical plane to auxiliary plane :

The first derivatives in the model equations for the first transformation are defined using the chain-rule as follows,

$$\frac{\partial}{\partial x} = \frac{\partial \overline{x}}{\partial x}\frac{\partial}{\partial \overline{x}} + \frac{\partial \overline{z}}{\partial x}\frac{\partial}{\partial \overline{z}}, \tag{5.36}$$

$$\frac{\partial}{\partial z} = \frac{\partial \overline{x}}{\partial z}\frac{\partial}{\partial \overline{x}} + \frac{\partial \overline{z}}{\partial z}\frac{\partial}{\partial \overline{z}}, \tag{5.37}$$

or in matrix form,

$$\begin{bmatrix} \dfrac{\partial}{\partial x} \\ \\ \dfrac{\partial}{\partial z} \end{bmatrix} = \begin{bmatrix} \dfrac{\partial \overline{x}}{\partial x} & \dfrac{\partial \overline{z}}{\partial x} \\ \\ \dfrac{\partial \overline{x}}{\partial z} & \dfrac{\partial \overline{z}}{\partial z} \end{bmatrix} \cdot \begin{bmatrix} \dfrac{\partial}{\partial \overline{x}} \\ \\ \dfrac{\partial}{\partial \overline{z}} \end{bmatrix} \tag{5.38}$$

where the first matrix on the right hand side of Eq. (5.42) can be rewritten as follows,

$$\begin{bmatrix} \dfrac{\partial \overline{x}}{\partial x} & \dfrac{\partial \overline{z}}{\partial x} \\ \\ \dfrac{\partial \overline{x}}{\partial z} & \dfrac{\partial \overline{z}}{\partial z} \end{bmatrix} = \begin{bmatrix} \dfrac{\partial x}{\partial \overline{x}} & \dfrac{\partial z}{\partial \overline{x}} \\ \\ \dfrac{\partial x}{\partial \overline{z}} & \dfrac{\partial z}{\partial \overline{z}} \end{bmatrix}^{-1} = \frac{1}{J} \begin{bmatrix} \dfrac{\partial z}{\partial \overline{z}} & -\dfrac{\partial z}{\partial \overline{x}} \\ \\ -\dfrac{\partial x}{\partial \overline{z}} & \dfrac{\partial x}{\partial \overline{x}} \end{bmatrix} \tag{5.39}$$

where

$$\begin{aligned} \frac{\partial \overline{x}}{\partial x} &= \frac{1}{J}\frac{\partial z}{\partial \overline{z}} & \qquad \frac{\partial \overline{x}}{\partial z} &= -\frac{1}{J}\frac{\partial x}{\partial \overline{z}} \\ \frac{\partial \overline{z}}{\partial x} &= -\frac{1}{J}\frac{\partial z}{\partial \overline{x}} & \qquad \frac{\partial \overline{z}}{\partial z} &= \frac{1}{J}\frac{\partial x}{\partial \overline{x}} \end{aligned} \tag{5.40}$$

The Jacobian of the transformation J in Eq. (5.39) represents the ratio of areas between coordinate systems, and defined as

$$J = \left|\frac{\partial(x,z)}{\partial(\overline{x},\overline{z})}\right| = \begin{vmatrix} \dfrac{\partial x}{\partial \overline{x}} & \dfrac{\partial z}{\partial \overline{x}} \\ \dfrac{\partial x}{\partial \overline{z}} & \dfrac{\partial z}{\partial \overline{z}} \end{vmatrix} = \left(\frac{\partial x}{\partial \overline{x}}\frac{\partial z}{\partial \overline{z}} - \frac{\partial x}{\partial \overline{z}}\frac{\partial z}{\partial \overline{x}}\right) \neq 0, \tag{5.41}$$

The first derivatives of the first coordinate transformation are shown as

$$\frac{\partial}{\partial x} = \frac{1}{J}\left[\frac{\partial z}{\partial \overline{z}}\frac{\partial}{\partial \overline{x}} - \frac{\partial z}{\partial \overline{x}}\frac{\partial}{\partial \overline{z}}\right] \tag{5.42}$$

$$\frac{\partial}{\partial z} = \frac{1}{J}\left[-\frac{\partial x}{\partial \overline{z}}\frac{\partial}{\partial \overline{x}} + \frac{\partial x}{\partial \overline{x}}\frac{\partial}{\partial \overline{z}}\right] \tag{5.43}$$

If $y = x + i\cdot z$ and $\overline{y} = \overline{x} + i\cdot\overline{z}$, where $x = x(\overline{x},\overline{z})$, $z = z(\overline{x},\overline{z})$, and $\overline{x} = (x,z)$, $\overline{z} = (x,z)$ are analytic in a region, and their partial derivatives are continuous,

$$\frac{dy}{d\overline{y}} = \frac{dx + i\cdot dy}{d\overline{x} + i\cdot d\overline{y}} = \begin{cases} d\overline{x} \to 0 \quad : & \dfrac{\partial z}{\partial \overline{z}} - i\cdot\dfrac{\partial x}{\partial \overline{z}}, \\ d\overline{z} \to 0 \quad : & \dfrac{\partial x}{\partial \overline{x}} + i\cdot\dfrac{\partial z}{\partial \overline{x}}, \end{cases} \tag{5.44}$$

then we have following equations,

$$\begin{aligned} \frac{\partial x}{\partial \overline{x}} &= \frac{\partial z}{\partial \overline{z}}, && \text{(real parts)}, \\ \frac{\partial z}{\partial \overline{x}} &= -\frac{\partial x}{\partial \overline{z}}, && \text{(imaginary parts)}. \end{aligned} \tag{5.45}$$

These equations are called the *Cauchy-Riemann conditions.*

Eq. (5.45) are calculated from Schwarz-Christoffel transformation $[dy/d\lambda]$, and using Cauchy-Riemann conditions,

$$\frac{\partial x}{\partial \overline{x}} = \frac{\partial z}{\partial \overline{z}} = \mathbf{Re}\left[\frac{\partial y}{\partial \lambda}\right] = R_1,$$

$$\frac{\partial z}{\partial \overline{x}} = -\frac{\partial x}{\partial \overline{z}} = \mathbf{Im}\left[\frac{\partial y}{\partial \lambda}\right] = I_1$$

and (5.46)

$$J = \left|\frac{\partial y}{\partial \lambda}\right|^2.$$

where **Re**[ ] and **Im**[ ] are real and imaginary parts of the Schwarz-Christoffel transformation, respectively.

Using Cauchy-Riemann conditions and Schwarz-Christoffel transformation results, the metrics and Jacobian of the transformation (Eq. 5.26) are rewritten as follows,

$$g_{11} = g_{22} = \sqrt{g} = J(x,z) = (R_1)^2 + (I_1)^2, \tag{5.47}$$

and

$$g^{11} = g^{22} = 1/\sqrt{g} = 1/J = 1/[(R_1)^2 + (I_1)^2], \tag{5.48}$$

and then the coordinate system is characterized by *only one metric coefficient.*

Transformation from auxiliary plane to computational plane :

In the Auxiliary coordinate system, horizontal grid spacing $\Delta\overline{x}$ are equal, but grid spacing $\Delta\overline{z}$ in vertical are not. Therefore, the second transformation is only applied for vertical coordinates.

$$\frac{\partial}{\partial \overline{x}} = \frac{\partial}{\partial \xi},$$

(5.49)

$$\frac{\partial}{\partial \overline{z}} = G\frac{\partial}{\partial \eta},$$

where G is a local derivative that is the ratio of vertical grid spacing between these two systems, and defined as,

$$G(\overline{z}) = \frac{\partial \eta}{\partial \overline{z}} \tag{5.50}$$

This function should be determined for the generated grid mesh. For the given Gaussian-shape topography we used the following functions,

$$\begin{aligned} \eta(\overline{z}) = \; & 2.469\ \overline{z}^{\,0.1} + 634.403\overline{z}^{\,0.8} - 3995.21\overline{z}^{\,1.1} + 31799.1\overline{z}^{\,1.4} + \\ & \text{-}42154.3\overline{z}^{\,1.5} + 16572\overline{z}^{\,1.7} - 2822.38\overline{z}^{\,2}, \end{aligned} \tag{5.51}$$

and

$$\begin{aligned} \mathrm{G}(\overline{z}) = \; & 0.2469\overline{z}^{\,-0.9} + 507.523\overline{z}^{\,-0.2} - 4394.74\overline{z}^{\,0.1} + 44518\overline{z}^{\,0.4} + \\ & \text{-}63231.5\overline{z}^{\,0.5} + 28173.3\overline{z}^{\,0.7} - 5644.76\overline{z}. \end{aligned} \tag{5.52}$$

When these two coordinate transformations are applied respectively, a set of general transformation equations can be found from physical domain to computational domain as follows,

$$\frac{\partial}{\partial x} = \frac{1}{J}\left(R_1 \frac{\partial}{\partial \xi} - G I_1 \frac{\partial}{\partial \eta} \right) \tag{5.53}$$

$$\frac{\partial}{\partial z} = \frac{1}{J}\left(I_1 \frac{\partial}{\partial \xi} + G R_1 \frac{\partial}{\partial \eta} \right) \tag{5.54}$$

5.6 Second Order Transformation Derivatives

In order to find the second order derivatives of transformation, we can derivate once the first order transformation derivatives (Eqs. 5.36 and 5.37).

$$\frac{\partial}{\partial x}\left(\frac{\partial}{\partial x}\right) = \frac{\partial}{\partial x}\left[\frac{1}{J}\left(\frac{\partial x}{\partial \overline{x}}\frac{\partial}{\partial \overline{x}} + \frac{\partial x}{\partial \overline{z}}\frac{\partial}{\partial \overline{z}}\right)\right] \tag{5.55}$$

$$\frac{\partial}{\partial z}\left(\frac{\partial}{\partial z}\right)=\frac{\partial}{\partial z}\left[\frac{1}{J}\left(\frac{\partial x}{\partial \overline{z}}\frac{\partial}{\partial \overline{x}}+\frac{\partial z}{\partial \overline{x}}\frac{\partial}{\partial \overline{z}}\right)\right] \tag{5.56}$$

$$\frac{\partial}{\partial x}\left(\frac{\partial}{\partial z}\right)=\frac{\partial}{\partial x}\left[\frac{1}{J}\left(\frac{\partial x}{\partial \overline{z}}\frac{\partial}{\partial \overline{x}}+\frac{\partial z}{\partial \overline{x}}\frac{\partial}{\partial \overline{z}}\right)\right] \tag{5.57}$$

As in the first transformation, we can use the Cauchy-Riemann conditions to find the terms in the second transformation derivatives. Taking the derivative as to $\overline{y}$ of the equation given in Eq. (5.44),

$$\frac{d}{d\overline{y}}\left(\frac{dy}{d\overline{y}}\right)=\frac{d}{d\overline{x}+i\cdot d\overline{y}}\left(\frac{dx+i\cdot dy}{d\overline{x}+i\cdot d\overline{y}}\right)=\begin{cases} d\overline{x}\to 0 & : -\dfrac{\partial^2 x}{\partial \overline{z}^2}-i\cdot\dfrac{\partial^2 z}{\partial \overline{z}^2}, \\ \\ d\overline{z}\to 0 & : \dfrac{\partial^2 x}{\partial \overline{x}^2}+i\cdot\dfrac{\partial^2 z}{\partial \overline{x}^2}, \end{cases} \tag{5.58}$$

and also taking the first derivatives of Cauchy-Riemann equations,

$$\begin{aligned} &\frac{\partial}{\partial \overline{x}}\left[\frac{\partial x}{\partial \overline{x}}=\frac{\partial z}{\partial \overline{z}}\right], \qquad && \frac{\partial}{\partial \overline{z}}\left[\frac{\partial x}{\partial \overline{x}}=\frac{\partial z}{\partial \overline{z}},\right], \\ &\frac{\partial}{\partial \overline{x}}\left[\frac{\partial z}{\partial \overline{x}}=-\frac{\partial x}{\partial \overline{z}}\right], && \frac{\partial}{\partial \overline{z}}\left[\frac{\partial z}{\partial \overline{x}}=-\frac{\partial x}{\partial \overline{z}}\right]. \end{aligned} \tag{5.59}$$

Considering the results in Eq. (5.58) and Eq. (5.59), then we find the following equations,

$$\begin{aligned} \frac{\partial^2 x}{\partial \overline{x}^2} &= -\frac{\partial^2 x}{\partial \overline{z}^2} = \frac{\partial^2 z}{\partial \overline{x}\partial \overline{z}} = \mathbf{Re}\left[\frac{\partial^2 y}{\partial \lambda^2}\right] = R_2, \\ \frac{\partial^2 z}{\partial \overline{x}^2} &= -\frac{\partial^2 z}{\partial \overline{z}^2} = -\frac{\partial^2 x}{\partial \overline{x}\partial \overline{z}} = \mathbf{Im}\left[\frac{\partial^2 y}{\partial \lambda^2}\right] = I_2, \end{aligned} \tag{5.60}$$

where $\partial^2 y/\partial\lambda^2$ is the second order local derivative of the Schwarz-Christoffel transformation. This is given as follows (Erdun *et al.*, 1996),

$$\frac{\partial^2 y}{\partial\lambda^2} = \frac{1}{\pi}\sum_{i=1}^{n}\left\{\frac{\partial y}{\partial\lambda}\left(\frac{\alpha_i}{\lambda - a_i}\right)\right\}. \tag{5.61}$$

Finally, we find the second order transformation derivatives from physical plane to computational plane.

$$\begin{aligned}
\frac{\partial^2}{\partial x^2} &= \frac{\partial}{\partial x}\left(\frac{\partial}{\partial x}\right)\\
&= \left(2\left[\frac{-R_1R_1(R_1R_2+I_1\ I_2\ )+R_1I_1\ (I_1\ R_2-I_2\ R_1)}{J^3}\right]+\left[\frac{R_1R_2+I_1\ I_2}{J^2}\right]\right)\frac{\partial}{\partial\xi}+\\
&\left(2\left[\frac{I_1\ R_1(R_1R_2+I_1\ I_2\ )-I_1\ I_1\ (I_1\ R_2-I_2\ R_1)}{J^3}\right]+\left[\frac{I_1\ R_2-R_1I_2}{J^2}\right]\right)G\,\frac{\partial}{\partial\eta}+\\
&\left(\frac{R_1R_1}{J^2}\right)\frac{\partial^2}{\partial\xi^2}+\left(G^2\,\frac{I_1\ I_1}{J^2}\right)\frac{\partial^2}{\partial\eta^2}+\left(-2G\,\frac{R_1I_1}{J^2}\right)\frac{\partial^2}{\partial\xi\partial\eta},
\end{aligned} \tag{5.62}$$

$$\begin{aligned}
\frac{\partial^2}{\partial z^2} &= \frac{\partial}{\partial z}\left(\frac{\partial}{\partial z}\right)\\
&= \left(2\left[\frac{-I_1\ I_1\ (R_1R_2+I_1\ I_2\ )+R_1I_1\ (I_1\ R_2-I_2\ R_1)}{J^3}\right]+\left[\frac{R_1R_2+I_1\ I_2}{J^2}\right]\right)\frac{\partial}{\partial\xi}+\\
&\left(2\left[\frac{-I_1\ R_1(R_1R_2+I_1\ I_2\ )-R_1R_1(I_1\ R_2-I_2\ R_1)}{J^3}\right]+\left[\frac{I_1\ R_2-R_1I_2}{J^2}\right]\right)G\,\frac{\partial}{\partial\eta}+\\
&\left(\frac{I_1\ I_1}{J^2}\right)\frac{\partial^2}{\partial\xi^2}+\left(G^2\,\frac{R_1R_1}{J^2}\right)\frac{\partial^2}{\partial\eta^2}+\left(2G\,\frac{R_1I_1}{J^2}\right)\frac{\partial^2}{\partial\xi\partial\eta},
\end{aligned} \tag{5.63}$$

$$\begin{aligned}
\frac{\partial^2}{\partial x\partial z} &= \frac{\partial}{\partial x}\left(\frac{\partial}{\partial z}\right)=\frac{\partial}{\partial z}\left(\frac{\partial}{\partial x}\right)\\
&= \left(2\left[\frac{-R_1I_1\ (R_1R_2+I_1\ I_2\ )+I_1\ I_1\ (I_1\ R_2-I_2\ R_1)}{J^3}\right]-\left[\frac{I_1\ R_2-R_1I_2}{J^2}\right]\right)\frac{\partial}{\partial\xi}+\\
&\left(2\left[\frac{-R_1R_1(R_1R_2+I_1\ I_2\ )+I_1\ R_1(I_1\ R_2-I_2\ R_1)}{J^3}\right]+\left[\frac{R_1R_2+I_1\ I_2}{J^2}\right]\right)G\,\frac{\partial}{\partial\eta}+\\
&\left(\frac{R_1I_1}{J^2}\right)\frac{\partial^2}{\partial\xi^2}+\left(-G^2\,\frac{R_1I_1}{J^2}\right)\frac{\partial^2}{\partial\eta^2}+\left(G\,\frac{R_1R_1-I_1\ I_1}{J^2}\right)\frac{\partial^2}{\partial\xi\partial\eta}.
\end{aligned} \tag{5.64}$$

These transformations provide the following equation

$$\left[\frac{\partial^2}{\partial x^2}+\frac{\partial^2}{\partial z^2}\right]=\frac{1}{J}\left[\frac{\partial^2}{\partial \overline{x}^2}+\frac{\partial^2}{\partial \overline{z}^2}\right]. \tag{5.65}$$

CHAPTER 6

NUMERICAL MODELING

Sets of simultaneous, nonlinear, partial differential equations cannot be solved using known analytic methods, but require numerical methods of computation where the equations are discretized and solved on a lattice. This lattice corresponds to the grid volume defined by Eq. (2.5).

There are several broad classes of solution techniques available to represent terms involving the derivatives in spatial coordinates of these differential equations including:

(1) **Finite difference** schemes, which utilize a form of truncated Taylor series expansion;

(2) **Spectral** techniques in which dependent variables are transformed to wavenumber space using a global basis function (e.g., a Fourier transform);

(3) **Pseudospectral** method which uses a truncated spectral series to approximate derivatives;

(4) **Finite element** schemes, which seek to minimize the error between the actual and approximate solutions using a local basis function; and

(5) **Interpolation** schemes in which polynomials are used to approximate the dependent variables in one or more spatial directions.

In mesoscale models generally only finite difference, finite element, and interpolation schemes have been used. The spectral technique has been shown to be highly accurate (Fox and Deardorff, 1972; Machenhauer, 1979; Orszag, 1971) and eliminates the fictitious feedback of energy to the larger scale called aliasing effects. However, the mathematical expressions that result from the

Fourier transformation are cumbersome to handle and have required periodic boundary conditions to make it work effectively. Thus, this scheme has not found acceptable among mesoscale modelers. The pseudospectral technique has been introduced by Fox and Orszag (1973) and has been contrasted with the spectral technique and conventional finite difference methods by Christensen and Prahm (1976). A brief review of the pseudospectral method is given in Merilees and Orszag (1979). Eliassen (1980) has summarized the uses of these and other representations in air pollution transport modeling. Although the pseudospectral technique appears to be a viable tool for use in mesoscale models, it also has not been adopted (However it is still investigating utility, Lee, 1981; Patrinos and Leach, 1982). The major reason for the neglect of these spectral schemes up to present may be the interest in finite element method and cubic spline interpolation approach, as well as the difficulty in handling non-periodic boundary conditions using either of the spectral techniques.

In the solution of the model we have used the finite-difference schemes due to simplicity of their using. The various finite difference schemes are given in Appendix-A.

6.1 Domain Structure of the Model

The selection of the domain size and grid increments in a mesoscale model are dictated by the dimensionality of the forcing, the spatial scales of the physical response to this forcing, and available computer resources.

In this model, because the model is designed for the shallow convection and meso-β scale, the vertical size of the model domain can be 4 km, and the horizontal size can be up to 200 km.

$$L_x \leq 4km \qquad\qquad L_z \leq 200km$$

In order to test the model, an axisymmetric Gaussian hill shape (called "Witch of Agnesi") for the topography is used for run (Fig 6.1).

$$h(x) = h_\circ \frac{a^2 - x^2}{a^2 + 9x^2} \tag{6.1}$$

where a is the half width of the hill (4000m), and $h_\circ$ the height of the hill (300m).

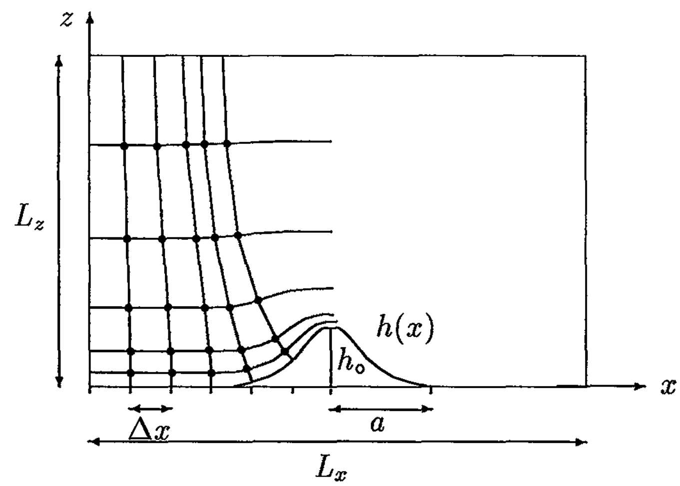

Fig 6.1 A Schematic representation of the structure of domain.

The height of the model L_z is taken to be 4 km, and the length of the domain L_x is 40 km (Fig 6.1). The mountain is centered in a computational domain. The domain has 50 $\times$ 21 grid points. The horizontal grid interval Δx is taken to be 810 m, and the vertical grid interval changes between 10 m and 400 m from the ground to the top since fine-mesh on near the ground and coarse mesh on the upper part of domain are used.

6.2 Initial Data

Local time 08:00 is chosen as the initial time of integration. In order to determine initial wind component in $x-$direction, $\overline{u}^{t_o}$ the following formulations are used.

$$\overline{u}^{t_o}_{(x,z)} = \begin{cases} 0 & \text{for} \quad (z \leq z_o), \\ \left[\dfrac{u_g}{\log(z_g)} \dfrac{\log(z_s)}{z_s}\right] z & \text{for} \quad (z_o < z \leq z_s), \\ \left[\dfrac{u_g}{\log(z_g)}\right] \log(z) & \text{for} \quad (z_s < z \leq z_g), \\ u_g & \text{for} \quad (z_g \leq z \leq L_z), \end{cases} \tag{6.2}$$

where z_o is the roughness height (0.20 m), z_s the surface layer height (100 m), z_g the gradient wind level (1500 m), L_z the top of the domain, and u_g the geostrophic wind component in $x-$direction taken to be constant (2.5 m $\sec^{-1}$) for the model (Fig 6.2).

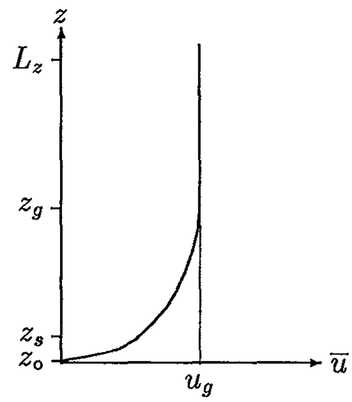

Fig 6.2 Horizontal wind profile used in the model.

The wind component in $y-$direction is assumed to be zero in the simulation.

$$\overline{v}^{t_o}_{(x,z)} = 0.$$

Vertical wind component w is calculated from continuity equation (Eq. 2.1).

$$\frac{\partial}{\partial z}\left(\frac{\partial \overline{u}}{\partial x} + \frac{\partial \overline{w}}{\partial z}\right) = 0. \tag{6.3}$$

After the coordinate transformations, this equation is solved in finite differences by using central scheme in space, and boundary conditions are taken as zero (Fig 6.3).

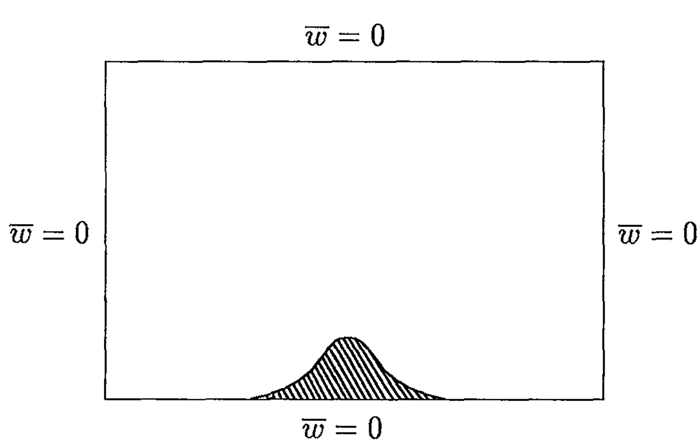

Fig 6.3 Boundary conditions for the calculation of initial vertical wind speed.

For initial temperature field, we are used a linear change with height. This change is denoted by γ in the equations.

$$\theta_s^{t_o}(z) = \theta_g + \gamma z, \tag{6.4}$$

where θ_g is the potential temperature on the ground, and taken to be $298°K$ and $\gamma = 0.5/100m$. Also temperature distribution of domain is $\theta_g < \theta_1 < \theta_2 < \cdots < \theta_{n-1} < \theta_n$ (Fig 6.4).

As this equation cold air at lower levels in the approach flow is pushed up the slope by the winds because the initial time is 08:00 local time (Banta, 1990).

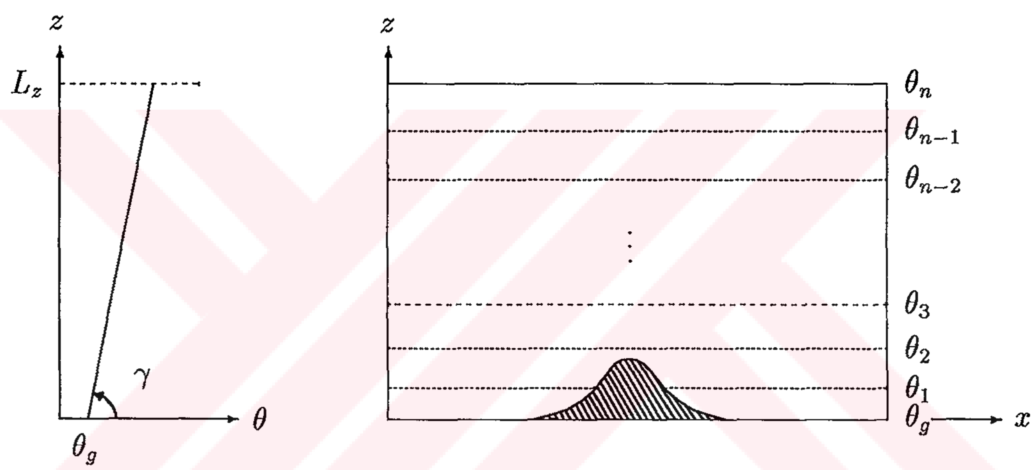

Fig 6.4 Initial potential temperature profile.

For the potential temperature perturbation field a linear change are assumed

$$\theta'^{t_o}_{(z)} = \theta'_g(-z/L_z + 1.), \tag{6.5}$$

where θ'_g is the potential temperature perturbation on the ground taken to be 1°C. At the top of domain, we assume $\theta' = 0$, thus implying that horizontal potential temperature structure does not change at the top of our model.

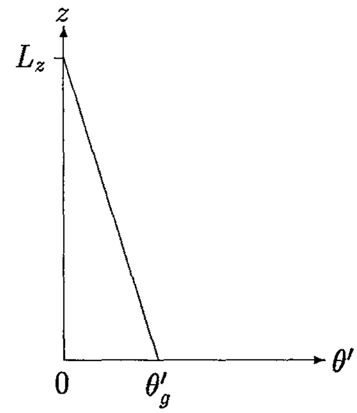

Fig 6.5 Initial potential temperature perturbation profile.

Initial pressure perturbation field is assumed to be zero.

$$p'^{\,t_o}_{(x,z)} = 0. \tag{6.6}$$

Initial subgrid scale eddy mixing coefficient $K_m(x,z)$ over the ground is calculated from the initial wind field given by Eqs (6.2) and (6.3). The lower boundary for K_m is zero.

6.3 Boundary Conditions

The only boundary for atmospheric models where physical boundary conditions can be formulated is the surface. All other boundaries are artificial. The formulation of these boundary conditions is dictated by the requirement that the interior flow be only marginally influenced by the treatment and position of these boundaries.

Boundary conditions for the horizontal component of wind speed is given in Fig 6.6. Lower boundary for wind is zero due to kinematic condition. Top boundary is taken as the value of geostrophic wind which is invariant with time. Left lateral boundary is taken to be as in initial horizontal wind field, which is also invariant with time. For the right lateral boundary, cyclic condition are used.

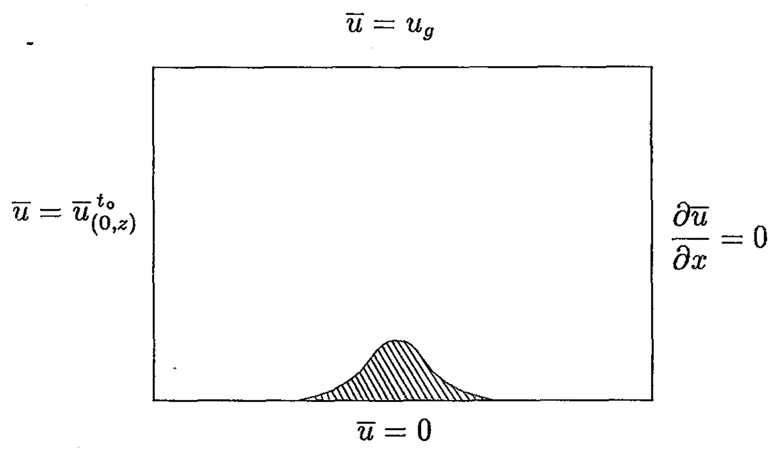

Fig 6.6 Boundary conditions for $\overline{u}$ wind component in $x-$direction.

Boundary conditions for the vertical component of wind speed is given in Fig 6.7. Lower boundary for vertical wind is zero due to kinematic condition. Top and right lateral boundaries are taken as cyclic conditions, i.e., normal derivatives are zero. Left lateral boundary is taken to be as in initial vertical wind field, which is invariant with time.

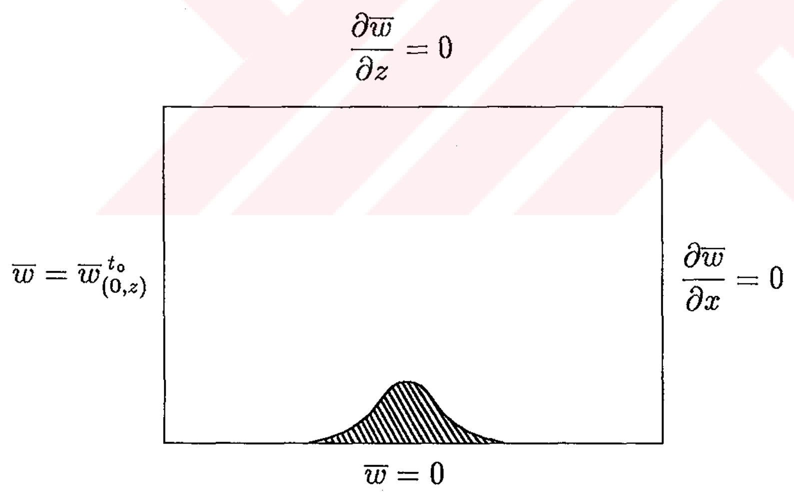

Fig 6.7 Boundary conditions for $\overline{w}$ wind component in $x-$direction.

For the potential temperature perturbation, boundaries except top boundary are taken as cyclic conditions (normal derivatives are zero). On top boundary potential temperature perturbation is assumed zero because there is no effect on the horizontal temperature structure at the top of our model (Fig 6.8).

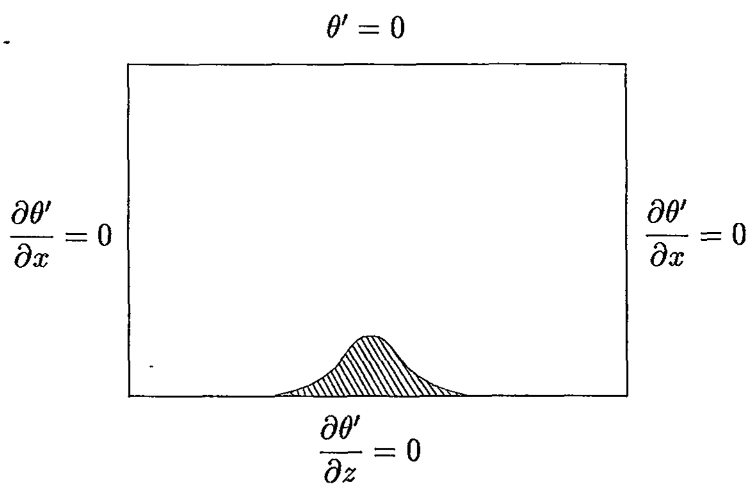

Fig 6.8 Boundary conditions for potential temperature perturbation.

In order to define boundary conditions for perturbation pressure are defined by following assumptions.

The normal velocity components, i.e. u at $x = L_x$ and w at $z = L_z$, are treated analogously

$$
\begin{aligned}
&\frac{\partial^2 \overline{u}}{\partial x^2} = 0, \\
&\frac{\partial^2 \overline{w}}{\partial z^2} = 0.
\end{aligned}
\tag{6.7}
$$

Outflow boundary conditions for the perturbation pressure are specified upon the requirement that mass conservation is strictly observed, i.e.

in 3-D

$$\iiint_V [\overline{u}(L_x, y, z) - \overline{u}(0, y, z)] + [\overline{v}(x, L_y, z) - \overline{v}(x, 0, z)] + [\overline{w}(x, y, L_z) - \overline{w}(x, y, 0)]\Big\} \, dV = 0, \tag{6.8}$$

and in 2-D it can be reduced to

$$\iint_S \Big\{ [\overline{u}(L_x, z) - \overline{u}(0, z)] \;+\; [\overline{w}(x, L_z) - \overline{w}(x, 0)] \Big\} \, dS = 0, \tag{6.9}$$

where $V = (L_x L_y L_z)$ and $S = (L_x L_z)$ is the volume and the area of the atmospheric domain, respectively.

In 2-D, the integral can be splited up to give

$$L_x \int_{z=0}^{z=L_z} [\overline{u}(L_x, z) - \overline{u}(0, z)]\, dz \;+\; L_z \int_{x=0}^{x=L_x} [\overline{w}(x, L_z) - \overline{w}(x, 0)]\, dx \;= 0. \qquad (6.10)$$

where $\overline{w}(x,0) = 0$ due to kinematic condition.

The horizontal velocity components at the outflow boundaries $\overline{u}(L_x, z)$ and $\overline{w}(x, L_z)$, are eliminated by use of Eq. (4.23) which reads in component form

$$\begin{aligned} \overline{u}^* &= \overline{u} + \frac{\Delta t}{\rho_o}\frac{\partial p'}{\partial x}, \\ \overline{w}^* &= \overline{w} + \frac{\Delta t}{\rho_o}\frac{\partial p'}{\partial z}. \end{aligned} \qquad (6.11)$$

Using these Eq. (6.11) and rearranging terms, one obtains from Eq. (6.10)

$$L_x \int_{z=0}^{z=L_z} [\overline{u}^*(L_x, z) - \overline{u}(0, z)]\, dz \;+\; L_z \int_{x=0}^{x=L_x} [\overline{w}^*(x, L_z)]\, dx \;= \frac{\Delta t}{\rho_o}\left\{ L_x \int_{z=0}^{L_z} \left.\frac{\partial p'}{\partial x}\right|_{x=L_x} dz \;+\; L_z \int_{x=0}^{L_x} \left.\frac{\partial p'}{\partial z}\right|_{z=L_z} dx \right\} \qquad (6.12)$$

In order to evaluate the right hand side of Eq. (6.11) the following conditions for the tangential velocities may be advantageously employed

$$\left.\frac{\partial \overline{w}^*}{\partial x}\right|_{x=L_x} = \left.\frac{\partial \overline{w}}{\partial x}\right|_{x=L_x}, \quad \text{and} \quad \left.\frac{\partial \overline{u}^*}{\partial z}\right|_{z=L_z} = \left.\frac{\partial \overline{u}}{\partial z}\right|_{z=L_z}. \qquad (6.13)$$

Comparison of Eq. (6.13) and Eq. (6.11) implies that the perturbation pressure gradients are constant on the corresponding outflow surfaces:

$$\left.\frac{\partial}{\partial x}\frac{\partial p'}{\partial z}\right|_{z=L_z} = 0, \quad \text{and} \quad \left.\frac{\partial}{\partial z}\frac{\partial p'}{\partial x}\right|_{x=L_x} = 0. \qquad (6.14)$$

Substituting Eq. (6.14) into Eq. (6.12) then gives

$$L_x \int_{z=0}^{z=L_z} [\overline{u}^*(L_x, z) - \overline{u}(0,z)]\, dz \;+\; L_z \int_{x=0}^{x=L_x} [\overline{w}^*(x, L_z)]\, dx \;=\; \frac{\Delta t}{\rho_\circ}(L_x L_z)\left\{ \left.\frac{\partial p'}{\partial x}\right|_{x=L_x} + \left.\frac{\partial p'}{\partial z}\right|_{z=L_z} \right\} \tag{6.15}$$

In the case of homogeneity in one of the horizontal directions, one of the terms on each side of Eq. (6.15) will vanish separately. Therefore, it seems appropriate to decompose Eq. (6.15) as

$$\begin{aligned} \frac{\partial p'}{\partial x} &= \frac{\rho_\circ}{\Delta t\, L_z} \int_{z=0}^{L_z} [\overline{u}^*(L_x, z) - \overline{u}(0,z)]\ dz \\ \frac{\partial p'}{\partial z} &= \frac{\rho_\circ}{\Delta t\, L_x} \int_{x=0}^{L_x} [\overline{w}^*(x, L_z)]\ dx \end{aligned} \tag{6.16}$$

For arbitrary oriented flow, there is no unique way to satisfy Eq. (6.15). Since the flow is assumed to be homogeneous along the entire inflow boundaries, however, Eq. (6.16), will approximately hold true in any case. Furthermore, this formulation always ensures mass conservation.

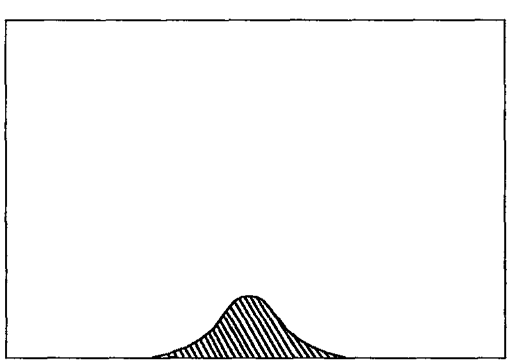

Fig 6.9 Boundary conditions for pressure perturbation.

Cyclic conditions are used for subgrid scale eddy mixing coefficients K_M on lateral and top boundaries. Lower boundary is defined with zero mixing coefficient due to zero wind speed (Fig 6.10).

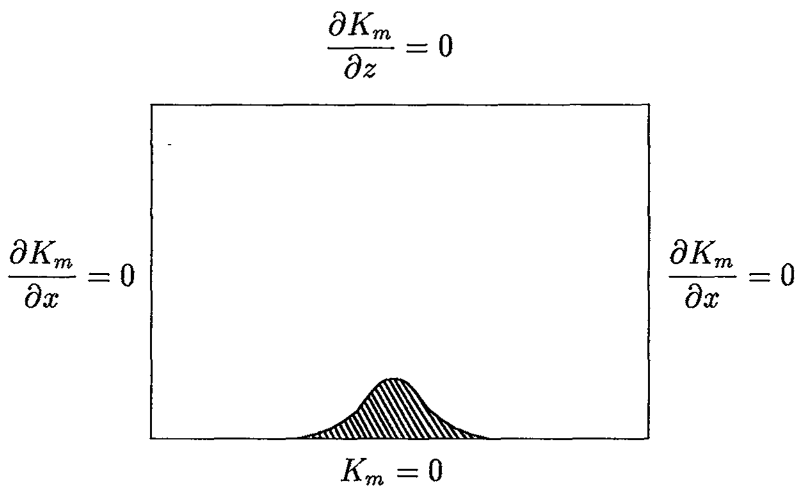

Fig 6.10 Boundary conditions for subgrid scale eddy mixing coefficients K_m.

6.4 Finite Difference Schemes Used in Discritization of the Model Equations

Different finite difference schemes are used in the solutions of the model equations. For time terms of equations, forward scheme are used in initial, and leapfrog scheme are used for the next time steps (see, Appendix-A).

In general, central scheme is used for space derivatives except those in advection terms of momentum equation. In advection term, upwind differencing scheme is used (see, Appendix-A).

In the solution of pressure perturbation gradient, centered space scheme with second order in space is used.

Using these schemes the model equations are solved implicitly in matrix system. In solving of the matrix system in the form of $[A][X] = [B]$, Givens algorithm which is one of general solution method for linear equations systems is used (Kadıoğlu, 1996).

For wind components $\overline{u}$, and $\overline{w}$, matrix structure has the following 5-band form :

$[A] =$ 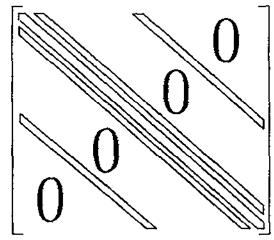

3-band matrix structure for pressure perturbation;

$[A] =$ 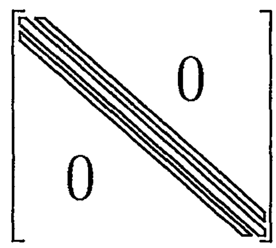

5-band matrix structure for potential perturbation;

$[A] =$ 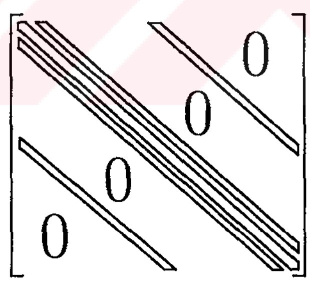

6.5 Stability Criteria

Attempts to solve partial differential equations by finite-difference methods often end in disaster. A finite-difference equation may have a rapidly growing and oscillating solution that in no way resembles the solution expected from the differential equation. In such a situation the difference equation is said to be *computational unstable.*

In order to save the stability of computations in the model the following criteria is used:

$$2K_m \frac{\Delta t}{\mathrm{Min}(\Delta x, \Delta z)^2} < \frac{1}{4}. \tag{6.17}$$

The time step is taken to be 2.5 sec to solve the model equations.

CHAPTER 7

RESULTS AND DISCUSSION

Conventionally, modeling of an atmospheric phenomenon over a complex topography is achieved through usage of a non-orthogonal grid system. This stems mainly from the fact that a non-orthogonal system (for example, terrain-following height coordinate system) instead of an orthogonal one is more suitable for development of a computer code. However, the non-orthogonality leads to considerable errors in especially the calculation of pressure gradient in the lower atmosphere where the slopes of topography are not much less than 45 degrees. Furthermore, additional terms in transformed equations pave way to an increase in computational time as compared to solution of original equations on an orthogonal grid.

Herein, Schwarz-Christoffel transformation is used to eliminate the above mentioned problems. This transformation allows generation of an orthogonal grid over topography with any arbitrary slope and scale. The atmospheric flow model is designed to be two-dimensional. Formulations are based on the shallow convection system and the meso-beta scale. The model under the anelastic and incompressibility assumptions includes the non-hydrostatic and the buoyancy terms in addition to geostrophic and Coriolis terms. For turbulence model, Smagorinsky and Lilly's subgrid scale mixing formulations are conveniently written by means of finite difference schemes in 2-D. Radiative processes and PBL (Planetary Boundary Layer) parameterizations are not used. The perturbation pressure field is calculated by using the diagnostic Poisson equation.

In order to test the model, a modified form of *"Witch of Agnesi"* mountain profile is used (Fig 7.1). This mountain is steeper than the original profile, and it is centered in a computational domain having a width of 40 km and a height of 4 km. The domain has 50×21 grid-points. The horizontal grid interval is 810 m, and time step is taken to be 2.5 sec from Eq. (6.17). Model outputs for the sample topography are presented in Fig 7.2-7.25.

A satisfactory description of turbulent airflow over mountains requires an understanding of the magnitude of the perturbation pressure in the atmosphere. The calculated perturbation pressure (P') fields have been shown in Fig 7.2-7.6. Following an initial field of zero perturbation pressure, a clear difference in the perturbation pressure values for upwind and downwind sides of the mountain occurs in later stages of the simulation. It appears that the perturbation pressure values on upwind side of the mountain are always greater than those on the downwind side (Meroney *et al.*,1978). This result can also be explained with the impulse of the fluid flowing on the upwind side of mountain (Meroney *et al.*, 1978). In earlier steps of the simulation (Fig 7.2- 7.5), positive perturbation pressure values on upwind side and negative perturbation pressure values on the downwind side have been appeared. However, negative pressure values have been disappeared as the flow evolves (Fig 7.6). This can be due to the fact that the mountain height used in the model is not high enough in comparison with the thickness of the approaching boundary layer (Ünal, 1997). Nevertheless, the perturbation pressure values on the upwind side always remain greater than those on the downwind side. The range of calculated perturbation pressure is between -15 mb and 25 mb.

Another important indicator of effects of a particular topography on surrounding turbulent flow field is the actual atmospheric pressure. The actual pressure fields which are found by adding the initial pressure field (P_s) to the calculated perturbation pressure fields (P') have been shown in Fig 7.7-7.11. Since the initial perturbation pressure field is taken to be zero, initial isobaric surfaces are parallel to the sea-level line (Fig 7.7). In later steps of simulation, evolving perturbation pressure field lead to high and low pressures on the upwind and downwind sides correspondingly (Fig 7.8-7.11). A downward bending of isobaric surfaces appears on downwind side due to different perturbation regimes between upwind and downwind side of the mountain (Fig 7.8-7.11). This bending and the upwind tilt of the lines of constant phase (Fig 7.11) are amongst the fundamental indicators of mountain effect (Durran, 1990). High and low surface pressure fields on the upwind and downwind sides of a mountain generate a downwind drag force on that mountain. The drag values of Durran's (1990) three-dimensional simulation for "*Witch of Agnesi*" mountain profile are compared as function of nondimensional mountain height with those computed through the present model for the modified form of Durran's mountain profile (Fig 7.12). The present values are larger probably due not only to the fact that the modified mountain is steeper but also the present simulation is two-dimensional. However, the qualitative agreement is reasonable and thus points to the fact that the calculated surface pressure distributions are at least globally realistic.

Subgrid-scale mixing coefficient K_m is calculated by Smagorinsky (1963) and Lilly (1965) formulation which includes atmospheric stability and wind-shears. Calculated K_m fields have been shown in Fig 7.13-7.17. The range of calculated K_m in the model is $0.001 - 2m^2/sec$. These values indicate that the atmosphere is stable. According to the given initial data, in the first step of the simulation a maximum K_m region appears on top of the mountain (Fig 7.13). In the following steps this maximum region moves to downwind side by the effect of advection and increasing total-deformation in the downwind side (Fig 7.14- 7.16). Eventually, the maximum region is broken into pieces (Fig 7.17) due to flow separation (see Fig 7.18-7.21) and variation in total deformation, and the magnitude of the maximum increases due to increasing total deformation. According to wind fields given in Fig 7.18-7.21 with mentioned above comments, wind fields have been modeled well in global meaning for the given topography.

Since the model doesn't include a radiation module, temperature field is affected only by the advective terms. The temperature field is chosen to be cold air at lower levels in thermic-stable atmosphere in order to assure that turbulence is generated by only the wind influence in the model (Banta, 1990). However, an artificial perturbation is added to initial temperature field as that in availability of radiation module in order to see the effects of advective and buoyancy terms in the model (Fig 7.22). In doing that, maximum perturbation temperature is chosen to be $1°C$ on the ground. During the simulated flow development, there are no important changes in the magnitude of perturbation potential temperature field, and perturbation temperature field is moved in direction of the fluid flowing due to advective terms (e.g. Fig 7.23). Of course, in absence of an initial perturbation potential temperature field (i.e., zero perturbation), it is not possible to see the combined effect of the advection and the buoyancy in the present model. This case is also evident in actual potential temperature fields found by adding perturbation potential temperature field to the initial potential temperature field (Fig 7.24 and 7.25). According to Fig 7.24 and 7.25, there is not a major turbulence generation due only to temperature effect but some low order fluctuations. These are expected to be important especially in influence of the buoyancy term when radiation module is added to the model. Results show that the model gives realistic results for the given sample topography.

In the future work, the model can be advanced to simulate other atmospheric parameters by adding extra formulations and by changing the model assumptions as follows:

(1) It can be used to model the gravity waves in upper atmosphere by changing the shallow system to the deep convection system.

(2) It can be used for the dispersion and transportation of pollutants by adding the transport and concentration equations.

(3) Cloud and fog formations due to topographical effects can be modeled by adding the conservation of water vapor equation, heat equation and radiation processes.

(4) Land-sea breeze interaction and effects of lakes on mountainous regions can be examined by adding the conservation of water vapor and heat equations, and radiation processes.

(5) It can be used partly for site-selection of wind-turbine in the field of wind energy.

(6) The model also can be advanced to 3-D by collecting the grid meshes generated by Schwarz-Chistoffel transformation, ordering in y-direction, and then jointing by terrain-following height coordinate transformation (Fig 7.26).

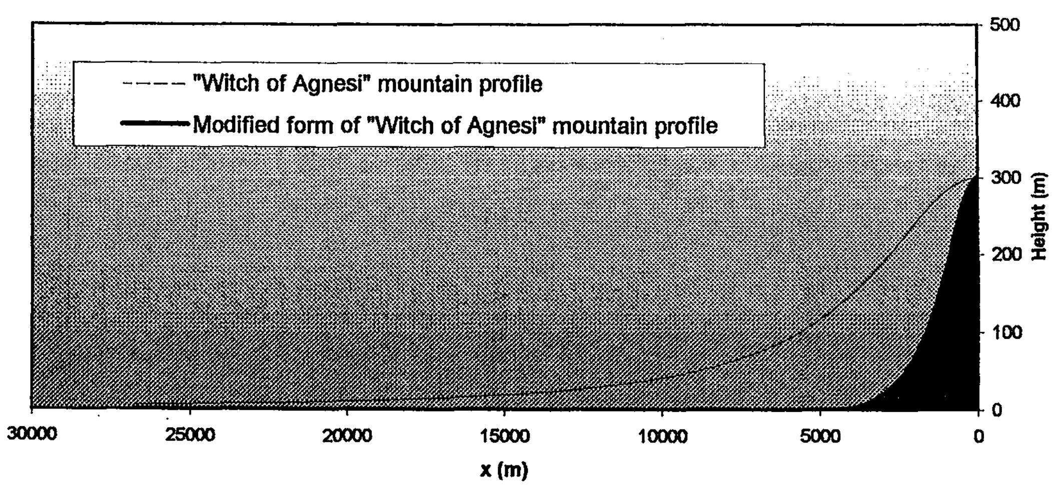

Fig 7.1 The topography used in the model (thick line), and "Witch of Agnesi" mountain profile (thin line).

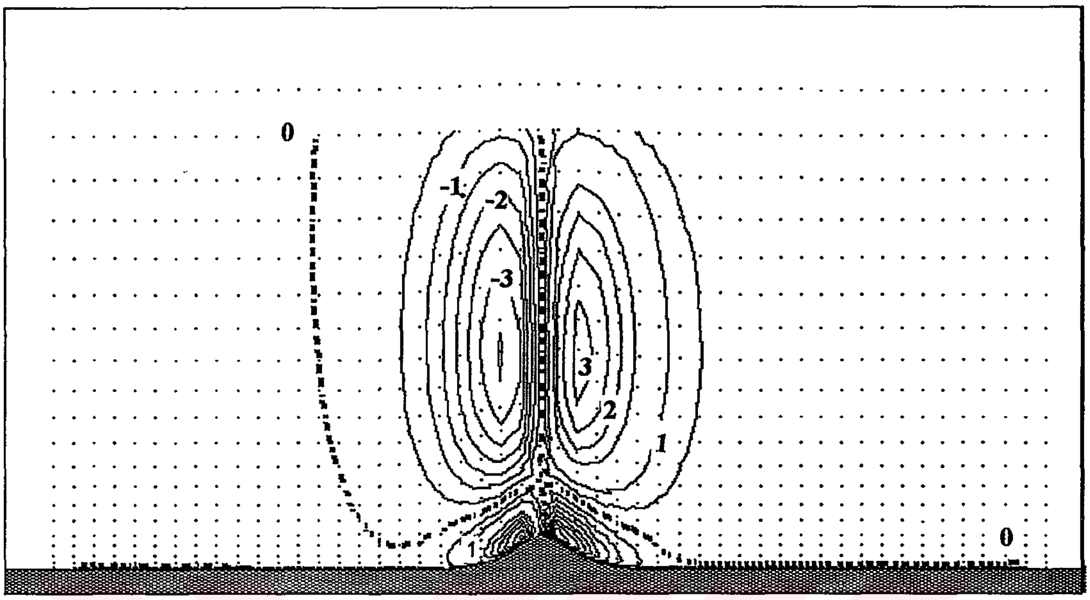

Fig 7.2 Perturbation pressure field at step=2.

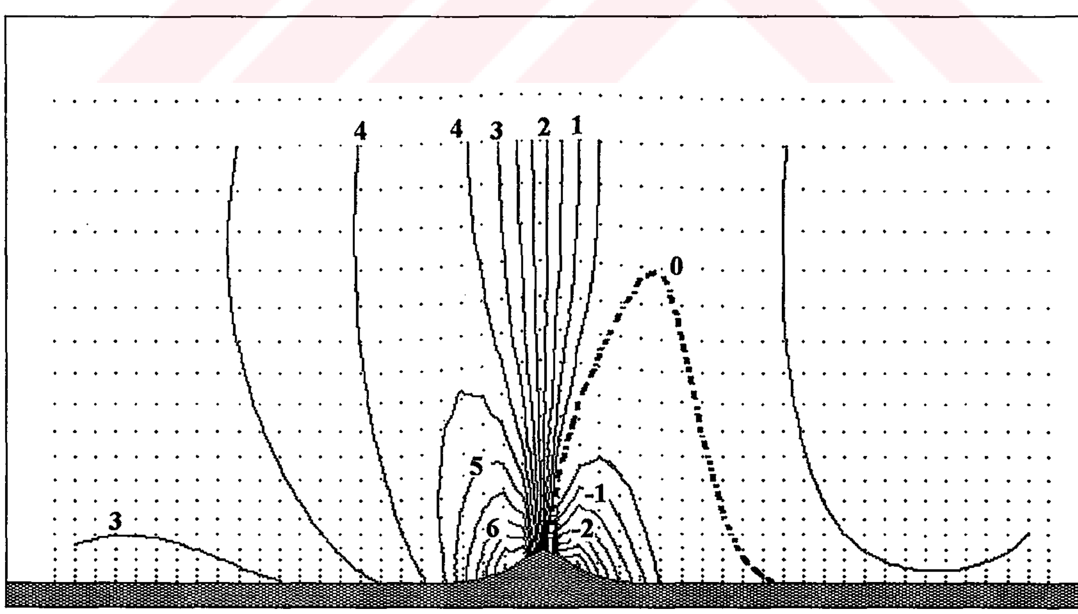

Fig 7.3 Perturbation pressure field at step=120.

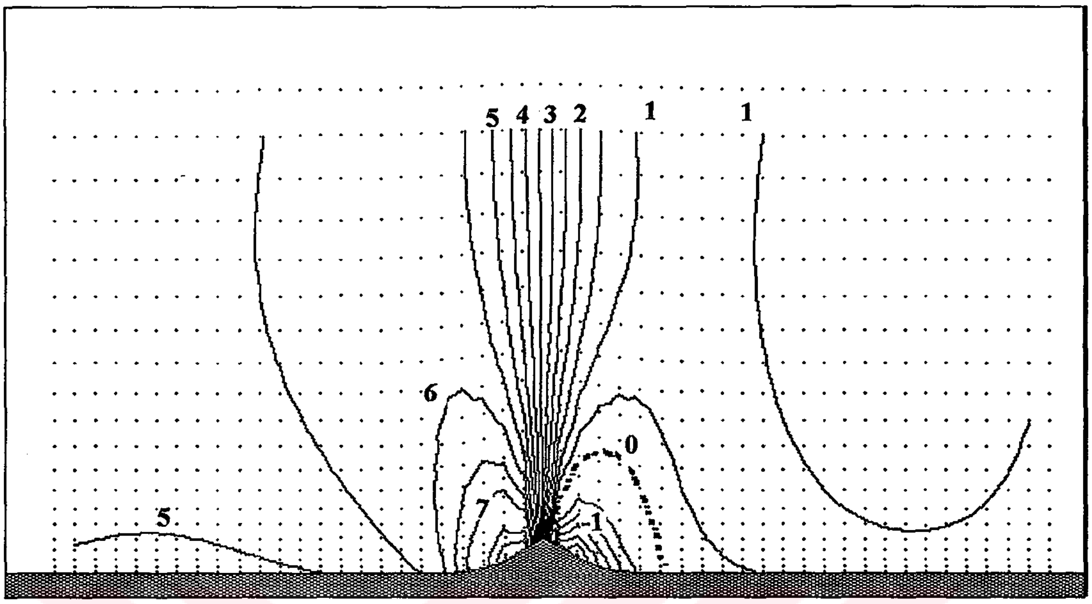

Fig 7.4 Perturbation pressure field at step=200.

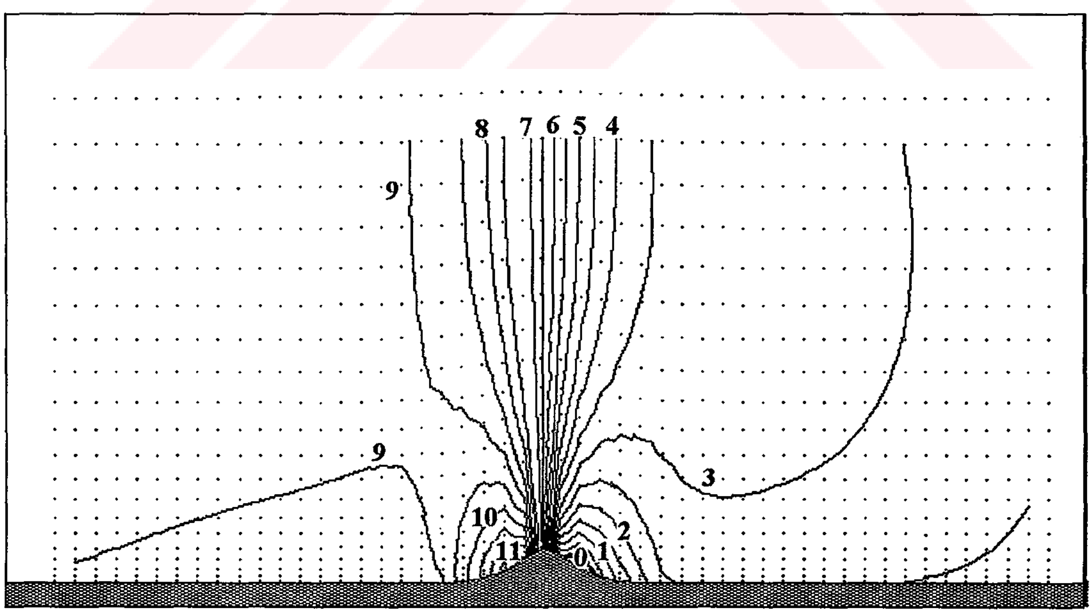

Fig 7.5 Perturbation pressure field at step=400.

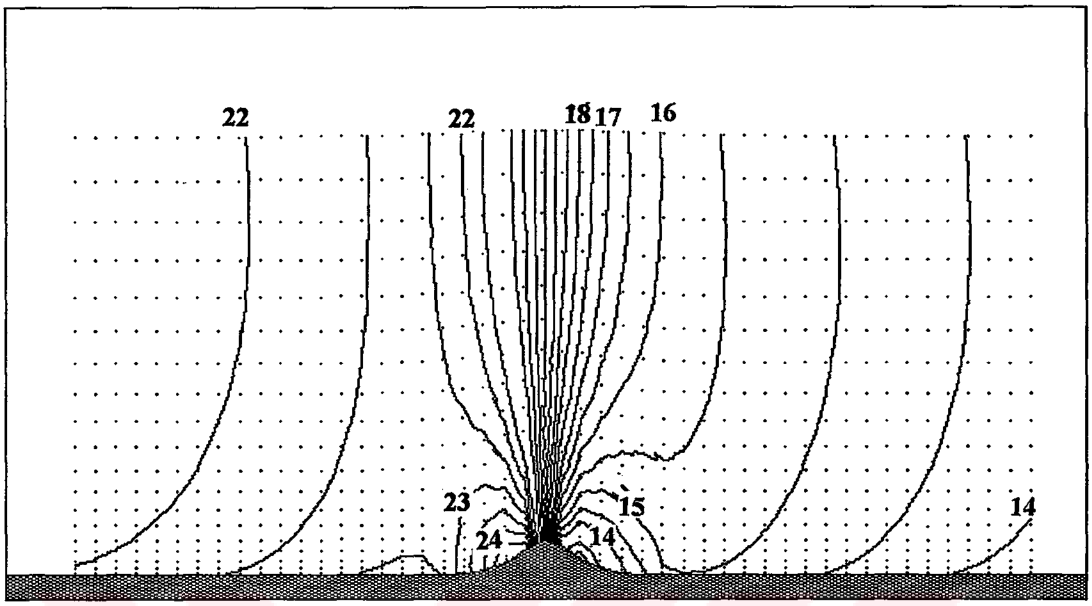

Fig 7.6 Perturbation pressure field at step=1250.

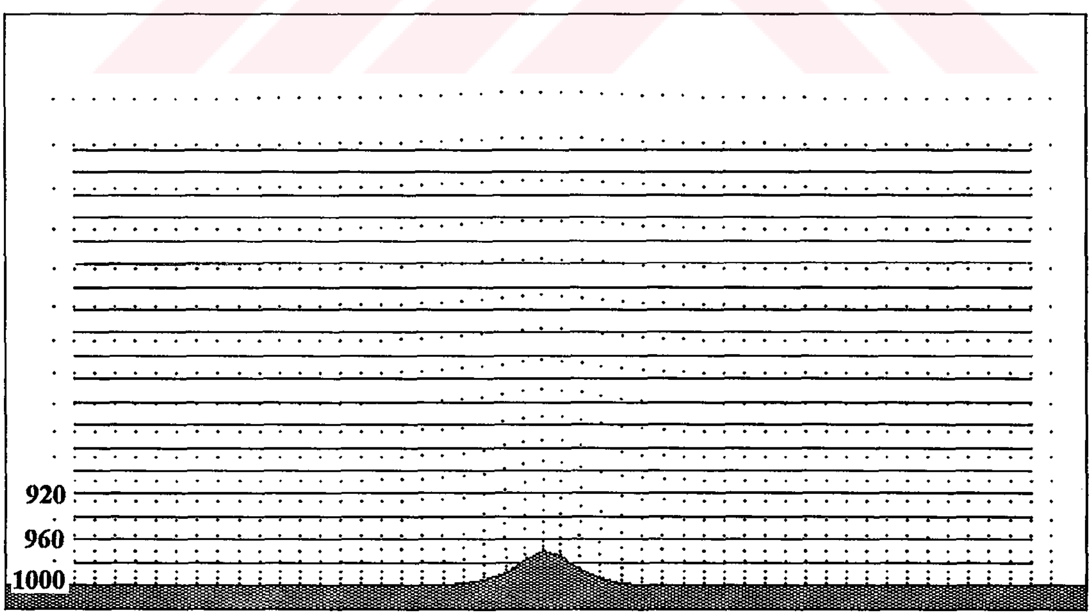

Fig 7.7 Initial pressure field.

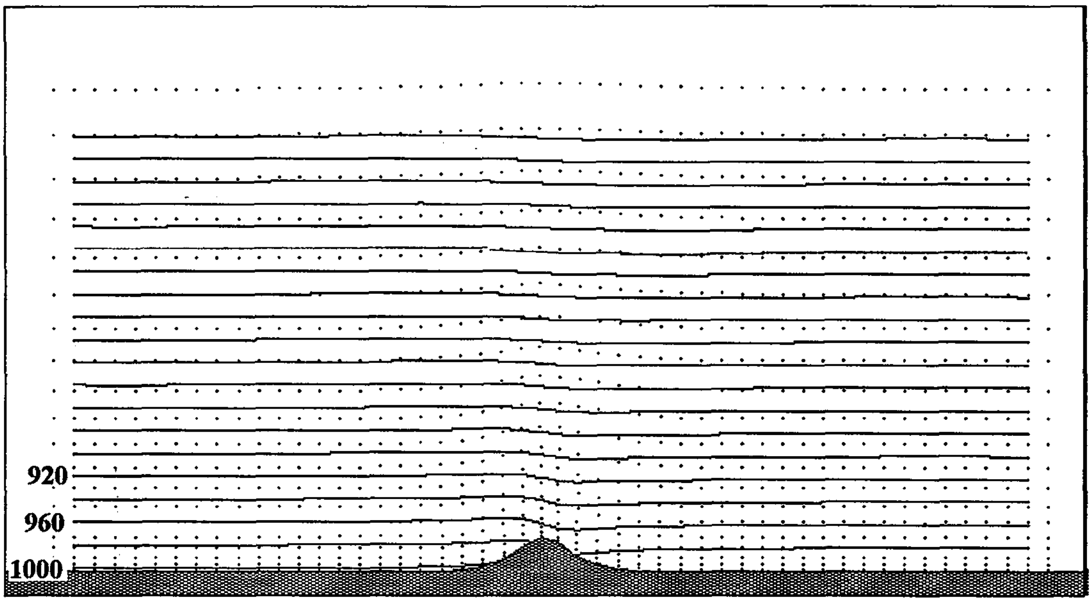

Fig 7.8 Pressure field at step=120.

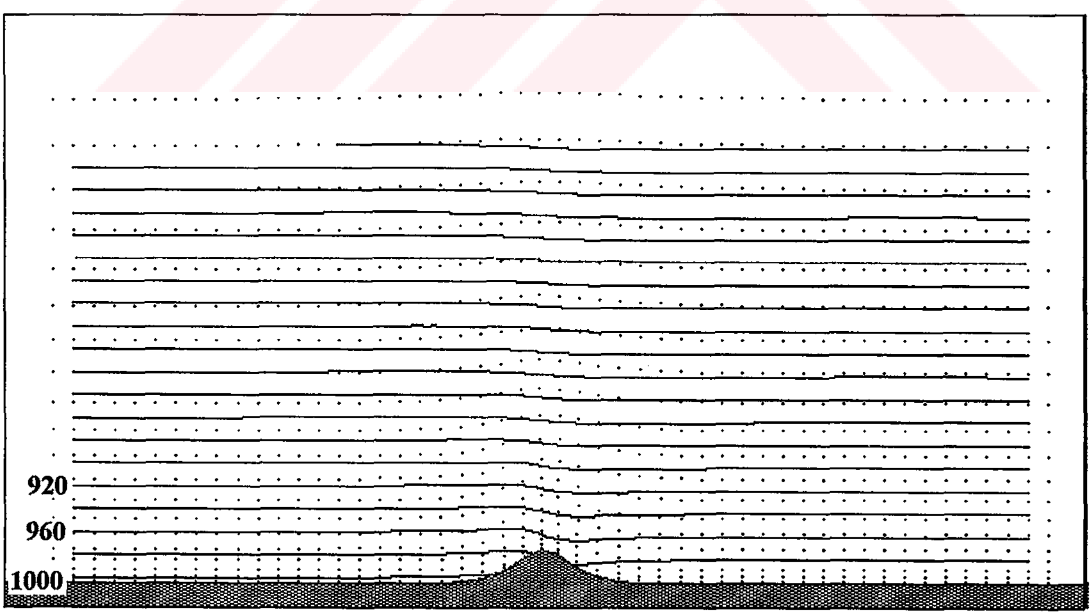

Fig 7.9 Pressure field at step=200.

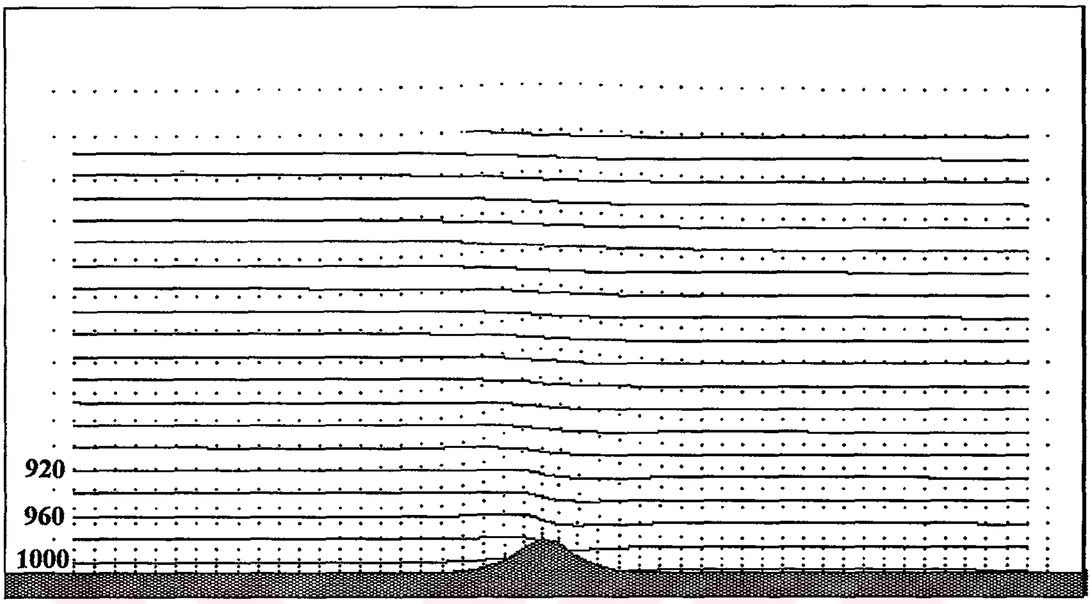

Fig 7.10 Pressure field at step=400.

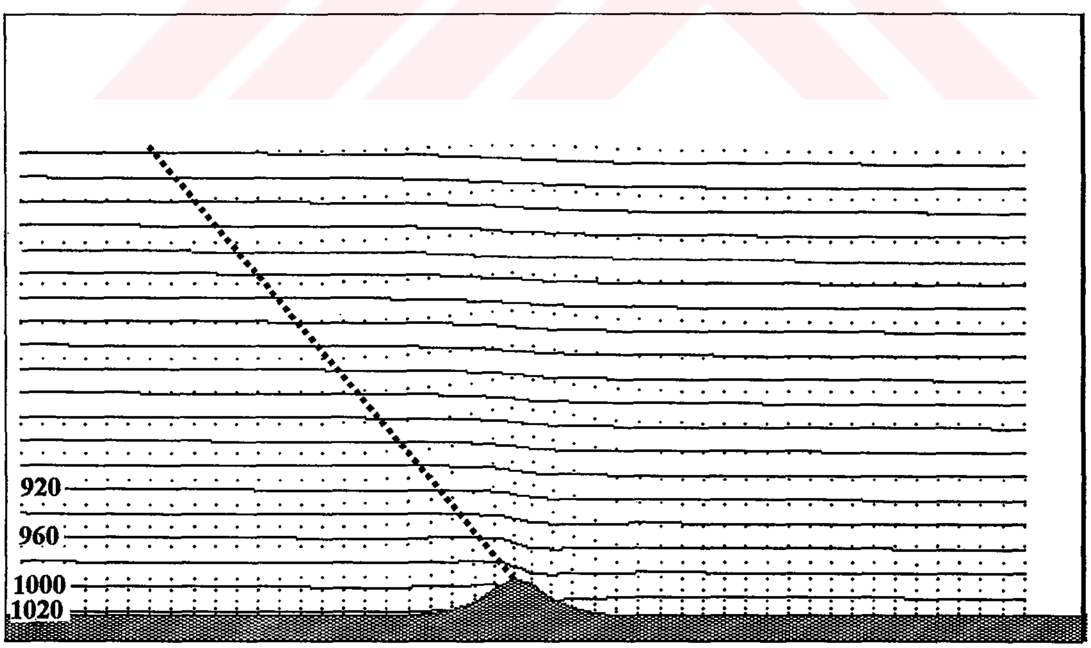

Fig 7.11 Pressure field at step=1250. The dashed line shows the upstream tilt of the lines of constant phase.

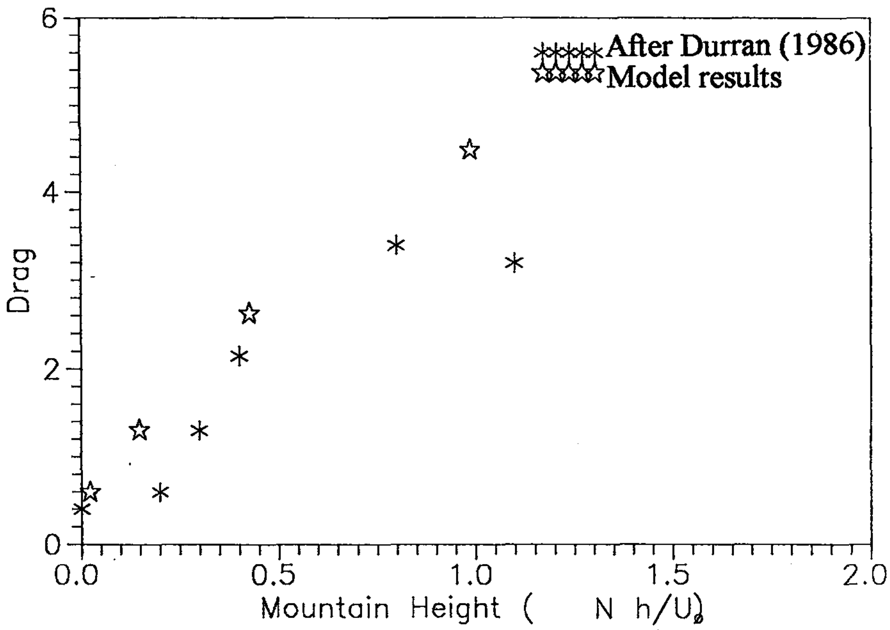

Fig 7.11 Pressure drags as a function of nondimensional mountain height Nh/u_o by Durran's (1986) mountain profile and the model. The drag is normalized by $\pi\rho N u_o h_m^2/4$ where ρ, u_o, and N are evaluated at the surface for stable atmosphere.

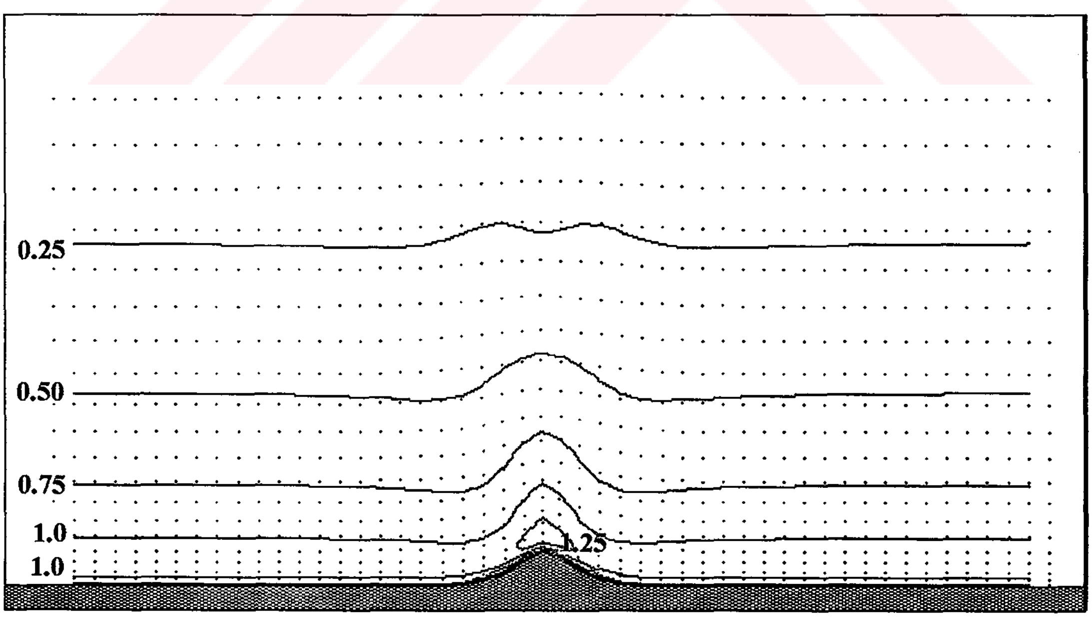

Fig 7.13 Subgrid-scale mixing coefficient field K_m at step=2.

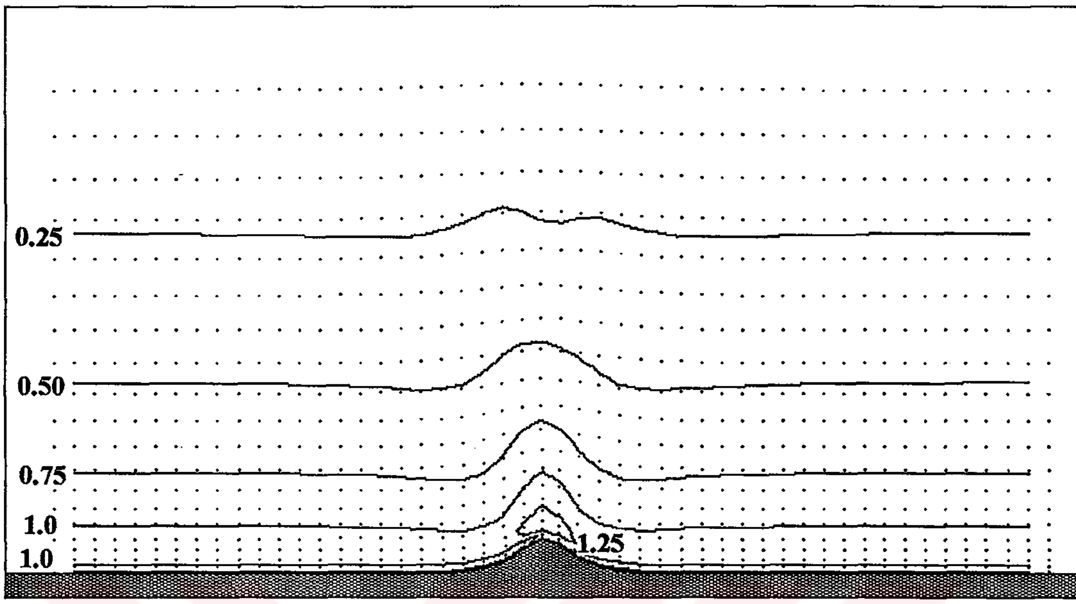

Fig 7.14 Subgrid-scale mixing coefficient field K_m at step=120.

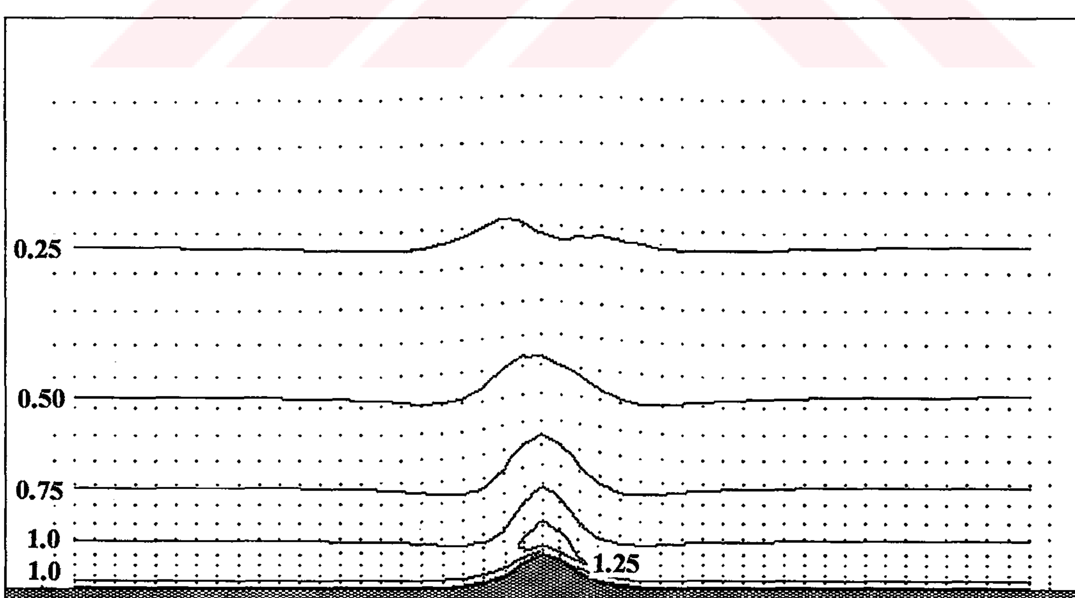

Fig 7.15 Subgrid-scale mixing coefficient field K_m at step=200.

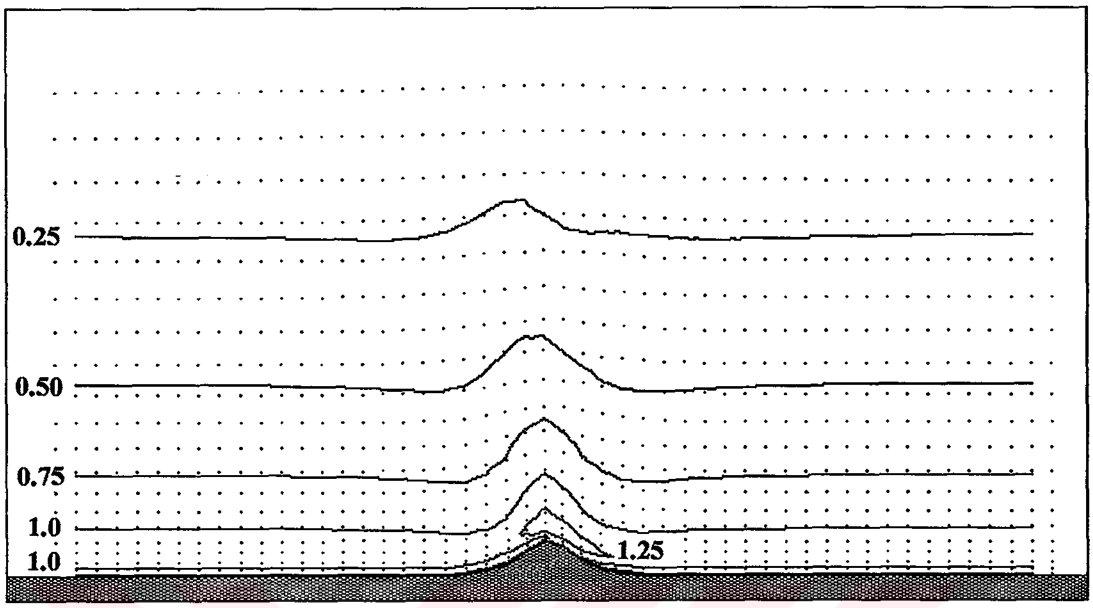

Fig 7.16 Subgrid-scale mixing coefficient field K_m at step=400.

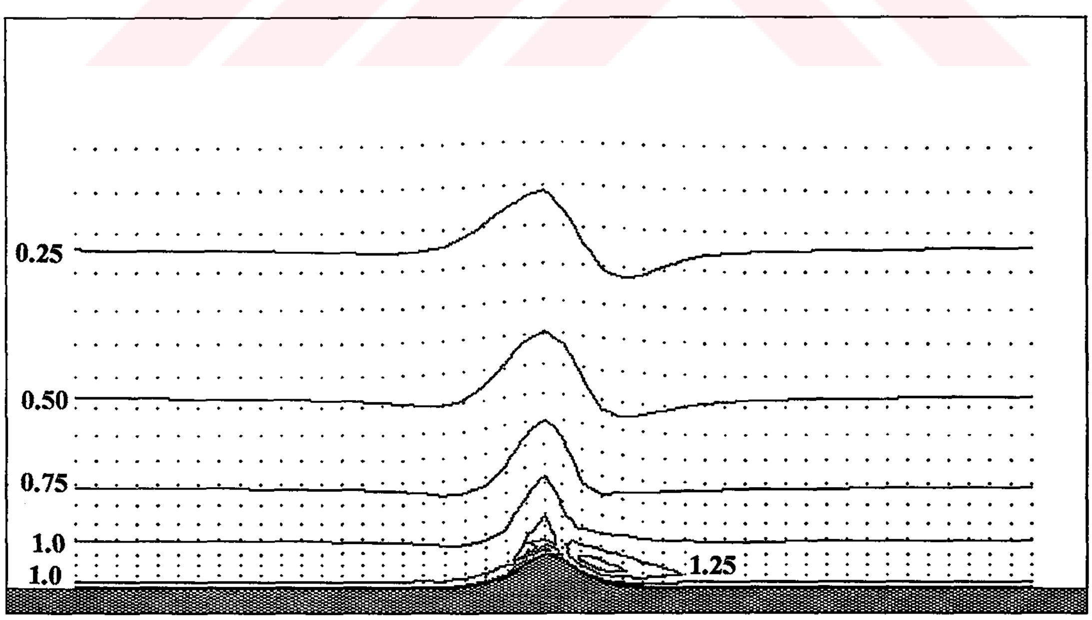

Fig 7.17 Subgrid-scale mixing coefficient field K_m at step=1250.

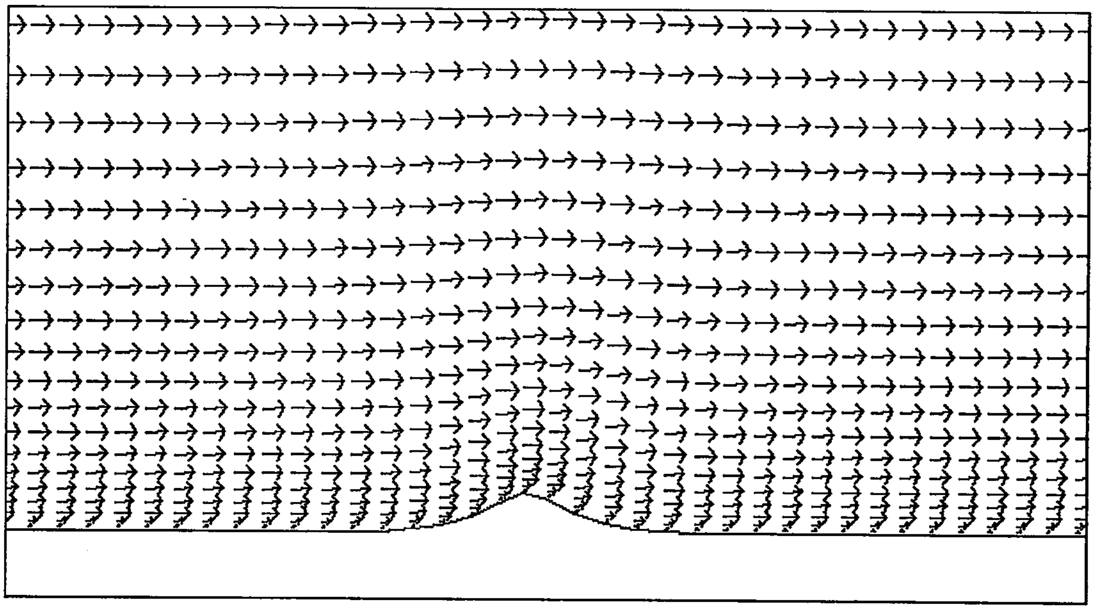

Fig 7.18 Wind field at step=10.

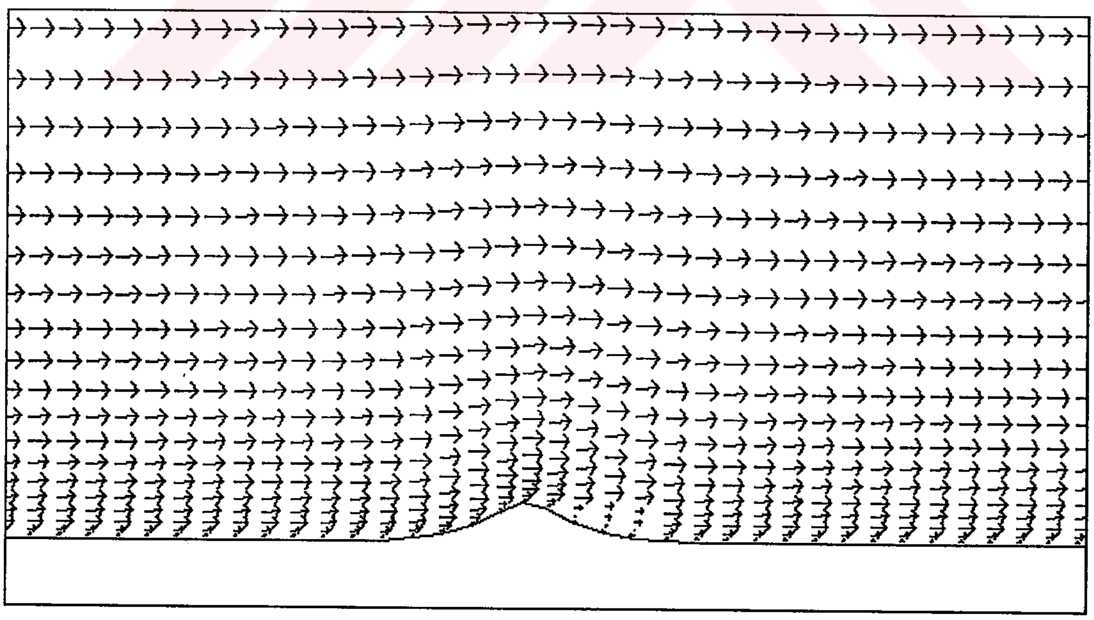

Fig 7.19 Wind field at step=200.

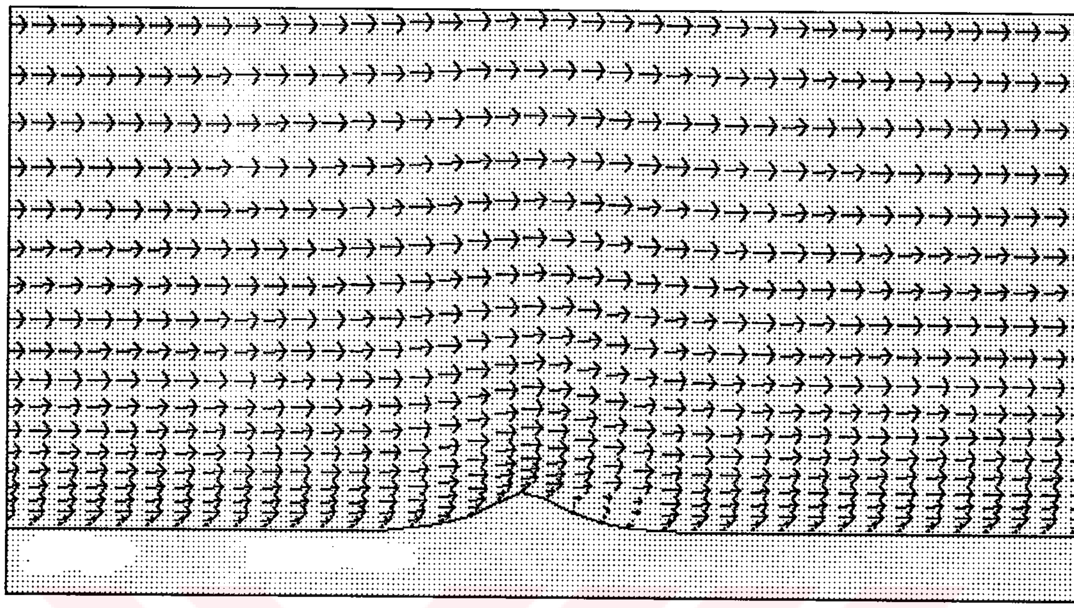

Fig 7.20 Wind field at step=400.

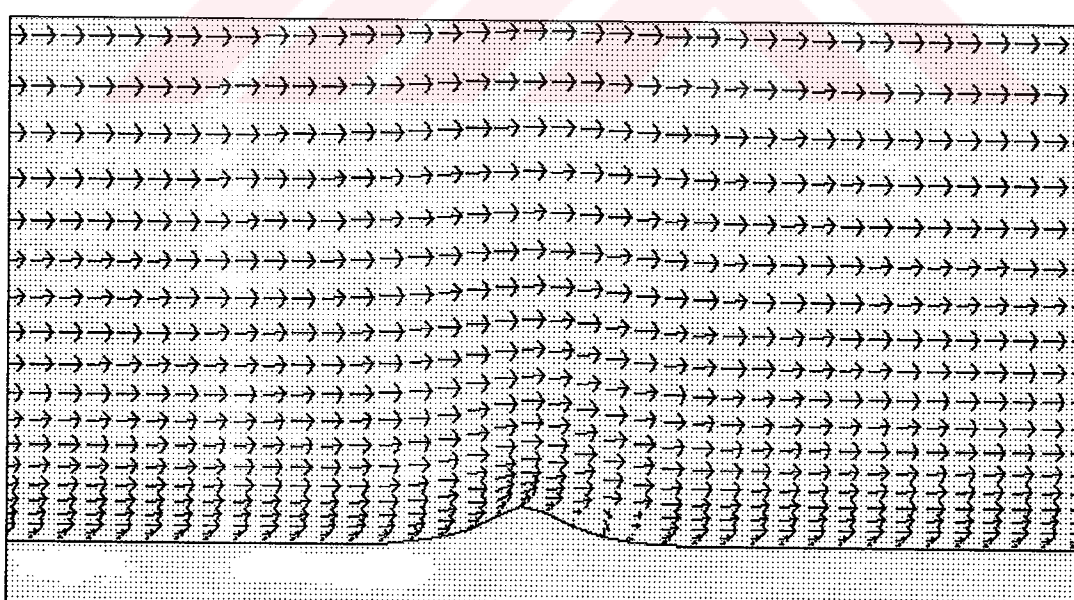

Fig 7.21 Wind field at step=1250.

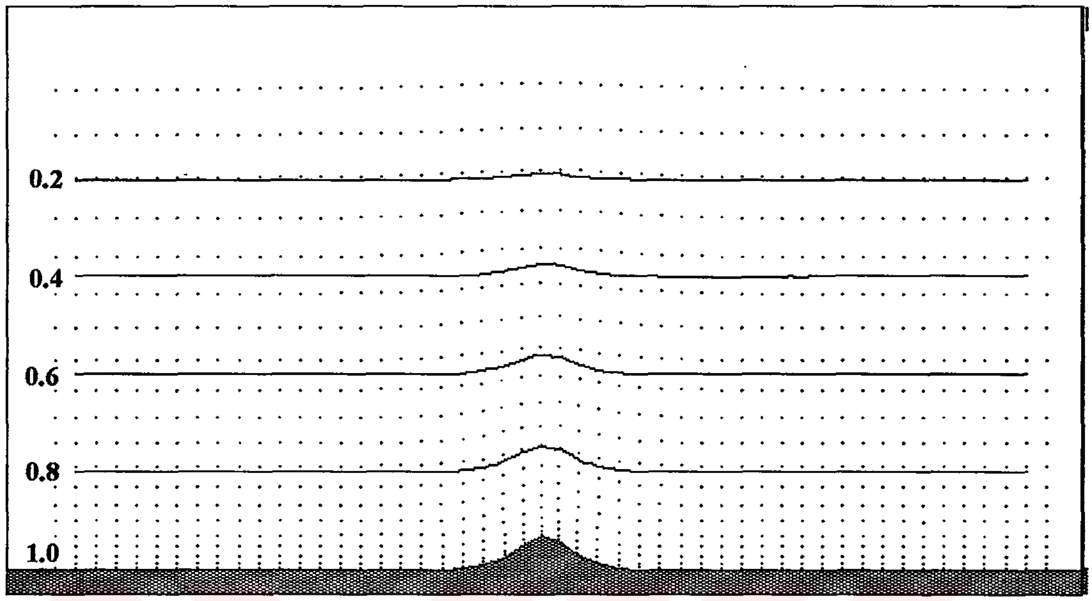

Fig 7.22 Perturbation potential temperature field at step=2.

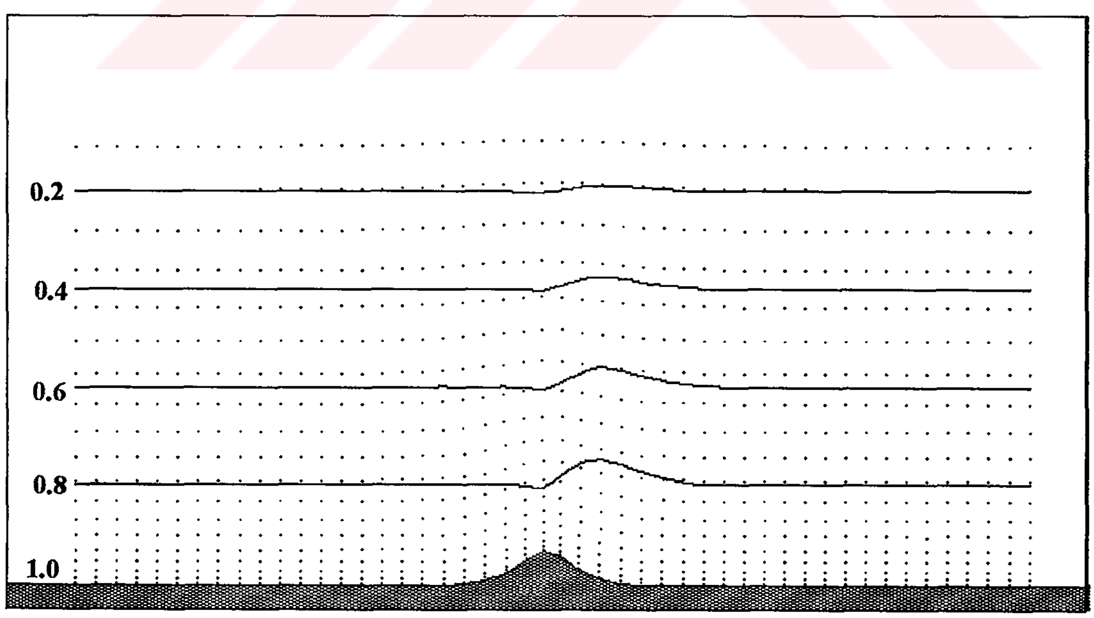

Fig 7.23 Perturbation potential temperature field at step=1250.

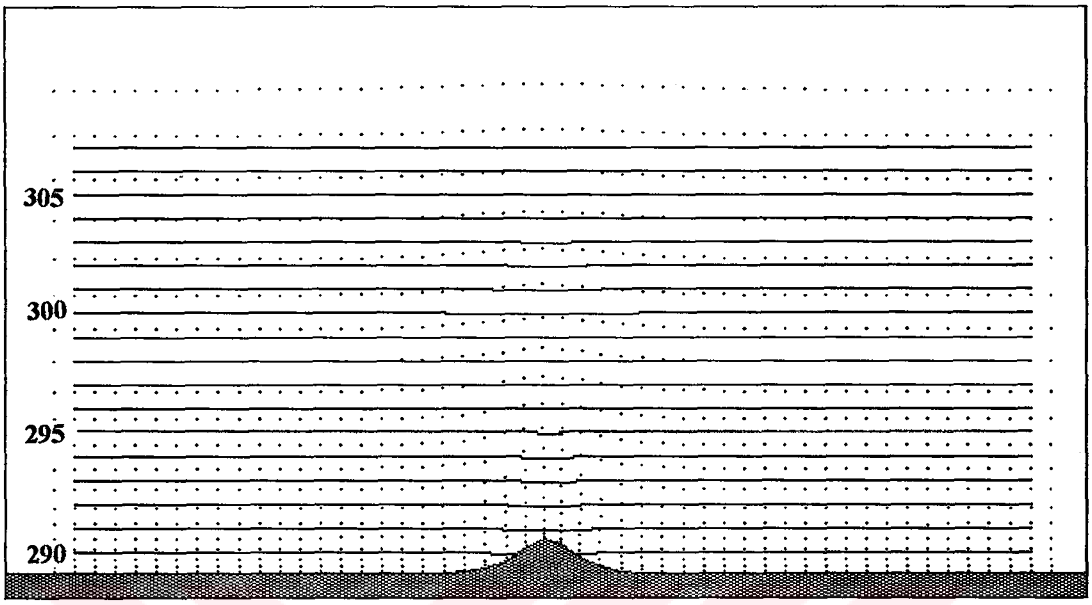

Fig 7.24 Potential temperature field at step=2.

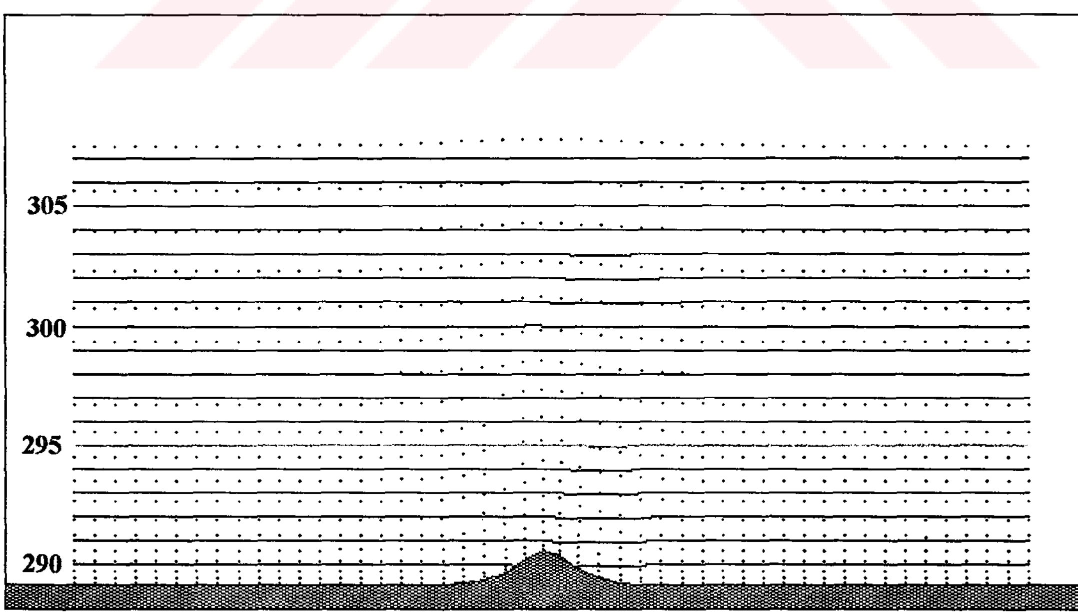

Fig 7.25 Potential temperature field at step=1250.

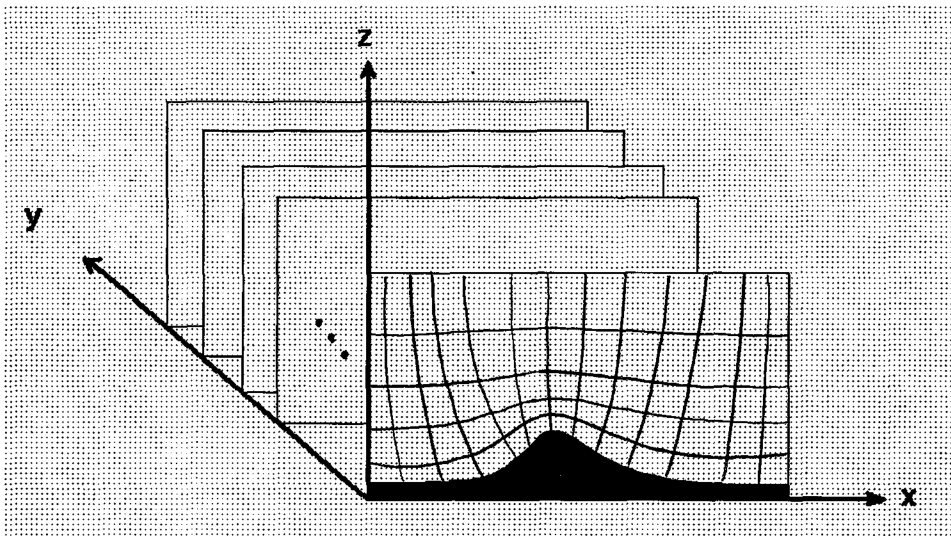

Fig 7.26 A schematic representation of the enhancing of the model to 3-D.

REFERENCES

Adams, J., R.G.Garcia, J.Hack, D.Haidvogel and V.Pizzo, (1992), Applications of Multigrid Software in the Atmospheric Sciences, M.Weather Rev.,120, 1447-1458.

Anderson, O.L., (1979), Calculation of Internal Viscous Flows in Axisymetric Ducts at Moderate to High Reynolds Numbers, to Appear in Computers and Fluids.

Arya, P., (1988), Introduction to Micrometeorology. Academic Press, 307pp.

Banta, R.M., (1990), The role of mountain flows in making clouds, Atmosp. Mete. Soc. Meteorological Monographs, Atmospheric Processes over Complex Terrain, Vol 23, 45, 229-283.

Batchelor, G.K., (1953), The Theory of Homogeneous Turbulence, Cambridge Science Classics Series, Cambridge Univ. Press, 197pp.

Batchelor, G.K., (1954), Heat Convection and Buoyancy Effects in Fluid, Q.J.Royal Meteor.Soc., 80, 339.

Beljaars, A.C.M., J.L.Walmsley and P.A.Taylor, (1987), A Mixed Spectral Finite Difference Model for Neutrally Stratified Boundary-Layer Flow over Roughness Change and Topography, Boundary-Layer Meteorology, 38, 273-303.

Bleck, R., (1973), Numerical Forecasting Experiments Based on the Conservation of Potential Vorticity on Isentropic Surfaces, J. Appl. Meteor., 12, 737-752.

Bleck, R., (1974), Short-Range Prediction in Isentropic Coordinates with Filtered and Unfiltered Numerical Models, M.Weather Review., 102, 813-829.

Bleck, R. and M.A.Shapiro (1976), Simulation and Numerical Weather Prediction Framed in Isentropic Coordinates. Weather Forecasting and Weather Forecasts: Models, Systems and Users, Vol. 1, NCAR Summary Colloqium, 154-169.

Bl̆eck, R., (1978), On the Use of Hybrid Vertical Coordinates in Numerical Weather Prediction Models, M.Weather Review, 106, 1233-1244.

Boussinesq, J., (1903), Theorie Analytique de la Chaleur Gauthier-Villars, Vol 2, 625pp.

Boybeyi, Z. and S.Raman, (1992), A Three-Dimensional Numerical Sensitivity Study of Convective over the Florida Peninsula, Boundary-Layer Meteorology, 60, 325-359.

Branković,C., (1981), A Transformed Isentropic Coordinate and its Use in an Atmospheric Model, M.Weather Review, 109, 2029-2039.

Bristow, D.R., (1977), Recent Improvements in Surface Singularity Methods for the Flow Field Analysis About Two-Dimensional Airfoils, AIAA 3rd Computational Fluid Dynamics Conference, A Collection of Technical Papers.

Businger, J.A., (1982), Equations and Concepts. Atmospheric Turbulence and Air Pollution Modeling, F.T.M. Nieuwstadt and H. van Dop, Ed., D.Reidel, 1-36.

Carpenter, K.M., (1979), An Experimental Forecast Using a Nonhydrostatic Mesoscale Model, Q.J.Royal Meteor.Soc., 105, 629-655.

Carrier, G.F., M.Krook and C.E.Pearson, (1966), Functions of A Complex Variable, McGraw-Hill Book Company.

Cebeci, T., (1981), Studies of Numerical Methods for the Plane Navier-Stokes Equations, Comput.Meth.Appl.Mech.Eng., 27, 13-44.

Charney, J.G. and N.A. Phillips, (1953), Numerical Integration of the Quasi-Geostrophic Equations for Barotrophic and Simple Baroclinic Flows, J. Meteor., 10, 71-99.

Christensen, O. and L.P.Prahm, (1976), A Pseudospectral Model for Dispersion of Atmospheric Pollutants, J.Appl.Meteorol., 15, 1284-1294.

Clark, T.L., (1977), A Small-Scale Dynamic Model Using a Terrain-Following Coordinate Transformation, J. Computational Physics, 24, 186-215.

Clark, T.L., (1979), Numerical Simulations with a Three-Dimensional Cloud Model: Lateral Boundary Condition Experiments and Multicellular Severe Storm Simulations, J.Atmos.Sci., 36, 2191-2215.

Corby, G.A., A.Gilchrist and R.L.Nweson, (1972), A General Circulation Model of the Atmosphere Suitable for Long Period Integrations, Q.J.Royal Meteor.Soc., 98, 809-832.

Courtney, M. and I.Troen, (1990), Wind Speed Spectrum from One year of Continuous 8Hz Measurements, Preprints, Denmark, Amer.Meteor.Soc., 302-304.

Cullen, M. J. P., (1974), Integraton of the Primitive Equations on a Sphere Using the Finite-Element Method, Quart.J.Royal Meteor.Soc., 100, 555-562.

Dapeng, X. and P.A. Taylor, (1992), A Nonlinear Extension of the Mixed Spectral Finite Turbulent Flow over Topography, Boundary-Layer Meteorology, 59, 177-186.

Davis, R.T., (1979), Numerical Methods for Coordinate Generation Based on the Schwarz-Christoffel Transformations, 4th Computational Fluid Dynamics Conference, AIAA, Paper No 79, 1463.

Deardorff, J.W., (1971), On the Magnitude of the Subgrid Scale Eddy Coefficient, J. Computational Physics, 7, 120-133.

Deardorff, J.W., K.Ueyoshi and Y.J.Han, (1984), Numerical Study of Terrain-Induced Mesoscale Motions and Hydrostatic Form Drag in a Heated, Growing Mixed Layer, J.Atmos.Sci., 41, 1420-1441.

Deaven, D.G., (1976), A Solution for Boundary Problems in Isentropic Coordinate Models, J.Atmos.Sci., 33, 1702-1713.

Desroziers, G. and J.P.Lafore, (1993), A Coordinate Transformation for Objective Frontal Analysis, M.Weather Review, 121, 1531-1553.

Dietchmayer, G.S., (1992), Applications of Continuous Dynamic Grid Techniques to Meteorological Modeling. Part II: Efficiency, M.Weather Rev., 120, 1707-1722.

Drake, R.L., D.C.Patrick and D.P.Anderson, (1974), The Effect of Nonlinear Eddy Coefficient on Rising Line Thermals, J.Atmos.Sci., 31, 2046-2057.

Durran, R.D., (1986) Another look at downslope windstorms, Part I: On the development of analogs to supercritical flow in an infinitely deep, continuously stratified fluid, J. Atmos. Sci., 43, 2527-2543.

Durran, R.D., (1990) Mountain waves and downslope winds, Atmosp. Mete. Soc. Meteorological Monographs, Atmospheric Processes over Complex Terrain, Vol 23, 45, 59-81.

Dutton, J.A. and G.H.Fichtl, (1969), Approximate Equations of Motion for Gases and Liquids, J.Atmos.Sci., 26, 241-254.

Dutton, J.A., (1976), The Ceaseless Wind, McGraw-Hill, 579pp.

Egger, J., (1972a), Incorporation of Steep Mountains into Numerical Forecasting Models, Tellus, 24, 324-335.

Egger, J., (1972b), Numerical Experiments on the Cyclogenesis in the Gulg of Geneo, Beitz. Phys. Atmos., 45, 320-346.

Egger, J., (1974), Numerical Experiments on Leecyclogenesis, M.Weather Review, 102, 847-860.

Eichhorn, J., R.Schrodin and W.Zdunkowski, (1988), Three-Dimensional Numerical Simulations of the Urban Climate, Beitr.Phys.Atmos., 61, 187-203.

Eiseman, P.R., (1982), Automatic Algebraic Coordinate Generation, (447-464, (see Thompson,J.F., 1982, Numerical Grid Generation, NewYork, North-Holland, 909pp).

Eliassen, A., (1962), On the vertical Circulation in Frontal Zones, Geofys. Publ., 24, 147-160.

Eliassen, A. and E.Raustein, (1968), A Numerical Integration Experiment with a Model Atmosphere Based on Isentropic Coordinate, Meteor. Ann., 5, 45-63.

Eliassen, A. and E.Raustein, (1970), A Numerical Integration Experiment with a Six-Level Atmospheric Model with Isentropic Information Surface, Meteorologiske Annaler, 5, 429-449.

Eliassen, A., (1980), A Review of Large-Range Transport Modeling, J.Appl.Meteorol., 19, 231-240.

Emanuel, K.A., (1982), Inertial Instability and Mesoscale Convective Systems, Part II. Symmetric CISK in a Baroclinic Flow, J.Atmos.Sci., 39, 1080-1097.

Erdun, H., S.İncecik, M.O.Kaya and İ.Özkol, (1996), Realistic Approach to the 2-D Flow Modeling for Complex Topography, 4th Workshop on Harmonization Within Atmospheric Dispersion Modeling for Regulatory Purposes, VITO, Oostende, Belgium, 275-284.

Fast, J.D. and S. Takle, (1988), Application of Quasi-Nonhydrostatic Parameterization for Numerically Modeling Neutral Flow over an Isolated Hill, Boundary-Layer Meteor, 44, 285-304.

Fox, D.G. and J.W.Deardorff, (1972), Computer Methods for Simulation of Multidimensional, Nonlinear, Subsonic, Incompressible Flow, J.Heat Transfer, Ser. C, 94, 337-346.

Fox, D.G. and S.A.Orszag, (1973), Pseudospectral Approximation to Two-Dimensional Turbulence, J. Comp. Physics, 11, 612-619.

Friend, A.L., D. Djuric and K.C. Brundidge (1977), A combination of Isentropic and Sigma Coordinates in Numerical Weather Prediction, Beitr. Phys. Atmos., 50, 290-295.

Fulton, S.R., P.E.Ciesielski, W.H.Schubert, (1986), Multi-grid Methods for Elliptic Problems: a Review, M.Weather Review, 114, 943-959.

Gadd,A.J., (1978), A Split Explicit Integration Scheme for Numerical Weather Prediction. Q.J.Royal Meteor.Soc., 104, 569-582.

Gal-Chen,T. and R.C. Somerville (1975a), On the Use of a Coordinate Transformation for the Solution of the Navier-Stokes Equations, J. Computational Physics, 17, 209.

Gal-Chen,T. and R.C. Somerville (1975b), Numerical Solution of the Navier-Stokes Equations with Topography, J. Computational Physics, 17, 276.

Gary,J.M., (1973), Estimate of Truncation Error in Transformed Coordinate Primitive Equation Atmosphere Models, J.Atmos.Sci., 30, 223-233.

Golding,B.W., (1990), The Meteorological Office Mesoscale Model, The Meteorological Magazine, 119, 81-96.

Gross,G., (1985), An Explanation of the "Maloja-Serpent" by numerical simulation, Contrib.Atmosp.Phys., 59, 97-114.

Haltiner,G.J., (1971), Numerical Weather Prediction, Wiley, NewYork, 317pp.

Haltiner,G.J. and R.T. Williams, (1980), Numerical Prediction and Dynamic Meteorology, 2nd ed., Wiley, NewYork.

Heikes,R., and D.A.Randall, (1995), Numerical Integration of the Shallow-Water Equations on a Twisted Icosahedral Grid. Part II: A Detailed Description of the grid and an Analysis of Numerical Accuracy, M.Weather Review, 123, 1881-1887.

Hess,J.L. and A.M.O.Smith, (1966), Calulation of Potential Flow About Orbitrary Bodies, Progress in Aeronautical Sciences, Vol 8, Pergamon Press.

Hinkelman,K., (1959), Ein Numerisches Experiment mit den Primitiven Gleichungen. In the Atmosphere and the Sea in Motion, Ed., B.Bolin, Rockefeller Institute Press, NewYork, 486-500.

Hirt,C.W. and J.L. Cook, (1972), Calculating Three-dimensional Flows Around Structure and Rough Terrain, J. Computational Physics, 10, 324.

Hoskins,B.J. and F.P.Bretherton, (1972), Atmospheric Frontogenesis Models: Mathematical Formulation and Solution, J.Atmos.Sci., 29, 11-37.

Hoskins,B.J., (1975), The Geostrophic Momentum Approximation and the Semigeostrophic Equations, J.Atmos.Sci., 32, 233-242.

Houghton,D.D., W.H.Camphell and N.D.Reynolds, (1981), Isolation of the Gravity-Inertial Motion Component in a Nonlinear Atmospheric Model, M.Weather Review, 109, 2118-2130.

Hunt,J.C.R. and J.E.Simpson, (1982), Atmospheric Boundary Layers over Nonhomogeneous Terrain, E.J.Plate ed., Engineering Meteorology, Elsevier, Amsterdam.

Ives,D.C., (1982), Conformal Grid Generation, 107-136, (see Thompson,J.F., 1982, Numerical Grid Generation, NewYork, North-Holland, 909pp).

Janjić,Z.I., (1990), The Step-Mountain Coordinate: Physical Package, M.Weather Review, 118, 1429-1443.

Ji-Fan,C., (1986), Treatment and Effects of Orography in NWP Models. Short- and Medium-Range Numerical Weather Prediction, Collection of Papers Presented at the WMO/IUGG NWP Symposium, Tokyo, 697-711.

Johnson,D.R., L.W. Uccelini (1983), A Comparison of Methods for Computing the Sigma-Coordinate Pressure Gradient Force for Flow Over Sloped Terrain in a Hybrid Theta-Sigma Model, M.Weather Review, 111, 870-886.

Kadıoğlu,M., (1996), Givens subroutine from GIVENS.FOR software, ITU. Ucak ve Uzay Bilimleri fakultesi, Meteoroloji Bolumu.

Kasahara,A. and W.M. Washington, (1967), NCAR Global General Circulation Model of the Atmosphere, M.Weather Review, 95, 389-402.

Kasahara,A., (1974), Various Vertical Coordinate Systems Used for Numerical Weather Prediction, M.Weather Review, 102, 509-522.

Klemp,J.B. and R.B.Wilhelmson, (1978), The simulation of Three-Dimensional Convective Storm Dynamics, J.Atmos.Sci., 35, 1070-1096.

Koss,W.J., (1971), Numerical Integration Experiments with Variable-Solution Two-Dimensional Cartesian Grids Using the Box Method, M.Weather Review, 99, 725-738.

Kurihara,Y., (1968), Note an Finite Difference Expressions for the Hydrostatic Relation and Pressure Gradient Force, M.Weather Review, 96, 654-656.

Lee,H.N., (1981), An Alternate Pseudospectral Model for Pollutant Transport, Diffusion and Deposition in the Atmosphere, Atmos. Environ., 15, 1017-1024.

Leith,C., (1965), Lagrangian Advection in an Atmospheric Model. WMO-IUGG Symposium on Research and Development Aspect of Long Range Forecasting, Boulder, Colo., WMO Tech. Note 66, 168-176.

Leslie,L.M. and B.J. McAvaney, (1973), Comparative Test of Direct and Iterative Methods for Solving Helmholtz-type Equations, M.Weather Review, 101, 235-239.

Lilly,D.K., (1962), On the Numerical Simulation of Buoyant Convection, Tellus, 14,148-172.

Lilly,D.K., (1965), On the Computational Stability of Numerical Solutions of Time-Dependent Nonlinear Geophysical Fluid Dynamics Problems, M.Weather Review, 93, 11-26.

Lipps, F.B. and R.S.Hemler, (1982), A Scale Analysis of Deep Moist Convection and Some Related Numerical Calculations, J.Atmos.Sci., 39, 2192-2210.

Machenhauer, B., (1979), The Spectral Model: Numerical Methods Used in Atmospheric Models, GARP Report, 17, 121-275, Vol II.

Mahrer, Y. and R.A.Pielke, (1975), A Numerical Study of the Air Flow over Mountains Using the Two-Dimensional Version of the University of Virginia Mesoscale Model, J.Atmos.Sci., 32, 2144-2155.

Mahrt, L., (1986), On the Shallow Motion Approximation, J.Atmos.Sci., 43, 1036-1044.

Manney, G.L., J.D. Farrara and C.R. Mechoso (1994), Simulations of the February 1979 Stratospheric Sudden Warming: Model Comparisons and Three-Dimensional Evolution, NWR, 122, 1115-1140.

Martin, C.L. and R.A.Pielke, (1983), The Adequacy of the Hydrostatic Assumption in Sea Breeze Modeling over Flat Terrain, J.Atmos.Sci., 40, 1472-1481.

Masten,C.W. and J.F.Thompson, (1978), Elliptic Systems and Numerical Transformations, J.Math.Anal.Appl., 62, 52-62.

Masuda, Y., (1969), A Finite-Difference Scheme by Making use of Hexagonal Mesh-Points. Proc. WMO/IUGG Symp. on Numerical Weather Prediction in Tokyo, Tech. Rep. of JMA, VII35-VII44, 649pp.

Masuda, Y., and H.Ohnishi, (1987), An Integration Scheme of the Primitive Equation Model with an Icosahedral-Hexagonal Grid System and its Application to the Shallow- Water Equations. Short- and Medium-Range Numerical Weather Prediction, Japan Meteorological Society, 317-326.

Mengelkamp, H.T, (1991), Boundary Layer Structure over an Inhomogeneous Surface: Simulation with a Non-hydrostatic Mesoscale Model, Boundary-Layer Meteorology, 57, 323-341.

Meriless, P.E. and S.A.Orszag, (1979), The Pseudospectral Method. Numerical Methods Used in Atmospheric Models, GARP Report, 17 Vol II, 276-299.

Meroney, R.N., and V.A. Sandborn, (1978), Sites for wind power installations: Physical modelling of the influence of hills, ridges and complex terrain on wind speed and turbulence. Final Report CER77-78RNM-VAS50b, Civil Eng. Dept., Colorado State Univ. 197pp.

Meschoso, C.R., M.J.Suarez, K.Yamazaki, J.A.Spahr and A.Arakawa, (1982), A Study of the Sensitivity of Numerical Forecasts to an Upper Boundary in the Lower Stratosphere, M.Weather Review, 110, 1984-1993.

Meesters, A., (1992), Feasibility of the Direct Method to Solving the Anelastic Pressure Equation in Nonhydrostatic Two-Dimensional Mesoscale Models, M.Weather Review, 120, 2390-2393.

Mesinger, F., (1984), A Blocking Technique for Representation of Mountains in Atmosphere Models, Riv. Meteor. Aeronatica, 44, 195-202.

Mesinger, F., (1985), The Sigma System Problem. The 7th AMS Conference on Numerical Weather Prediction, June 17-20, Montreal, Canada, 340-347.

Mesinger, F. and Z.I. Janjić (1987), Numerical Technique for the Representation of Mountains. Observation, Theory and Modeling of Orographic Effects, Seminar 1986, Vol. 2, ECMWF, Reading, England, 29-80.

Mesinger, F., S. Nickovic, D. Gavrilov and D.G. Deaven (1988), The Step- Mountain Coordinate: Model Description and Performance for Cases of Alphine Lee Cyclogenesis and for a Case of an Appalachian Redevelopment, M.Weather Review, 116, 1493-1518.

Moore, J.T. and G.E. VanKnowe, (1992), The Effect of Jet-Streak Curvature on Kinematic Fields, M.Weather Review, 120, 2429-2441.

Moretti, G., (1980), Grid Generation Using Classical Techniques, 1-36, (see Smith,R.E, ed.-1980. Numerical Grid Generation Techniques, NASA CP 2166, 574pp).

Neumann, J. and Y.Mahrer, (1971), A Theoretical Study of the Land and Sea Breeze Circulations, J.Atmos.Sci., 28, 532-542.

O'Brien, J.J., (1970), A Note on the Vertical Structure of the Eddy Exchange Coefficient in the Planetary Boundary Layer, J.Atmos.Sci., 27, 1213-1215.

Ogura,Y. and N.A.Phillips, (1962), Scale Analysis of Deep and Shallow Convection in the Atmosphere, J.Atmos.Sci., 19, 173-179.

Orlanski, I., B.Ross and L.Polinsky, (1974), Diurnal Variation of the Planetary Boundary Layer in a Mesoscale Model, J.Atmos.Sci., 31,965-989.

Orlanski, I., (1975), A Rational Subdivision of Scales for Atmospheric Processes, Bull.Americ.Meteorol.Soc., 56, 527-530.

Orszag, S.A., (1971), Numerical Simulation of Incompressible Flows within Simple Boundaries: Accuracy, J. Fluid Mech., 49, 76-112.

Orville, H.D., (1965), A Numerical Study of the Initiation of Cumulus over Mountainous Terrain, J.Atmos.Sci., 22, 684.

Orville, H.D., (1967), Orographic Convection in "Thermal Convection: A Colloquium", NCAR-TN-24, 385-430, NCAR, Boulder, Colorado.

Orville, H.D., (1968), Ambient wind effects on the Initial and Development of Cumulus clouds over Mountains, J.Atmos.Sci., 25, 385.

Orville, H.D. and L.J. Sloan (1970), Effects of Higher Advection Techniques on a Numerical Cloud Model, M.Weather Review, 98, 7.

Paegle, J. and D.W.David, (1983), Numerical Modeling of Diurnal Convergence Oscillations above Sloping Terrain, M.Weather Review, 111, 67-85.

Panofsky, H.A and G.W.Brier, (1968), Some Applications of Statistics to Meteorology, Penn State Univ.

Patrinos, A.N.A. and M.J.Leach, (1982), On the Use of the Pseudospectral Technique in Air-Pollution Modeling, Preprint, 3rd Joint Conf. on Appl. of Air Pollution Meteor., San Antonio, Texas, AMS, Boston, Jan. 11-15, 1982.

Patrinos, A.A.N. and A.L.Kistler, (1977), A Numerical Study of the Chicago Lake Breeze, Boundary-Layer Meteorology, 12, 93-123.

Physick, W.L., (1988), Review: Mesoscale Modeling in Complex Terrain, Earth-Science Reviews, 25, 199-235.

Phillips, N.A., (1957), A Coordinate System Having Some Special Advantages for Numerical Forecasting, J.Meteor., 14,184-185.

Phillips, N.A., (1974), Application of Arakawa's Energy-Conserving Layer Model to Operational Numerical Weather Prediction, NMC Office Note, 104, 40pp.

Pielke, R.A. and E.Kennedy, (1980), Mesoscale Terrain Features, Rep. No. UVA-ENV SCI-MESO-1980-1.

Pielke, R.A. and C.L.Martin, (1981), The Derivation of a Terrain-Following Coordinate System for Use in a Hydrostatic Model, J.Atmos.Sci., 38, 1707-1713.

Pielke, R., (1984), Mesoscale Meteorological Modeling, Academic Press, 612pp.

Richardson, L.F., (1922), Weather Prediction by Numerical Process, London, Cambridge Univ. Press/reprinted:Dover, 1965, 236pp.

Sadourny, R., A.Arakawa and Y.Mintz, (1968), Integration of the nondivergent barotropic vorticity equation with an icosahedral-hexagonal grid for the sphere, M.Weather Review, 96, 351-356.

Sadourny, R., O.P. Sharma, K. Laval and J. Canneti (1981), Modeling of the Vertical Structure in Sigma Coordinate: A Comparative Test With FGGE Data Analysis and Results, Bergen, 23-27 June 1980, 294-302.

Salmon,J.R., J.L.Walmsley and P.A.Taylor, (1981), Development of a Model of neutrally Stratified Boundary Layer Flow over Real Terrain, Internal Rep., Boundary Layer Division, Atmospheric Environment Service, Downsview, Ontorio, Canada.

Shapiro, M.A., (1973), Numerical Weather Prediction and Analysis in Isentropic Coordinates, Atmospheric Technology, NCAR, Boulder, Colo., 3, 67-70.

Shapiro, M.A. and J.T. Hastings, (1973), Objective Cross-Section Analysis by Hermit Polynomial Interpolation on Isentropic Surfaces, J. Appl. Meteor., 12, 753-762.

Sharman.R.D., T.L.Keller and M.G.Wurtele, (1988), Incompressible and Anelastic Flow Simulations on Numerically Generated Grids, M.Weather Review, 116, 1124-1136.

Simmons, A.J. and D.M.Burridge (1981), An Energy and Angular-Momentum Conserving Finite-Difference Scheme and Hybrid Vertical Coordinates, M.Weather Review, 109, 758-766.

Simmons, A.J. and R. Strüfing (1981), An Energy and Angular-Momentum Conserving Finite-Difference Scheme, Hybrid Coordinates ECMWF Tech. Rep. No. 28, 68pp.

Smagorinsky, J., (1963), General Circulation Experiments with the Primitive Equations: I. The Basic Experiment, M.Weather Review, 91, 99-164.

Smagorinsky, J., S.Manabe and J.L.Holloway, (1965), Numerical Results from a Nine-Level General Circulation Model of the Atmosphere, M.Weather Review, 93, 727-768.

Smagorinsky,J., R.F.Strickler, W.E.Sangster, S.Manabe, J.L.Halloway and G.D.Heinbree, (1967), Prediction Experiments with a General Circulation Model. Proc.Int.Symp.Dynamic of Large Scale Atmospheric Processes, USSR, Izdatel'stvo "Nanka", Moskow, 70-134.

Song, J.L., R.A.Pileke, M.Segal, R.W.Arritt and R.C.Kessler, (1985), A Method to Determine Nonhydrostatic Effects Within Subdomains in a Mesoscale Model, J.Atmos.Sci., 42, 2110-2120.

Spiegel, E.A. and G. Veronis, (1960), On the Boussinesq Approximation for a Compressible Fluid, Astrophysical Journal, 442-447, 131 pp.

Stadius, G., (1977), Construction of Orthogonal Curvilinear Meshes by Solving Initial Value Problems, Numer.Math., 28, 25-48.

Steger, J.L. and R.Sorenson, (1979), Automatic Mesh-point Clustering Near a Boundary in a Grid Generation with Elliptic Partial Differential Equations, J. Computational Physics, 33, 405-416.

Stewartson, K., (1974); Multistructured Boundary Layers on Flat Plates and Related Bodies, in Advances in Applied Mechanics, Vol 14, p145, Academic Press.

Stratton, J.A., (1940), Electromagnetic Theory, McGraw-Hill, 615pp.

Stull, R., (1988), An Introduction to Boundary Layer Meteorology, Kluwer Academic, 666pp.

Suarez, M.J. and A. Arakawa, (1979), Description and Preliminary Results of the 9-Level UCLA General Circulation Model, Preprints, Fourth Conf. Numerical Weather Prediction, Silver Spring, Amer. Meteor. Soc., 290-297.

Sundqvist, H., (1975), On Truncation Errors in Sigma-System Models, Atmosphere, 13, 81-95.

Sundquist, H., (1979), Vertical Coordinates and Related Discretization." Numerical Methods Used in Atmospheric Models", GARP Report, 17, Vol II, 1-150.

Tapp, M.C. and P.W.White, (1976), A Nonhydrostatic Mesoscale Model, Q.J.Royal Meteor. Soc., 102, 277-296.

Thompson, J.F., F.C.Thames and C.W.Masten, (1974), Automatic Numerical Generation of Body-fitted Curvilinear Coordinate System for Field Containing any Number of Arbitrary Two-Dimensional Bodies, J.Computational Physics, 15, 299.

Thompson, J.F., Z.U.Warsi and C.W.Masten, (1976), Numerical Grid Generation: Foundations and Applications, North-Holland, 483pp.

Thompson, J.F., F.C.Thames and C.W.Masten, (1977), TOMCAT-A Code for Numerical Generation of Boundary-fitted Curvilinear Coordinate Systems on Fields Containing any Number of Arbitrary Two-Dimensional Bodies. J.Computational Physics, 24, 274-302.

Thompson, J.F., Z.U.A. Warsi and C.W.Masten, (1985), Numerical Grid Generation, North-Holland, 483pp.

Thuburn, J., (1993), Use of a Flux-Limited Scheme for Vertical Advection in a GCM, Q, J. Royal Meteor.Soc., 119, 469-487.

Thunis, P., (1995), Formulation and Evaluation of a Nonhydrostatic Vorticity Mode Mesoscale Model, Ph.D. dissertation, Universite Louvain-la-Neuve, Catholique de Louvain, Belgium, 116pp.

Thunis, P. and R.Bornstein, (1996), Hierarchy of Mesoscale Flow Assumptions and Equations, J.Atmos.Sci., 53, 380-397.

Tibaldi, S., (1985), The Representation of Orography in Weather Prediction Models, ECMWF Lecture Note, No 3.5, 79pp.

Trefethen, L.N., (1979), Numerical Computation of the Schwarz-Christoffel Trarsformation, Stanford University Computer Science Report, STAN-CS-79-710.

Trevisan, A., (1976), Numerical Experiments on the Influence of Orography on Cyclone Formation with an Isentropic Primitive Equation Model, J.Atmos.Sci., 33, 768-780.

Tripoli, G.J. and W.R.Cotton, (1982), The Colorado State University Three-Dimensional Cloud/Mesoscale Model-1982, Part I. General Theoretical Framework and Sensitivity Experiments, J.Rech.Atmos., 16, 185-219.

Uccelini, L.W., D.R. Johnson, R.E. Schlesinger (1979), An Isentropic and Sigma Coordinate Hybrid Numerical Model: Model Development and Some Initial Tests, J.Atmos.Sci., 36, 390-414.

Ünal, F., (1997), Private communication, ITU, Uçak ve Uzay Bilimleri Fakültesi, Uçak Müh. Bölümü.

Van Dyke, M., (1975), Perturbation Methods in Fluid Mechanics, The Parabolic Press.

Van Tuyl, A.H. and J.A.Young, (1982), Numerical Simulation of Nonlinear Jet Streak Adjustment, M.Weather Review, 110, 2038-2054.

Vičelli, J.A., (1971), A Computing Method for Incompressible Flows Bounded by Moving Walls, J. Computational Physics, 8, 119.

Wallace, J.M. and P.V.Hobbs, (1977), Atmospheric Science: An Introductory Survey, Academic Press, NewYork.

Walker, M., (1964), The Schwarz-Christoffel Transformation and Its Applications-A Simple Exposition, Dover Publications Inc., New York, 116pp.

Walmsley, J.L., J.R.Salmon and P.A.Taylor, (1982), On the Application of a Model of Boundary-Layer Flow over Low Hills to Real Terrain. Boundary-Layer Meteorology, 23, 17-46.

Williamson, D.L., (1968), Integration of the Barotropic Vorticity Equation on a Spherical Geodesic Grid, Tellus, 20, 642-653pp.

Williams, G.P., (1969), Numerical Integration of the 3D Navier-Stokes Equations for Incompressible Flow, J. Fluid. Mech., 37, 727-750.

Wilhelmson, R.B. and J.H. Ericksen, (1977), Direct Solutions for Poisson's Equation in the Three Dimensions, J. Computational Physics, 25, 319-331.

Winslow, A.M., (1967), Numerical Solution of the Quasilinear Poisson Equation in a Nonuniform Triangle Mesh, J.Computational Physics, 2, 149-172.

Wipperman, F., (1981), The Applicability of Several Approximations in Mesoscale Modeling- a Linear Approach, Contrib.Atmosp.Phys., 54, 298-308.

Woods, L.C., (1961), The Theory of Subsonic Plane Flow, Cambridge University Press.

Young, J.A., (1968), Comparative Properties of Some Time Differencing Schemes for Linear and Non-linear Oscillations, M.Weather Review, 96, 357-364.

Young, G.S., (1987), Mixed Layer Spectra from Aircraft Measurements, J.Atmos.Sci., 44, 1251-1256.

Young, G.S. and R.A.Pielke, (1983), Application of Terrain Height Variance Spectra to Mesoscale Modeling, J.Atmos.Sci., 40, 2555-2560.

Zhang, M. and M.A. Geller, (1994), Selective Excitation of Tropical Atmospheric Waves in Wage-CISK: The Effect of Vertical Wind Shear, J.Atmos.Sci., Vol. 51, No 3, 353-368.

APPENDIX A

A.1 Finite Difference Schemes

Most mesoscale models are utilized the finite difference method because of its comparative ease of coding onto a computer as well as its conceptual simplicity. This technique simply involves approximating the differential terms, including time, by one or more terms in a Taylor series expansion.

A.1.1 Finite difference space schemes

One of the first steps to be taken in establishing a finite-difference procedure for solving a partial differential equation is to replace the continuous problem domain by a finite-difference mesh or grid. As an example, suppose that we wish to solve a partial differential equation for which $u(x,z)$ is the dependent variable in the rectangle domain $0 \leq x \leq 1$, $0 \leq z \leq 1$. We establish a grid on the domain by replacing $u(x,z)$ by $u(i\Delta x, j\Delta z)$. Points can be located according to values of i and j so difference equations are usually written in terms of the general point (i,j) and its neighbors. This labeling is illustrated in Fig A.1

Thus, if we think of $u_{i,j}$ as $u(x_\circ, z_\circ)$ then

$$u_{i+1,j} = u(x_\circ + \Delta x, z_\circ) \qquad u_{i-1,j} = u(x_\circ - \Delta x, z_\circ)$$

$$u_{i,j+1} = u(x_\circ, z_\circ + \Delta z) \qquad u_{i,j-1} = u(x_\circ, z_\circ - \Delta z)$$

Often in the treatment of marching problems, the variation of the marching coordinate is indicated by a superscript, such as u_j^{n+1}, rather than a subscript. Many different finite-difference representations are possible for any given partial differential equation and it's usually impossible to establish a "best" form on an absolute basis. First of all, the accuracy of a difference scheme may depend on the exact form of the equation and problem being solved and secondly, our selection of a "best" scheme will be influenced by the aspect of the procedure which we are trying to optimize, i.e., accuracy, economy, programming simplicity, etc.

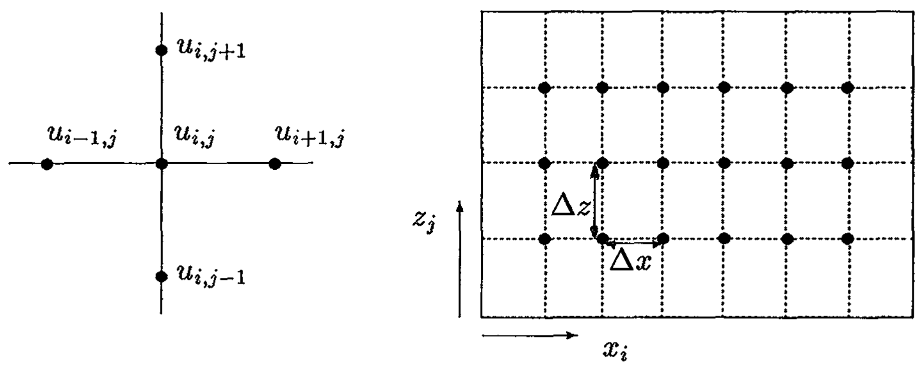

Fig A.1 A typical finite-difference grid.

The idea of a finite-difference representation for a derivative can be introduced by recalling the definition of the derivative for the function $u(x, z)$ at $x = x_\circ$, $z = z_\circ$.

$$\frac{\partial u}{\partial x} = \lim_{\Delta x \to 0} \frac{u(x_\circ + \Delta x, z_\circ) - u(x_\circ, z_\circ)}{\Delta x} \tag{A.1}$$

Here, if u is continuous, it is expected that $[u(x_\circ + \Delta x, z_\circ) - u(x_\circ, z_\circ)]/\Delta x$ will be a "reasonable" approximation to $\partial u/\partial x$ for a "sufficiently" small but finite Δx. In fact, the mean value theorem assures us that the difference representation is exact for some point within the Δx interval. The difference approximation can be put on a more formal basis through the use of either a *Taylor series expansion* or *Taylor's formula* with a remainder. Developing a Taylor-series expansion for $u(x_\circ + \Delta x, z_\circ)$ about $u(x_\circ, z_\circ)$ gives:

$$u(x_\circ + \Delta x, z_\circ) = u(x_\circ, z_\circ) + \left.\frac{\partial u}{\partial x}\right|_\circ \Delta x + \left.\frac{\partial^2 u}{\partial x^2}\right|_\circ \frac{(\Delta x)^2}{2!} + \cdots \left.\frac{\partial^{n-1} u}{\partial x^{n-1}}\right|_\circ \frac{(\Delta x)^{n-1}}{(n-1)!} + \left.\frac{\partial^n u}{\partial x^n}\right|_\xi \frac{(\Delta x)^n}{(n)!} \tag{A.2}$$

for $x_\circ \leq \xi \leq (x_\circ + \Delta x)$, and here, the last term can be identified as the remainder. Thus, we can form the "*forward*" difference by rearranging Eq. (A.2).

$$\left.\frac{\partial u}{\partial x}\right|_{x_\circ, z_\circ} = \frac{u(x_\circ + \Delta x, z_\circ) - u(x_\circ, z_\circ)}{\Delta x} - \left.\frac{\partial^2 u}{\partial x^2}\right|_\circ \frac{(\Delta x)^2}{2!} - \cdots \tag{A.3}$$

Switching now to the i, j notation for brevity, we consider

$$\left.\frac{\partial u}{\partial x}\right|_{i,j} = \frac{u_{i+1,j} - u_{i,j}}{\Delta x} + \text{Truncation error} \tag{A.4}$$

where $(u_{i+1,j} - u_{i,j})/\Delta x$ is obviously the finite-difference representation for $\partial u/\partial x|_{i,j}$. The truncation error is the difference between the partial derivative and its finite-difference representation. We can characterize the limiting behavior of the truncation error by using the order of $O[\,]$ notation whereby we write,

$$\left.\frac{\partial u}{\partial x}\right|_{i,j} = \frac{u_{i+1,j} - u_{i,j}}{\Delta x} + O[\Delta x] \tag{A.5}$$

where $O[\Delta x]$ has a precise mathematical meaning. Here, when the truncation error is written as $O[\Delta x]$ we mean $|\textit{truncation error}| \leq K|\Delta x|$ for $\Delta x \to 0$ (sufficiently small Δx). K is a positive real constant. As a practical matter, the order of the truncation error in this case is found to be Δx raised to the largest power which is common to all terms in the truncation error.

Note that $O[\Delta x]$ tells us nothing about the exact size of the truncation error but rather how it behaves as Δx tends toward zero. If another difference expression had a *Truncation error*$=O[(\Delta x)^2]$, we might expect or hope that the truncation error of the second representation would be smaller than the first for a convenient Δx but we could only be sure that this would be true if we refined the mesh "sufficiently", and "sufficiently" is a quantity which is hard to estimate.

An infinite number of difference representations can be found for $\partial u/\partial x|_{i,j}$. For example we could expand "*backwards*"

$$u(x_\circ - \Delta x, z_\circ) = u(x_\circ, z_\circ) - \left.\frac{\partial u}{\partial x}\right|_\circ \Delta x + \left.\frac{\partial^2 u}{\partial x^2}\right|_\circ \frac{(\Delta x)^2}{2!} - \left.\frac{\partial^3 u}{\partial x^3}\right|_\circ \frac{(\Delta x)^3}{3!} + \cdot \tag{A.6}$$

and obtain the "*backwards*" difference representation,

$$\left.\frac{\partial u}{\partial x}\right|_{i,j} = \frac{u_{i,j} - u_{i-1,j}}{\Delta x} + O[\Delta x] \tag{A.7}$$

We can subtract Eq. (A.6) from Eq. (A.2), rearrange, and obtain the "*central*" difference

$$\left.\frac{\partial u}{\partial x}\right|_{i,j} = \frac{u_{i+1,j} - u_{i-1,j}}{2\Delta x} + O[(\Delta x)^2] \tag{A.8}$$

We can also add Eq. (A.2) and Eq. (A.6) rearrange to obtain an approximation to the second derivative

$$\left.\frac{\partial^2 u}{\partial x^2}\right|_{i,j} = \frac{u_{i+1,j} - 2u_{i,j} + u_{i-1,j}}{(\Delta x)^2} + O[(\Delta x)^2] \tag{A.9}$$

It should be emphasized that these are only a few examples of the possible ways in which first and second derivatives can be approximated.

Most of the partial differential equations arising in fluid mechanics and heat transfer involve only first- and second-partial derivatives, and generally we strive to represent these derivatives using values at only two or three grid points. Within these restrictions, the most frequently used first-derivative approximations on a grid for which Δx=constant are

$$\left.\frac{\partial u}{\partial x}\right|_{i,j} = \frac{u_{i+1,j} - u_{i,j}}{\Delta x} + O[\Delta x] \tag{A.10}$$

$$\left.\frac{\partial u}{\partial x}\right|_{i,j} = \frac{u_{i,j} - u_{i-1,j}}{\Delta x} + O[\Delta x] \tag{A.11}$$

$$\left.\frac{\partial u}{\partial x}\right|_{i,j} = \frac{u_{i+1,j} - u_{i-1,j}}{2\Delta x} + O[(\Delta x)^2] \tag{A.12}$$

$$\left.\frac{\partial u}{\partial x}\right|_{i,j} = \frac{-3u_{i,j} + 4u_{i+1,j} - u_{i+2,j}}{2\Delta x} + O[(\Delta x)^2] \tag{A.13}$$

$$\left.\frac{\partial u}{\partial x}\right|_{i,j} = \frac{3u_{i,j} - 4u_{i-1,j} + u_{i-2,j}}{2\Delta x} + O[(\Delta x)^2] \tag{A.14}$$

The most common three-point second-derivative approximations for a uniform grid, Δx=constant, are

$$\left.\frac{\partial^2 u}{\partial x^2}\right|_{i,j} = \frac{u_{i,j} - 2u_{i+1,j} + u_{i+2,j}}{(\Delta x)^2} + O[\Delta x] \tag{A.15}$$

$$\left.\frac{\partial^2 u}{\partial x^2}\right|_{i,j} = \frac{u_{i,j} - 2u_{i-1,j} + u_{i-2,j}}{(\Delta x)^2} + O[\Delta x] \tag{A.16}$$

$$\left.\frac{\partial^2 u}{\partial x^2}\right|_{i,j} = \frac{u_{i+1,j} - 2u_{i,j} + u_{i-1,j}}{(\Delta x)^2} + O[(\Delta x)^2] \tag{A.17}$$

Some difference approximations for derivatives which involve more than three grid points are given in Table A.1. For completeness, a few common difference representations for mixed partial derivatives are presented in Table A.2. The mixed derivative approximations in Table A.2 can be verified by using the Taylor-series expansion for two variables

$$\begin{aligned} u(x_o + \Delta x, z_o + \Delta z) = \quad & u(x_o, z_o) + \left(\Delta x \frac{\partial}{\partial x} + \Delta z \frac{\partial}{\partial z}\right) u(x_o, z_o) + \frac{1}{2!}\left(\Delta x \frac{\partial}{\partial x} + \Delta z \frac{\partial}{\partial z}\right)^2 u(x_o, z_o) + \cdots \\ & \cdots + \frac{1}{n!}\left(\Delta x \frac{\partial}{\partial x} + \Delta z \frac{\partial}{\partial z}\right)^n u(x_o + \theta\Delta x, z_o + \theta\Delta z) \qquad \text{for } (0 \le \theta \le 1). \end{aligned} \tag{A.18}$$

Table A.1 Difference approximations using more than three points.

$$\left.\frac{\partial u}{\partial x}\right|_{i,j} = \frac{-u_{i+2,j} + 8u_{i+1,j} - 8u_{i-1,j} + u_{i-2,j}}{12\Delta x} + O[(\Delta x)^4] \tag{A.19}$$

$$\left.\frac{\partial^2 u}{\partial x^2}\right|_{i,j} = \frac{-u_{i+2,j} + 16u_{i+1,j} - 30u_{i,j} + 16u_{i-1,j} - u_{i-2,j}}{12(\Delta x)^2} + O[(\Delta x)^4] \tag{A.20}$$

$$\left.\frac{\partial^2 u}{\partial x^2}\right|_{i,j} = \frac{2u_{i,j} - 5u_{i-1,j} + 4u_{i-2,j} - u_{i-3,j}}{(\Delta x)^2} + O[(\Delta x)^2] \tag{A.21}$$

$$\left.\frac{\partial^2 u}{\partial x^2}\right|_{i,j} = \frac{-u_{i+3,j} + 4u_{i+2,j} - 5u_{i+1,j} + 2u_{i,j}}{(\Delta x)^2} + O[(\Delta x)^2] \tag{A.22}$$

$$\left.\frac{\partial^3 u}{\partial x^3}\right|_{i,j} = \frac{5u_{i,j} - 18u_{i-1,j} + 24u_{i-2,j} - 14u_{i-3,j} + 3u_{i-4,j}}{2(\Delta x)^3} + O[(\Delta x)^2] \tag{A.23}$$

$$\left.\frac{\partial^3 u}{\partial x^3}\right|_{i,j} = \frac{-3u_{i+4,j} + 14u_{i+3,j} - 24u_{i+2,j} + 18u_{i+1,j} - 5u_{i,j}}{2(\Delta x)^3} + O[(\Delta x)^2] \tag{A.24}$$

$$\left.\frac{\partial^3 u}{\partial x^3}\right|_{i,j} = \frac{u_{i+2,j} - 2u_{i+1,j} + 2u_{i-1,j} - u_{i-2,j}}{2(\Delta x)^3} + O[(\Delta x)^2] \tag{A.25}$$

$$\left.\frac{\partial^4 u}{\partial x^4}\right|_{i,j} = \frac{u_{i+2,j} - 4u_{i+1,j} + 6u_{i,j} - 4u_{i-1,j} + u_{i-2,j}}{(\Delta x)^4} + O[(\Delta x)^2] \tag{A.26}$$

Table A.2 Difference approximations for mixed partial derivatives.

$$\left.\frac{\partial^2 u}{\partial x \partial z}\right|_{i,j} = \frac{1}{\Delta x}\left[\frac{u_{i+1,j}-u_{i+1,j-1}}{\Delta z} - \frac{u_{i,j}-u_{i,j-1}}{\Delta z}\right] + O[\Delta x, \Delta z] \quad \text{(A.27)}$$

$$\left.\frac{\partial^2 u}{\partial x \partial z}\right|_{i,j} = \frac{1}{\Delta x}\left[\frac{u_{i,j+1}-u_{i,j}}{\Delta z} - \frac{u_{i-1,j+1}-u_{i-1,j}}{\Delta z}\right] + O[\Delta x, \Delta z] \quad \text{(A.28)}$$

$$\left.\frac{\partial^2 u}{\partial x \partial z}\right|_{i,j} = \frac{1}{\Delta x}\left[\frac{u_{i,j}-u_{i,j-1}}{\Delta z} - \frac{u_{i-1,j}-u_{i-1,j-1}}{\Delta z}\right] + O[\Delta x, \Delta z] \quad \text{(A.29)}$$

$$\left.\frac{\partial^2 u}{\partial x \partial z}\right|_{i,j} = \frac{1}{\Delta x}\left[\frac{u_{i+1,j+1}-u_{i+1,j}}{\Delta z} - \frac{u_{i,j+1}-u_{i,j}}{\Delta z}\right] + O[\Delta x, \Delta z] \quad \text{(A.30)}$$

$$\left.\frac{\partial^2 u}{\partial x \partial z}\right|_{i,j} = \frac{1}{\Delta x}\left[\frac{u_{i+1,j+1}-u_{i+1,j-1}}{2\Delta z} - \frac{u_{i,j+1}-u_{i,j-1}}{2\Delta z}\right] + O[\Delta x, (\Delta z)^2] \quad \text{(A.31)}$$

$$\left.\frac{\partial^2 u}{\partial x \partial z}\right|_{i,j} = \frac{1}{\Delta x}\left[\frac{u_{i,j+1}-u_{i,j-1}}{2\Delta z} - \frac{u_{i-1,j+1}-u_{i-1,j-1}}{2\Delta z}\right] + O[\Delta x, (\Delta z)^2] \quad \text{(A.32)}$$

$$\left.\frac{\partial^2 u}{\partial x \partial z}\right|_{i,j} = \frac{1}{2\Delta x}\left[\frac{u_{i+1,j+1}-u_{i+1,j-1}}{2\Delta z} - \frac{u_{i-1,j+1}-u_{i-1,j-1}}{2\Delta z}\right] + O[(\Delta x)^2, (\Delta z)^2] \quad \text{(A.33)}$$

$$\left.\frac{\partial^2 u}{\partial x \partial z}\right|_{i,j} = \frac{1}{2\Delta x}\left[\frac{u_{i+1,j+1}-u_{i+1,j}}{\Delta z} - \frac{u_{i-1,j+1}-u_{i-1,j}}{\Delta z}\right] + O[(\Delta x)^2, \Delta z] \quad \text{(A.34)}$$

$$\left.\frac{\partial^2 u}{\partial x \partial z}\right|_{i,j} = \frac{1}{2\Delta x}\left[\frac{u_{i+1,j}-u_{i+1,j-1}}{\Delta z} - \frac{u_{i-1,j}-u_{i-1,j-1}}{\Delta z}\right] + O[(\Delta x)^2, \Delta z] \quad \text{(A.35)}$$

A.1.2 Finite difference time-schemes

Schemes used for the time derivatives terms within the primitive equations are relatively simple, usually of the second and sometimes even only of the first order of accuracy. There are several reasons for this. First, it is a general experience that schemes constructed so as to have a high order of accuracy are mostly not very successful when solving partial differential equations. This is in contrast to the experience with ordinary differential equations, where very accurate schemes, such as the Runge-Kutta method, are extremely rewarding. There is a basic reason for this difference. With an ordinary differential equation, the equations and a single initial condition is all that is required for an exact solution. Thus, the error of the numerical solution is entirely due to the inadequacy of the scheme. With a partial differential equation, the error of numerical solution is brought about both by the inadequacy of the scheme and by insufficient information about the initial conditions, since they are known only at discrete space points. Thus, an increase in the accuracy of the scheme improves only one of these two components, and the results are not too impressive.

Another reason for not requiring a scheme of high accuracy for approximations to the time derivative terms is that it is usually necessary to choose a time step significantly smaller than that required for adequate accuracy. With the time step usually chosen, other errors, for example in the space differencing, are much greater than those due to the time differencing. Thus, computational effort is better spent in reducing these other errors, and not in increasing the accuracy of the time differencing. This does not mean that it is not necessary to consider carefully the properties of various possible time differencing schemes. Accuracy, is only one important consideration in choosing a scheme.

To define some schemes, we consider the equation

$$\frac{dU}{dt} = f(U,t), \qquad U = U(t). \tag{A.36}$$

The independent variable t is here called time. We divide the time axis into segments of equal length Δt. We shall denote by $U^{(n)}$ the approximate value of U at time $(n\Delta t)$. We assume that we know at least the first of the values $U^{(n)}$, $U^{(n-1)}, \ldots$ and we want to construct a scheme for computation of an approximate value $U^{(n+1)}$. There are many possibilities.

A. Two level schemes

These are schemes that relate values of the dependent variable at two time levels: n and $n+1$. Only a two level scheme can be used to advance an integration over the first time step, when just a single initial condition is available. With such a scheme we want to approximate the exact formula

$$U^{(n+1)} = U^{(n)} + \int_{n\Delta t}^{(n+1)\Delta t} f(U,t)\, dt. \tag{A.37}$$

We shall first list several schemes which do not use an iterative procedure.

i) Euler (Forward) scheme.

This is the scheme

$$U^{(n+1)} = U^{(n)} + \Delta t \cdot f^{(n)},$$

where (A.38)

$$f^{(n)} \equiv f(U^{(n)}, n\Delta t).$$

The truncation error of this scheme is $O[\Delta t]$. Thus, this is a first order accurate scheme. For the integrand in Eq. (A.37) we have here taken a constant value equal to that at the lower boundary of the time interval. Thus, f in Eq. (A.38) is not centered in time, and the scheme is said to be uncentered. In general, *uncentered schemes* will be found to be of the first order of accuracy, and simple centered schemes to be of the second order of accuracy.

ii) Backward scheme.

We can also take a constant value of f equal to that at the upper boundary of the time interval. We then obtain

$$U^{(n+1)} = U^{(n)} + \Delta t \cdot f^{(n+1)}. \tag{A.39}$$

If, as here, a value of f depending on $U^{(n+1)}$ appears in the difference equation, the scheme is called *implicit*. For an ordinary differential equation, it may be simple to solve such a difference equation for the desired value $U^{(n+1)}$. But, for partial differential equations, this will require solving a set of simultaneous equations, with one equation for each of the grid points of the computation region. If a value of f depending on $U^{(n+1)}$ does not appear in the difference equation the scheme is called *explicit*.

The truncation error of Eq. (A.39) is also $O[\Delta t]$.

iii) Trapezoidal scheme.

If we approximate f in Eq. (A.37) by an average of the values at the beginning and the end of the time interval, we obtain the trapezoidal scheme

$$U^{(n+1)} = U^{(n)} + \frac{1}{2}\Delta t \cdot (f^{(n)} + f^{(n+1)}). \tag{A.40}$$

This is also an *implicit scheme.* Its truncation error, however, is $O[(\Delta t)^2]$.

To increase the accuracy or for other reasons we can also construct iterative schemes. Two schemes that we will now define are constructed in the same way as Eq. (A.39) and Eq. (A.40), except that an iterative procedure is used to make them explicit.

iv) Matsuno (Euler-backward) scheme.

With this scheme a step is made first using the Euler scheme; the value of U obtained for time level $(n+1)$ is then used for an approximation to $f^{(n+1)}$, and this approximate value $f^{(n+1)*}$ is used to make a backward step. Thus,

$$\begin{aligned} U^{(n+1)*} &= U^{(n)} + \Delta t \cdot f^{(n)}, \\ U^{(n+1)} &= U^{(n)} + \Delta t \cdot f^{(n+1)*}, \end{aligned} \tag{A.41}$$

where

$$f^{(n+1)*} \equiv f(U^{(n+1)*}, (n+1)\Delta t).$$

This is an *explicit scheme*, of the first order of accuracy.

v) Heun scheme.

Here, in much the same way, an approximation is constructed to the trapezoidal scheme. Thus,

$$U^{(n+1)*} = U^{(n)} + \Delta t \cdot f^{(n)},$$

$$U^{(n+1)} = U^{(n)} + \frac{1}{2}\Delta t \cdot (f^{(n)} + f^{(n+1)*}). \tag{A.42}$$

Thus, this is also an *explicit scheme.* It is of the second order of accuracy.

B. Three level schemes

Except at the first step, one can store the value $U^{(n-1)}$, and construct schemes taking advantage of this additional information. These are three level schemes. They may approximate the formula

$$U^{(n+1)} = U^{(n-1)} + \int_{(n-1)\Delta t}^{(n+1)\Delta t} f(U,t)\, dt. \tag{A.43}$$

or, they can use the additional value $U^{(n-1)}$ to make a better approximation to f in Eq. (A.37).

i) Leapfrog scheme.

The simplest way of making a centered evaluation of the integral in Eq. (A.43) is to take for f a constant value equal to that at the middle of the interval $2\Delta t$. This gives the leapfrog scheme

$$U^{(n+1)} = U^{(n-1)} + 2\Delta t \cdot f^{(n)}. \tag{A.44}$$

Its truncation error is $O[(\Delta t)^2]$. This is probably the scheme most widely used at present in atmospheric models. It has been called the "*mid-point rule*", or "*step-over*" scheme.

ii) Adams-Bashforth scheme.

The scheme that is usually called the Adams-Bashforth scheme in the atmospheric sciences is, in fact, a simplified version of the original Adams-Bashforth scheme, which is of the fourth order of accuracy. The simplified version is obtained when f in Eq. (A.37) is approximated by a value obtained at the center of the interval Δt by a linear extrapolation using values $f^{(n-1)}$ and $f^{(n)}$. This gives

$$U^{(n+1)} = U^{(n)} + \Delta t \cdot \left(\frac{3}{2} f^{(n)} - \frac{1}{2} f^{(n-1)} \right). \tag{A.45}$$

This also is second order accurate scheme.

There are many other rather obvious possibilities. For example, one can approximate the integral in Eq. (A.43) using Simpson's rule , that is, fitting a parabola to the values $f^{(n-1)}$, $f^{(n)}$ and $f^{(n+1)}$. The implicit scheme obtained in this way is called the Milne-Simpson scheme. To illustrate the wealth of possible alternatives we note that in a paper by Young (1968) properties of

13 different schemes have been studied. Furthermore, when we are solving a more complicated partial differential equation, or a system of such equations, time (or space-time) differencing schemes can be constructed which are more complex than those which can be defined using the simple equation Eq. (A.36). Such schemes are widely used in atmospheric models.

A.1.3 Schemes with Uncentered Space Differencing

The space derivatives in the following equation can also be approximated using uncentered differencing.

$$\frac{\partial U}{\partial t} = -v\frac{\partial U}{\partial x} + \cdots \tag{A.46}$$

Still using values at two points for this approximation it is attractive for physical reasons to have one of these points as the central point and the second located on the side from which the fluid is being advanced toward the centre. Therefore we approximate the above equation by

$$\frac{U_j^{n+1} - U_j^n}{\Delta t} = -v_j^n \begin{cases} \dfrac{U_j^{n+1} - U_{j-1}^{n+1}}{\Delta x}, & -v_j^n > 0 \\[2ex] \dfrac{U_{j+1}^{n+1} - U_j^{n+1}}{\Delta x}, & -v_j^n < 0 \end{cases} \tag{A.47}$$

The simplest way to model the transport properties "better" is to use *upwind differencing* (Fig A.2)

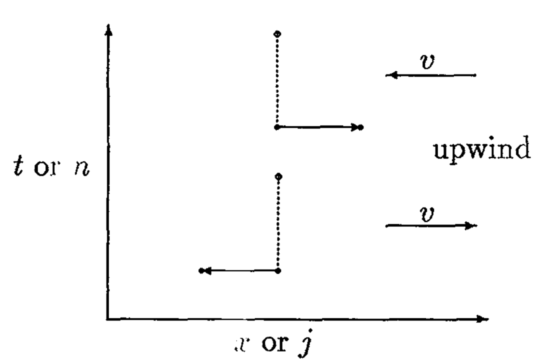

Fig A.2 Representation of upwind differencing schemes. The upper scheme is stable when the advection constant v is negative; the lower scheme is stable when the advection constant v is positive, also as shown.

Note that this scheme is only first-order, not second-order, accurate in the calculation of the spatial derivatives. How can it be "better" ? The answer is one that annoys the mathematicians: The goal of numerical simulations is not always "accuracy" in a strictly mathematical sense, but sometimes "fidelity" to the underlying in a sense that is looser and more pragmatic. In such contexts, some kinds of error are much more tolerable than others. Upwind differencing generally adds fidelity to problems where the advected variables are liable to undergo sudden changes of state, e.g., as they pass through shocks or other discontinuities.

CURRICULUM VITAE

Hakan ERDUN was born in Istanbul, Turkey on November 7, 1965. He completed high school in 1979. He got a B.Sc. degree from Istanbul Technical University, Faculty of Aeronautics and Astronautics, Department of Meteorological Engineering in 1986. He obtained his M.Sc. degree from Istanbul Technical University, Institute of Science and Technology, Meteorology Program in 1988. He has been working as a research assistant in the Department of Meteorology since 1989.

He worked as a researcher in Florida State University, Geophysical Fluid Dynamic Institute in 1995. He also worked as a guest scientist in Super Computations Research Institute of Florida State University in 1995. He got short scholarships from UNESCO, NATO and KOC Foundation.